Catalytic growth of carbon nanotubes

Vincent Jourdain

ACADEMIE DE MONTPELLIER

UNIVERSITE MONTPELLIER II
SCIENCES ET TECHNIQUES DU LANGUEDOC

Habilitation à diriger des recherches

Document de synthèse

Discipline :	**Milieux denses et matériaux**
Ecole Doctorale :	**I2S**

Vincent JOURDAIN

« De la croissance catalytique des nanotubes de carbone »

Soutenue le 12 décembre 2012 devant le jury composé de :

Pr Alan Windle	Professeur, University of Cambridge	Rapporteur
Dr Martine Mayne-L'Hermite	Directrice de Recherche, CEA Saclay	Rapporteur
Dr Philippe Poulin	Directeur de Recherche CNRS, CRPP, Bordeaux	Rapporteur
Dr Annick Loiseau	Directrice de Recherche ONERA, LEM, Châtillon	Examinateur
Pr Stephanie Reich	Professeur, Freie Universität, Berlin	Examinateur
Dr Jean-Louis Sauvajol	Directeur de Recherche CNRS, L2C, Montpellier	Examinateur

ACADEMIE DE MONTPELLIER

UNIVERSITE MONTPELLIER II
SCIENCES ET TECHNIQUES DU LANGUEDOC

Habilitation thesis

Synthesis document

Discipline:	**Condensed matter and materials**
Graduate school:	**I2S**

Vincent JOURDAIN

« Catalytic growth of carbon nanotubes »

Defended on December 12th, 2012, before the jury composed of:

Pr Alan Windle	Professor, University of Cambridge	Reviewer
Dr Martine Mayne-L'Hermite	Research director, CEA Saclay	Reviewer
Dr Philippe Poulin	Research director, CNRS, CRPP, Bordeaux	Reviewer
Dr Annick Loiseau	Research director, ONERA, LEM, Châtillon	Examiner
Pr Stephanie Reich	Professor, Freie Universität, Berlin	Examiner
Dr Jean-Louis Sauvajol	Research director, CNRS, L2C, Montpellier	Examiner

Foreword

The "*habilitation à diriger des recherches*" (HDR) is the highest degree for university studies in France. Based on the creation decree of 8 November 1988, HDR attests to the holders' high scientific level, the originality of their approach in a scientific domain, the ability to master a research strategy in a sufficiently broad field of investigation and to supervise young scholars. Moreover, it qualifies the holders to supervise PhD theses and to apply for university professorship. In a researcher's career, the passing of HDR is therefore a special step by acknowledging the aptitude to independently design and lead scientific investigations. As such, it represented the first motivation of the present document. The decree stipulates that the jury evaluates the ability of the candidate to "design, lead, animate and coordinate research and valorisation activities" but gives no other indication concerning the content of the *habilitation* document. Because of this freedom and of researchers' creativity, HDR manuscripts vary widely in structure and content.

Looking forward in search of the next big thing (and likely to be funded) is a motto of current scientific research. This participates to make research an exciting (and often hectic) activity. However, there are few opportunities for a researcher to look backward to his/her own work. *Habilitation* is a notable exception since presenting a summary of the research one led is a central part of the exercise. Here, I chose to not give an exhaustive description of the projects I have been involved in as a tenure researcher. Instead, I found more pertaining to focus on the topic which has constituted my main research interest for the last twelve years which is the growth mechanism of carbon nanotubes. In doing so, I notably aimed at taking a fresh, critical and general look to our works to find which results were comforted, which important data were overlooked or which interpretation now appears mistaken. This critical synthesis is the purpose of the second part of this manuscript.

Eric J. Mittemeijer wrote in "Fundamentals of Materials Science" that "a prerequisite of scientific research is command of existing literature". In the field of carbon nanotubes, about 5000 publications come out each year. Given this torrent of publications, one has to find strategies to keep up-to-date with the literature and tools to organize the collected information. In most cases, people will either focus on a very specific field or rely on the works reported in a few selected conferences and journals. This is a common source of frustration since researchers frequently argue with each other with different references in mind. Fortunately, every two or three years, a literature review may come out. I first learned about carbon nanotubes by coming upon a literature review by Pulickel Ajayan in the library of Elf Atochem (now Arkema) in Lyon during my Master internship. Since then, my amazement for these exquisite structures has never stopped. HDR represented an opportunity for me to allow time on synthesizing my own reading notes into a document that I could share with my students (especially fresh ones) and colleagues. This was also a unique opportunity of scientific (and humorous) exchanges with my theoretician colleague Christophe Bichara at Cinam, Marseille, who significantly contributed to the theoretical aspects and to the general quality of this review. The first part of this document is constituted by this review.

This document is written in English (or, more precisely, in the English-like dialect used by researchers to communicate with each other). The historians J.C. Barreau and G. Bigot wrote that "when a people cease to teach in their own language, they disappear". As a teacher, I feel concerned by this and I regularly emphasize to my students the importance of using and mastering their native language (especially at writing) even for scientific careers. As a researcher, exchange observations and opinions with my colleagues around the world is a central aspect of my activity and this is usually and most efficiently done in English, the current Koinè. Since this manuscript is primarily a research document, I chose to write this

document in English even though this is still relatively unusual for a French *habilitation*. It also gave me the opportunity to have this document reviewed by and shared with colleagues sharing the same research interests without limitation of language.

Bonne lecture.

Table of contents

à Florence et Simon

1. General introduction

The last two decades have seen a burst of synthetic nanomaterials stimulated by the prediction of novel properties stemming from their nanoscale dimensions. Among them, carbon nanotubes (CNTs) are particularly attractive nano-objects notably because of the strong influence of their structural features on their electrical and optical properties. Single-walled carbon nanotubes (SWCNTs) [1] constitute a family of tubular molecules that have diameters in the nanometer range and are made solely of carbon atoms linked by sp^2 bonds (Figure 1-1a). Their periodic structure can be defined either by their diameter and chiral angle (between -30° and +30°) or by (n,m) Hamada indices which are the coordinates of the vector describing the circumference of the unrolled nanotube in the referential frame of graphene. SWCNTs with (n-m) values that are multiples of 3 are metallic conductors while SWCNTs with (n-m) values that are not multiples of 3 are semiconductors with an energy gap that is inversely proportional to their diameter. All SWCNTs exhibit characteristic singularities in their electronic densities of states, the so-called Van Hove singularities, which results in optical transitions specific to each (n,m) nanotube (Figures 1-1b,c).

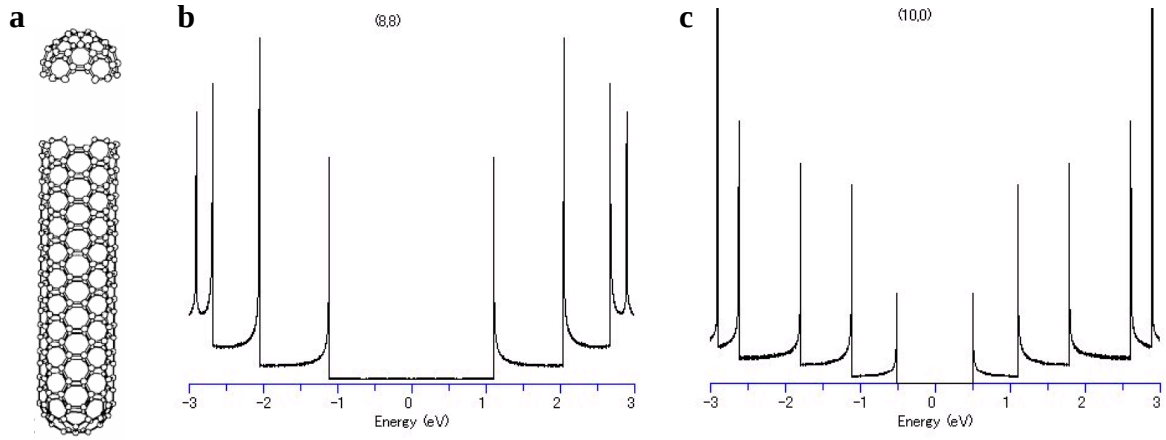

Figure 1-1. (a) Schematic structure of a (6,6) carbon nanotube. Calculated densities of electronic states of (b) an (8,8) metallic nanotube and (c) a (10,0) semiconducting nanotube.

Controlling their structural features soon appeared to be a particularly challenging task. Various synthesis approaches, such as arc discharge and laser ablation, were developed aiming at producing pure and well-controlled CNT samples in large quantity [2]. Due to its higher degree of control and its scalability, Catalytic Chemical Vapour Deposition (CCVD) is now the standard synthesis method of CNTs. CCVD is at the crossing of two important chemical methods: thin-film growth by Chemical Vapour Deposition (CVD) and chemical conversion by Gas-Solid Heterogeneous Catalysis (GSHC). CCVD consists in the catalytic conversion of a gaseous precursor into a solid material at the surface of catalyst particles or of a continuous catalyst film. Novel aspects specific to CCVD arise from the combination of CVD and GSHC. For instance, the template effect of the catalyst surface on the shape of the growing material is central in CCVD: in the case of catalyst nanoparticles, one-dimensional objects such as nanotubes and nanowires can be grown; if the catalyst is in the form of a continuous film, two-dimensional materials such as graphene can be prepared. Compared with GSHC, the catalyst in CCVD is not only in contact with the gas phase and a support, but presents an additional interface with the growing solid material. This imposes a supplementary difficulty because both interfaces must be preserved to continuously grow nanotubes/nanowires without disrupting the gaseous supply.

The simplest system to grow CNTs by CCVD consists of catalyst nanoparticles brought to high temperature in presence of gaseous carbon-bearing molecules. The nanoparticles are commonly of a transition metal such as Fe, Ni or Co, but other elements and compounds have recently proven to be efficient catalyst as well. In many cases, the catalyst particles are deposited on a support material such as SiO_2 or Al_2O_3. It is apparent from the beginning that the size and shape of the catalyst particle and its interactions with the other components of the system play central roles in CCVD. Generally speaking, it is commonly accepted that efficient catalyst particles should fulfil the following functions [3-6].

1) Catalyze the dissociation of the gaseous carbon-bearing molecules.

2) Allow the diffusion of carbon intermediates and their chemical interaction.

3) Provide a nanoscale template for the nucleation and growth of a nanotube.

4) Keep a reactive nanotube rim.

Functions 1 and 2 are also found in heterogeneous catalysis and justify the use of the term *catalyst particle*, *i.e.* a particle that helps in rapidly achieving the chemical equilibrium between the carbon-bearing molecules and a graphene-type material. Functions 3 and 4 are unique to CCVD catalysts and impose different constraints compared with GSHC catalysts, which justifies the use of the alternative term *seed particle*.

Since the first reports of catalytic formation of filamentous carbon in the early 1970s [7-11], significant progress has been made in terms of synthesis yield, nanotube alignment and sample purity [12]. However, CCVD-grown samples still generally suffer from a lack of structural control over the nanotube chirality, the semiconducting / metallic ratio, and the nature and density of defects. This observation highlights that numerous aspects of the growth mechanism remain ill-understood.

The next chapter aims at giving a review of the current understanding of CNT growth by CCVD.

2. Literature review

2.1. Introduction

There have been previous reviews in the field [3-6,13-15] with different objectives (*e.g.* chronological description of the achievements and evolution of methods, focus on simulation works, on the role of the catalyst particles or on a particular type of CCVD such as plasma-enhanced). Compared with them, this chapter will largely ignore the chronological and technological aspects and focus only on the fundamental aspects of the growth mechanism of CNTs by CCVD. The first part gives background knowledge derived from neighbouring fields which is relevant to the understanding of the catalytic growth of CNTs. It is firstly aimed at beginners in the field (*e.g.* Master and PhD students). The second part aims at providing a synthesis of the most relevant works addressing the experimental dependence of CNT features on CCVD conditions. Finally, the third part is devoted to describe important questions that are still open and to discuss the related hypotheses currently proposed.

2.2. Background knowledge

In this chapter is provided some background knowledge useful to have before starting to investigate the peculiarities of the catalytic growth of CNTs. This background knowledge is mostly derived from chemical vapour deposition, heterogeneous catalysis and metallurgy. The chapter is divided in five parts devoted to: i) the type of carbon precursors used for CNT growth and their chemical reactivity, ii) the type of nanoparticles used to grow CNTs in CCVD and the size dependence of their physical properties, iii) the interactions of transition metals with carbon, iv) the catalytic activity of transition metals, and v) the interactions of transition metal nanoparticles with their solid and gaseous environments.

2.2.1 Carbon precursors

- *Types of carbon precursors*

A large number of carbon-bearing molecules can be used as a carbon source to grow CNTs in CCVD: hydrocarbons (gaseous [16] or liquid [17]), alcohols [18], aromatic compounds [19] or even naturally-occurring carbon resources [19]. Ethylene, acetylene, methane, carbon monoxide and ethanol are presently the most frequent precursors of CNTs in CCVD (Figure 2-1). It is important to keep in mind that such gaseous carbon precursors not only bear carbon but also other elements such as hydrogen and/or oxygen. These elements are not compulsory since CNTs can be grown from pure carbon [20,21] as commonly achieved in arc discharge and laser ablation syntheses by sublimation of graphite [2]. However, the by-production of hydrogen- and oxygen-bearing molecules such as H_2 and H_2O may impact the formation of CNTs. H_2 and H_2O are actually common additives in CCVD with recognized influence on CNT growth as discussed hereafter. Nitrogen- [22], phosphorus- [23] and boron-bearing [24] precursors are known to form substitutionally doped CNTs. However, the influence of oxygen and hydrogen on the defects of CCVD-grown CNTs is still poorly known.

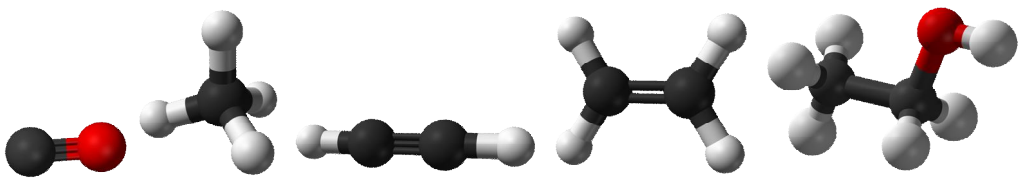

Figure 2-1. Common carbon precursors of CNTs in CCVD. From left to right: carbon monoxide, methane, acetylene, ethylene and ethanol (black: carbon, red: oxygen, white: hydrogen).

- *Reactivity*

Thermodynamic stability is obviously an important feature of a chemical precursor. Figure 2-2 shows the standard Gibbs energy of formation for different carbon precursors as a function of temperature in the Ellingham approximation. Except for methane, all precursors decompose exothermally. It is seen that methane is more stable than graphite for temperatures lower than 600-700°C. At atmospheric pressure, acetylene, ethylene and ethanol are less stable than graphite at all temperatures while carbon monoxide is more stable than graphite at temperatures higher than about 700°C. It is important to remember that the conversion equilibriums and the inversion temperatures will vary with the partial pressures of the involved gaseous species.

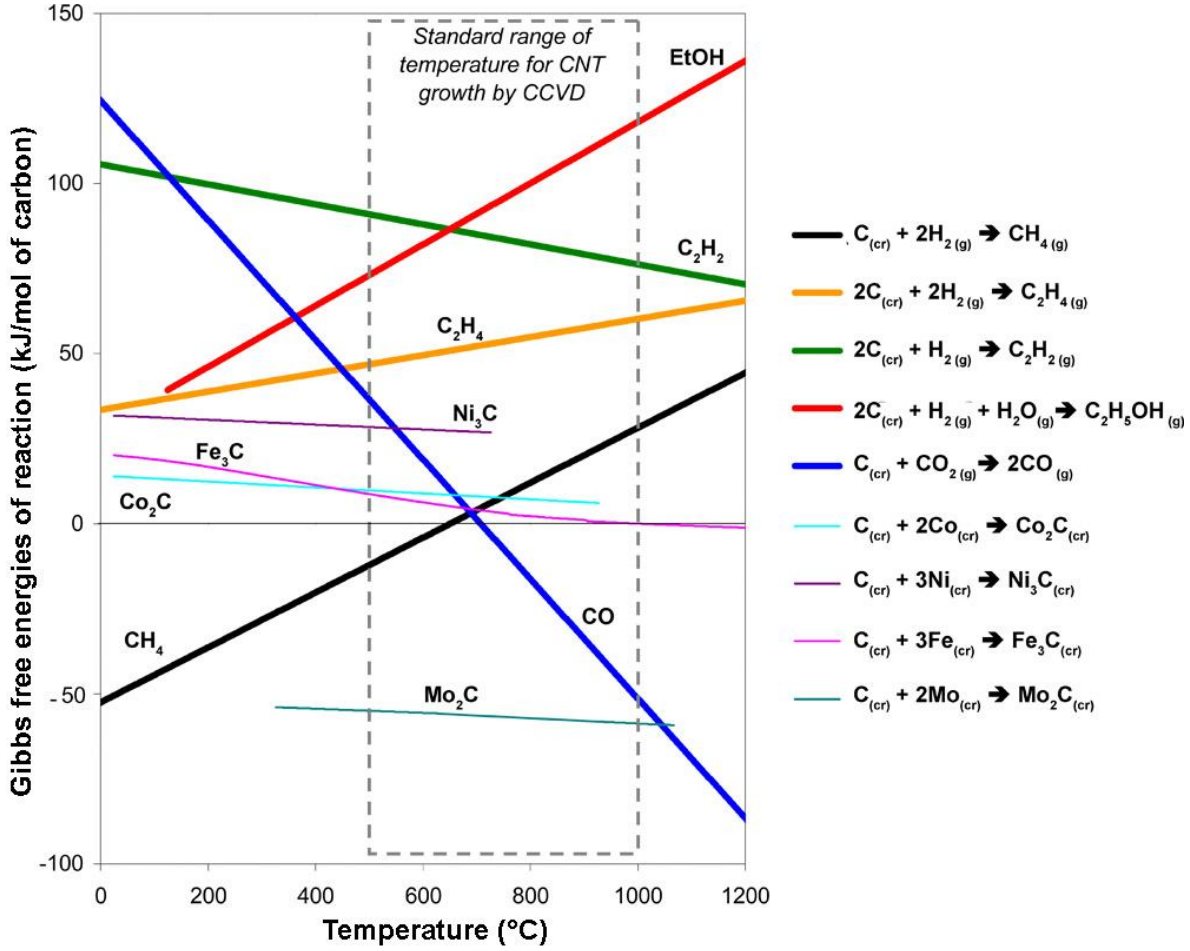

Figure 2-2. Gibbs free energies of reaction per mole of carbon for the formation of some common carbon feedstocks and metal carbides. "cr" and "g" respectively stand for crystalline and gaseous. Data from [25,26].

This being said, some general comments can still be drawn. The pyrolysis of methane requires high temperatures to become thermodynamically allowed. Its conversion into higher organic compounds is thermodynamically restricted: experimentally, the main products of methane decomposition are simply carbon and dihydrogen [27]. If coupled with oxygen, methane can form other compounds such as CO_2, CO [27], C_2H_4 and C_2H_6 [28,29]. At the opposite, the decomposition of acetylene, ethylene and ethanol is thermodynamically allowed at all temperatures and occurs readily provided a sufficient activation. Due to their high Gibbs energies of formation, these latter compounds can self-decompose into carbon, dihydrogen and a large variety of volatile organic compounds and polycyclic aromatic hydrocarbons [30-33]. The disproportionation of CO into carbon and CO_2 (*i.e.* the Boudouard reaction) is the

main reaction path in the absence of other reactants (*e.g.* H_2 [34]). The reaction being highly exothermic, the reaction equilibrium shifts toward the reactants when increasing the temperature. Since the number of gaseous molecules decreases in the Boudouard reaction, the equilibrium conversion also increases with increasing pressure.

Beside Gibbs free energies, the stability of a carbon precursor is illustrated by the strength of its chemical bonds. Table 2-1 presents the dissociation energy of the weakest C-H bond of different hydrocarbons. It is apparent that the strength of the C-H bond decreases with increasing the number of carbon neighbours. A similar trend is observed in the case of a carbon-metal bond as described in §2.2.3.

Hydrocarbon	*Weakest C-H bond*	*C-H bond dissociation energy (kJ/mol) / (eV)*	*Atomic charge on H*
Methane	Primary	440 / 2.7	+0.087
Ethane	Primary	420 / 2.6	+0.002
Propane	Secondary	401 / 2.5	-0.051
Isobutane	Tertiary	390 / 2.4	-0.088

Table 2-1. Dissociation energies of C-H bonds and charge on H of some light hydrocarbons. From [35].

2.2.2 Catalyst nanoparticles

- *Types of nanoparticles*

Nickel, iron and cobalt are the most common catalysts for CNT growth by CCVD. Over the years, many other elements have proven suitable. Beside Fe, Ni and Co, MWCNT growth have been reported using nanoparticles of Pd [36], Pt [36], Au [37], Mn [36], W [36], Ti [36], TiC [38], Mg [36], Al [36], In [36], Na [36], K [36] and Cs [36]. These nanoparticles were usually larger than 3 nm. Beside Fe, Ni and Co, SWCNT growth was reported using nanoparticles of other late transition metals (Pd [39], Pt [39], Ru [40]), noble metals (Cu [39,41], Ag [39], Au [39,42]), early transition metals (Mn [43], Cr [44], Mo [45]), elements of the carbon family (diamond [46], Si [47], Ge [47], Sn [44], Pb [44]), lanthanides (Gd [48], Eu [48]) and other mixed compounds ($FeSi_2$ [49], SiC [47,50], SiO_2 [51,52], Al_2O_3 [52], TiO_2 [52], Er_2O_3 [52], ZnO [53]). These nanoparticles were usually less than 3 nm.

Binary mixtures of active catalysts such as Ni, Fe and Co are frequently used and often observed to display a higher activity than individual elements [54]. Non- or weakly active elements are also frequently mixed as co-catalysts, notably to prevent or control the coarsening of the catalyst. They notably include Mo [55,56] and Mg [57] mixed with Fe or Co.

Considering this wide variety of active elements and compounds, one may wonder which properties are actually required to promote the growth of CNTs. Hereafter are summarized some important properties of nanoparticles starting by the size dependence of their physical properties.

- *Vapour pressure and melting point*

The physical state of the catalyst during CNT growth (*i.e.* solid or liquid) is important because it influences several properties of the catalyst such as the solubility of carbon and its diffusion rate. It is still a highly debated issue (see §2.4.1) whose resolution is complicated by three effects.

First, in the presence of carbon, the melting point can be decreased by up to a few hundred degrees for the elements displaying a eutectic point in their phase diagram with carbon (*e.g.* Fe, Co, Ni, Pt, Pd, Rh, Ru, Ir, Re). Second, for particles in the range of 1-10 nm, the equilibrium vapour pressure is significantly increased which is usually approximated by the Kelvin (or Gibbs-Thomson) equation. The equilibrium vapour pressure of a particle of radius r in contact with a vapour phase can be written as:

$$p = p_0 \exp\left(\frac{2\sigma_{sg}V}{kTr}\right)$$

where p and p_0 are the equilibrium vapour pressures over curved and flat surfaces, respectively; σ_{sg} is the surface tension at the particle-gas interface, V is the volume of an atom in the particle, k is the Boltzmann constant and T is the temperature. The relation illustrates the fact that particles with a higher surface-to-volume ratio have a lower stability. A practical consequence is that particles tend to evolve toward larger sizes as first described by W. Ostwald (see Ostwald ripening in §2.2.5). In the case of a liquid or solid environment, an analogous equation can be written to express the equilibrium concentration in the outer environment surrounding the nanoparticle. Another consequence is that the melting point of nanoparticles is significantly depressed. The melting point of a nanoparticle in its own liquid can be approximated by:

$$T_m(r) = T_m^{bulk}\left(1 - \frac{4\sigma_{sl}}{H_f \rho r}\right)$$

where $T_m(r)$ and T_m^{bulk} are, respectively, the particle and bulk melting points, σ_{sl} is the surface tension at the solid-liquid interface, H_f is the bulk latent heat of fusion per volume unit and ρ is the density of the particle.

All these effects originate from the large contribution of surface atoms to the total energy of the system. If the nanoparticles are deposited on a substrate, the interaction is therefore also expected to affect the melting point, which is the third effect to consider. As an example, Shibuta *et al.* [58] calculated that the melting point of a nickel cluster could increase by up to 200°C with increasing interaction with the support.

2.2.3 Interaction of carbon with transition metals

- *Affinity for carbon: carbon solubility and formation of carbides*

In general, the ability of transition metals to bond with carbon atoms increases with the number of unfilled d-orbitals. Metals without d-vacancies in their electron configuration, such as Zn or Cu, display a negligible affinity for carbon. Metals with few d-vacancies such as Ni, Fe and Co exhibit finite carbon solubility. Transition metals with many d-vacancies such as Ti and Mo can form strong chemical bonds with carbon and highly stable carbides. For transition metals, the affinity for carbon therefore increases from the right to the left of the periodic table [59-61]. For example, the solubility of carbon at 700°C (a typical synthesis temperature for CNTs) is below detection limit in Zn, 0.01% at. in Cu, 0.3-0.5% at. in Ni and 1.2% at. in fcc-Co. Elements from Mn to Ti form carbides of increasing stability and increasing carbon share (Figure 2-3). Fe is an intermediate case: Fe forms the metastable Fe_3C carbide, the solubility of carbon is relatively low in α-Fe (~0.1% at. at 700°C) but substantial in γ-Fe (~4% at. at 800°C). At some exceptions, the solubility of carbon atoms in metals generally increases with temperature as apparent in the related binary phase diagrams.

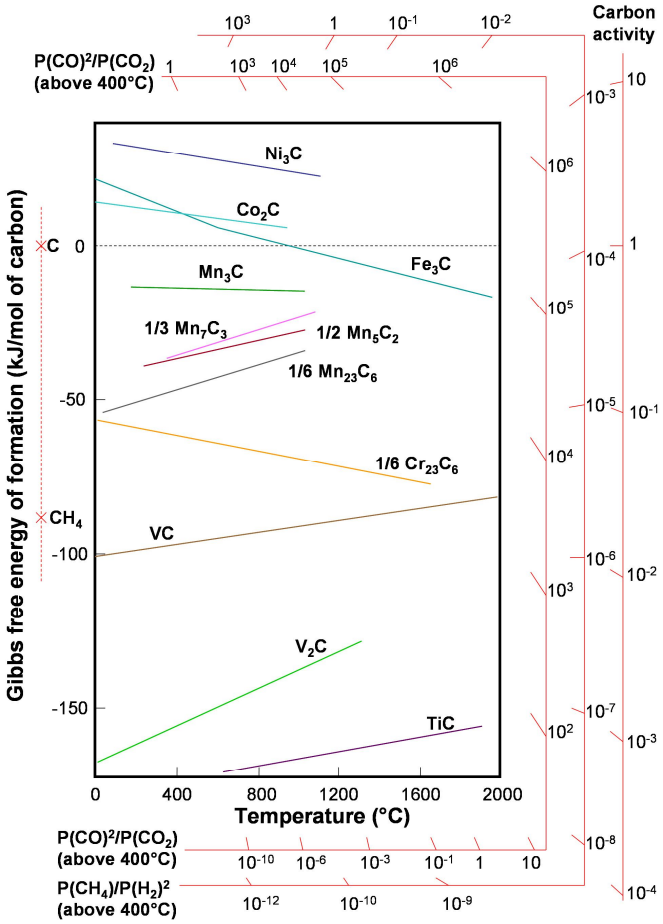

Figure 2-3. Ellingham diagram for carbides of 3d transition metals. Adapted from [25].

Graphitic carbon will be allowed to form if the carbon concentration overcomes the solubility of carbon in the catalyst particle. For elements that do not form stable carbides (*e.g.* Cu, Ni, Co, Pb, Sn, Au, Ag, Zn, Cd, Pd, Pt) [62], the critical concentration for the segregation of graphitic carbon is therefore the solubility limit of carbon in the metal. For carbide-forming elements, the carbon concentration must exceed the carbon content of the highest carbide (*e.g.* Mn_3C for Mn, TiC for Ti) for graphitic carbon to form.

A complicating factor is the influence of the particle size on the solid solubility of impurities, such as carbon, and on the stability of mixed compounds (*i.e.* carbides) [63-65]. The solubility of carbon in nanoparticles is not well established and is still a subject of controversy. Experimentally, there are many reports of increased solubilities inside nanoparticles [64-68], including a giant increase of carbon solubility in Au nanoparticles [69]. A Kelvin-type relation has sometimes been used to explain the experimental observations although this relation actually describes the solubility in the medium around the nanoparticle, as already stressed by A. Harutyanyan [6], and not the solubility inside the nanoparticle. Over the last years, thermodynamic models specifically addressing the solid solubility of impurities inside nanoparticles have been devised based on different assumptions: size-dependent entropy [70], regular solution theory [71], quantum confinement of elementary excitations [72], size-dependent melting enthalpy, entropy and atomic interaction energy [73] or linear concentration dependence of the surface energy [74]. In general, these thermodynamic models predict an increase of the solubility of impurities inside nanoparticles of decreasing size. In certain models, however, both solubility increase and decrease are possible depending on the relative binding strengths between atoms in the system. The matter is therefore not well established yet in both the general case and in the particular case of the dissolution of carbon

inside metal nanoparticles. Recently, Diarra *et al.* [75] reported Grand Canonical Monte Carlo simulations to calculate the adsorption isotherms of carbon on nickel nanoparticles of varying size: they found that at a given carbon chemical potential and temperature, smaller nickel nanoparticles dissolve a larger fraction of carbon than larger ones due to the larger carbon solubility in subsurface than in the bulk.

Experimental observations long supported that catalysts having intermediate carbon solubilities (between 0.5 and 1.5 wt.%) and not forming stable carbides were required to promote CNT growth [38] although the reason for that was unclear. The reports of novel catalysts displaying both low (*e.g.* Cu) and high (*e.g.* Ti) affinities for carbon should probably lead to reconsider this conclusion.

- *Carbon diffusion: bulk, surface and subsurface*

The diffusion mode of carbon atoms during CNT growth (bulk *versus* surface diffusion) has long been and still is a debated issue. The solid-state diffusion of impurities in metals has been studied for many years, notably for metallurgy purposes. Figure 2-4 shows the solid-state diffusion constants of carbon in various bulk metals and metal carbides as a function of temperature. Despite the absence of a simple rule, some general trends can be drawn [76].

i) The bulk diffusion of carbon atoms is much faster than that of the atoms of the solid metal host since the former ones diffuse interstitially while the latter ones diffuse substitutionally.

ii) Interstitial diffusion depends on the geometry of the host lattice and is faster in more open structures. For instance, the activation energy for carbon diffusion is 1.53-1.57 eV in close-packed fcc Fe while only 0.83 eV in bcc Fe [77,78].

iii) The higher the melting-point of the host, the smaller the diffusion constant of the solute atoms. For instance, in the case of α-Fe, V and Mo that are all bcc metals, but with significantly different melting points, the diffusion constants inversely follow the order of melting points, that is Fe (T_m=1808 K) > V (T_m=2160 K) > Mo (T_m=2890 K).

iv) The diffusion constant depends inversely upon the solid solubility, being least for metals which form a continuous series of compounds (*i.e.* carbides in the case of carbon diffusion). For instance, in the case of Pd, Ni and γ-Fe which are all fcc metals with close melting points, the diffusion constants inversely follow the order of carbon affinity, that is Pd > Ni > Fe.

Studies of carbon diffusion revealed a strong dependence of the diffusion coefficients on the carbon concentration [76,79,80]**.** For instance, the activation energy for bulk diffusion of carbon in fcc-Fe decreases from 1.55 eV to 1.24 eV if the amount of dissolved carbon is increased by 6 at. % [81]. In Ni, calculations predict that for carbon concentrations above 50 at. % in the first subsurface layer, the carbon diffusion barrier would decrease from 1.6 eV to below 1.0 eV [82]. This effect is usually explained by the lattice expansion caused by the addition of carbon. It has also been proposed that the repulsion between carbon atoms at close distance could enhance the diffusivity of interstitial carbons [83].

However, for very high carbon contents as encountered in carbides, it is commonly observed that the activation energies for carbon diffusion are much higher than in the corresponding metals (see Figure 2-4). This is tentatively explained by the fact that carbon diffusion in carbides is no longer interstitial but mediated by thermal vacancies in the metal and carbon sub-lattices [84]. For instance, the activation barrier is 1.60-1.92 eV in Fe_3C [85-87], 3.4 eV in TiC [88], 3.1 eV in VC [89] and 2.9-3.6 eV in Mo_2C [90] and 2.6 eV in WC

[89]. As a consequence, the bulk diffusion constants of carbon in metal carbides are usually much lower than in the corresponding metals as apparent in Figure 2-4. It is worth noting that the diffusional mobility of the metal atoms in carbides is still several orders lower than that of carbon atoms [91].

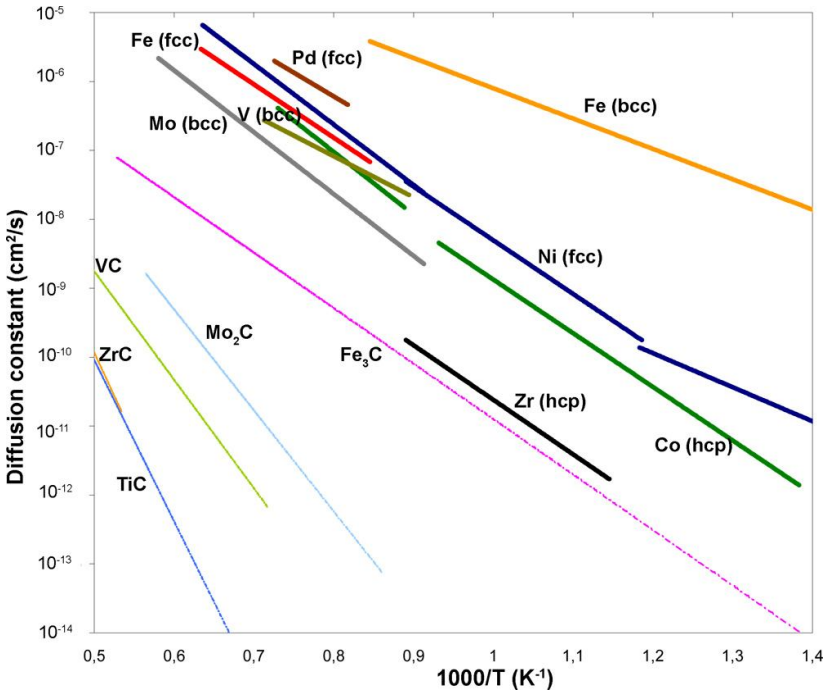

Figure 2-4. Bulk diffusion constants of carbon in various metals and metal carbides as a function of temperature. The activation energies for bulk diffusion of carbon was measured to be 1.44-1.74 eV in Ni (fcc) [78,82,92,93] (at the exception of Massaro *et al.* [94] who found 0.87 eV in the range 350-700°C), 1.50-1.68 eV in Co (hcp) [78,95], 1.53-1.57 eV in fcc Fe [77,78], 0.83 eV in bcc Fe [77,78], 1.20 eV in V [78,96,97], 1.37 eV in Pd [98,99], 1.44-1.78 eV in Mo [78,100] and 1.58 eV in Zr [101].

Addition of other elements also influences the diffusion rate of carbon. For instance, the diffusion constant of carbon in fcc-Fe increases with the concentration of Ni and Cu, but decreases in the presence of carbide-forming elements such as Cr, W, Mo and others [79]. Other elements like Si and Co raise or lower the diffusion coefficient of carbon, depending on the temperature and their concentration [79,102]. In agreement with these measurements, calculations predict that the addition of small amounts of Au would dramatically reduce the diffusion barrier from 1.6 eV for pure Ni to 0.07 eV for Ni with 6 at. % of Au [92].

Much less data are available concerning the surface diffusion of carbon. In general, the activation barriers are found to be significantly lower than for bulk diffusion. For instance, calculations on the surface diffusion on Ni(111) and Ni (110) yielded a barrier of 0.4-0.5 eV [103] in good agreement with the experimental value of 0.3 eV measured on a polycrystalline Ni surface [104]. First-principles calculations by Yazyev and Pasquarello [60] on Ni, Pd, Pt, Cu, Ag and Au yielded that bulk diffusion has systematically a higher activation barrier than surface and subsurface diffusions. Surface-to-subsurface diffusion is another interesting case to consider: Xu and Saeys [82] calculated an activation barrier for carbon on Ni(111) of 0.7 eV at low carbon coverage, a value that is intermediate between surface and bulk diffusion.

Like solubility, the diffusion rate of carbon in nanoparticles may be dependent on the particle size. Despite some experimental observations [105], this potential effect is still insufficiently documented.

- *Theoretical aspects of the interaction of carbon structures with metal surfaces*

For the catalytic growth of CNTs, a key aspect is the carbon-metal interaction which strongly depends on the nature of the metal. The problem is made complex by the unique ability of carbon to form various structures with different bonding characters. The adsorption energy also depends on the different surface sites available on different structures (flat surface with different orientations, steps, clusters …). Interstitial subsurface and bulk sites have been considered in the literature as well as carbon dimers.

For Ni, Pd, Pt, Cu, Ag and Au [60,82,106-108], the adsorption of a single carbon atom is less stable than its incorporation in a graphene layer, with energy differences of the order of 1 eV per carbon atom for Ni, Pd, Pt and 2-4 eV per carbon atom for noble metals. Subsurface sites are more favourable than bulk incorporation or adsorption on various surface sites. For Ni and Co, hollow (100) semi-octahedral sites are more favourable than compact facets [109,110]. When suitable surface coverage is reached, this leads to the (2x2) P4g "clock" surface reconstruction observed on Ni (100) [111,112]. Complex behaviour is also predicted on different facets of Fe, an important catalyst for CNT growth. Carbon adsorption on the different facets of bcc Fe has be shown to substantially modify their surface energies [113-115]. At low surface coverage, carbon atoms are separated from each other and their binding on late transition metal surfaces is stronger on open sites than on compact facets. On a bcc Fe (100) facet with a somehow larger (2/3) surface coverage, carbon chain structures have been experimentally evidenced and found to be strongly interacting with the surface [116,117].

Carbon dimers are found to be the most stable adsorbed species on noble metals, and close to it on Ni [118]. More precisely, acetylene which can be consider as a prototype of carbon dimer is more strongly adsorbed on Ni than on Pd, Pt and Rh (111) surfaces [119] in agreement with the chemisorption model of Nørskov (see §2.2.4). Tight binding calculations, allowing the relaxation of large simulation boxes, indicate, in agreement with experiments, that dimers can be stabilized in subsurface, involving strong local distortions [120].

Starting from individual atoms, dimers and chains on the metal surface, the next step is the study of the interaction of caps or tubes with flat surfaces or metal nanoparticles. In this case, carbon atoms have already formed bonds with other neighbouring carbons, and, as a consequence, the interaction with the metallic surface is weaker. This kind of calculations still relies on some assumptions, concerning, in particular, the structure of the metal catalyst, generally taken as pure (no carbon dissolved in) and crystalline. In view of explaining chiral selectivity, Reich *et al.* [121] calculated the interaction of carbon caps of different chiralities with a flat Ni (111) surface, showing small energy differences between them. Ding *et al.* [122] have calculated the strength of the carbon nanotube-metal interaction and found a stronger binding with Fe, Co and Ni bind than with Pd, Cu and Au. Larsson *et al*. [123] calculated that the adhesion energy between metal clusters and SWCNT caps follows the order Fe~Co>Ni. Depending on the tube chirality, bond strengths were found to be in the range of [-2.5, -1.5] eV/bond in the case of iron.

Much weaker interaction energies are expected for carbon structures (*e.g.* flakes) lying almost flat on the metal surface. Lacovig *et al*. [124] studied the evolution of the binding energy of carbon flakes on Ir (111) as a function of the flake size, starting from almost zero (graphene layer) to -1.2 eV per carbon atom for a C_6 ring, emphasizing the role of the edge atoms contribution in the binding. When the flakes grow larger, one tends towards a graphene structure that generally interacts weakly with metal surfaces. It may be expected that the adhesion strength of the graphene sheet also depends on the amount of carbon dissolved in the metal particle although this dependence is still rarely addressed in the literature.

In summary, one can qualitatively consider that the interaction of carbon with a metal surface is strongest for isolated atoms and decreases when C-C bonds with neighbouring carbon atoms, corresponding to strong lateral interaction, are formed. The ultimate limit is the formation of a full graphene layer on a flat metal surface that has weak adhesion energy.

2.2.4 Catalytic activity of transition metal nanoparticles

- *Dissociative adsorption on transition metal surfaces*

The role of a catalyst is to aid in rapidly achieving a chemical equilibrium by creating a transition state of lower energy. The decrease of activation energy depends on the strength of the adsorbate-substrate bond which experimentally reflects in the heat of adsorption [125]. There is a general trend for the heats of adsorption to decrease from the left to the right of the periodic table. For instance, the heat of adsorption of CO on polycrystalline Ti is 6.5 eV, but only 0.9 eV on polycrystalline Cu [125]. This trend can be explained by the chemisorption model developed by Nørskov [126] stipulating that molecules adsorbing on transition metals preferentially interact with the d-states near the Fermi level that give rise to bonding and anti-bonding levels. The d-electron contribution to the adsorbate bonding is therefore inversely proportional to the degree of filling of the d-band.

When a molecule is adsorbed on a metal surface, the activation barrier for its dissociation is lowered. For instance, the activation barrier for the dissociation of acetylene was measured to be 1.4 eV on Ni(111) instead of 5.6 eV for self-decomposition [103]. If the surface bonds are too strong, the reaction intermediates will remain on the surface and block the adsorption of new reactant molecules. Forming adsorbate-substrate bonds of intermediate strength is an important property of a good catalyst. As a consequence, the catalytic activity of transition metals for a given reaction often displays a volcano-shaped pattern across the periodic table [127]. For instance, acetylene and ethylene are observed to be very weakly adsorbed on noble metals such as Au, Ag and Cu [125] while, on other transition metals, the adsorption of unsaturated hydrocarbons is generally strong and dissociative. When one adsorbs an unsaturated hydrocarbon onto a transition-metal surface at low temperature and then heats the surface, the molecule decomposes and leaves the surface covered with partially dehydrogenated fragments (*e.g.* ethylidyne) or carbon, rather than desorb from the surface. At higher temperatures, polymeric carbon chains with the general formula C_xH are formed, which progressively transforms in a graphitic layer [125].

It was also demonstrated that the dissociative adsorption of hydrocarbons often leads to the population of subsurface sites even in metals having low carbon solubility. For instance, Teschner *et al.* [128] reported a carbon content of 35 to 45 at % in the three top layers of Pd under alkyne exposure at 350 K while the bulk solubility of carbon in Pd is less than 1 at. % at this temperature. The surface carbide was found to be stable only in the reaction ambient. Importantly, the degree of subsurface population by carbon was found to strongly influence the catalytic activity and selectivity.

- *Catalytic activity of transition metal carbides*

Many metal surfaces will form carbides when exposed to carbon-bearing molecules at high temperatures (see Figure 2-2 for examples). Compared with pure metals, carbides generally display lower adsorbate-surface bonds [129-131] and are therefore often considered as having no or weak catalytic activity. Carbides of metals of the groups 4-6 have been studied for their catalytic activity in oxidation, hydrogenation/dehydrogenation, isomerisation and hydrogenolysis, and in many cases have been found to rival the performance of metals of the Fe-group [132,133]. While refractory carbides do not display high activity for oxidation

reactions, they are often as active as transition metals for hydrogenation and dehydrogenation reactions. These observations explain why, despite their weaker adsorption energies, carbides are frequently considered for catalysis in extreme conditions due to their high hardness and melting points.

- *Catalytic activity of oxide surfaces*

Nanoparticles of different oxide compounds (*e.g.* SiO_2 [51,52], Al_2O_3 [52], TiO_2 [52], Er_2O_3 [52], ZnO [53]) have recently been shown to be efficient catalysts of SWCNT growth. In addition, many oxides that are commonly used as catalyst supports in CCVD display catalytic activity. For instance, Yoshihara *et al.* [134] observed that Al_2O_3 and TiO_2 catalyzed the decomposition of acetylene but not that of methane. Although heterogeneous catalysis mostly involves metal catalysts, many processes make use of oxides [125,135] such as zeolites (cracking of crude oil), chromium oxide (polyethylene synthesis) or zinc oxide (water-gas shift reaction). Polar oxide surfaces (*e.g.* NiO(111)) display higher adsorption energies than non-polar ones (*e.g.* NiO(100)) [136] but, overall, oxides have lower heats of adsorption than the corresponding metals [137,138]. An oxide catalyst is referred to as acidic or basic according to the propensity of the metal ions to donate or accept electrons (Lewis acidity) or protons (Brønsted acidity) [125]. Regarding CNT growth by CCVD, Magrez *et al.* [139] notably observed a dramatic enhacement of the yield when the surface of the support was made basic or when the acidity of the support was modified from Lewis to Brønsted using water activation.

- *Size effects on the catalytic activity of metal nanoparticles*

It has long been recognized that the size and the surface structure of catalysts can influence the catalytic activity. A catalytic reaction is defined as *structure-sensitive* if its conversion rate changes markedly as the size of the catalyst particles is changed. For instance, while bulk gold has no catalytic activity, gold nanoparticles were reported to catalyze the oxidation of carbon monoxide [140]. Using size-controlled gold nanoparticles, Tsunoyama *et al.* observed a relationship between the particle size and the catalytic activity for the oxidation of alcohol, the smaller nanoparticles being more active [141]. This is correlated by the observations that Pd nanoclusters of decreasing size display larger heats of adsorption [142].

The reactivity of a metal surface is generally associated to both its geometric features and its electronic structure. Classically, the structure sensitivity of a catalytic reaction is associated to a modification of the population of reactive sites (terrace, steps, kinks, surface defects) with decreasing particle size. For instance, the rate of H_2 dissociation decreases from 0.9 on a stepped Pt(332) surface to less than 10^{-3} on a defect-free Pt(111) surface [143]. Several authors reported modifications of the electronic structure of metal nanoparticles when reducing their size [142]. The decrease of the density of states at the Fermi level has sometimes been proposed to explain the size effects observed in catalysis. In the case of very small particles of a few tens of atoms, the electronic properties can be dramatically changed relatively to bulk material due to quantum confinement effects. Small catalyst particles are also in closer interaction with the support and are therefore more sensitive to support effects.

2.2.5 Interactions of metal nanoparticles with their environment

- *Redox interactions between metal nanoparticles and gas species*

Catalysts are frequently subjected to an oxidative pre-treatment (*i.e.* calcination) to remove carbon contaminants or to reduce the surface mobility and the coarsening of catalyst particles. Even, aging of nickel, cobalt and iron thin films in air can result in oxide and

hydroxide formation accompanied by a modification of the surface morphology [144,145]. The propensity of an element to be oxidized or reduced as a function of the gaseous atmosphere is apparent in an Ellingham diagram for oxides (Figure 2-5). Oxides and hydroxides of iron, cobalt and nickel are generally reduced under hydrogen [146], ammoniac [147] or hydrocarbon [148] atmospheres. It is apparent from Figure 2-5 that oxides commonly used as supports (SiO_2, Al_2O_3, MgO) are extremely stable and are not expected to be reduced in standard growth conditions. Other oxides such as TiO_2, MnO, Cr_2O_3 and ZnO are also very stable. At some exceptions, the affinity for oxygen among transition metals generally increases from the right to the left of the periodic table, similarly to the affinity for carbon. As an example, FeO is more difficult to reduce than NiO and CuO. Ellingham diagrams are often useful to estimate the stability of oxides at a given temperature and in a given atmosphere. However, when dealing with nanoparticles, surface and interface effects come into play. The chemical stability of nanoparticles can be strongly modified by interaction with the support. For instance, an XPS analysis by J. Lu [149] indicated that under similar reducing conditions, Fe(III) nanoparticles on silicon oxide were substantially reduced to Fe(0), but failed to do so when supported on silicon nitride. The different interactions of metal nanoparticles with oxide substrates are discussed in more detail in the following part.

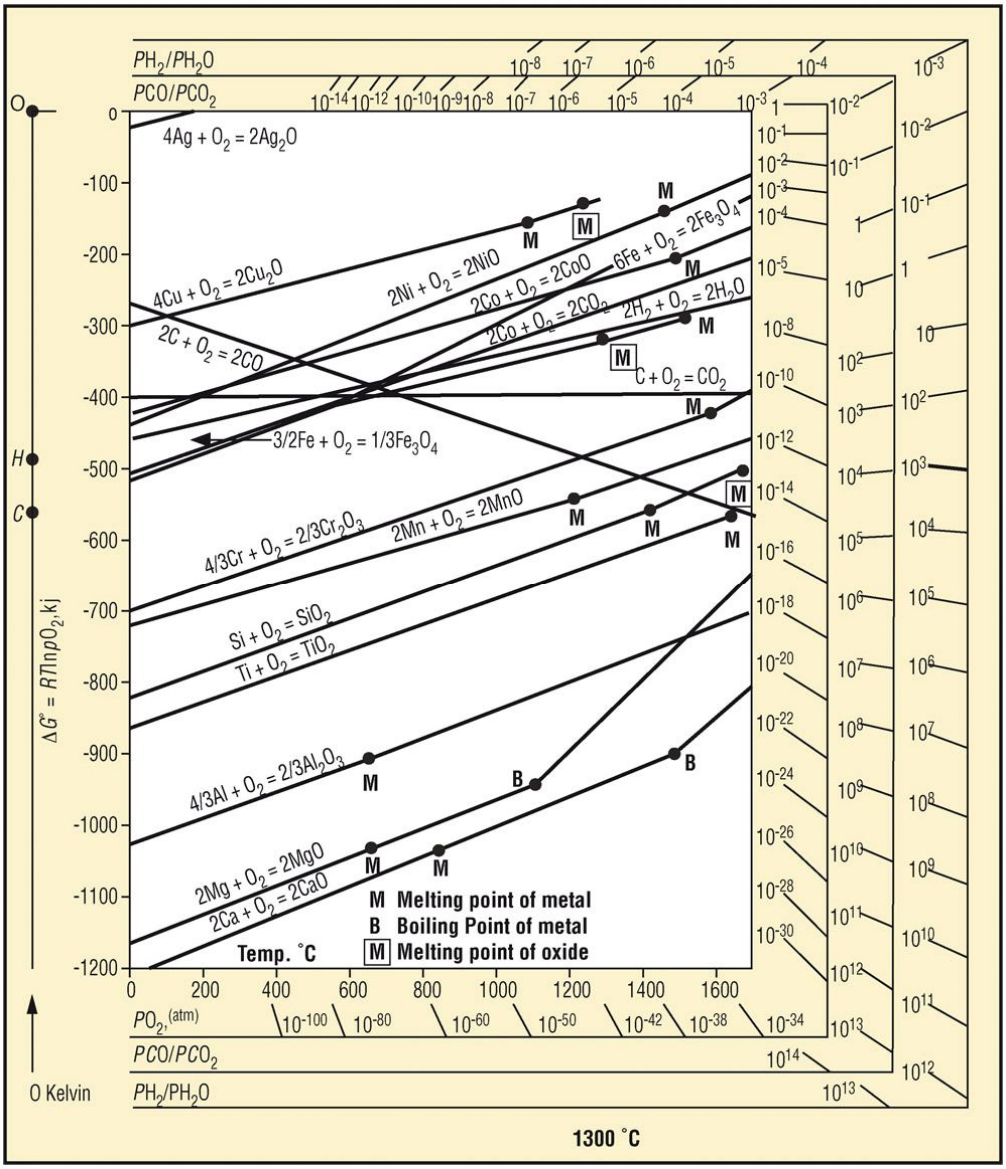

Figure 2-5. Ellingham diagram for oxides. After [150].

- *Interactions of metal nanoparticles with oxide supports*

The chemisorption behaviour of a metal cluster not only depends on its size and surface structure but also on its interaction with the substrate [142]. For example, gold clusters are found to be catalytically active when deposited on Fe_3O_4, FeO or TiO_2 but inactive when deposited on Al_2O_3 [136,140,142]. Strong metal-support interactions (SMSI) is the general term used for the reduction of catalytic activity observed on certain supports. Generally speaking, two aspects should be considered when dealing with the interactions of metal nanoparticles with oxide supports: (i) the electronic interaction corresponding to the charge redistribution at the metal-oxide interface and (ii) the chemical interaction corresponding to atom diffusion at the metal-oxide interface.

Electronic interaction: charge redistribution

Contact between a metal particle and an oxide surface results in charge redistribution at the interface [151]. Local charge redistribution occurs within the first few atomic layers at the interface. This local electronic interaction is the dominant effect in the case of insulating oxide supports such as Al_2O_3, MgO and SiO_2 since electrons are strongly localized and the production and diffusion of ionic defects are limited. Local charge redistribution is driven by the difference of electronegativities between the metal and the oxide but is also affected by the surface properties of the oxide (surface stoichiometry, defects and terminations).

The electronic interaction affects the catalytic properties of the particles. For instance, Yoon *et al*. [152] observed that, due to charge transfer with the support, Au_8 clusters are catalytically active when supported on defect-rich MgO(100) surfaces but inert when deposited on a virtually defect-free MgO surface. The modification of the electronic properties and reactivity of the metal particles by the support is usually significant only for particles smaller than 2 nm [142]. In the case of conducting oxides such as TiO_2, ZrO_2 and ZnO, charge redistribution is long range and driven by the difference of Fermi energies similarly to a metal/semiconductor junction [151]. In such a case, the electric field generated at the interface can significantly enhance the diffusion of ionic defects and promote long-range chemical interactions.

Atomic diffusion: wetting, coarsening and encapsulation

From Bauer's criterion [153], a thin metal layer deposited on a substrate will preferentially form 3D islands rather than a 2D layer if $\gamma_{metal} + \gamma_{metal-substrate} > \gamma_{substrate}$ where γ_i denote surface free energies. Metal oxides generally have lower surface energies than metals which favours the growth of 3D metal islands on oxide surfaces. Conversely, oxidizing metal particles generally leads to a flattening of metal particles supported on oxide surfaces [154]. The interface term $\gamma_{metal-oxide}$ has also to be taken into account. Because γ_{metal} and $\gamma_{metal-oxide}$ are usually difficult to estimate directly, γ_{metal} is usually approximated by the heat of sublimation which also reflects the strength of metal-metal lateral interactions while $\gamma_{metal-oxide}$ is approximated by the heat of formation of the most stable oxide of the metal since it reflects the strength of the metal-oxygen interaction. Figure 2-6 displays the wetting behaviour of different metals on TiO_2 as a function of their heat of sublimation and of oxide formation. It is apparent that transition metals with high electronegativity and high cohesion tend to dewet from oxide surfaces while the more electropositive and less cohesive metals tend to wet them [155].

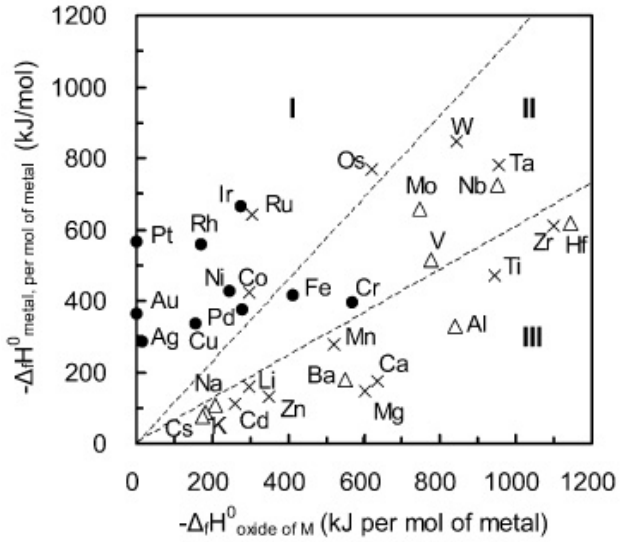

Figure 2-6. Description of the growth mode of metals on TiO_2(110) versus the heat of formation of the most stable metal oxide ($\Delta_f H_0^{oxide}$) and the heat of sublimation ($\Delta_f H_0^{metal}$), in which ● and △ represent experimentally observed 3D island and 2D layer growth modes, respectively; and × represents metals whose growth modes have not been determined. In Zone I, metal/metal lateral interactions are stronger than metal/TiO_2 interfacial interactions so that metals tend to grow in the 3D island mode. In Zone III, metal/metal lateral interactions are weaker than metal/TiO_2 interfacial interactions so that metals tend to grow in the 2D layer mode. Zone II is a transition domain where metals show either 3D island or 2D layer growth, depending on secondary factors. From [156].

Surface energies can also be dramatically modified by adsorption of molecular compounds present in the gas phase [157]. In general, adsorbates increase the anisotropy of surface energy between crystal planes, resulting in strong faceting. Encapsulation (also called decoration) is another way to minimize surface energy. It involves mass transport from the oxide support onto the surface of the metal particle and results in the covering of the particle by a thin layer of reduced oxide support or even its immersion into the oxide support [151]. It preferentially impacts metals with high surface energy deposited on oxide surfaces of low surface energy. Typical examples are Pt and Pd particles on TiO_2 and CeO_2 supports. From a kinetic point of view, encapsulation is also favoured when the outward diffusion of oxide cations is promoted by the surface electric field, *i.e.* when the Fermi level of the metal is lower than that of the oxide.

If one now considers an ensemble of interacting particles on an oxide support, coarsening is another way to minimize the energy of the system [158,159]. Particle coarsening can occur in essentially two ways: either by the diffusion of single atoms (or molecules) from small particles to large ones (which is termed Ostwald ripening or interparticle transport), or by the migration and coalescence of whole particles (which is sometimes referred to as Smoluchowski ripening). Ostwald ripening is driven by the fact that vapour pressure varies inversely with particle size (see §2.2.2). It follows that metal atoms escape more quickly from small particles than from large ones, resulting in a net flow of matter from the former to the latter. The nature of the diffusion process (surface or gas phase) and of the diffusing species (individual atoms or molecular species) can vary from one system to another. In numerous cases, it was found that the presence of oxygen greatly enhanced the rate of Ostwald ripening, which is usually attributed to the formation of more mobile metal oxide compounds [160]. The likelihood of the coalescence mechanism increases with the particle migration coefficient which increases with temperature and is influenced by the particle's features (diameter, shape, composition). In practice, the different coarsening modes are characterized by different kinetic laws of the type:

$$\bar{d}^n - \bar{d}_0^n = Kt$$

where $\bar{d}$ is the mean diameter after time t, $\bar{d}_0$ the initial mean diameter, K a temperature-dependent constant and n an integer which varies with the type of coarsening mechanism. Such studies on SiO_2-supported Ni particles [161], Al_2O_3-supported Ni particles [162] and Al_2O_3-supported Pt particles [163] indicated a change in the predominant coarsening mechanism from migration-coalescence at low temperatures (typically less than 700°C) and short times (typically less than 1h) to Ostwald ripening at higher temperatures and longer times.

Chemical reactions: redox reactions and alloy formation

Silicon wafers are standard substrates for nanotube growth. However, metals tend to diffuse into silicon and to form silicides that are inactive for CNT growth. For instance, in the case of nickel, cobalt or iron deposited on silicon, formation of silicides were observed to occur at temperatures as low as 225°C for nickel [164,165], 450°C for cobalt [166] and 800-850°C for iron [167,168]. The propensity of a given metal to form silicides is apparent in the silicide formation enthalpies shown in Figure 2-7. As previously highlighted, such bulk thermodynamic data are useful in first approximation to predict interface reactions. However, their practical use commonly requires approximations (*e.g.* the Ellingham approximation) and in the case of nanoparticles, the contribution of the surface energy can significantly shift the total free energy of the reaction.

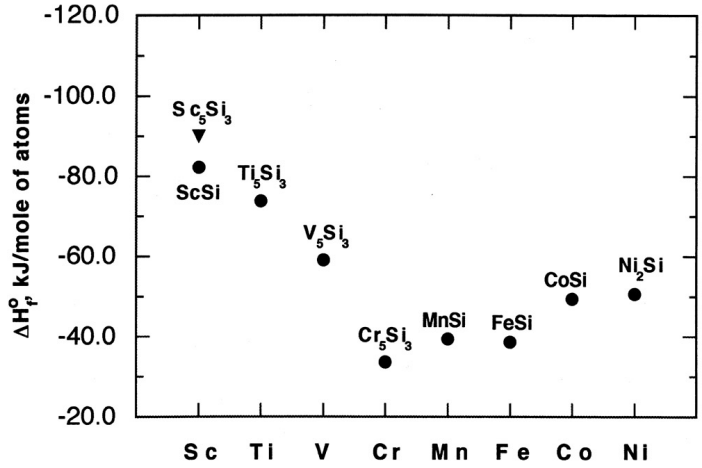

Figure 2-7. Standard enthalpies of formation of some 3d transition metal silicides (from [169]).

To circumvent the problem of silicide formation, a diffusion barrier of SiO_2 or Al_2O_3 is commonly employed. Simmons *et al.* reported that a 4-nm silicon dioxide layer is the minimum diffusion barrier thickness to prevent iron silicide formation below 900°C [167]. The efficiency of the diffusion barrier depends not only on its thickness and structural quality, but also on the type of metal, the processing time and the gas ambient. For instance, silicide formation at metal/SiO_2 interface was reported for many metals after prolonged heating under hydrogen atmosphere (*e.g.* Ni_3Si formation at Ni/SiO_2 interface [170]). At elevated temperatures, even low-reactivity metals (such as Pt, Pd, Rh, Cu and Ni) deposited on SiO_2 and Al_2O_3 can form silicide and aluminide layers [171,172] while highly reactive metals (such as Ti, Zr, Hf) tend to form a thin layer of aluminide or silicide sandwiched between a top layer of metal oxide and the oxide substrate [173,174].

Pauling electronegativity is a good indicator to predict the chemical affinity of transition metals for oxide surfaces. Metals with electronegativity lower than 1.5 tend to form

strong chemical bonds with SiO_2 [151]. The more electronegative metals do not reduce a TiO_2 surface whereas the more electropositive metals can reduce one or more TiO_2 layers, thereby forming an interfacial bond that increases their adhesion energy [155]. Mattevi *et al.* [175] observed that metallic Fe on Al_2O_3 formed Fe(II) and Fe(III) interface states making the interaction of Fe with Al_2O_3 much stronger than with SiO_2 in agreement with the lower electronegativity of Al compared to Si. They proposed that these interface states anchor Fe particles to the oxide surface and limit their coarsening.

Finally, metal thin films on silica/alumina can also form surface silicates/aluminates when heat-treated [176-181]. In the case of Co_2SiO_4 and Ni_2SiO_4, the gain in Gibbs free energies of formation from the corresponding metal oxide is of the order of 5-15 kJ/mol [182]. In Fischer-Tropsch synthesis with Co/SiO_2, silicate formation during catalyst ageing is a major cause of catalyst deactivation [183]. In presence of oxygen, a mixed oxide interlayer of $NiAl_2O_4$ can form by interdiffusion between Ni and Al_2O_3 [184]. A Mössbauer study by Oshima *et al.* [178] showed that a quarter of α-Fe deposited on SiO_2/Si changed to Fe_2SiO_4 when heat-treated at 840°C under an hydrogen/argon/water atmosphere. Upon ethylene exposure at high temperature, Fe_2SiO_4 was observed to be predominantly carbonized into Fe_3C. At least for cobalt, silicate formation is activated by water vapor [183,185] and was observed to occur at temperatures as low as 220°C [185]. Following silicate formation, the catalytic activity can be partially recovered by a reducing treatment. For instance, cobalt silicates and aluminates can be partially reconverted into cobalt using hydrogen, but this requires higher reduction temperatures (~700-900°C) than Co_3O_4 and CoO cobalt oxides (~300-400°C under H_2). Accordingly, Li *et al.* [176] reported that following a high-temperature reduction treatment, surface cobalt silicates can form well-dispersed Co nanoparticles highly efficient for SWCNT growth.

2.2.6 Summary

CNTs can be grown using a large variety of carbon-bearing molecules and of catalyst nanoparticles. Ellingham diagrams are useful tools to estimate the thermodynamic ability of a carbon precursor to form graphitic or carbide materials at a given temperature and composition of the gas phase. When going from the right to the left of the periodic table, transition metals display a stronger affinity for carbon as explained by the d-band model of Nørskov. This results in higher carbon solubility, higher propensity to form stable carbides and higher heats of adsorption. The catalytic activity of transition metals for a given reaction generally displays a volcano-shaped pattern across the periodic table, which reflects the necessity for a catalyst to form adsorbate-substrate bonds of intermediate strength. Compared to the corresponding metals, metal carbides and metal oxides generally have lower but non negligible catalytic activities for hydrocarbon dissociation. Bulk diffusion of carbon through metals proceeds interstitially, making it much faster than the bulk diffusion of metal atoms but still slower than the diffusion of carbon on the metal surface. Bulk diffusion of carbon through metal carbides is always slower than through the corresponding metals. Qualitatively, the interaction of carbon atoms with a metallic surface is stronger for isolated atoms and decreases with the number of C-C bonds formed with other carbon atoms. The ultimate limit is the formation of a full graphene layer of a flat metal surface which has weak adhesion energy.

Due to the large number of interfacial atoms, nanoparticles have size-dependent properties that can significantly differ from their bulk counterparts: increased vapour pressure, depressed melting point, modified carbon solubility, increased catalytic activity, and increased sensitivity to the environment. The reactivity of supported metal nanoparticles is strongly influenced by the electronic and chemical interactions with the oxide support. For insulating

oxides, the electronic interaction is localized at the interface and driven by the difference of electronegativities. For conducting oxides, charge redistribution is long range and driven by the difference of Fermi energies. For insulating oxide supports such as Al_2O_3, MgO and SiO_2, chemical reactions (redox, alloy formation) are confined at the interface and are notably driven by the differences of electronegativity between metals. For conducting oxides such as TiO_2, ZrO_2 and ZnO, the spatial extent of the interfacial reaction can be significantly increased by the electric field created at the metal/oxide interface.

Since metal oxides generally have lower surface energies than metals, the growth of 3D metal islands is favoured on oxide supports. The more electronegative transition metals tend to dewet oxide surfaces while the more electropositive metals tend to wet them. Oxidation of metal particles generally leads to flattening of the particles. Particles can coarsen by Oswald ripening or migration-coalescence, which are both dependent on the particle sizes, type of support and composition of the gas phase. Experimentally, the different coarsening mechanisms can be differentiated by their kinetic behaviours. Metal particles can also be encapsulated by a thin layer of support oxide, a phenomenon which preferentially impacts metals of high surface energy deposited on oxide surfaces of low surface energy.

2.3. Synthesis-structure relationship in carbon nanotubes grown by catalytic chemical vapour deposition

The structural features of carbon nanotubes grown by CCVD strongly depend on the experimental conditions which include the preparation and pre-treatment of the catalyst and the synthesis conditions (Figure 2-8). This section aims at summarizing the synthesis-structure relationship in CNTs grown by CCVD as reported in the current literature. Considering the huge amount of articles published in the field since the mid-90s, an exhaustive summary is a nearly impossible task, and probably a useless one considering the diversity of experimental systems. Instead, this summary focuses on the most significant studies with respect to a particular experimental dependence. For each structural feature, the experimental dependence is summarized trying to highlight the most influential parameters and the dominant trends.

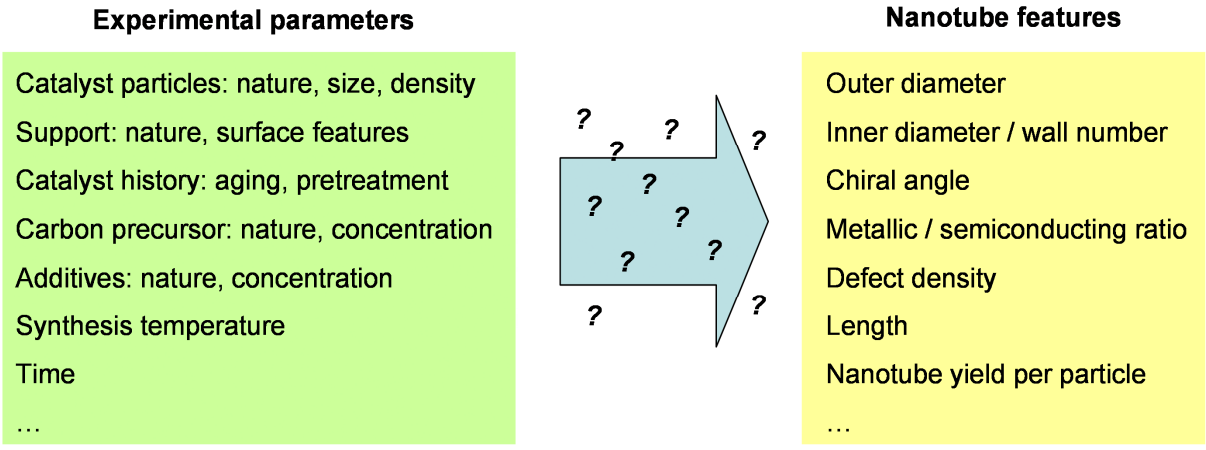

Figure 2-8. Input synthesis parameters and output structural features of CNTs grown by CCVD

2.3.1 Nanotube outer diameter

A correlation between the size of the catalyst particles and the diameter of the resulting nanotubes is frequently observed. For instance, Cheung *et al.* [186] reported that iron nanoparticles of average diameters d_{NP} of 3, 9, and 13 nm produced multi-wall carbon nanotubes with average diameters d_{NT} of 3, 7, and 12 nm, respectively, which corresponds to

a ratio d_{NT}/d_{NP} close to 1. Schäffel *et al*. [187] obtained a comparable value of the d_{NT}/d_{NP} ratio using iron particles of 3 to 18 nm. Chen *et al*. [188] reported that the diameter distribution of SWCNTs was correlated with the size of the used SiO_2 particles with a ratio d_{NT}/d_{NP} of the order of 0.8-0.9.

Such correlations based on the initial size distribution of the catalyst particles raise the concern of certain particles being inactive during CNT growth. A more appropriate approach is based on the direct observation of particle-tube connections by HR-TEM**.** In the case of Fe particles of 1.3-2.0 nm, Nasibulin *et al*. [189] measured a consistent d_{NT}/d_{NP} ratio of ~0.6-0.7 within a given batch. Using a similar approach, Hiraoka *et al*. [190] measured a d_{NT}/d_{NP} ratio of ca. 0.3-0.5 in the case of Fe particles of 2-3 nm and Zhang *et al*. a d_{NT}/d_{NP} ratio close to 1 in the case of Fe particles of 1-3 nm [191]. In the case of Co particles of 1-10 nm, Fiawoo *et al*. [192] actually observed that two configurations of nanotube-nanoparticle junctions coexisted: a perpendicular configuration corresponding to d_{NT}/d_{NP} ratio lower than 0.75 and a tangential configuration for d_{NT}/d_{NP} ratio higher than 0.75. Interestingly, they observed that the perpendicular configuration was dominant at short synthesis times (typically less than 2 min) and the tangential one at longer times.

The direct observation of the nanotube-particle relationship by *in situ* TEM during CNT growth [193-199] is probably the best approach to address the question. A first result of *in situ* TEM studies is that active particles are rarely spherical during CNT growth: a dynamic reshaping of the particle occurs, at least in the case of the standard Fe, Co and Ni catalysts. In many cases (in particular for MWCNT growth on large particles), the catalyst particle displays a pear-like shape, the top of which fits the inner diameter of the tube and the bottom of which fits the outer diameter (Figure 2-9). To date, all *in situ* TEM observations on MWCNTs showed a direct correlation between the nanotube outer diameter and the lateral dimension of the catalyst particle. A similar observation is made for SWCNTs although this conclusion is somehow tempered by the still small number of *in situ* TEM observations. From the simulations of SWCNT growth on a Ni particle performed by W. Zhu *et al*. [200], the d_{NT}/d_{NP} ratio should be lower than 0.8-0.9 to prevent the nanotube rim to close spontaneously and to terminate the growth.

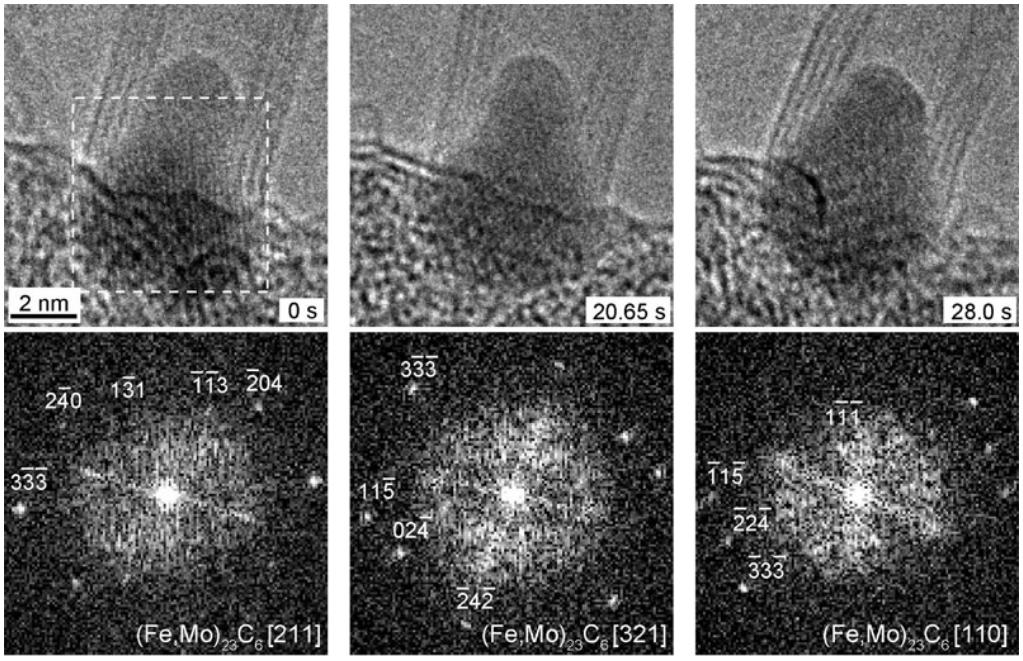

Figure 2-9. In situ TEM observation of the growth of a four-wall CNT from a fluctuating catalyst nanoparticle of $(Fe,Mo)_{23}C_6$-type structure. From [197].

Because of the relationship between the nanotube outer diameter and the lateral dimensions of the particle, controlling the size distribution of catalyst particles is empirically the best way to tune the nanotube diameter distribution. This is commonly achieved by controlling the thickness of the deposited catalyst [201,202], its coarsening [146,203] or its evaporation [204-207] during the thermal pre-treatment preceding the growth. However, the *ex situ* observations of two coexisting configurations of nanotube-particle junctions [192] and the *in situ* observations of the dynamic restructuring of the catalyst particles during CNT growth [193-199] suggest that the nanotube diameter is influenced by other parameters than the particle size. Growth conditions such as the temperature and the feedstock supply are notably reported to influence the nanotube diameter distribution.

In general, increasing the growth temperature is reported to shift the CNT diameter distribution toward larger diameters [208-213]. By analogy with the influence of the thermal pre-treatment, such results are often accounted for by an increased catalyst coarsening with increasing temperature [209]. Yet, a study of Yao *et al*. [214] showed an opposite temperature dependence at the level of individual SWCNTs. Following the same individual nanotube, Yao *et al*. found that changing the temperature during growth resulted in a change of the nanotube diameter even though the catalyst particle remained the same: the SWCNT diameter increased when decreasing the growth temperature and inversely. A similar trend was reported by Mahjouri-Samani *et al*. [215]. Yao *et al.* [216] found that the diameter change was strongly related to the initial nanotube diameter and that there was a limit to the range of diameter variation mediated by the temperature. As an example, for an initial nanotube diameter of 1.6 nm, the maximum diameter variation was found to be 0.4 nm.

The dependence of the diameter distribution on the carbon supply is the subject of even more controversy. Lu *et al*. [217] first reported that small-diameter SWCNTs are preferentially grown at low carbon feeding rates even when highly polydisperse nanoparticles are used as catalyst. Tanioku *et al.* [210] and Geohegan *et al*. [218] also reported that the proportion of small-diameter SWCNTs increases as the feedstock pressure or flux are reduced. At the opposite, Saito *et al*. [219] and Wang *et al*. [220] reported that increasing the flow rate of ethylene or the pressure of carbon monoxide resulted in SWCNTs of smaller diameter. As detailed in §3.5, our own results [221] show that, for the same catalyst system, both behaviours can be observed depending on the studied range of growth conditions.

2.3.2 Nanotube inner diameter

In 1983, Gary Tibbetts [222] studied a sample of tubular carbon filaments grown by CCVD and reported a linear relationship between the inner and outer diameters of the filaments. In the case of the sample studied by Tibbetts, the proportionality coefficient d_i/d_o was ~0.6. More recently, a statistical analysis of MWCNT samples grown in different CCVD conditions [223] also yielded a linear relationship between the average number of walls N_{Walls} and the average outer diameter d_o in a given sample: $N_{Walls} \cong d_o(nm) - 2$, which corresponds to $d_i/d_o \sim 0.3\text{-}0.4$. This relationship explains why adjusting the size of the catalyst particles (or the catalyst thickness) is empirically among the most efficient methods to tune the outer diameter but also the number of walls. As an example, using catalyst nanoparticles of controlled sizes, Schäffel *et al*. [187] and Chiang *et al*. [224] showed that increased catalyst sizes lead to increased wall numbers. Zhao *et al.* [202] reported that CNTs of larger outer diameters and larger wall numbers were obtained by increasing the catalyst thickness. Yamada *et al.* [225] even showed that a high selectivity for double-walled CNTs could be achieved by precisely adjusting the catalyst thickness. However, the statistical analysis of Chiodarelli *et al.* [223] yields a quite large standard deviation σ_N which increases with the

average outer diameter: $\sigma_N \cong 0.17\ d_o$. This suggests that the inner diameter is not only related to the outer diameter, but is also influenced by other growth parameters.

The precursor supply for instance notably influences the inner diameter. Sharma *et al.* [226] observed that the number of walls decreased at lower precursor supply. Zhang *et al.* [227] reported that low ethylene supply leads to CNTs with small outer diameters and few walls and that selective synthesis of single- and double-walled CNTs could be achieved by tuning the flow rates. These results suggest that a decreased carbon concentration of the catalyst particle (*i.e.* a lower chemical potential of carbon) leads to a decreased number of walls, as can be deduced from the initial model of Tibbetts [222]. *In situ* TEM observations reported by Gamalski *et al.* [198] show that, in certain cases, the number of walls of a nanotube decreases during the growth. In the experiments of Gamalski *et al.*, the progressive thinning of the wall finally led to the detachment of the nanotube from the catalyst particle and to the nucleation of a new CNT reproducing the same behaviour. During my own investigations, I also studied MWCNTs displaying periodic fluctuation of their inner diameter associated with periodic inclusion of catalyst material [228]. The size evolution of the carbon units along the MWCNT could be quantitatively explained by periodic fluctuations of the carbon concentration of the catalyst particle. Together, these results support that the inner diameter is influenced by the instantaneous carbon concentration of the catalyst particle which depends on both the carbon supply and consumption.

The temperature dependence of the inner diameter finds no general agreement in the literature. For instance, Mudimela *et al.* [229] reported larger wall numbers (and larger outer diameters) at higher growth temperature, while Sharma *et al.* [226] reported that both the number of walls and the outer diameter decrease with increasing temperature. As evidenced later, the influence of temperature is commonly the most difficult to rationalize given the large number of thermally-activated processes and conditions experimentally investigated.

Adding sulphur to the catalyst particles is reported by several authors to reduce the inner diameter and increase the wall number [230-232]. For instance, Ci *et al.* [231,232] reported that the addition of sulphur favoured the formation of DWCNTs with small inner diameters at the expense of SWCNTs. At the opposite, Pan *et al.* [233] reported an enlargement of the inner diameter of CNTs by adding boric acid (HBO_3) to the catalyst.

2.3.3 Nanotube chiral angle

Many authors report a higher occurrence of high-chiral-angle SWCNTs (*i.e.* near-armchair) in nanotube samples [234-241]. The fact that both indirect (*i.e.* photoluminescence excitation) and direct methods (*i.e.* electron diffraction) of structural identification lead to the same result strengthens this conclusion. In more detail, all reported works agree on the higher occurrence of near-armchairs among relatively small-diameter CNTs (*i.e.* diameter circa less than 3 nm). However, Hirahara *et al.* [239] observed that this preferential occurrence disappeared for CNTs larger than 3 nm while Arenal *et al.* [241] reported a preferential occurrence of near-armchairs even for few-walled CNTs of diameters between 3 and 8 nm.

Beyond this general observation, highly-selective syntheses of high-chiral-angle SWCNTs were reported using specific catalysts such as Co-MCM41 [242], Co–Mo [243,244], Fe-Ru [245], Fe-Co [236], Fe-Cu [246] or Al-Cu-Fe [247] (Figure 2-10). He *et al.* [246] notably reported the predominant growth of (6,5) SWCNTs using Fe-Cu nanoparticles at low synthesis temperature. Using Ni_xF_{e1-x} catalyst nanoparticles of controlled sizes, Chiang and Sankaran showed that the chirality distribution could be influenced at constant particle size by varying the Ni/Fe ratio of the particles [54].

Optimized gaseous feeds are also usually required to achieve a high chiral selectivity. Lolli *et al*. reported that increasing the synthesis temperature resulted in an increase in nanotube diameter without a change in the chiral angle while varying the composition of the gaseous feed significantly modified the chiral distribution [248]. Wang *et al*. confirmed the influence of the gaseous feed by reporting that high-chiral-angle SWCNTs were preferentially grown at high CO pressure [220] or under vacuumed ethanol or methanol [244]. Ghorannevis *et al*. [249] reported that an appropriate hydrogen concentration was the critical factor in achieving a narrow chirality distribution of (6,5) tubes when using a gold catalyst in plasma-enhanced CVD.

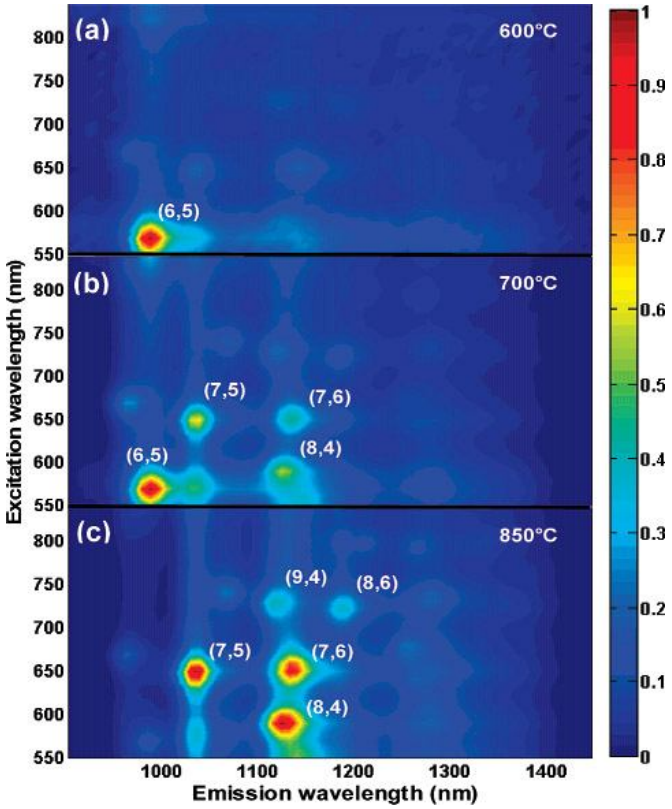

Figure 2-10. Contour plots of normalized photoluminescence emission intensities under various excitations for the Fe-Ru SWCNTs grown at three different temperatures. From [245].

Additional factors are reported to affect the chirality distribution. Koziol *et al*. [250] notably observed that the addition of a nitrogen-containing compound in the hydrocarbon feedstock leads to the growth of large MWCNTs in which all the walls are either of the armchair or zigzag structure. Recently, they showed that nitrogen interacted with the catalyst in the form of ammonia which causes a restructuring of the catalyst surface and a stabilization of the iron catalyst in its Fe_3C carbide phase [251]. Such a restructured catalyst is proposed to promote the epitaxial growth of MWCNT with only armchair and zigzag walls. The catalyst support is also reported to influence the chiral distribution. Lolli *et al*. [248] reported that changing the catalyst support from SiO_2 to MgO resulted in nanotubes with similar diameter but different chiral angles. Using monocrystal sapphire as growth substrate, Ishigami *et al*. [211] reported the preferential growth of near-zigzag tubes on the A-plane and of near-armchair tubes on the R-plane.

2.3.4 Metallic / semiconducting nanotube ratio

Structurally, two-thirds of SWCNTs are semiconducting (SC) and one-third is metallic (M). In the absence of chiral selectivity, a nanotube sample is expected to present such

proportions. Actually, there are several reports of syntheses yielding SWCNT samples enriched in semiconducting or metallic tubes.

Several examples of semiconductor-enriched SWCNT samples were notably reported using plasma-enhanced CVD (PECVD). Based on electrical measurements, Y. Li *et al*. reported a percentage of semiconducting tubes of 89%. Later, they found that higher percentages of semiconducting SWCNTs are especially obtained when the growth parameters are adjusted to produce SWCNTs of small diameters, *i.e.* of the order of 1.1 nm [252]. Electrical measurements preformed by Mizutani *et al*. [253] confirmed that most CNTs grown by PECVD display a semiconducting behaviour. However, their Raman characterization revealed several radial breathing modes corresponding to metallic SWCNTs. Scanning gate microscopy measurements suggested that the semiconducting behaviour observed for CNTs fabricated by PECVD process may actually result from the opening of a band gap caused by irradiation damages during PECVD. Also using Raman spectroscopy, L. Qu *et al*. [254] found at the opposite that arrays of SWCNTs grown by PECVD combined with fast heating, contained ~96% of semiconducting tubes. These results suggest a higher sensitivity of metallic SWCNTs to plasma conditions leading to a modification of their electrical properties or even to their selective removal.

Other examples of selective removal of metallic tubes in reactive environments can be found in the literature. Hong *et al*. [255] found that applying a UV irradiation during the CVD growth of SWCNTs on quartz increased the proportion of semiconducting tubes up to 95% (as assessed by both Raman and electrical measurements). Similarly, Yu *et al*. [256] reported that introducing a small amount of oxygen during SWCNT synthesis by the floating catalyst method led to the selective removal of metallic SWCNTs (based on Raman measurements). Parker *et al*. [257] found that the semiconducting SWCNT percentage peaked at 85% using isopropanol as carbon source while 2-butanol and methane yielded 70% and 32% of semiconducting SWCNTs, respectively. Using different alcohols as carbon precursors, Wang *et al*. [258] observed that the proportion of semiconducting tubes grown from an Fe–Co/MgO catalyst increased when decreasing the ratio of carbon atoms to oxygen atoms in the precursor composition. Similarly, L. Ding *et al*. [259] observed that increasing the proportion of methanol in the ethanol precursor increases the proportion of semiconducting tubes grown on quartz. Both groups proposed a selective etching of metallic tubes by hydroxyl radicals to explain the semiconductor enrichment. However, Che *et al*. [260] reported that isopropanol yielded a much higher fraction of semiconducting tubes (up to 97%) than ethanol suggesting that a too high amount of water may be detrimental to semiconducting tubes.

Harutyunyan *et al*. [261] reported that the M/SC ratio was highly sensitive to the composition of the atmosphere used during the annealing stage preceding the introduction of the carbon source and notably to the presence of water. The presence of water in Ar ambient was found to favour the growth of semiconducting tubes whereas the same amount of water in He ambient promoted the growth of metallic tubes. Using an optimized atmosphere, the proportion of metallic tubes could reach 91%, as characterized by both Raman and electrical measurements.

Finally, the nature of the catalyst is reported to affect the M/SC ratio. Using Ni-Fe catalyst particles of controlled size and composition, Chiang *et al*. [262] showed that the semiconducting content (assessed by optical absorption and Raman spectroscopy) significantly changed with the Ni-Fe ratio and could reach 90% for $Ni_{0.27}Fe_{0.73}$ nanoparticles of 2.0 nm mean diameter. Using europium oxide (Eu_2O_3) catalyst particles, Qian *et al*. [263] found that 80% of the as-grown SWCNTs were semiconducting based on Raman measurements.

2.3.5 Defect density and carbonaceous impurities

Several methods exist to quantify the defect density of CNTs, including microscopic observations (HR-TEM, STM) and electrochemical labelling. Most usually, the crystalline quality of CNT samples is assessed by Raman spectroscopy which provides a rapid and statistical assessment of the defect density based on the intensity ratio of the defect-induced D-band to the graphitic G-band [1,264-268]. A difficulty of this approach is the potential contribution of carbonaceous impurities to the D-band, even though these contributions can often be distinguished by their positions and linewidths [269-276] or by their deposition kinetics [277]. For instance, Yasuda *et al*. [277] performed Raman measurements of the G/D ratio at different synthesis times showing that the level of carbonaceous impurities solely depends on the cumulated time of exposure to the carbon source.

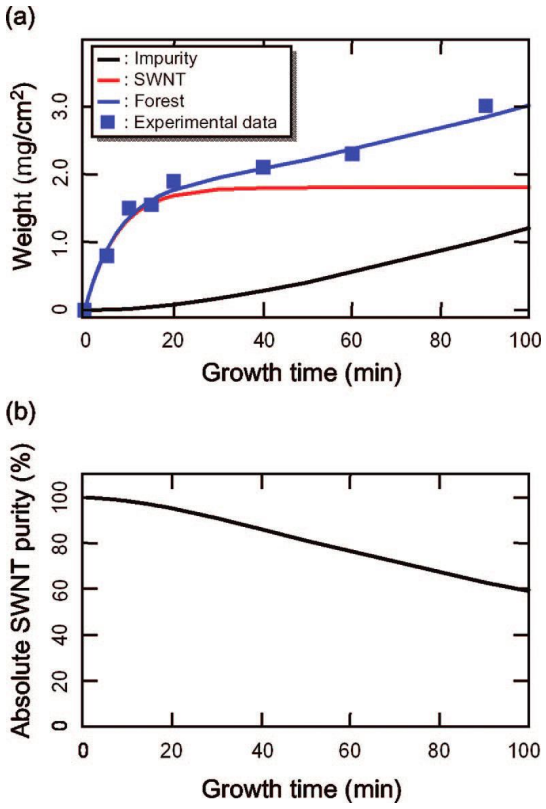

Figure 2-11. (a) Time evolution of the calculated weights of SWCNTs (red line), carbonaceous impurities (black line), and forest (blue line and squares). (b) Time evolution of the absolute purity in SWCNT. From [277].

By analogy with standard crystal growth, the crystalline quality of CNTs is expected to increase with decreasing supply and increasing mobility of the elementary building blocks. Qualitatively, *in situ* TEM observations of Sharma *et al*. [226] confirm that straight nanotubes tend to form at high temperatures and low precursor pressures while bent and defective nanotubes form at low temperatures and high precursor pressures. As detailed in §3.6, our own results show that the defect density of CNT sample follows a power law with precursor pressure [278]. The dependence of D/G on the growth temperature is more complex. Most authors [278-280] report three different regimes: with increasing growth temperatures, D/G first decreases, then remains stable for an intermediate range of temperatures and finally increases again. Concerning the high temperature regime, Kwok *et al* [280] and ourselves [278] observed that the increase of D/G was proportional to the growth duration and was to be attributed to the activated deposition of pyrolytic carbon in agreement with the results of Yasuda *et al*. from a coupled TEM-Raman studies [277] and of Feng *et al*. based on coupled

TEM-thermal analyses [281]. The decrease of D/G in the first regime is usually attributed to the increase of crystalline quality resulting from the higher surface mobility of carbon intermediates with increasing temperatures. This interpretation notably agrees with the STM observations of Jacobson *et al.* in the model case of graphene grown on a metal surface [282], showing a size increase of the graphene crystalline domains with increasing growth temperature. As detailed in §3.6, our own results show that the study the defect density of SWCNT is complicated by the presence of different types of carbonaceous by-products which severely affect the G/D values of the samples grown at low temperature.

Certain molecular species are reported to act as defect-promoters. Noda *et al.* notably reported that the addition of water to ethylene degrades the quality of as-grown SWCNTs [283]. Similarly, Gao *et al.*[284] found that an oxygen-containing precursor such as ethanol yielded a higher linear density of defects than methane.

An important question that remains is the influence of the catalyst on the defect density of CNTs. Theoretical works [285] support that the catalyst may strongly influence the processes of defect creation and annealing, but dedicated experimental studies are still missing.

2.3.6 Nucleation efficiency of catalyst particles

After growth, it is commonly observed that many catalyst particles did not yield nanotubes. Different denominations are used in the literature for the ratio of the number of synthesized nanotubes to the number of catalyst particles, such as “catalyst activity”, “synthesis yield” or “nanotube yield”. To avoid confusion with other features of the catalyst or of the synthesis process, I will use the term nucleation yield (NY). The NY is best evaluated when using well separated catalyst particles deposited on a support. For instance, using individual Ni particles of 4.7±1.5 nm in different growth conditions, Paillet *et al.* [286,287] measured NY ranging between 0.5% and 20%. Using spatially ordered Fe particles of 1.7±0.6 nm, Ishida *et al.* [288] measured similarly low NYs of ~10%. Y. Li *et al.* [289] led post-growth HRTEM observations to understand the low NY obtained with discrete Fe particles of 1-2 nm and 3-5 nm. They observed that inactive particles yield only single spherical graphitic shells around them and that smaller nanoparticles (<1.8 nm) tend to be more active in producing SWCNTs with appreciable lengths. In agreement with the observations of J. Liu that particle activity for nanotube growth was strongly size-dependent [217], Li *et al.* proposed that the disparity in particle size was the likely cause of the low NY. The encapsulation of inactive particles by a graphitic shell is commonly observed during post-growth HRTEM analyses (Figure 2-12) and frequently invoked to explain the inactivity [290]. Rummelli *et al.* [291] proposed that the nucleation of a carbon cap proceeds by precipitation of carbon from a supersaturated catalyst particle. They suggested that the biggest particles displaying a too large volume to surface area ratio would therefore be encapsulated by the precipitating carbon. Using the same argument and based on the observation that the ratio of the number of encapsulating graphitic layers, N_L, to the particle diameter, D_P, is typically 0.2-0.3 nm^{-1}, Ding *et al.* [292] suggested that encapsulating layers were formed by precipitation of carbon from a carbide particle of precise composition M_3C (*e.g.* Fe_3C). Experimentally remains the question of whether these encapsulating shells were formed during the exposure to the carbon precursor (therefore causing the inactivity) or at a later stage (*e.g.* during cooling). *In situ* TEM observations frequently reveal inactive particles larger or smaller than some active neighbours [198] but, up to now, the origin of their inertness was not directly assessed.

When considering a possible encapsulation of the catalyst particle by carbon, the exact nature of the carbonaceous material has to be considered since their reactivity can greatly vary with their composition (*e.g.* H or O contents) and structural disorder. For instance, Davis *et al.* [293] showed that the dissociation of ethylene on a Pt(111) surface leads to the formation of a carbonaceous overlayer containing a large fraction of hydrogen. With increasing time, increasing temperature or decreasing hydrogen partial pressure, the hydrogen concentration of the overlayer decreases, finally leading to a graphitic layer that is irreversibly adsorbed and displays no catalytic activity [294]. In the case of propylene conversion on Mo at 600°C, Wu *et al.* [295] also confirmed the slow transformation of an easily removed hydrogen-rich overlayer into an inactive and irreversibly adsorbed graphitic layer. In the case of nanotube growth, Schünemann *et al*. [296] observed that the carbonaceous layer deposited by pyrolytic decomposition of cyclo-hexane did not prevent the growth of CNTs, but acted indeed as a carbon source. Interestingly, after monitoring the growth of an individual tube by *in situ* field emission imaging, Marchand *et al*. [297] found that increasing the temperature by a few tens of degrees reactivated the nanotube growth. This observation suggests that at low temperatures, deactivation is mainly caused by the encapsulation of the catalyst particle by a disordered carbonaceous layer.

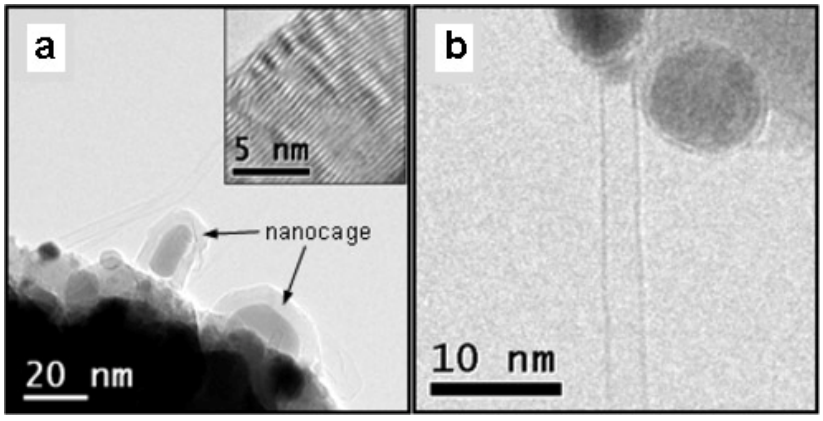

Figure 2-12. Nickel particles encapsulated by a thick (a) or single-layer (b) graphitic observed after nanotube growth together with active catalyst particles. From [290].

Accordingly, preventing the particle encapsulation and reducing the catalyst coarsening are the two main ways reported in the literature to grow high-density CNT samples. The vertically aligned CNT (VACNT) forests prepared by the so-called "super-growth" [298] are among the best examples of high-density samples. Using iron on alumina as catalyst and a controlled addition of water vapour to the ethylene precursor, they obtained NY values of up to 84% [299]. Later, they showed that other oxygen-containing compounds such as CO_2, ethanol or acetone, also act as growth enhancers [300]. They interpreted that a controlled amount of oxygen supplied by the growth enhancer activates the catalysts by cleaning off the carbon coating that deactivates them. In another example of high-density growth, the growth of aligned CNT arrays on quartz, Zhou *et al.* [301] reported that the nucleation efficiency can be enhanced by a factor 3-4 by performing multiple cycles of growths separated by a short argon exposure. A similar observation was reported by Bin Wu *et al.* [302]. Based on the observation of nanotube etching with increasing the number of cycles, they postulated that oxygen-containing functions (*e.g.* –OH) reacted with the most reactive forms of carbon (amorphous carbon, small-diameter SWCNTs). Using Fe/Al_2O_3 catalysts presenting a gradient of iron thickness, Hasegawa *et al*. [303] evidenced that millimetre-tall VACNT forests can be grown without addition of water if the carbon precursor supply is set below a certain limit in order to retain an active catalyst; water only extends the catalyst lifetime when an excess precursor supply is used. They also found water addition to

widen the window of catalyst thickness for VACNT growth toward higher thicknesses and to suppress nanotube growth from the smallest catalyst particles [283].

The carbon etching effect of oxygen-bearing enhancers may not be the only reason for the high nucleation yield of the super-growth. Zhu *et al.* [304] and Noda *et al.* [305] reported that replacing Al_2O_3 support beneath the Fe catalyst by SiO_2 decreases the nanotube yield by nearly two orders of magnitude under the same growth conditions. Studying Fe catalysts supported on different types of alumina, Amama *et al.* [306] observed that SWCNT forest growth was strongly dependent on the type of alumina. Highest nanotube yields were obtained using alumina of high porosity (*e.g.* sputtered Al_2O_3), which was correlated with low Ostwald ripening rates and mild subsurface diffusion rates. Burt *et al.* [307] also observed that the VACNT yield was strongly dependent on the grain size of the sputtered alumina layer. From the work of Noda *et al.*, using cobalt as catalyst instead of iron had little effect, but using nickel instead of iron reduced the CNT forest height by 2-3 orders of magnitude [305]. These results highlight the importance of the catalyst-support interaction for growing high-density CNT samples. Mattevi *et al.* [175] proposed that interaction of Fe on Al_2O_3 is much stronger than that on SiO_2, and restricts Fe surface mobility. The resulting much narrower Fe catalyst particle size distribution on Al_2O_3 would lead to a higher CNT nucleation density. This is in line with the report of Esconjauregui *et al.* [308] that plasma-assisted thermal pre-treatment of catalyst films of Ni, Co or Fe on TiN greatly facilitates the direct growth of high-density arrays of CNTs by promoting a stronger catalyst-support interaction and hence stabilizes smaller catalyst particles with a higher number density. Amama *et al.* [309] reported that the addition of water contributed to reduce the migration of iron catalysts on alumina and proposed that the formation of hydroxyl groups at the surface of alumina by water was at the origin of the reduced surface diffusivity of catalyst atoms. At the opposite, Hasegawa *et al.* observed no influence of water addition to the rate of catalyst coarsening inferred from the evolution of CNT diameter from top to bottom of CNT forests [303]. After exploring a large range of growth condition, Hasegawa and Noda [310] concluded that both a moderate carbon supply and a suppressed catalyst restructuring are key requirements in order to grow dense millimetre-tall SWCNT forests. As a consequence, they observed that the optimal growth domain for high-density SWCNT growth followed a diagonal in the temperature-carbon supply diagram [310].

2.3.7 Nanotube length

Experimentally, the elongation rate (or growth rate) of nanotubes is observed to decrease with time until complete termination of the growth (Figure 2-13). In Figure 2-13, one can observe that nanotube kinetics is characterized by an initial growth rate and a lifetime corresponding to the saturation of the nanotube length. This general behaviour was observed at the level of individual nanotubes [226,290,297], of thin nanotube carpets [221,311] and of thick nanotube forests [312-315]. The final length of a nanotube depends not only on the nature of the growth limiting step but also on the nature of the deactivation process(es) limiting the lifetime. Obviously, the nature of the rate-limiting step and of the dominating deactivation process may vary with the experimental conditions. Hereafter is described the parameter dependence of the growth rate and lifetime and discussed the particular case of the kite growth method which produces the longest nanotubes to date.

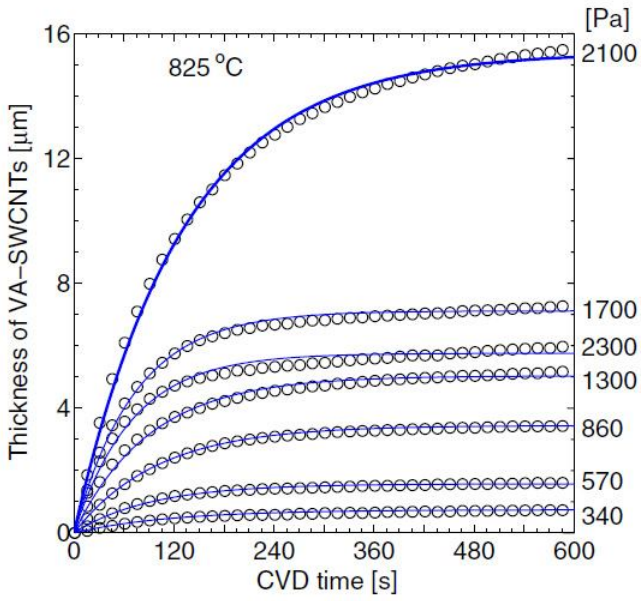

Figure 2-13. Time evolution of the thickness of a forest of VACNT measured by in situ optical absorbance for different partial pressures of carbon precursor (ethanol). The growth temperature is 825°C. From [314].

- *Growth rate*

Growing carbon filaments from acetylene at low temperatures (350-600°C), Baker *et al*. measured growth activation energies that were remarkably correlated with the activation energy for solid-state carbon diffusion through the corresponding bulk metals [10,316,317]. This supported that, in these conditions, bulk diffusion through a solid-state catalyst particle was the rate-determining step. A similar correlation was noted by other authors [318-320] usually when using low temperatures (400-600°C) and relatively reactive carbon sources (*e.g.* acetylene, propylene, butadiene).

However, many authors did not observe this correlation in their experimental conditions. Using acetylene in microwave plasma-assisted CVD, Bartsch *et al*. [320] measured an activation energy of 1.4–1.6 eV (in agreement with values for carbon diffusion in solid metals) for the formation of bamboo-like CNTs at 800-900°C but an activation energy of 0.3–0.6 eV for the growth of MWCNTs at 900-1100°C. They inferred that bulk diffusion was the rate-determining step in both cases, but through a solid or a liquid particle depending on the temperature range. Other authors reported high activation energies of the order of 2-2.8 eV at low temperatures [221,313,321,322] which may be compatible with gas-phase conversion of the carbon or bulk diffusion of carbon through carbide metals, but not with bulk diffusion through pure metals (see §2.2.3).

In contradiction with the hypothesis that growth kinetics is simply determined by the diffusion rate of carbon, the measured activation energy is often reported to depend on the gas phase reactivity. For instance, using plasma-assisted growth from acetylene at 150-500°C, Hofmann *et al*. [103] reported activation energies of 0.23–0.4 eV much lower than the value of 1.2 eV that Ducati *et al*. measured for thermal growth [323] or the value of 1.5 eV measured by Baker *et al*.. They concluded that the rate-limiting step in plasma-assisted conditions was the surface diffusion of carbon on the catalyst particle and that precursor decomposition was the limiting step in thermal conditions. Meshot *et al*. [324] also showed that the growth activation energy was dependent on the pre-treatment of the gas mixture and

increased from 1.02 to 1.88 eV when increasing the preheating temperature of the gas mixture from 980 to 1120°C.

In addition, the growth rate is often reported to increase with increasing precursor pressure. The reported reaction orders are usually close to unity [221,281,314,321,325] except for Wirth *et al*. [315] who measured a reaction order of 0.6 for low-pressure acetylene growth on Fe/Al_2O_3. Noteworthy, several authors reported that above a critical precursor pressure, the growth rate is independent of the precursor pressure [221,281,314] which was interpreted by Picher *et al*. [221] and Feng *et al*. [281] as the transition from a kinetic regime controlled by gas diffusion to a surface-controlled regime.

Many growth models predict that the nanotube growth rate will either increase [326,327] or decrease [313] with diminishing size of the catalyst particle. For instance, the model proposed by Puretzky *et al.* [313] stipulates that the larger diameter nanotubes should grow faster than the smaller diameter ones due to their higher surface area to circumference ratio. They later refined this model by including a size-dependent activation energy for feedstock dissociation to account for the experimental bell-like distribution of nanotube diameters [218]. Experimentally, there is no general agreement on the variation of the nanotube growth rate with the particle size or nanotube diameter. Growing arrays of aligned MWCNT by PECVD, Huang *et al*. [328] observed that the CNT growth rate was diminished when reducing the catalyst thickness from 35 nm to 10 nm. A similar observation was reported by Lee *et al*. [329] using a lower range of catalyst thicknesses (0.7-10 nm). Using a gradient of catalyst thickness, Zhang *et al*. [32] reported that the growth rate increased with increasing catalyst thicknesses, while Hasegawa *et al*. [330] found that the initial growth rate of thick CNT forests was rather constant for catalyst thicknesses of 0.4-3.0 nm. Contrary to Zhang *et al*., Patole *et al*. [331] observed that the CNT growth rate increased when decreasing the catalyst thickness from 3.0 to 0.5 nm. They also noted that the growth rate decreased with time as $t^{1/2}$, which supports that the rate was controlled by a thickening diffusion barrier (*i.e.* CNT or amorphous carbon mat) rather than by a catalyst size-related effect. This illustrates the difficulty to use CNT arrays to address this question because of the possible combination with other effects: diffusion through the stack, competitive/synergetic effects between neighbouring particles [332,333]. In this context, it is worth mentioning the *in situ* study of CNT length by aerosol size classification of Chiang *et al*. [334] who reported that reducing the catalyst size from 2.6 nm to 2.2 nm increased the CNT growth rate by a factor 3.

Since the nature of the catalyst strongly affects the physical and chemical properties of the particles, it may significantly influence the CNT growth rate. For instance, growth simulations performed by Page *et al*. [335] predict that the growth rate on Ni particles would be 69% larger than on Fe particles due to a faster integration of carbon chains into the nanotube. However, experimental comparisons of CNT growth rates for different natures of catalyst are quite few. Comparing the efficiency of Ni, Co and Fe catalyst films in the same PECVD conditions, Huang *et al*. [328] found that Ni yielded the highest growth rate, largest diameter and thickest wall, whereas Co results in the lowest growth rate, smallest diameter and thinnest wall. The CNT growth rates with SiO_2 [336] and Al_2O_3 [337] nanoparticles are usually of the order of 10 nm/s, which is much lower than with standard iron-group catalysts. Motta *et al.* [338] also reported that the presence of sulphur facilitates the formation of nanotubes. They found that sulphur forms a layer on the surface of the catalyst particles which may play a role in encouraging nanotube growth by surface diffusion.

- *Lifetime*

Several authors reported on the temperature dependence of the lifetime. Studying the growth of CNT forest from ethylene at 600-700°C, Bronikowski [322] found that the lifetime

decreases with increasing temperature with an apparent activation energy of 3.4 eV for an alumina underlayer and 2.1 eV for a silica underlayer. Studying the growth kinetics of thick CNT forests at higher temperatures (650-1000°C), Vinten *et al.* [279] also observed that the lifetime generally decreases with increasing temperature. In addition, they identified a critical temperature above which the initial growth rate started to plateau and the lifetime decreased even more abruptly. Monitoring the mass uptake of an Fe-Mo/Al_2O_3 catalyst during CNT growth, Feng *et al.* [281] observed that, with increasing temperature, the catalyst lifetime first slightly decreased, then increased and finally declined.

Several studies also showed the dependence of the lifetime on the gas phase. Using ethylene as carbon source and an Fe/Al_2O_3 catalyst, Futaba *et al* [312] reported that the lifetime tended to decrease with increasing precursor supply. Using other types of catalysts (Ni/SiO_2, Fe-Mo/Al_2O_3) and carbon sources (acetylene, ethanol), Feng *et al.* [281] and ourselves [221] also found that the lifetime generally decreases with increasing precursor pressure. When applying a separate preheating of the process gas for the growth of CNT forests, [324], Meshot *et al.* observed that the lifetime strongly varied with the preheating temperature and peaked for a certain value. As already highlighted, Futaba *et al.* showed that the addition of water at an appropriate concentration could increase the growth lifetime [312]. Using ultrapure process gases free of oxygen and water contaminations, In *et al.* [321] found that the lifetime was significantly lower with purified gases than with unpurified ones, but was strikingly insensitive to variations in ethylene or hydrogen pressures.

Finally, in the case of thick base-grown CNT forests, the diffusion of gaseous species through the growing mat of CNTs may become limiting. Observing that the growth rate decreases with time as $t^{1/2}$, Zhu *et al.* attributed the decrease to the growing diffusion resistance of the mat to gaseous species [339]. Based on diffusion modeling, Xiang *et al.*[340] argued that this explanation could only hold for highly dense millimetre-tall SWNT arrays, but not for other types of CNT samples.

- *Ultralong carbon nanotubes obtained by kite growth*

To understand the processes controlling the nanotube length, it may be useful to learn from the syntheses yielding the longest CNTs. At the time of writing, the longest reported nanotubes were obtained by kite growth, a particular mode of CVD growth where one extremity of the CNT floats in the gas phase and is oriented by the gas flow [341,342]. Such CNTs can reach lengths of 4-20 cm [343]. Their growth rates extrapolated from the synthesis duration and the CNT length can reach 10-90 µm/s [343]. Ethanol, carbon monoxide and methane are the main carbon sources used for the growth of such ultralong CNTs by kite growth. It is worth noting that the addition of an appropriate amount of water to methane [343] or ethanol [344,345] significantly enhances the growth rate of such ultralong CNTs. Different catalysts show high efficiency such as Co, Cu, Fe and Fe-Mo. The growth temperatures are relatively high (850-1000°C) compared to standard CVD conditions. In kite growth, ultralong CNTs are believed to grow by the tip-growth mechanism, *i.e.* with the catalyst particle attached at the floating end of the nanotube. This supports that substrate-related deactivation processes are major causes limiting the nanotube length.

2.3.8 Summary

The structural features of carbon nanotubes grown by CCVD strongly depend on the support-catalyst system and on the synthesis conditions. From *in situ* TEM observations, the catalyst particle undergoes a dynamic reshaping to accommodate the growing tube. In many cases, the reshaping leads to a pear-shaped catalyst particle. The outer diameter of the nanotube is observed to correlate with the lateral dimension of the catalyst particle. However,

for a given particle, the nanotube diameter is also found to vary with the growth temperature although the operating mechanism is still unclear. Carbon supply strongly influences the overall nanotube diameter distribution, but the reported trends are often contradictory supporting that its influence is strongly dependent on the growth conditions and of the studied systems. The nanotube inner diameter is often found proportional to the outer diameter with a proportionality coefficient which varies with the growth conditions. Consequently, adjusting the size of the catalyst particles is a common way to obtain CNTs of controlled wall numbers. Other parameters are also influent. A decreased carbon supply generally reduces the number of walls as expected from the original model of Tibbetts. The temperature dependence of the inner diameter is still unclear and gives rise to contradictory reports. The addition of sulphur is reported to reduce the inner diameter of CNTs.

Concerning the chiral angle, a higher occurrence of near-armchair SWCNTs in CCVD samples is frequently reported. Obtaining such chirality-enriched samples usually requires special (often binary) catalyst systems, low synthesis temperatures and optimized gaseous feeds. The origin of this chiral selectivity is debated as detailed in §2.4.4. The addition of nitrogen was also reported to promote the growth of achiral tubes. The growths of semiconducting- or metallic-enriched samples were reported by several groups. Most preferential growths of semiconducting SWCNTs can be attributed to a higher sensitivity of metallic SWCNTs to reactive environments (plasma, UV irradiation, oxygen-containing atmosphere) leading to a modification of their electrical properties or to their selective removal. The growth of samples highly enriched in metallic SWCNTs was also reported by an optimization of the annealing of the catalyst under a water-containing helium atmosphere. At the time of writing, this preferential growth of metallic SWCNTs remains largely unexplained.

The defect density of sp^2 carbon materials is commonly assessed from Raman measurements. In first approximation, the defect density of CNTs increases with increasing carbon supply and decreasing synthesis temperature as expected from classical crystal growth theory. Actually, different regimes of defect formation displaying different activation energies are observed when varying the growth temperature. Different hypotheses were proposed to explain this behaviour (*e.g.* change of state of the catalyst, formation of defective carbon by-products), but the matter is still debated. The use of oxygen- or nitrogen-containing precursors and the addition of water were shown to increase the defect density of CNTs.

In most CCVD syntheses, the percentage of particles yielding a nanotube is low (typically less than 10%). Particle inactivity is usually attributed to the stochastic nature of nanotube nucleation or to its dependence on the particle size. Water and diverse oxygen-containing precursors were found to increase the percentage of active particles and to promote the growth of highly dense CNT forests. Their effect is usually attributed to the prevention of particle encapsulation by cleaning off carbon species at the surface of the particle. Fe/Al_2O_3 used with ethylene and water traces is a popular catalyst for growing high-density CNT forests whose efficiency is attributed to both the etching effect of water and the limited coarsening of iron particles on alumina.

For given conditions, the final length of a nanotube depends on the growth limiting step, on the main deactivation process, and on their respective parameter dependences. Growth activation energies are commonly used to infer the nature of the limiting step. However, the reported values (0.2-3 eV) greatly vary from one catalyst system to another and with the growth conditions. The good correlation between the values measured by Baker (0.7-1.5 eV) and the values corresponding to bulk diffusion through solid metals supported this latter stage to be limiting. Other groups measured lower values (0.2-0.6 eV), which led them to assign the limiting step to surface diffusion or to bulk diffusion through a liquid particle. Higher values (1.5-3 eV) were also reported which were usually attributed to the surface or

gas-phase conversion of carbon precursors. This latter proposition is additionally supported by the dependence of the activation energies on the gas phase reactivity (plasma activation, preheating, precursor pressure). From these reports, it is reasonable to conclude that the nature of the limiting step can vary with the catalyst system and the growth conditions although what actually fixes the limiting step is still not rationalized. A particularly unsettled aspect concerns the influence of the nature and size of the catalyst particle on the nanotube growth rate. The growth lifetime generally decreases with increasing precursor supply. This can be counteracted by a controlled addition of an appropriate oxygen-containing additive such as water. In a large range of precursor pressure and temperature, the lifetime is observed to be inversely correlated with the growth rate. These results support that carbon encapsulation is a major cause of catalyst deactivation. However, the complex temperature dependence of the lifetime supports that other deactivation processes, such as catalyst coarsening, may be at play, especially at high temperature and low carbon supply. It is apparent that the same phenomena (catalyst coarsening, particle encapsulation) are invoked for both the growth deactivation and the catalyst inactivity, supporting that, in many cases, particles inactivity may be considered as an early deactivation. It is worth mentioning that the longest tubes to date, which were grown by kite growth, were obtained using both catalyst particles detached from the support (*i.e.* tip growth) and a controlled addition of water.

2.4. Open questions and current hypotheses

This part addresses a few selected questions that are currently considered as important in the field of nanotube growth and are the subjects of intense investigations. These questions directly impact on the experimental dependence of the nanotube features described in the preceding section. For each question, the associated hypotheses are described together with the pros and cons from experimental observations and *in silico* simulations.

2.4.1 State of the particle

- *Physical state*

The physical state of the particle (liquid or solid) is a subject of controversy. As described in §2.2.2, the melting point of a metal particle can be significantly lowered by the size effects or the incorporation of carbon atoms, or increased by interaction with the substrate. Simulations performed by Diarra *et al*. [346] show that, at the standard temperatures of CNT growth and in the absence of carbon, nickel nanoparticles down to 147 atoms (~1 nm) are solid. However, they observed that the incorporation of carbon tend to amorphize or melt the outer layer of the nanoparticle, eventually leading to a complete melting for smaller nanoparticles and large carbon fractions (*i.e.* larger than 10% at.).

In the 70s, Baker [9,10,347] proposed that the growth of carbon filaments proceeded via the vapour-liquid-solid (VLS) model developed by Wagner and Ellis for the growth of silicon whiskers [348]. In the original VLS model of Wagner and Ellis, the role of the particle is to form a liquid alloy droplet which acts as a preferred site for silicon deposition from the vapour. Once the liquid particle is supersaturated, the filament starts growing by precipitation of silicon atoms from the droplet. There are therefore two main and different hypotheses in the VLS model of Wagner and Ellis: i) the particle is liquid and ii) reactant atoms diffuse through the bulk of the particle. Actually, the proposition of Baker *et al* found massive support because the growth activation energies they measured were in excellent agreement with the values corresponding to the bulk diffusion of carbon through the corresponding metals. The results of Baker not only supported that bulk diffusion was a required step, but also that it was the rate determining step of carbon filament growth. However, it is often

forgotten that the activation energies measured by Baker were in excellent agreement with those of bulk diffusion through the metals in the solid state and not with the values expected through liquid metals. The results of Baker therefore provided a strong support for the second hypothesis of the VLS model (the bulk diffusion hypothesis), but were in contradiction with its first hypothesis (the liquid particle hypothesis). The use of the VLS term by opposition to a model where the particle would be solid is therefore often misleading. Preferably, one should specify which hypothesis of the VLS model is considered.

Experimentally, the rounded and elongated shapes of nickel catalyst particles observed after nanotube growth led Kukovitsky *et al.* [349] to conclude that the particles were liquid during the growth process. However, *in situ* TEM observations by Helveg *et al.* [193] and other groups [194-197] demonstrated that, although highly deformable, nickel and iron catalyst particles remained crystalline during CNT growth. It is worth mentioning that, to date, all *in situ* TEM observations of crystalline particles correspond to rather large particles (typically larger than 4 nm) and to low temperatures (typically less than 700°C). Experimentally, the physical state of transition metal catalyst particles of a few nanometres that are active for SWCNT growth is still an open question.

If one considers the present list of active catalysts for SWCNT growth (see §2.2.2), the melting temperature of the bulk phase ranges from 327°C (Pb) to 3550°C (diamond) for individual elements and up to 2830°C (SiC) for mixed compounds. Even by taking into account the influence of the particle size, carbon content and support, one must conclude that at standard growth temperatures (600°C-1000°C), some catalyst particles are probably liquid (*e.g.* Pb) while other ones are solid (*e.g.* diamond). For instance, the quantum-based molecular dynamics simulations reported by Page *et al.* [350] support that, during CNT growth, the surface of SiO_2 nanoparticles is converted to an amorphous SiC layer while the core of the SiO_2 nanoparticle remains oxygen-rich and solid. From all these results, one must conclude that both liquid and solid particles can support the growth of a CNT. However, the physical state does modify several properties of the particle (*i.e.* carbon solubility and diffusivity, deformability) that may influence the efficiency and features of CNT nucleation, growth or deactivation. For a given element, a solid or liquid state may therefore be preferred to assist the growth of CNTs. In the case of a crystalline particle, an epitaxial relation between the nanotube edge and the crystal structure of the particle may also be considered (see §2.4.4).

- *Chemical state*

The chemical state of transition metal particles during CNT growth is also a controversial subject, especially in the case of iron. Essentially, the question is how much carburized is the metal particle during the growth: is it still metallic or carbidic? Is carbon dissolved in the bulk, only in subsurface sites, or does it remain at the surface of the particle? Obviously, one may expect from the content of §2.2.3 that the answer varies with the considered metal, its carbon affinity and its propensity to form carbides.

Esconjauregui *et al* [36] performed *in situ* X-Ray diffraction (XRD) studies of CNT growth from a large range of elements as catalyst. They observed that all transition metal particles undergo carburization during the induction phase. At the onset of CNT growth, higher transition metal carbides such as Ni_3C tended to decompose while lower transition metal carbides, such as WC, remained stable during CNT growth. Other metal carbides, such as Mo_2C, were found stable but inactive for CNT growth. They also reported that MWCNTs could be grown by using pre-carburized Ni_3C particles as catalyst. The *in situ* TEM studies reported by Lin *et al.* [290] confirmed that Ni particles of 1-10 nm remain metallic during CNT growth and do not transform into Ni_3C carbide [351]. *In situ* XPS studies of Wirth *et al.* also showed that Ni, Co and Fe catalyst particles are in the metallic state during CNT growth.

The case of iron requires special attention. As can be seen in Figure 2-3, the stability of Fe_3C at the considered temperatures is close to that of graphite. Therefore, one should expect the stability of Fe_3C to strongly depend on the experimental conditions (*i.e.* temperature and carbon activity of the gas phase). Hofmann *et al*. observed the presence of additional carbide peaks in XPS in the case of iron, but not in the case of nickel and cobalt catalysts [352]. In line with the results of Esconjauregui *et al*, Emmeneger *et al.* [353] reported *in situ* XRD data showing that, Fe_2O_3 particles exposed to C_2H_2 were progressively converted into Fe_3C which decomposed after 20-30 min into Fe and graphite, this process coinciding with the onset of CNT growth. This result supports that Fe is in the metallic state during CNT growth and in the carbidic state before CNT nucleation. In contrast with these results, *in situ* TEM observations of different groups showed that CNTs nucleate and grow from Fe_3C particles [20,196,354]. It is worth mentioning the post-growth analysis by TEM reported by Z. He *et al.* [355]. These authors observed that, in the same sample, both Fe and Fe_3C particles could be found at nanotube ends. Interestingly, the ratio of Fe and Fe_3C particles was found to vary with the synthesis temperature, Fe_3C particles being more abundant at low temperature. In addition, CNTs connected to Fe_3C particle were all bamboo-like and were much shorter than the CNTs connected to Fe particles.

2.4.2 Reaction intermediates

A still open question concerns the nature of the reaction intermediates incorporated at the nanotube edge. This is important since the nature of the intermediates affects the mechanism of carbon incorporation in the nanotube and, hence, the growth rate, defect density and chiral selectivity. Simulations reported by Wang *et al*. [356] notably predict that changes of chirality would be more frequent in the case of the addition of carbon adatoms than in the case of carbon dimers.

Many studies were devoted to study the dissociation mechanism of carbon precursor molecules on a metal surface. Studying the dissociation of C_2H_2 on Fe(001) by first-principles calculations, Lee *et al*. [357] observed C-C bond breaking, leading to the formation of CH fragments. Molecular dynamics simulations performed by Vasenkov *et al* [358] also supported a C-C bond scission of C_2H_2, but highlighted that surface contamination by oxygen could impede the dissociation. Experimentally, Moors *et al*. [120] studied the surface products of acetylene decomposition on a nickel nanocrystal using field-assisted desorption coupled with mass spectrometry. They found that, for short reaction times ($t<10ms$), the carbon spectrum is dominated by C_1 species, demonstrating rapid C-C bond scission during acetylene decomposition. Only at longer reaction times ($t>10ms$) were higher C_n carbon oligomers ($n=2-4$) observed to form from C_1. Using C^{13}-marked ethanol as carbon source, Maruyama *et al*. [359] demonstrated that a smaller amount of site-1 carbon atom (*i.e.* next to OH) was incorporated into the CNTs, also supporting a prior scission of C-C bond in ethanol. Studying ethanol dissociation on Rh(111) by X-ray photoelectron spectroscopy and temperature-programmed desorption, Vesselli *et al*. [360] confirmed that C-C bond cleavage is the preferential dissociation channel, while C-O bond scission was not observed.

Other works support that chains of a few carbon atoms may be the actual intermediates of carbon incorporation in the CNT. Growth simulations performed by Irle *et al*. [361] support that carbon incorporation proceeds via carbon chains that are covalently attached to the nanotube edge. The image of an octopus on a rock was used by the Irle group to popularize this hypothesis. Simulations of nanotube nucleation and growth by Amara *et al*. [192,362] and Neyts *et al.* [363] also support that both processes proceed via carbon chains. Additional support was provided by the calculations of graphene nucleation and growth on a Cu(111) surface [364] showing that the formation of carbon chains of 3–13 atoms was

preferred compared to two dimensional compact islands of equal sizes. Experimentally, the afore mentioned study of Moors *et al*. [120] support a rapid aggregation of C_1 into carbon oligomers of 2-4 units. Studying graphene growth on Ru by low-energy electron microscopy, Loginova *et al*. [365] found that graphene growth essentially occurs through addition of carbon clusters of about five atoms. Even if the octopus hypothesis can account for SWCNT and graphene growth, it does not seem applicable in the case of the inner walls of MWCNTs.

Some reports support the possibility of a direct polymerization of carbon precursors, such as alkynes and benzene, without C-C bond scission. When monitoring the decomposition products of benzene by mass spectrometry during the CCVD growth of MWCNTs, Tian *et al* [19] surprisingly observed no possible hydrocarbon species derived from benzene. Concluding that the carbon-hydrogen bonds of benzene were dissociated but not the carbon-carbon bonds, they proposed that CNT growth proceeded by direct integration of six-membered rings. Their conclusion was supported by density functional theory calculations [366] showing the formation of biphenyl from two benzene molecules on the Ni(111) surface. The calculations indicate that the C-H bond of benzene could be selectively dissociated while the C-C bond was still retained. Observing that the growth kinetics of CNT forests were characteristic of heterogeneous chain reactions, Eres *et al*. [367] proposed that acetylene could self-assemble without C-C bond dissociation into larger carbon structures such as chains and nanotubes. Plata *et al*. [368] studied the effect of different alkyne additives on the growth kinetics of MWCNT forests in a cold-wall reactor. They observed that multiple alkynes react with ethylene to accelerate MWCNT growth, suggesting a polymerization-like formation mechanism without full dissociation of the carbon precursors into C_1 or C_2 units.

2.4.3 Mechanism of nanotube nucleation

Numerous works have been devoted to understand the nucleation mechanism of a nanotube. *In situ* TEM studies have now unambiguously demonstrated that SWCNT growth in CCVD is initiated by the formation of a carbon cap at the surface of the particle. These results validated the yarmulke hypothesis originally proposed by Hongjie Dai *et al.* [369]. The experimental conditions favouring a high density of nucleation have already been described in §2.3.6. Here are described the different theoretical approaches that have been reported to rationalize the nucleation process.

- *Thermodynamic models*

Analytical models based on thermodynamic arguments are an interesting first approach to identify the processes at play during nucleation and evaluate their respective contributions. Kuznetsov *et al*. [370] considered the probability of formation of a carbon nucleus at the surface of a metal/carbon particle and the corresponding critical radius. They hypothesized that the carbon nucleus has the form of a flat saucer whose edges are bent in order to bond to the metal surface. The change in Gibbs free energy for the formation of the nucleus includes four contributions: the free energy of precipitation of the carbon atoms from the particle, the free energy associated with the surfaces of the nucleus, the free energy associated with the nucleus edges and the strain energy arising from bending of the graphene layer. The model predicts that the critical radius of nucleus formation decreases with increasing temperature, increasing saturation of the metal-carbon solution and decreasing specific edge free energy. The authors observed a good agreement between this critical diameter and the average diameter of CNTs formed by different methods as a function of the catalyst nature and synthesis temperature. Dijon *et al*. [371] used a similar approach to compare the probability of two models of nanotube nucleation leading to either base-growth or tip-growth as a function of the particle size and oxidation state of the catalyst.

The model developed by Kanzow *et al.* [372] addressed the thermodynamic conditions for a graphene plane at the surface of a liquid metal/carbon particle to bend and form a fullerene-like cap. The formation of a cap will be preferred if the available thermal energy exceeds the work of adhesion at the graphene/particle interface and the strain energy associated with the cap formation. The work of adhesion depends on the nature of the metal and decreases with the carbon content of the particle. The strain energy per unit area decreases when the diameter of the graphene plane increases. Although simple, the model could reproduce the general trends of the nanotube diameter distribution observed in arc discharge and laser ablation when varying the catalyst nature and the growth temperature. More recently, Schebarchov *et al.* [373] developed a model based on a flexible graphitic cap with its free edge constrained to the surface of a rigid spherical particle. They considered that the cap will lift if the curvature energy penalty in the collapsed state exceeds the work of adhesion. Their model provided a prediction of the catalyst-to-nanotube diameter ratio in good agreement with experimental observations for nickel and iron catalysts. However, a model based on a rigid catalyst particle appears somewhat unrealistic with regard to the deformability of the particle revealed by *in situ* TEM.

- *Computer simulations*

Such macroscopic models provide useful insights, but they generally lack reliable input data and their applicability at the nanoscale and the building hypotheses can often be questioned. For instance, all models consider a rigid particle which is contrary to most recent experimental observations. Contrary to thermodynamic models that consider idealized objects such as perfect cap structures on a spherical nanoparticle, but lack of reliable energy parameters, computer simulation approaches generally start from a validated interatomic energy model. As discussed in §2.2.3, different atomic interaction models for metal and carbon have been proposed, ranging from simple empirical models to more sophisticated and more demanding in computer resources *ab initio* calculations. Not all models give the same carbon solubility in the metal nanoparticle but a general trend is that the cap nucleation takes place once the nanoparticle is saturated with carbon [362,374]. In many models [362,374,375], carbon chains appear on the surface before a cap is formed. Although no direct experimental evidence has been produced, the presence of carbon chains during the nucleation and growth has been suggested by Eres *et al.* [367] and by Loginova *et al.* [365] in the case of graphene. The length of the observed carbon chains depends on the model and the precise nucleation and growth conditions and lead to more of less disordered structures. Quite interestingly, Neyts *et al.* [376] observed that the almost defect-less carbon nucleus formed could change its chirality in the early stages of the growth, thus discarding a possible determination of the tube chirality at the nucleation stage.

Once a cap is formed, it has to detach from the nanoparticle in order to avoid the encapsulation of the catalyst. Different explanations have been proposed to explain the cap detachment and lift-off. By systematically varying temperature and work of adhesion of the graphitic cap on the nanoparticle, Ribas *et al.* [377] could identify conditions leading either to a successful growth or to nanoparticle encapsulation. To explain the formation and lift-off of carbon domes observed by *in-situ* TEM during the formation of a MWCNT on an Au doped Ni catalyst, Pigos *et al.* [378] identified two critical factors: the surface energy of the nanoparticle, that can be modified by chemisorbed carbon species, and the faceting of the nanoparticle. More recently, Diarra *et al.* [346] showed that the wetting properties of carbon sp^2 walls on a Ni nanoparticle strongly depend on the fraction of carbon dissolved, and demonstrated that the cap lift-off takes place when the carbon concentration in the catalyst is within a critical window.

2.4.4 Chiral selectivity

Chiral selectivity is an important issue in nanotube research due to the large number of applications requiring nanotubes having controlled electrical and optical properties. A higher proportion of high-chiral-angle SWCNTs (*i.e.* near-armchair) in nanotube samples is commonly reported as was already detailed in §2.3.3. The origin of this higher occurrence is still a matter of questioning. In the following are reviewed the theoretical works that have been devoted to this question and the hypotheses that have been proposed.

- *Nucleation selectivity*

A first possibility is that chiral selectivity is set at the nucleation stage. This hypothesis relies on the fact that the structure of a cap uniquely determines the chirality of the nanotube that will grow from it. In other words, in the absence of defects, the nanotube structure is an amplification of the rim structure of the cap. There is a statistical or entropic aspect to this question, *i.e.* how many different cap configurations exist for a given (n,m) tube. Brinkman *et al.* [379] established a census of the nanotube caps compatible with all tubes up to a diameter of 3 nm. Considering either general caps or isolated-pentagon caps, they found that the number of compatible caps increases quasi-exponentially when increasing the nanotube diameter. Reich *et al.* [380] performed a detailed study of the geometry, structure, and energetics of nanotube caps. They observed that tubes with diameters smaller than 6.8 Å have only caps that violate the isolated pentagon rule. The caps with isolated pentagons were found to have an average formation energy of 0.29 eV/atom while a pair of adjacent pentagons required a formation energy of 1.5 eV. This much larger formation energy justifies the isolated pentagon rule and would explain the quasi-absence of SWCNTs of diameters less than 7 Å in nanotube samples. The (5,5) nanotube is the smallest diameter tube that has a cap obeying the isolated pentagon rule (a half C_{60}). The other tubes with only one cap fulfilling the isolated pentagon rule are (9,0), (9,1), (8,2), and (6,5). Therefore, these results cannot account for the higher abundance of (6,5) and high-chiral angle SWCNT in many samples. This statistical approach is interesting in the first place, but all cap sizes are not equally probable since caps progressively grow in size and are constrained by the catalyst particle. In addition, considering that pentagons are randomly formed neglects the chemistry of formation of carbon cycles and the probable influence of the catalyst surface.

Reich *et al.* [381] performed *ab initio* calculations of the stability of different caps on a flat Ni surface. The results suggested that certain caps may be thermodynamically preferred due to lattice matching with the catalyst surface. However, the energy differences were quite small (of the order of the thermal energy). The energy of graphene edges were calculated by Liu *et al.* [382] who found that the energy of an arbitrary graphene edge was significantly dependent on the orientation (from armchair to zigzag) and on the chemical functionnalization of the edge (*i.e.* –H or –Ni). They proposed that this difference of edge energies may influence the chiral selectivity at the nucleation stage. At the opposite, Zhu *et al.* [200] calculated the formation energies of (10,0) and (5,5) SWCNT caps sitting on a Ni_{55} cluster and found the energy difference to be too small to expect a preferential nucleation of caps corresponding to either high or low chiral angles SWCNTs.

Most of these simulations were performed starting from pure Ni or Co catalysts but, in some cases, carbide particles may be more relevant. For instance, Koziol *et al.* [250] reported the preferential growth of achiral CNTs (zigzag and armchair) when nitrogen was added during the growth. They observed that the catalyst particles are iron carbide and are preferentially oriented with the [010] direction parallel to the nanotube axis and, more precisely, to either the [100] or [210] graphene direction [383]. Their studies support that the

role of nitrogen is to stabilize iron carbide catalyst particles which act as epitaxial template for the selective nucleation of achiral CNTs.

- *Growth-rate selectivity*

A second possibility is that the growth rate of SWCNTs is chirality-dependent. All such models assume that carbon integration, the last stage of the growth mechanism, is the rate-determining step and that its rate varies with the nanotube chirality. Experimentally, this is supported by several observations of higher reactivity of armchair edges compared to zigzag edges in the case of graphene [384-386]. Shu *et al.* [387] calculated that connecting a Cu atom to an armchair site lowers the barrier of incorporating carbon atoms onto graphene edge from 2.5 eV to 0.8 eV, which would result in a much faster growth of armchair edges compared to zigzag edges. In the case of SWCNTs, Rao *et al.* reported *in situ* Raman measurements of the growth rates of index-identified tubes [388] showing a positive correlation between the nanotube growth rate and chiral angle.

On the theoretical side, several works were devoted to the question of chirality-dependent kinetics. Zhao *et al.* [389] found that the energy of the frontier orbitals for (5,5) and (6,6) armchair carbon nanotubes bonded to Ni atoms exhibits a periodic behaviour when increasing the number of carbon atoms in the nanotube. In contrast, the energy of the frontier orbitals of the (6,5) tube was found constant as the number of carbon atoms increases. They proposed that the energetic smoothness of carbon addition in (6,5) SWCNT may account for its experimentally high occurrence. Wang *et al.* [390] simulated the growth of armchair (5,5), chiral (6,5), and zigzag (9,0) nanotubes on a relaxed Ni_{55} cluster and studied the reactivity caused by charge transfer between the metal particle and the tube. They notably found that the edge of a (6,5) tube presents a single particularly reactive site which could explain the preferential growth of chiral (6,5) nanotubes over armchair (5,5) and zigzag (9,0) nanotubes. Gómez-Gualdrón *et al.* studied the energetics of frontier orbitals for different caps connected to a 9-atom Co cluster during C_2 addition [391]. The LUMO orbital expected to participate in the C_2 addition reaction was found to be located in a more favourable part of the cap rim for near-armchair than for near-zigzag caps. They concluded that the carbon atoms in the near-armchair caps may have a better predisposition for continuation of the nanotube growth reaction when the growth proceeds by C_2 addition.

Also considering carbon addition to either armchair or zigzag nanotube edges connected to metal steps, Ding *et al.* [392] calculated that the addition of carbon to an armchair site has essentially no barrier while, for a zigzag edge, the barrier energy is of the order of 1.1-1.5 eV. Building on that, they proposed that the lengthening rate of a nanotube is proportional to the linear density of armchair sites (*kinks*) at the nanotube edge, which is approximately proportional to the chiral angle of the tube (Figure 2-14). Dumlich and Reich [393] theoretically considered the geometric constraints for the addition of C_2 dimers to armchair kinks at the edge of a nanotube. Observing that nanotube growth basically proceeds via the conversion of dangling bonds from armchair (a) to zigzag (z) and vice versa, they concluded that all armchair kinks are not equivalent and that a nanotube edge actually contains three types of armchair kinks (•) for C_2 addition: aa•aa, aa•z and z•z. In the case of a low energy difference between zigzag and armchair dangling bonds, the growth rate is proportional to the density of armchair kinks, which is a conclusion similar to that of Ding *et al.* In the case of a much larger energy for zigzag dangling bonds than for armchair ones, the model predicts that (n, n/2) chiral tubes would be kinetically favoured.

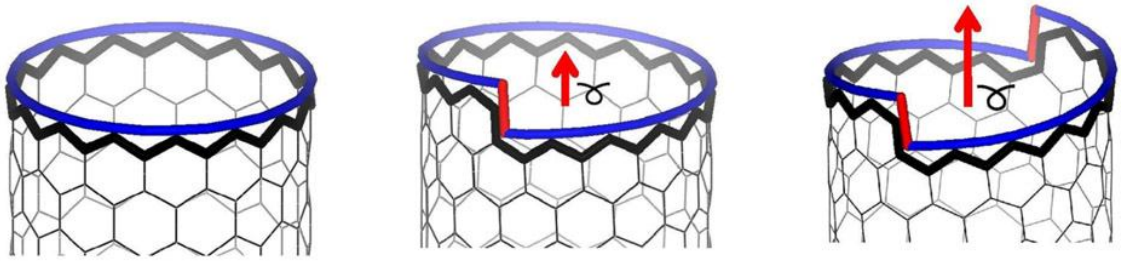

Figure 2-14. Schematic rim structures of (n, 0), (n, 1) and (n, 2) nanotubes showing that the number of kinks (armchair sites) is proportional to the chiral angle. Red arrows denote the Burgers vectors describing the axial screw dislocation associated with each tube. Adapted from [392].

- *Lifetime selectivity*

A third possibility is that the resistance of a growing tube regarding growth termination or chiral change is chirality-dependent. Environmental TEM observations frequently show the introduction of defects and the creation of kinks during CNT growth [199]. Changes of chirality along CNTs were experimentally observed [394]. Yao *et al.* [214] showed that chiral changes could be induced by slight modifications of the conditions (*e.g.* temperature) during the nanotube growth. Recently, Kim *et al.* [395] simulated the dynamics of SWCNT chirality during growth and observed that improper defect healing could lead to changes in the SWCNT chirality. In this respect, zigzag SWCNTs were found significantly inferior in maintaining their chirality compared to armchair SWCNTs. Besides defect integration, a major cause of growth termination or of chirality change is the coarsening of the catalyst particles. Using first principles calculations, Börjesson *et al.* [396] studied the influence of the nanotube chirality on the Ostwald ripening of the attached particle. They found that the Ostwald ripening of metal particles attached to CNTs not only depends on the particle size, but also on the nanotube chirality. Particles attached to armchair and zigzag nanotubes of similar diameters were found to have different propensity to ripening. For both hypotheses (defect integration and catalyst coarsening), experimental studies of the chiral dependence are still missing.

2.4.5 Summary

Concerning the state of the particle, *in situ* TEM studies show that catalyst particles of iron, nickel and cobalt are highly deformable, but still crystalline during growth. These observations were made on rather large particles (typically larger than 4 nm), which leaves open the question of the physical state in the case of smaller nanoparticles. Considering the range of elements active for CNT growth, certain particles are likely to be liquid (*e.g.* Pb) and other ones solid (*e.g.* diamond) at the temperatures of nanotube growth. Having an either liquid or solid particle does not appear to be a requirement for growing a CNT, although the nanotube and growth features are likely to be strongly impacted. From *in situ* studies (TEM, XPS, XRD), nickel and cobalt particles are usually in a metallic state during nanotube growth while iron particles may either display a metallic or carbidic structure.

The nature of the reaction intermediates (adatoms, dimers, chains, undissociated precursors) is still unsettled. Different *in situ* studies revealed the presence of C_1 species at short synthesis times. At longer times, the conversion of carbon adatoms into higher C_n oligomers (n=2-5) is reported both experimentally and *in silico*. In the case of alkynes and aromatic precursors, the hypothesis of a direct polymerization without C-C bond scission has been proposed by certain groups to account for the unusual kinetic behaviour.

Concerning the mechanism of nanotube nucleation, the formation of a carbon cap at the surface of the particle (the *yarmulke* hypothesis) has now been validated by *in situ* TEM observations. Thermodynamic models support a strong influence of the carbon concentration, metal-carbon interaction and temperature on the formation of a carbon nucleus of critical size. Numerical simulations also confirm that surface formation of carbon structures takes place once the nanoparticle is saturated with carbon. They highlight the critical importance of the carbon cap-metal surface adhesion in the process of cap lift-off and its dependence on the type of metal and fraction of carbon dissolved in the particle.

To explain the chiral selectivity experimentally observed, three general hypotheses are considered: chiral-selective nucleation, chiral-dependent growth rate and chiral-dependent lifetime. The selective nucleation hypothesis is now somehow abandoned due to the small differences of formation energies calculated for caps of different chiralities. Growth-rate selectivity is currently preferred based on calculations showing a large difference of barrier energies for carbon integration at armchair and zigzag sites and on experimental measurements of the growth rate of individual SWCNTs of different chiral angles. The lifetime selectivity assuming a chiral-dependent propensity of growth termination or chiral change has found some support from simulation works, but is still to be experimentally verified.

2.5. Conclusion

As apparent from this review, the growth mechanism of CNTs in CCVD is complex and still ill-understood. Its understanding is noticeably complicated by the variety of studied systems: catalyst, support, carbon precursor, growth conditions. Too many and too different experimental systems often lead to observations too different to allow unification and rationalization. In addition, the studied systems are frequently insufficiently controlled and characterized. Learning from other fields of research such as heterogeneous catalysis or molecular biology, one may identify two successful approaches to work out complex mechanisms: the study of model systems and the development of numerical simulations. As evidenced in this review, numerical simulations have already been extremely beneficial for orienting experimental works and improving our understanding of CNT growth mechanism. With increasing calculating capacities, simulation will probably become an essential prediction tool for the phenomena that are still too difficult to study experimentally. I leave this exciting task to my colleague Christophe Bichara and his other theoretician fellows.

On the experimental side, the field would probably benefit from the establishment and study of model systems, as was successfully demonstrated in the field of heterogeneous catalysis with the study of model surfaces and clusters. Fe/Al_2O_3 used with ethylene as carbon source and water as additive is an example of such a model system which has self-established due to its high nanotube yield. Other model systems having characteristic features important for fundamental studies such as catalyst clusters of uniform size, no or negligible catalyst coarsening, known limiting step or known dissociation products, would also be highly desirable. Finally, we now have a qualitatively good description of many phenomena acting during CNT growth, but quantitative relations are often lacking (*e.g.* quantitative parameter dependences of the defect density, growth rate, number of walls, outer and inner diameters). More quantitative models would be extremely helpful for orienting experimental works and facilitating the analysis of experimental data.

3. Investigations

"Application of Raman spectroscopy to the study of the catalytic growth of carbon nanotubes"

3.1. Introduction

3.1.1 Chronology

The main focus of my research interest has been the synthesis-structure relationship in catalytically-grown carbon nanotubes and nanostructures in general. I first thought about using Raman spectroscopy to monitor and characterize nanotube growth when I was a postdoc at the Engineering Department in Cambridge. I had the chance to share my office with another postdoc, Stephan Hoffman, who had the same research interests. At that time, I had started investigating the CCVD growth of SWCNTs using a laboratory-standard tubular furnace. I became quickly depressed by the time wasted at performing week-long parametric studies yielding samples showing little interest when characterized a few days later. I was also frustrated by our ignorance of what was going on at the different stages of the synthesis. I thought that a smaller reactor would probably do as well and allow one to test many more conditions in a shorter time for a systematic investigation of the growth parameters. As importantly, a smaller reactor could allow an easier access for *in situ* characterization measurements by a method that had to be chosen. While my officemate Stephan went for *in situ* XPS and TEM studies, my preference went to optical spectroscopies which were closer to my original background. In addition, I was amazed by the recent breakthroughs concerning the optical properties of SWCNTs. The theoretical possibility of selectively exciting one type of nanotube with a laser beam during the growth represented an additional source of motivation. When I obtained a tenure position in France, I decided to build this setup using Raman spectroscopy as characterization technique. Here again, I was lucky to have a colleague expert in Raman spectroscopy, Eric Anglaret, who was interested in collaborating on the project. Raman spectroscopy brings several advantages. It is sufficiently fast to allow *in situ* monitoring at the second timescale and *ex situ* systematic characterization of a large number of samples. Both structural and quantitative data can be collected and compared with growth models. There was already a preliminary study by the group of Shigeo Maruyama [397] at Tokyo University demonstrating the possibility of monitoring CNT growth with Raman spectroscopy but there was still lot of place for systematic studies and data rationalization. The work presented hereafter was the subject of the master internship and PhD thesis of Matthieu Picher (2006-2010) and of the PhD thesis of Hugo Navas (2010-2012) which I co-supervised with my colleague Eric Anglaret. Several colleagues additionally contributed to this work, notably Raul Arenal (LEM-ONERA, Châtillon), Etienne Quesnel (LITEN, CEA Grenoble), Thierry Michel and Saïd Tahir (L2C, Montpellier).

3.1.2 Raman scattering of carbon nanotubes

Raman spectroscopy relies on the inelastic scattering of light resulting from the interaction between the incident light and vibrational modes (or other excitation modes) of the system. Raman spectroscopy is extensively used for the structural characterization of carbon-based materials in general and of carbon nanotubes [398] in particular. The Raman spectrum of SWCNTs presents several modes of interest (Figure 3-1): the radial breathing modes (RBMs) between 100 and 400 cm^{-1}, the D band around 1350 cm^{-1}, the G band around 1580 cm^{-1}, and the G' band (also called 2D or D*) around 2600 cm^{-1}. The G band is a first-order peak which is common to all sp^2 carbon systems and corresponds to C-C bond stretching

modes tangential to the nanotube wall. The curvature effects in carbon nanotubes, give rise to multiple peaks in the G-band compared to the single G peak of graphene. The G-band of a SWCNT sample is the sum of the contributions of many structurally-different SWCNTs. It is generally the most intense signal. RBMs are also first-order Raman modes which correspond to an out-of-plane bond-stretching for which all the carbon atoms move coherently in the radial direction. The RBM frequency is inversely proportional to the nanotube diameter. The D band is a second-order mode involving a non-zone-centre tangential phonon mode. It is theoretically non-active in Raman scattering but becomes activated in the presence of defects causing an elastic scattering of electrons. The intensity ratio of the D and G bands are commonly used to assess the density of defects of sp^2 carbon materials or the presence of defective carbonaceous impurities. In first approach, the G' band can be considered as an overtone of the D band corresponding to a second-order process involving two phonons of opposite wave vectors. The G' band does not require the presence of defects to be active. However, resulting from a double-resonant process, it is particularly sensitive to the modifications of the electron and phonon structures [399]. The D and G' bands are both dispersive modes, which means that their frequency shifts with the incident laser energy.

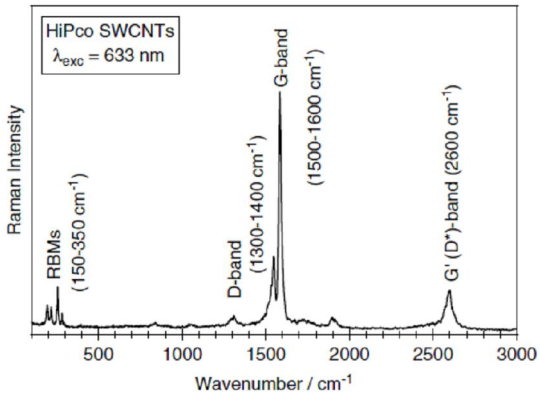

Figure 3-1. Typical Raman spectrum of a SWCNT sample (HiPco nanotubes). From [400].

Raman scattering of SWCNTs is a resonant process, which means that the Raman signal is enhanced by a few orders of magnitude when the excitation energy matches an allowed optical transition of the system. A Raman scattering intrinsically intense is important for the targeted studies since it decreases with increasing growth temperature due to anharmonic effects [401]. In first approximation, these optical transitions can be considered to correspond to transitions between van Hove singularities in the electron density of states but the last studies showed that a more correct description implies excitonic states caused by the quantum confinement. The optical transitions of SWCNTs are commonly plotted as a function the tube diameter in a so-called Kataura plot (Figure 3-2).

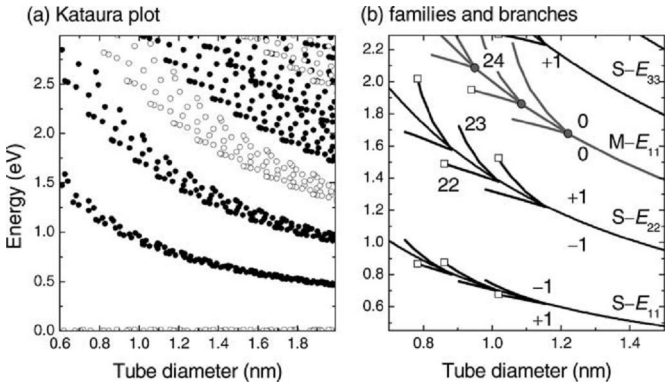

Figure 3-2. (a) Kataura plot: calculated transition energies of semiconducting (filled symbols) and metallic (open) nanotubes as a function of tube diameter. (b) Expanded view of the Kataura plot. From [402].

3.2. Materials and methods

In most studies, catalysts consisted of 5 Å-thick layers of nickel or cobalt deposited by evaporation or ion beam sputtering on Si(100) support with a 100 nm layer of thermal silicon oxide (later denoted as SiO_2/Si). To remove carbonaceous impurities and reduce the coarsening of the catalyst during the CVD ramp, the catalysts were calcined at 700°C under air or pure oxygen before the CVD growth.

A commercial stage (Linkam TS-1500) equipped with a resistive heating crucible, an integrated thermocouple and a silica window was used to perform CNT syntheses monitored by optical measurements (Figure 3-3). Gaseous feeds (argon, acetylene, methane, ethylene) were supplied through mass flow controllers while the supply of water or ethanol vapours was authorized by an thermo-regulated bubbler. Oxygen and water concentrations were measured by in-line detectors at the outlet of the cell. Typical oxygen and water concentrations during CNT growth were of the order of 2 ppm and 20 ppm, respectively.

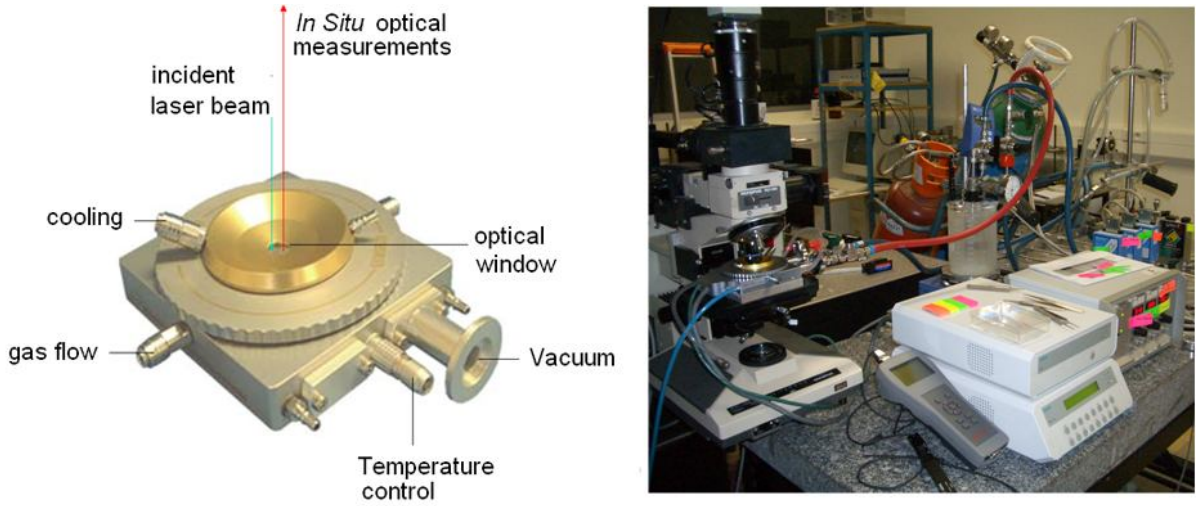

Figure 3-3. Setup for *in situ* Raman measurements: CCVD cell (left) and general view (right).

In situ Raman measurements were performed in micro-Raman mode with a Jobin Yvon T-64000 spectrometer (simple or triple grating configurations). Laser excitations were mostly performed at either 532 nm or 647 nm, with a x50 objective and laser powers on the sample between 5 and 12 mW. We checked that such laser powers induces no heating of the carbon nanotubes (Figure 3-4a). In order to compare growth kinetics acquired at different temperatures, we measured an intensity correction factor for each feature of the Raman spectrum (G band, D band, Si peak at 521 cm^{-1}) as a function of the temperature (Figure 3-4b). This correction factor was systematically applied to the kinetic data shown hereafter. Raman spectra were also acquired post-growth at room temperature in the cell under argon flow and before air exposure.

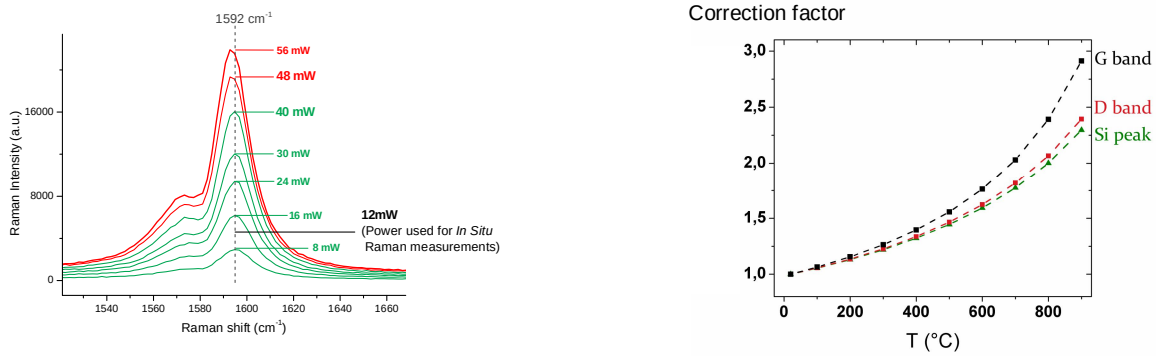

Figure 3-4. (a) Power dependence of the G-band of carbon nanotubes on SiO_2/Si. No Raman shift is observed below 40 mW. (b) Calibrated temperature correction factors for the G band, D band of an as-grown SWCNT sample and for the main peak of Si at 521 cm^{-1}.

TEM grids were prepared by scratching the surface of CNT samples with a diamond tip and collecting the detached substrate pieces on a holey carbon grid. High-resolution transmission electron microscopy (HRTEM) was performed by Raul Arenal at ONERA and U. Zaragoza using three different field-emission TEMs: a Zeiss Libra 200FE (operating at 200 kV) and two FEI Tecnai F20 and F30 (working at 200 and 80 kV, respectively). SEM characterizations of the samples were also performed using two different field-emission gun microscopes (FEI Quanta FEG 200, Hitachi S4800).

3.3. Post-growth characterization and arising questions

Before detailing the benefits of *in situ* Raman measurements, I will first describe the data obtained after growth from standard *ex situ* characterization techniques when a systematic exploration of the growth conditions is performed. Such an analysis raised questions that we tried to address in the following.

3.3.1 Electron microscopy

SEM characterization of as-grown samples shows that the nanotube density significantly varies as a function of the growth conditions. SEM pictures corresponding to two extreme samples are shown in Figure 3-5. Lowest yield samples display a few long CNTs lying on the silicon oxide surface. Between the few long SWCNTs, a high density of short nanostructures is apparent. These samples rapidly display charge effects under electron illumination making difficult their characterization at high magnification. Highest yield samples display a thin mat of entangled nanotubes lying parallel to the surface plus a few ones protruding and particularly apparent due to tip effects. Side views (Figure 3-6) show that the thickness of the nanotube layer is typically less than 50 nm. This is confirmed by the observation that, in most growth conditions, the silicon supports keep displaying a good reflectivity after nanotube deposition.

In view of quantitative Raman measurements, these SEM observations suggest that the absorption and interference effects caused by the nanotube layer will usually be negligible and that the Raman intensity will be directly proportional to the surface density of SWCNTs in resonant conditions. With our x50 objective, the size of the laser spot on the sample is typically 2 µm, which is about the height of the SEM image in Figure 3-5b. This means that during a typical experiment, there will be hundreds of SWCNTs probed by the laser beam. From a statistical point of view, one can expect that the measured Raman signal corresponds to a large population of SWCNTs in resonance with the laser energy and does not correspond to only one or a few individual nanotubes.

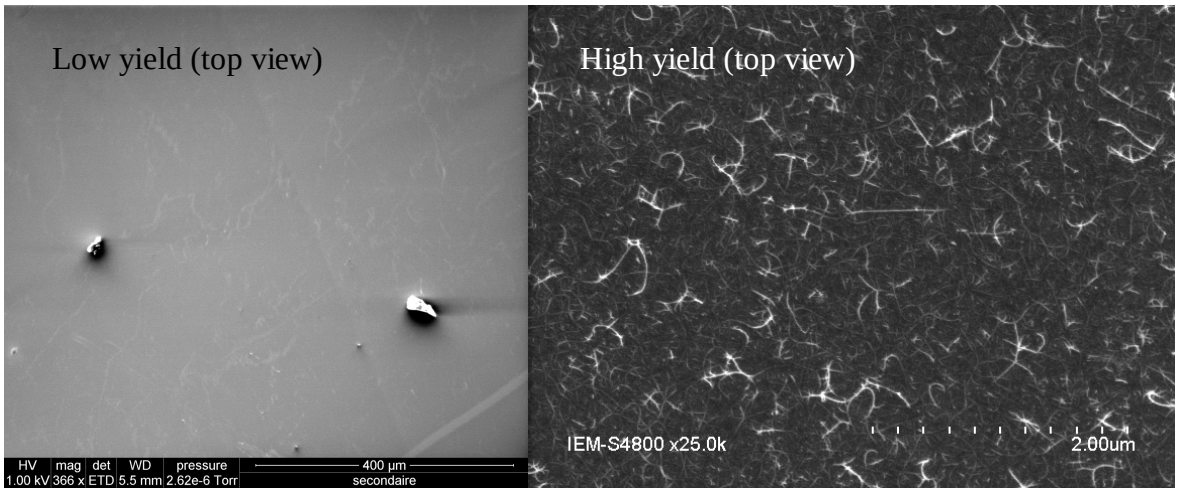

Figure 3-5. Top-view SEM pictures of samples displaying different nanotube yields. (a) Low yield sample (575°C, P_{EtOH}=533Pa). (b) High yield sample (800°C, P_{EtOH}=59 Pa).

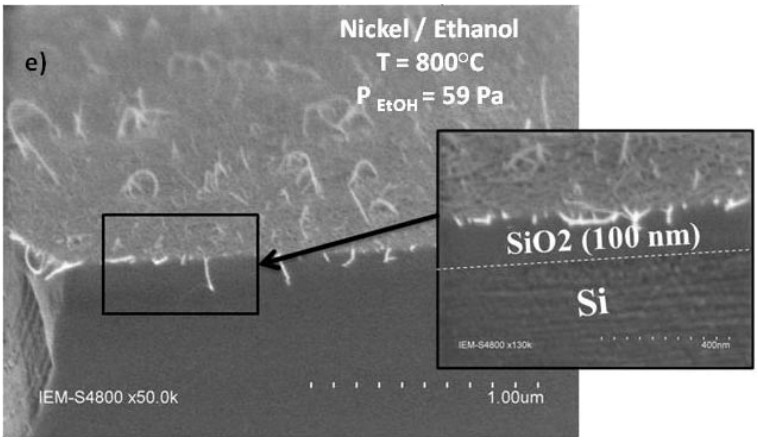

Figure 3-6. Side-view SEM picture of a high yield sample.

HRTEM observations were initially performed on the samples grown with the Ni-EtOH couple which constituted the main system of our investigations. From HRTEM observations, samples grown at high temperatures essentially consist of long bundled SWCNTs (length>200 nm) with negligible amounts of amorphous carbon on their walls (Figure 3-7a-b). No DWCNT or MWCNT could be observed. The SWCNT grown at high temperatures appear very straight with few defects. By contrast, low-temperature samples display defective and extremely short nanotubes (Figure 3-7c-d). Some SWCNTs can reach 30 nm in length but most of them are less than 10-nm long. SWCNT bundles are very scarce in low-temperature samples probably because there are too few long SWCNTs. Instead, the samples are dominated by agglomerates of very short and defective single-layer carbon structures mixed with catalyst nanoparticles. Their walls display several kinks but are essentially free of amorphous carbon deposits. Some structures are so short and defective that they may not be qualified of tubes anymore but of nanohorns or nanobubbles instead. However, their single-layer structure attests that they have a certain degree of order and are definitely not amorphous or pyrolytic carbon. Catalyst particles are frequently observed to be connected to, embedded with or even encapsulated by these carbon structures, which additionally supports that the formation of the latter is catalytically assisted.

3.3.2 Raman spectroscopy

As illustrated on Figure 3-7e-g and Figure 3-8, Raman spectra acquired post-growth at room temperature significantly vary with the growth conditions. The G band of the samples typically displays a high-frequency G^+ component at around 1590 cm^{-1} and one or several G^- components at lower frequencies between 1520 and 1580 cm^{-1} (Figure 3-8). Such features are characteristic of SWCNT samples.

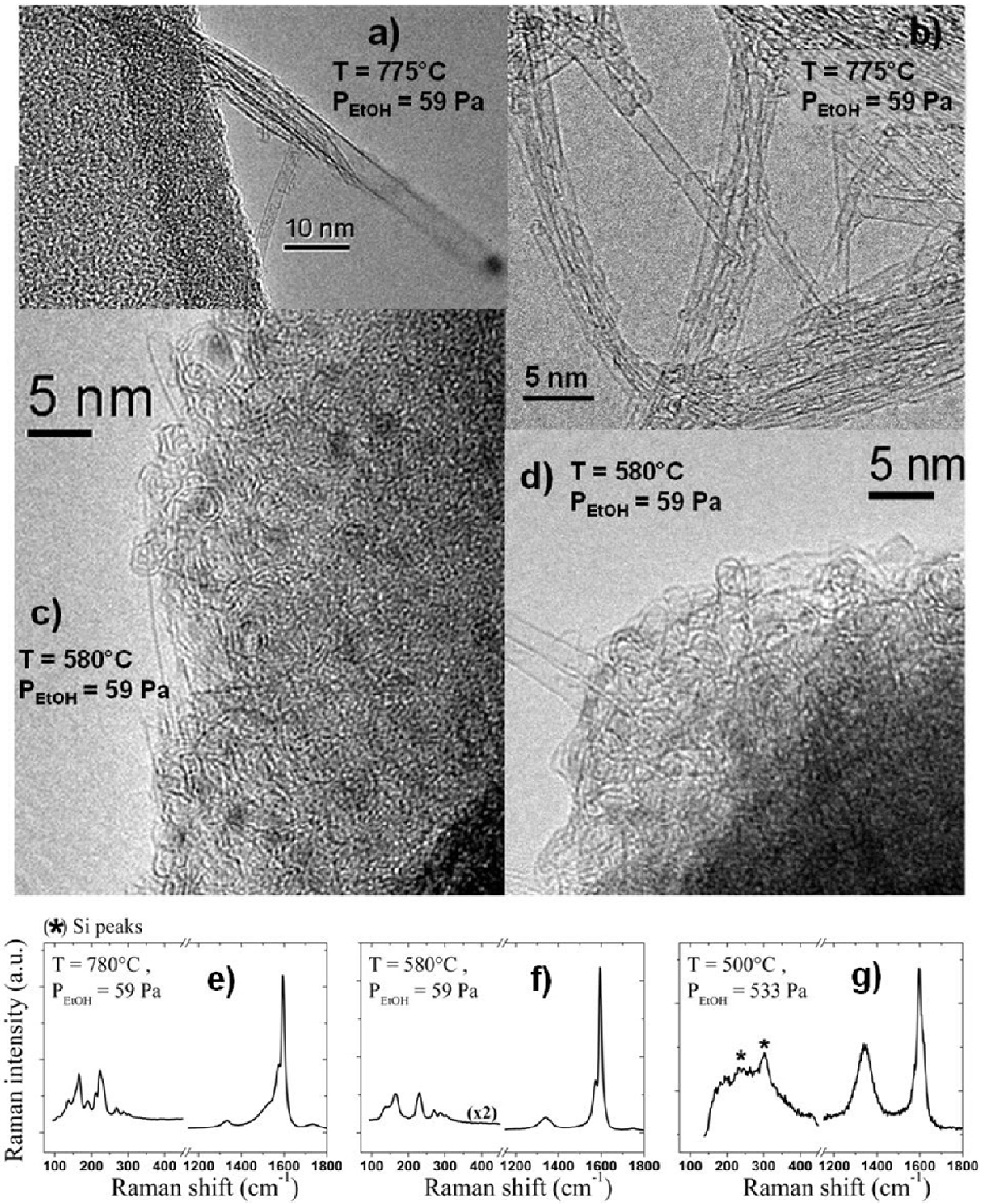

Figure 3-7. Typical HRTEM for samples prepared at high (a-b) and low (c-d) temperatures, respectively. (e-f-g) Typical Raman Spectrum for samples prepared at high (780°C), low (580°C) and very low temperature (500°C), respectively (excitation line at 532 nm).

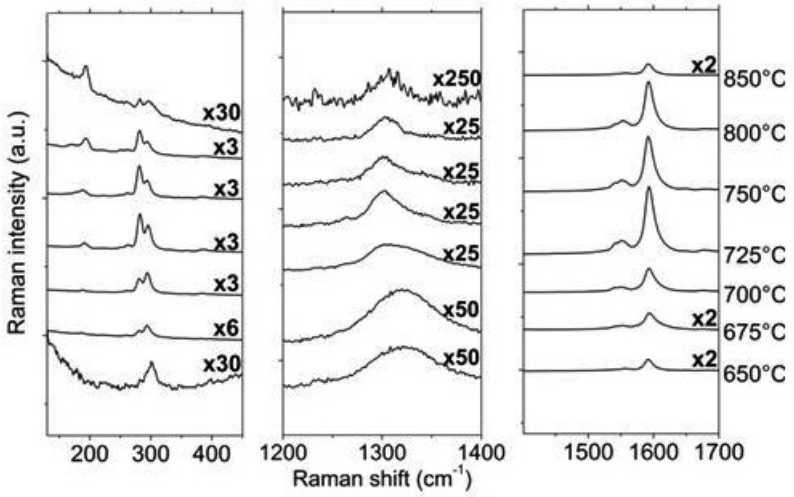

Figure 3-8. Raman spectra of SWCNT samples grown with the cobalt-acetylene couple as a function of the growth temperature. The spectra were recorded at room temperature at a laser excitation line of 647 nm.

All samples display RBMs (see Figure 3-9 and Figure 3-10) at the exception of those grown at extremely low temperatures and high precursor pressure (see Figure 3-7g). Figure 3-9 shows the RBM profiles at λ=532 nm for the samples grown with the nickel-ethanol couple as a function of the temperature T and precursor pressure P. One can observe that the relative weight of high frequency RBMs (*i.e.* of small-diameter SWCNTs) increases with temperature until 675°C. Above 675°C, the intensity of high frequency RBMs decreases to the benefit of the low-frequency RBMs. The RBM profile is also very dependent on the ethanol partial pressure. For each temperature, one can define an optimal ethanol pressure for high frequency RBMs (Figure 3-10b). This optimal pressure increases with increasing temperature: 8 Pa at 550°C, 59 Pa at 625°C, 4.800 Pa at 800°C. The same evolution is observed at the excitation wavelength of 647 nm (Figure 3-10c). Note that at 532 nm, high frequency RBMs correspond to metallic nanotubes while they are assigned to semiconducting ones at 647 nm. It must be concluded that the changes in the RBM profiles primarily reflects an evolution of the diameter distribution and not of the metal/semiconducting ratio.

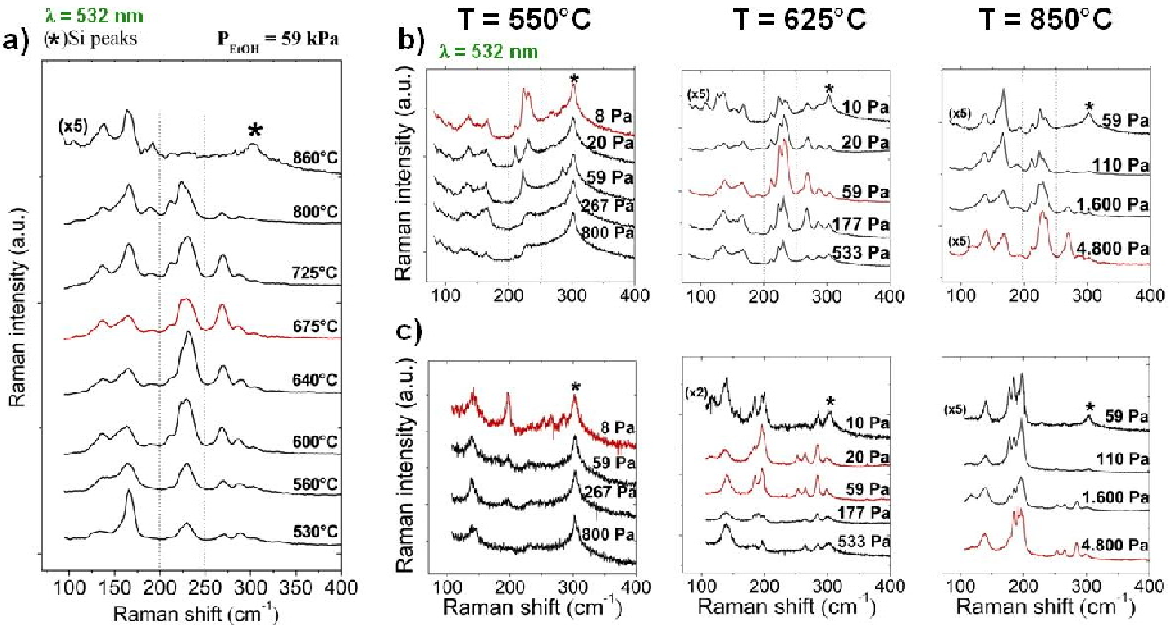

Figure 3-9. (a) Evolution of the RBM spectra as a function of the growth temperature. (b) Evolution of the RBM spectra as a function of the ethanol pressure at 550, 625, and 850°C for λ=532 nm. (c) Same as (b) for λ=647 nm. Red curves correspond to the maximal proportion of small diameter nanotubes.

From these results, one can identify two distinct domains with opposite influences of T and P on the diameter distribution. In the low T - high P domain, increasing the temperature or decreasing the precursor pressure favours the growth of small diameter SWCNTs. On the contrary, in the high T – low P domain, the synthesis of small diameter SWCNTs is promoted by decreasing the temperature or increasing the precursor pressure. The highest proportions of small diameter SWCNTs are obtained at the frontier of these two domains.

Other carbon precursors (methane, acetylene and ethylene) were used with nickel to check the generality of this behaviour. The evolutions of the RBM profiles as a function of temperature for methane, acetylene and ethylene are shown in Figure 3-10 and the ratio of small- over large-diameter RBMs in Figure 3-13. One can observe that the trends observed for ethanol-nickel are also observed for nickel-ethylene and nickel-methane. For these systems as for nickel-ethanol, the proportion of small-diameter SWCNTs peaks between 600 and 700°C. In the case of the nickel-acetylene system and of the cobalt-ethanol system, the average diameter increase at high temperature is also observed while the diameter increase at low temperature is not (or much less) apparent (Figure 3-13d-e). This could be attributed either to a lack of data at lower temperatures or to the absence of this regime for these two systems.

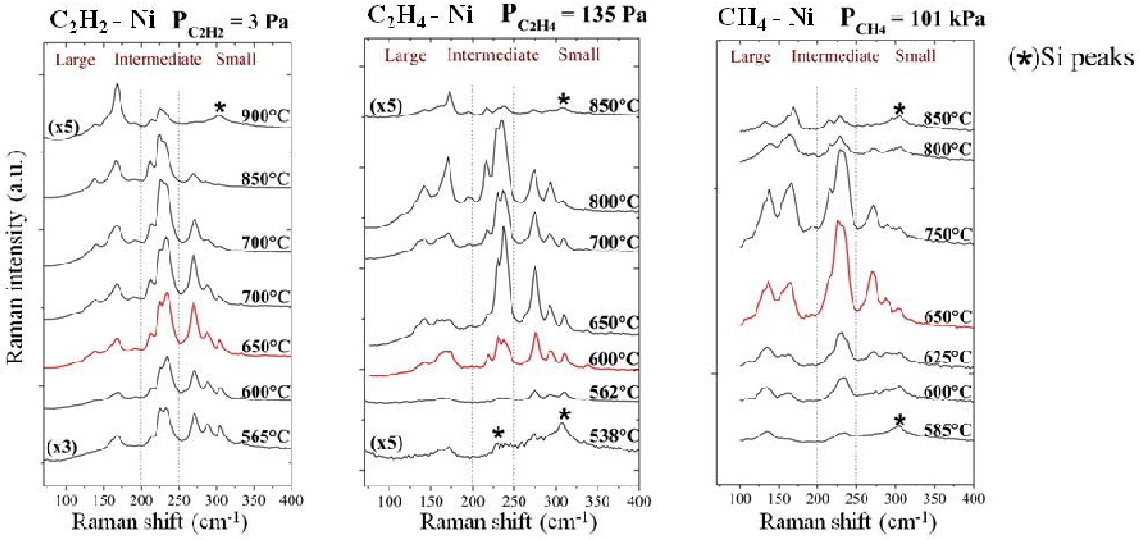

Figure 3-10. Evolution of the RBM spectra as a function of synthesis temperature for C_2H_2, C_2H_4 and CH_4 combined with nickel. The red curves signal the highest proportion of small diameter SWCNTs.

The RBM profiles show that the measured Raman spectra result from the contributions of numerous different tubes in resonant conditions. As a consequence, the G-band intensity of these samples can be considered as a good indicator of the nanotube yield. The final intensity of the G band as a function of the growth conditions is shown in Figure 3-11a in the case of the couple nickel-ethanol. One can observe that no carbon deposition is observed below a threshold temperature and a threshold pressure. This threshold pressure increases with increasing temperature. It is also apparent that each temperature displays an optimal precursor pressure for the nanotube yield (see also Figure 3-12). This optimal pressure increases with increasing temperature. Figure 3-11b shows the integrated intensity ratio of the G and D bands as a function of the growth conditions. In first approach, the evolution of the G/D ratio is rather simple: G/D increases with increasing temperature and decreasing precursor pressure. It is worth mentioning that a decrease of G/D is sometimes observed at high temperature, high precursor supply and long synthesis times as discussed in §3.6.2 and accounted for by the deposition of pyrolytic carbon.

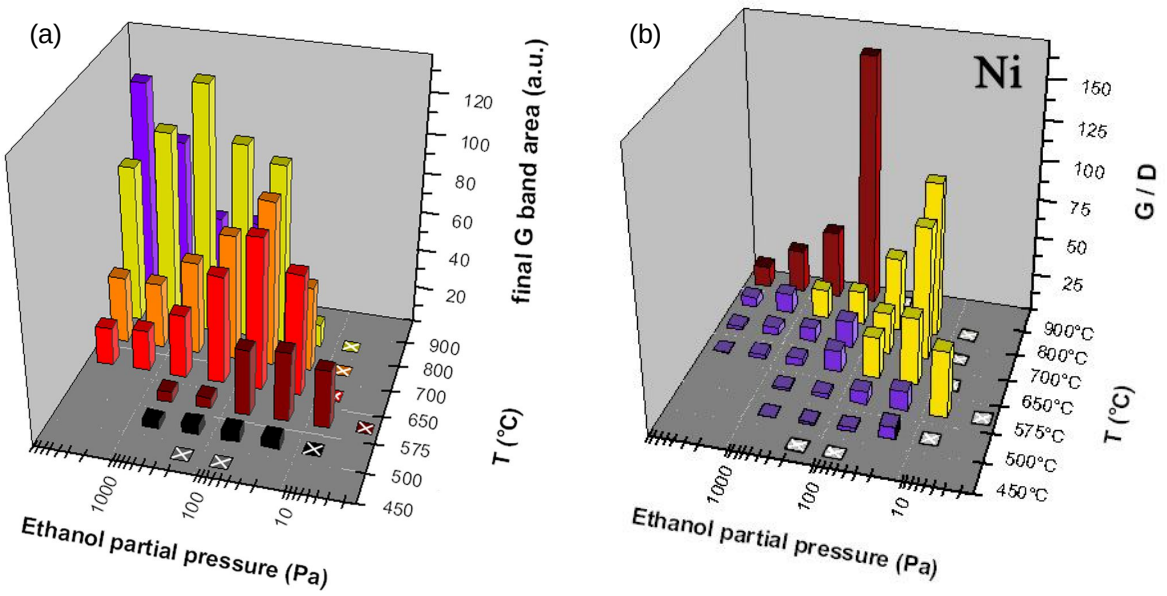

Figure 3-11. Evolution of (a) the G band intensity and of (b) the G/D ratio with the growth temperature and precursor pressure for the Ni-ethanol system. The excitation wavelength is 532 nm.

Beside these general trends, a more thorough study as a function of the temperature and precursor pressure brings additional information. Figure 3-12 displays the dependence of the TM features on the precursor pressure P in the case of the Ni-EtOH system for two different temperatures. One can observe that ln(D/G) scales very well with $\ln(P/P_0)$ with a slope (that can be assimilated to a reaction order for the creation of defects) of 0.54 at 575°C and 0.34 at 800°C (see blue dash lines in Figure 3-12). Increasing the precursor pressure also leads to an upshift and broadening of the D band.

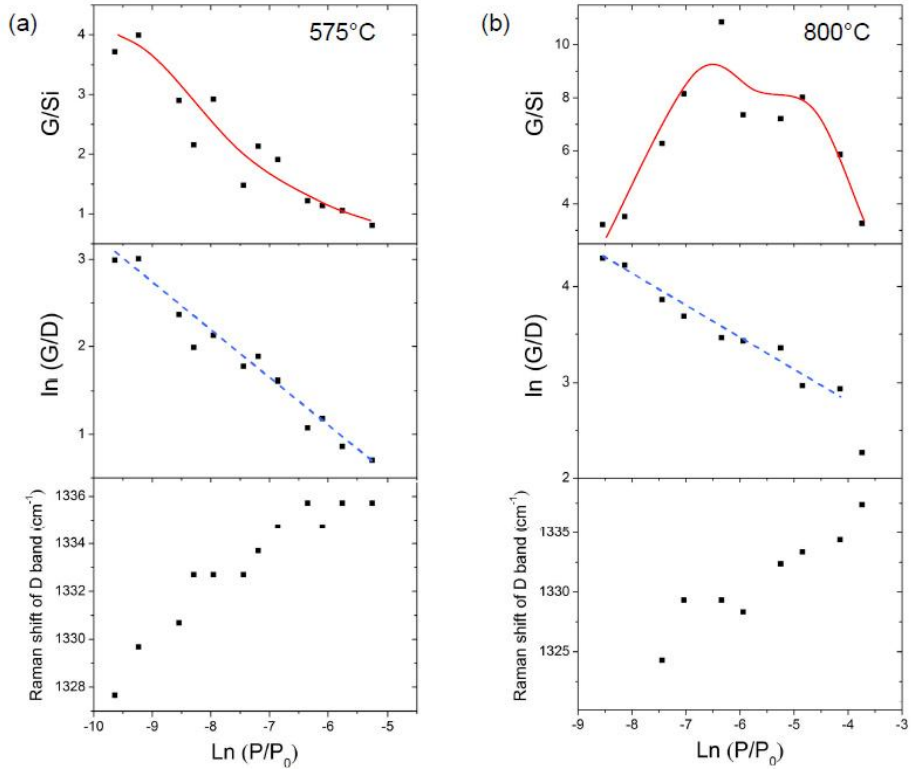

Figure 3-12. Features of the tangential modes of CNT samples as a function of the precursor pressure for the nickel-ethanol couple at (a) 575°C and (b) 800°C: G-band intensity normalized to the Si signal, G/D ratio, position of the D band. The excitation wavelength is 532 nm. The P_0 value is taken as 1 bar.

Figure 3-13 summarizes the dependence of the Raman features on the growth temperature T for the five catalyst-precursor systems studied. The trends systematically observed for all the systems are described below.

- With increasing temperature, the *nanotube yield* characterized by G/Si displays three different regimes limited by two threshold temperatures T_L (green dash line in Figure 3-13) and T_H (burgundy dash line in Figure 3-13) at, respectively, low and high temperatures. Below T_L: G/Si displays an exponential increase stage. Between T_L and T_H, G/Si appears much less dependent on the temperature and marks a plateau stage. Above T_H, G/Si decreases abruptly.

- With increasing temperature, the overall *crystalline quality* of the samples characterized by G/D displays two different regimes. At low temperature, G/D increases markedly following an Arrhenius law (*i.e.* $\ln G/D \propto T^{-1}$) characterized by an activation energy in the range of 1-2.3 eV. This regime is also marked by a significant downshift of the D-band with increasing temperature. At high temperature, G/D increases more slowly following an Arrhenius law characterized by an activation energy of 0.3-0.6 eV. In this regime, the D-band frequency stabilizes at a characteristic value (*i.e.* 1328-1330 cm^{-1} for λ=532 nm). Remarkably, the threshold temperature between the two regimes is systematically correlated with T_L, the low transition temperature observed for G/Si (see green dash lines in Figure 3-13). However, the D-band does not display any systematic modification of intensity or frequency at T_H.

- With increasing temperature, the *nanotube diameter distribution* characterized by the intensity ratio of small- over large-diameter RBMs (I_S/I_L) displays either two or three regimes depending on the studied system. At low temperature, the proportion of small-diameter tubes increases with T in the case of the Ni-ethanol, Ni-ethylene and Ni-methane systems. In the case of the Ni-acetylene and Co-ethanol systems, this regime is not apparent, which could be attributed to insufficient data at low temperature or simply to the absence of this regime in these two cases. At intermediate temperatures, the diameter distribution remains relatively unchanged while, above a threshold temperature, the proportion of small-diameter tubes decreases markedly with T. Remarkably, this high threshold temperature is systematically correlated with T_H, the high transition temperature observed for G/Si (see burgundy dash lines in Figure 3-13). However, I_S/I_L does not display a systematic modification at T_L.

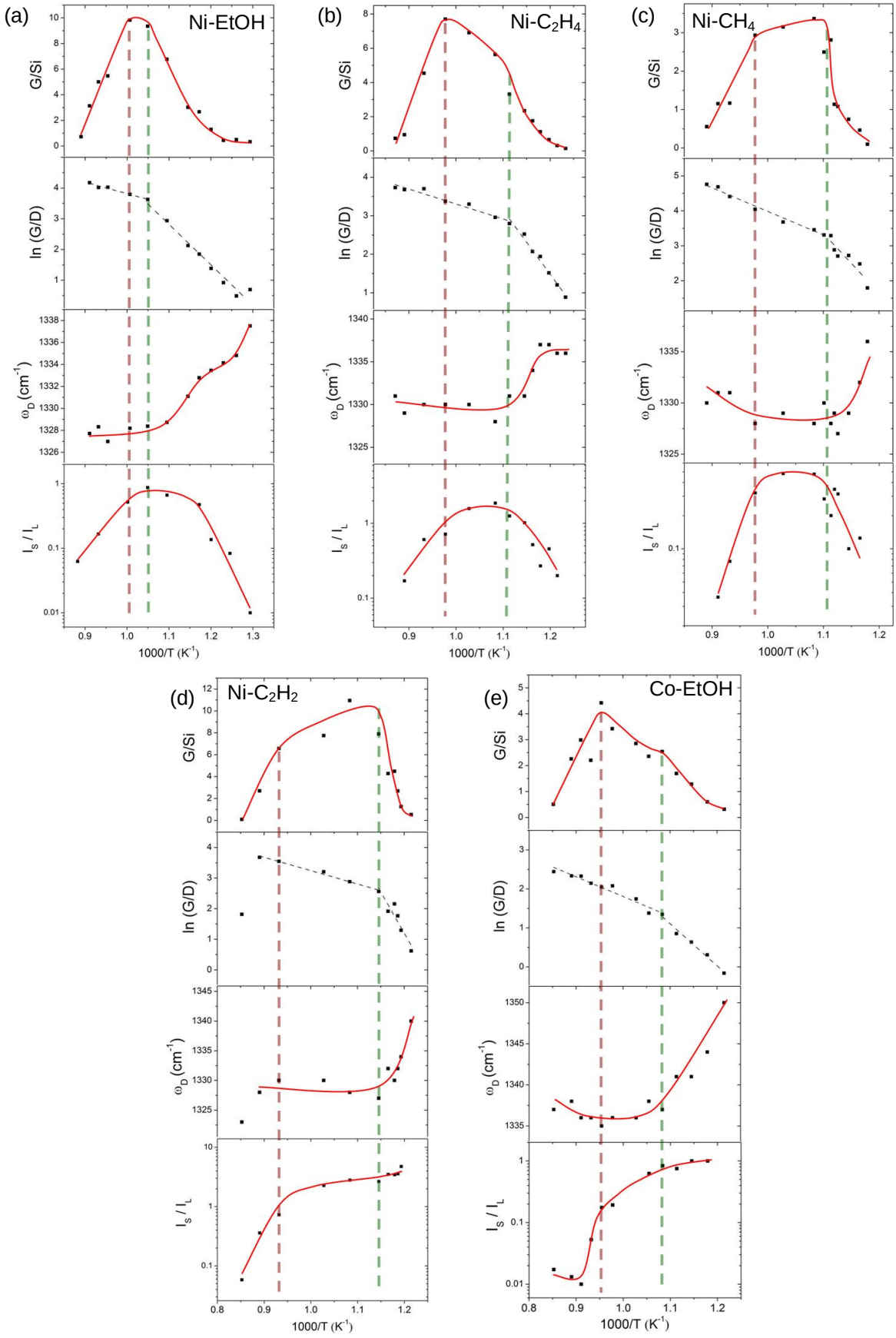

Figure 3-13. Features of the Raman spectra as a function of the inverse growth temperature: G-band intensity, G/D ratio, D-band position, ratio of small- (ω>250 cm^{-1}) over large-diameter (ω<250 cm^{-1}) RBMs. The excitation wavelength is 532 nm, except for Co-EtOH for which λ=514 nm.

3.3.3 Arising questions

Following this description of the post-growth data, several questions emerge.

- What is the origin of the threshold precursor pressure below which no nanotube growth occurs?
- What is the origin of the exponential increase of the yield observed at low temperature?
- What is the origin of the yield plateau observed at intermediate temperatures?
- What is the origin of the abrupt decrease of the yield at high temperatures?
- Why does G/D display two different Arrhenius regimes as a function of temperature? Why does the D band downshift and narrow with increasing temperature? Why is the change of regime in G/D correlated with the transition of the yield from exponential increase to plateau?
- Why do small-diameter SWCNTs fade away when going to high temperatures? Why is it correlated with the transition of the yield from plateau to abrupt decrease?
- Why do small-diameter SWCNTs disappear when going to low temperatures for several catalyst-precursor systems?

Answering these questions is of general interest for improving our understanding of the growth mechanism and synthesizing CNT samples of higher purity and structural control in higher yields. The next sections describe our investigations of these questions. Section 3.4 is devoted to the activation of SWCNT growth, section 3.5 to the diameter distribution of SWCNTs, section 3.6 to the carbonaceous by-products and to the defect density of SWCNTs and section 3.7 to the kinetics of growth and deactivation controlling the SWCNT yield.

3.4. Activity of catalyst particles for SWCNT growth

3.4.1 Introduction

We already saw in §2.3.6 that the percentage of active particles is usually low in the CCVD growth of SWCNTs although the reason for that is still ill-understood. The HRTEM picture in Figure 3-14 illustrates this low yield in the case of Ni particles supported on SiO_2. As common in the field of heterogeneous catalysis, determining the origin of inactivity of supported particles of a few nanometres is a difficult task. As detailed in sections 2.2.4, 2.2.5 and 2.3.6, the catalytic activity of metal nanoparticles are strongly dependent on their size and on their interactions with the environment. In the case of SWCNT growth, it is frequently proposed that the low nucleation yield originates from the large distribution of catalyst sizes although the reason why size matters is unclear. Size effects are suggested to impact on the formation of carbon germs at the particle surface, on the process of cap lift-off or on the encapsulation of the particle by a carbon shell (§2.4.3). Hereafter, I will describe the conditions favouring the activation of catalyst particles for SWCNT growth for the catalyst systems we studied and the result of the experiments devoted to understanding the origin of catalyst inactivity.

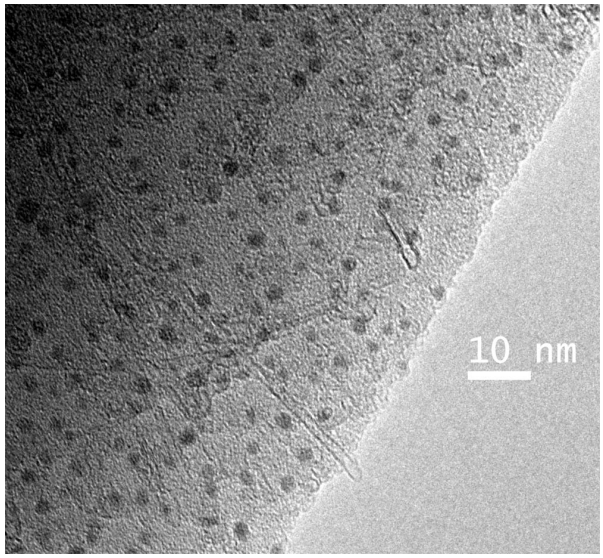

Figure 3-14. HRTEM picture of Ni nanoparticles on a thin film of amorphous oxide of silicon (SiO_2) after CCVD at 575°C with ethanol. SWCNTs are also visible but most particles did not yield nanotubes.

3.4.2 Catalyst pre-treatment

The catalyst pre-treatment has a significant influence on the selectivity and efficiency of supported catalysts. The effect of the temperature and atmosphere of pre-treatment on the studied catalysts systems (essentially Ni or Co supported on /SiO_2) was assessed by Atomic Force Microscopy (AFM). As shown in Figure 3-15, the Ni/SiO_2 catalyst displayed very little increase in surface roughness during calcination under oxygen even at temperature as high as 900°C. At the opposite, the surface of the Co/SiO_2 catalyst was significantly modified by annealing. Figure 3-16 shows the evolution of the surface of the Co/SiO_2 catalyst after a pre-treatment under H_2 or O_2 at different temperatures. The surface roughness is observed to increase with increasing annealing temperature under both H_2 and O_2 atmospheres. Catalyst coarsening is significantly higher under oxygen with many particles as high as 8-10 nm.

Oxygen is frequently reported to increase the coarsening of particles by Ostwald ripening which is usually attributed to the formation of oxide intermediates of higher mobility (see §2.2.5 and [160]). Co/SiO_2 being an important Fischer-Tropsch catalyst, its modifications during calcination are well documented. In agreement with our observations, calcination commonly leads to the aggregation of cobalt oxide into large Co_3O_4 particles [403]. Chernavskii *et al.* observed a faster coarsening rate under oxygen leading to a bimodal distribution of nanoparticles [404]. Calcination is also accompanied by the partial transformation of Co_3O_4 into CoO at temperatures above 350°C [405]. The latter can interact with SiO_2 to produce cobalt silicate of formula $CoSiO_3$.

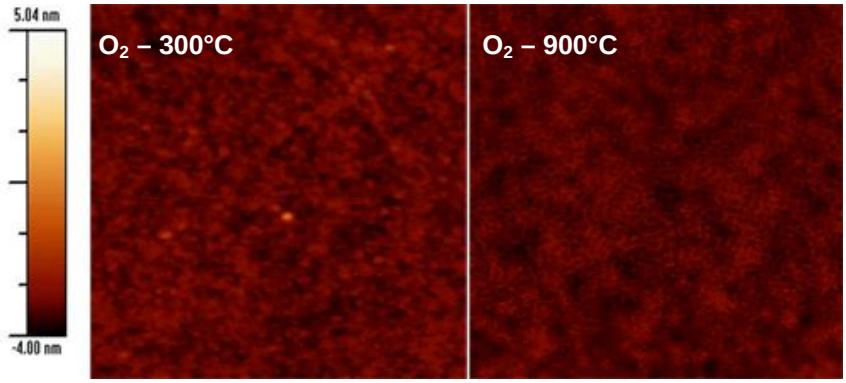

Figure 3-15. AFM images of Ni 5Å/SiO_2 after annealing under O_2 at 300°C and 900°C.

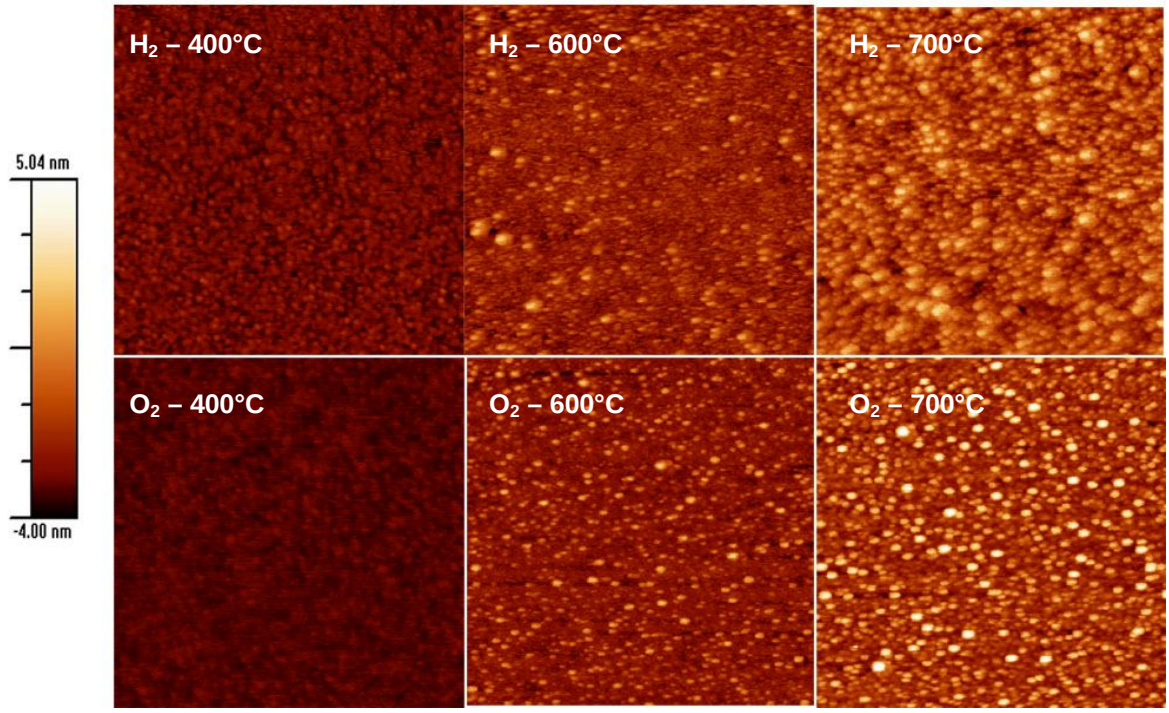

Figure 3-16. AFM images of Co 5Å/SiO_2 for different atmospheres and temperatures of pre-treatment.

Synthesis tests were performed after the different types of pre-treatment and a calcination pre-treatment under O_2 (or air) at 700°C showed the highest yields of SWCNTs as assessed by Raman spectroscopy. As discusses in §2.2.5, calcination under air is a common catalyst pre-treatment used to remove carbon impurities or to form oxide particles less prone to further coarsening. In the following, catalysts were systematically submitted to this calcination pre-treatment before CCVD.

3.4.3 Catalyst oxidation state

To get an idea of the conditions of oxidation and reduction of nickel and cobalt layers in our reactor cell, we prepared metal layers sufficiently thick to be monitored by Raman spectroscopy during their oxide conversion. As an example, Figure 3-17a shows the appearance of the characteristic Raman features of Co_3O_4 when a 50 nm-thick layer of cobalt is annealed under pure oxygen. A successive experiment under hydrogen shows that the as-formed Co_3O_4 can be reduced by heating under pure H_2 at temperatures above 300°C. Importantly for carbon nanotube growth, carbon precursors can also reduce oxides of nickel and cobalt. For instance, Figure 3-17b shows that a 50 nm-thick layer of Co_3O_4 is readily reduced by ethanol from 400°C. It is also apparent that the growth of a defective carbon layer occurs as soon as the catalyst is reduced. When performing the same experiments using pre-reduced catalysts, the onset of carbon deposition was observed to occur at a temperature equal or slightly lower than the temperature previously measured for the catalyst reduction by the carbon precursor. In most of our growth experiments without reducing pre-treatment, catalyst reduction by the carbon precursor is therefore expected to be a pre-requisite for nanotube growth. The threshold temperature of catalyst reduction by the carbon precursor fixes the lowest temperature for nanotube growth. When using thinner catalyst layers (typically 0.5 nm) for SWCNT growth, we observed that the minimum temperature for carbon deposition was noticeably higher than the reduction temperature measured for thick layers. For instance, the lowest temperature for carbon deposition was found to be 500°C with 0.5 nm Ni/SiO_2 (see Figure 3-11a) while the temperature of reduction (and of carbon deposition) of a 50 nm Ni layer on SiO_2 was 450°C.

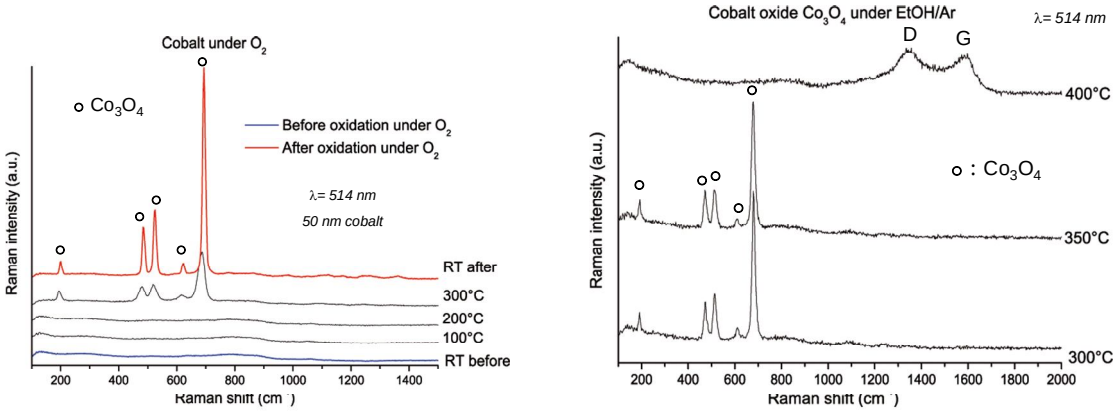

Figure 3-17. (a) Oxidation of a 50 nm layer of Co into Co_3O_4 under oxygen monitored by Raman measurements. (b) Successive reduction of Co_3O_4 by ethanol and simultaneous formation of a defective carbon layer monitored by Raman.

In favourable cases (*e.g.* cobalt catalyst monitored at 532 nm), catalyst reduction by carbon precursor molecules can also be observed in SWCNT growth conditions. Figure 3-18 shows Raman spectra acquired at different times after the introduction of the carbon precursor for a 0.5 nm thick cobalt layer. The signal of Co_3O_4 is much less intense in this case due to the lower catalyst thickness used for nanotube growth but one can still observe the main peak of Co_3O_4 at around 670 cm^{-1} superposed on the background signal of the silicon support. Importantly, the Co_3O_4 peak readily disappears in the first seconds or tens of seconds following the introduction of the carbon precursor. It is also apparent that nanotube growth starts after the disappearance of the oxide peak.

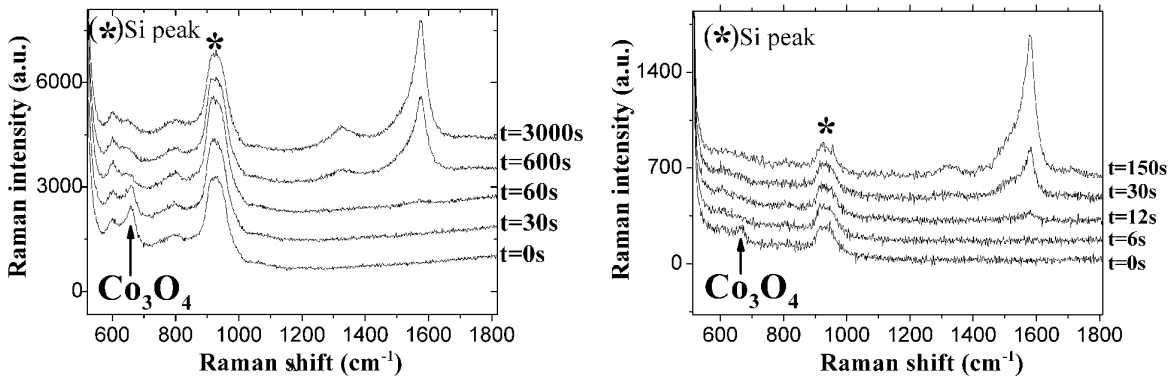

Figure 3-18. Reduction of Co_3O_4 observed during the first instants following the introduction of methane (a) and ethanol (b) and preceding the onset of nanotube growth.

Despite this informative result, Raman spectroscopy is not a surface technique and is therefore not the most adapted to assess the oxidation state of catalyst layers of nominal thicknesses of 3-20Å. X-Ray Photoelectron Spectroscopy (XPS) measurements were additionally performed on CNT samples to confirm the reduction of the catalyst after exposure to the carbon precursor. To minimize air exposure, the samples were directly transferred from the CVD reactor to the XPS chamber. Figure 3-19a and b show the XPS spectra in the Co $2p_{3/2}$ energy range for two CNT samples grown with acetylene at low (675°C) and high (850°C) synthesis temperatures, respectively. One can observe that the Co spectrum is largely dominated by the contribution of Co(0) at 778.2 eV. However, a contribution from Co(II) can also be observed as a shoulder peak at 782.5 eV. Its intensity is highest in the low temperature sample. These results show that most cobalt particles are

reduced to Co(0) after exposure to the carbon precursor but that a small fraction remains oxidized, especially at low growth temperatures.

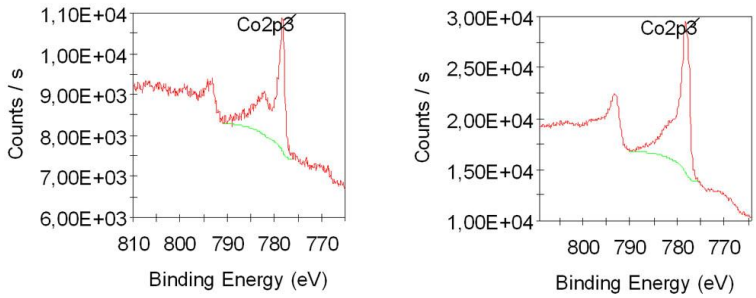

Figure 3-19. XPS spectra in the Co $2p_{3/2}$ energy range performed for two CNTs samples grown with acetylene at (a) 675°C) and (b) 850°C.

3.4.4 Threshold precursor pressure

As previously highlighted, Raman characterization evidenced no SWCNT growth or even carbon deposition under a threshold pressure of carbon precursor. This threshold pressure can be seen on Figure 3-11a in the case of the Ni-EtOH system. The threshold pressure is seen to increase with increasing growth temperature. To understand its origin, we heated the catalyst to a standard growth temperature and increased the partial precursor pressure step by step while monitoring the onset of nanotube growth by *in situ* Raman measurements. Figure 3-20 shows the evolution of the G-band intensity during such an experiment. One can observe that when a critical pressure is reached, nanotube growth starts at once. The fact that the G band displays such a sharp transition at the threshold pressure suggests that the onset of nucleation corresponds to a thermodynamic transition and not simply to an increase of the carbon deposition rate with increasing carbon supply.

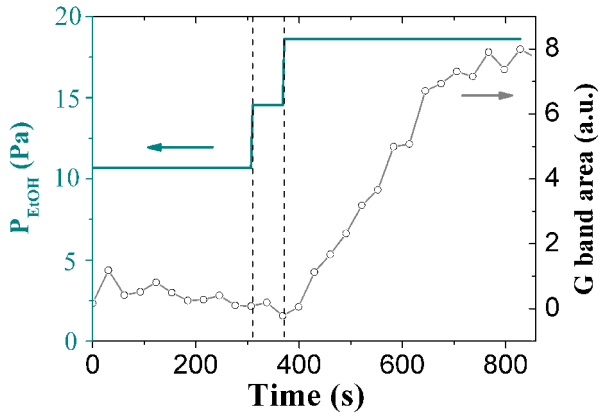

Figure 3-20. *In situ* measurements of the G band intensity with increasing the ethanol pressure step by step until the onset of nanotube growth. The threshold pressure of ethanol is 17 Pa. The catalyst consists of 0.5 nm of nickel on SiO_2/Si.

Different explanations can be proposed to account for the existence of this threshold activation pressure. From the review presented in chapter 2, one can extract several requirements for a metal particle to nucleate a carbon nanotube. It must:

1) allow/favour the dissociation of the carbon precursor (which requires a reduced metal particle in the case of Co and Ni as shown in 3.4.3),

2) allow/favour the formation of a sp^2 carbon material at its surface,

3) allow/favour the lift-off of a carbon cap,

4) prevent its encapsulation by unreactive carbon.

In the present case, the fourth hypothesis can be ruled out since increasing the carbon supply is not a expected to help removing a pre-existing carbon shell. The third hypothesis is supported by the simulations of Diarra et al. [346] showing that increasing the carbon content of a metal particle reduces its surface energy therefore favouring the lift-off of the carbon cap. The second hypothesis is supported by the thermodynamic models predicting that the particle must reach a threshold carbon concentration in order to form a stable germ of critical size. Finally, the first hypothesis is supported by the requirement of reducing the nickel and cobalt particles by the carbon precursor in our experimental conditions as shown in §3.4.3. As apparent in the Ellingham diagram in Figure 2-5, there is a threshold reducer pressure for the reduction of an oxide at a given temperature.

We performed additional experiments to discriminate between the different hypotheses. To investigate the influence of the particle size, we studied how the threshold activation pressure varies with the catalyst thickness. Figure 3-21 shows this dependence using acetylene and cobalt thicknesses of 0.3 nm, 0.5 nm and 2.0 nm. It is observed that the threshold pressure increases from about 15 Pa to 45 Pa with decreasing the catalyst thickness from 2 nm to 0.3 nm. The simulations of Diarra *et al.* [75] predict that smaller metal nanoparticles would display a higher carbon solubility but also a surface segregation of carbon at a lower chemical potential of carbon. Based on these calculations, the second hypothesis would be in disagreement with the observed size dependence. At the opposite, the lower reducibility of metal oxide nanoparticles on oxide supports with decreasing particle size is commonly reported in heterogeneous catalysis [406-411]. Nanoparticle-support interactions are usually invoked to explain this effect. This feature appears in good agreement with the observed size dependence of the threshold pressure of SWCNT growth.

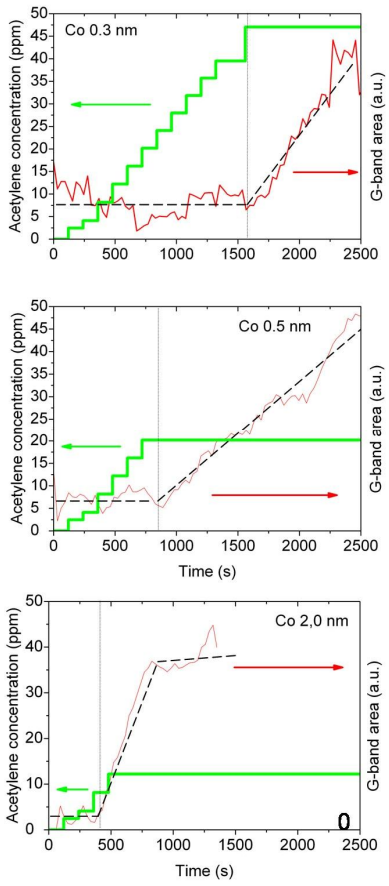

Figure 3-21. Threshold activation pressure of acetylene measured for different thicknesses of cobalt catalyst: (a) 0.3 nm, (b) 0.5 nm, (c) 2.0 nm.

To study the influence of the oxidation state of the catalyst particles, we performed similar experiments with and without a reducing pre-treatment under hydrogen. As shown in Figure 3-22, the activation pressure for the lowest catalyst thickness (0.3 nm) is significantly decreased after a reducing pre-treatment. This strongly supports that the threshold activation pressure corresponds to the reduction pressure of catalyst particles and that the observed size dependence originates from a lower reducibility of smaller catalyst particles.

It is worth noting that in the case of pre-reduced catalysts, another lower threshold activation pressure is observed, which appears independent of the particle size (Figure 3-22). Following the same reasoning, this second threshold pressure should be associated with one of the two remaining hypotheses (germ nucleation or cap lift-off). Other studies would be needed to determine its parameter dependence and assign it.

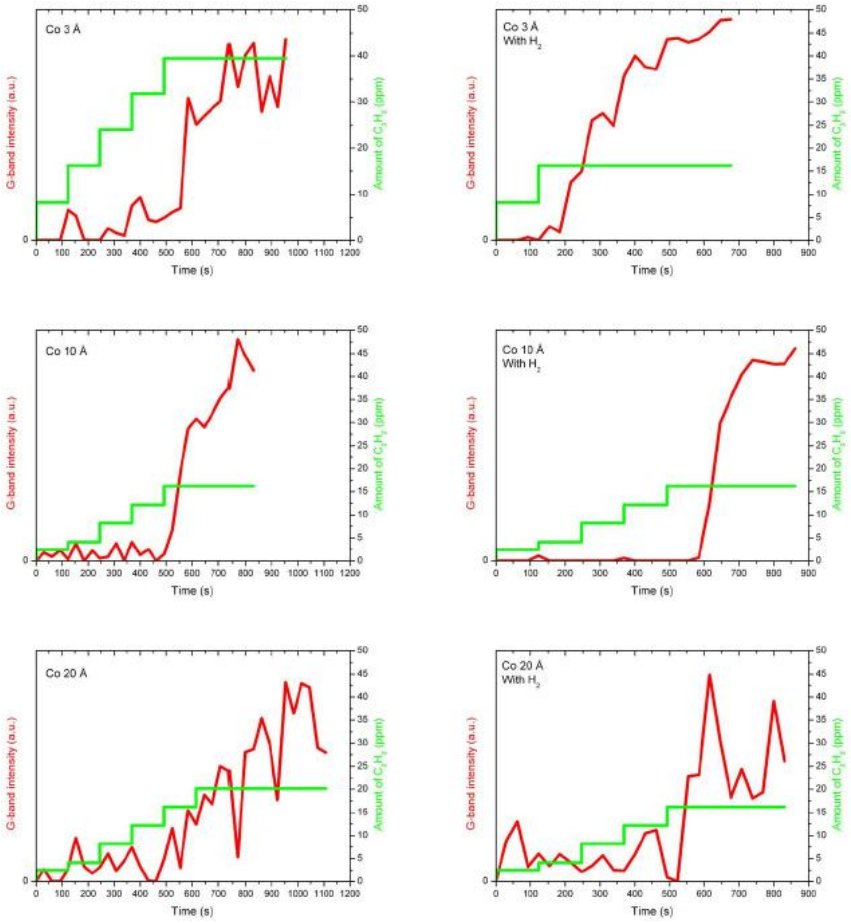

Figure 3-22. Evolution of the threshold activation pressure without (left column) and with a reducing pre-treatment under hydrogen (right column) for different thicknesses of cobalt catalyst.

3.4.5 Conclusion

This study confirmed that standard carbon precursors can reduce the oxides of catalysts such as nickel and cobalt in the conditions of SWCNT growth. Due to the lower electronegativity of Fe, FeO was found more difficult to reduce to Fe(0) using standard carbon precursors. Raman measurements show that the oxide reduction is activated above a threshold temperature which varies with the type of metal oxide and of reducing species. Catalyst reduction by a carbon precursor is always accompanied by the deposition of carbon material. XPS measurements show that most catalyst particles are reduced to the metallic state after exposure to the carbon precursor but also evidence that a certain fraction of the catalyst particles remain oxidized especially in the samples grown at low temperatures.

In SWCNT growth conditions where the catalyst has been oxidized by calcination, *in situ* Raman monitoring show that SWCNT growth is always preceded by the reduction of the catalyst oxide. These results confirm that particles of higher transition metals such as Ni and Co must be in the metallic state to give rise to nanotube growth.

Below a threshold precursor pressure, no carbon deposition or nanotube growth is observed. This activation pressure increases with increasing temperature and decreasing particle size. Based on its dependence on reducing treatments and on particle size, this threshold precursor pressure for SWCNT growth is assigned to the threshold pressure of reduction of the catalyst particles.

3.5. Processes controlling the diameter distribution of SWCNT samples

3.5.1 Introduction

Controlling the diameter and, more generally, the chirality of SWCNT samples is critical for numerous applications requiring well-controlled electrical and optical properties. Samples of CCVD-grown SWCNTs generally display a large distribution of tube diameters except for a few optimized catalysts (§2.3.3). As previously described (§3.3), the diameter distribution is significantly dependent of the growth conditions (see Figure 3-9 and Figure 3-10). For several systems (*i.e.* Ni-EtOH, Ni-C_2H_4, Ni-CH_4), the proportion of small-diameter SWCNTs increases with increasing temperature until a threshold temperature. This regime is not or less apparent in the case of Ni-C_2H_2, Co-EtOH and even Co-C_2H_2 (latest data). For all systems, the proportion of small-diameter SWCNTs is observed to stagnate for a certain temperature range and to decrease above a critical temperature to the benefit of larger-diameter tubes. The diameter distribution is also very dependent on the partial pressure of precursor, as shown in Figure 3-9b-c in the case of the Ni-EtOH system. For each temperature, there is an optimal precursor pressure for obtaining small-diameter SWCNTs. Consequently, one can define an optimal domain for the growth of small-diameter SWCNTS in the temperature (T) - precursor pressure (P) space (Figure 3-23). This "small-diameter island" follows a diagonal line in the T-P space. This diagonal separates two domains displaying high proportions of large-diameter SWCNTs: one at high-temperature/low pressure and another at low temperature/high pressure. Hereafter are described our studies devoted to understanding the parameter dependence of the SWCNT diameter distribution.

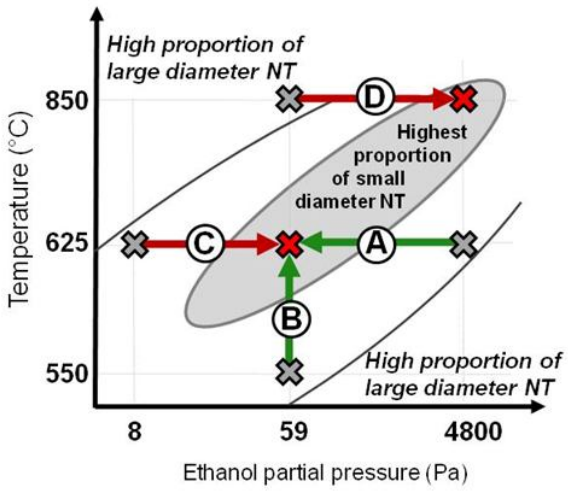

Figure 3-23. Schema of the evolution of the SWCNT diameter distribution as a function of temperature and ethanol pressure. Each arrow corresponds to a two-step growth experiment (see text hereafter).

3.5.2 Two-steps experiments

To understand the absence of small-diameter SWCNTs in each side domain, we performed synthesis experiments consisting of two steps. A first growth is performed in one of the side domains where the proportion of small-diameter SWCNTs is low (gray crosses in Figure 3-23). The growth is monitored by Raman measurements. Once no more evolution of the Raman spectrum is observed, the synthesis is stopped and a first Raman spectrum (labelled as #1) is recorded at room temperature. A second growth is carried out on the same sample, in conditions that are now optimal for small diameter SWCNTs (red crosses in Figure 3-23). Once again, a Raman spectrum (labelled as #2a) is recorded at room temperature and at the same position on the sample. The two RBM profiles are compared to the growth directly performed in the conditions optimal for small diameters (labelled as "reference synthesis"). If the spectrum #2a is similar to #1 or too different from the spectrum of the reference synthesis, we perform a soft oxidation step under oxygen at 500°C for 5 min to remove carbon species and perform the same synthesis again (labelled as #2b). During the whole experiment, the sample remains in the controlled environment of the cell.

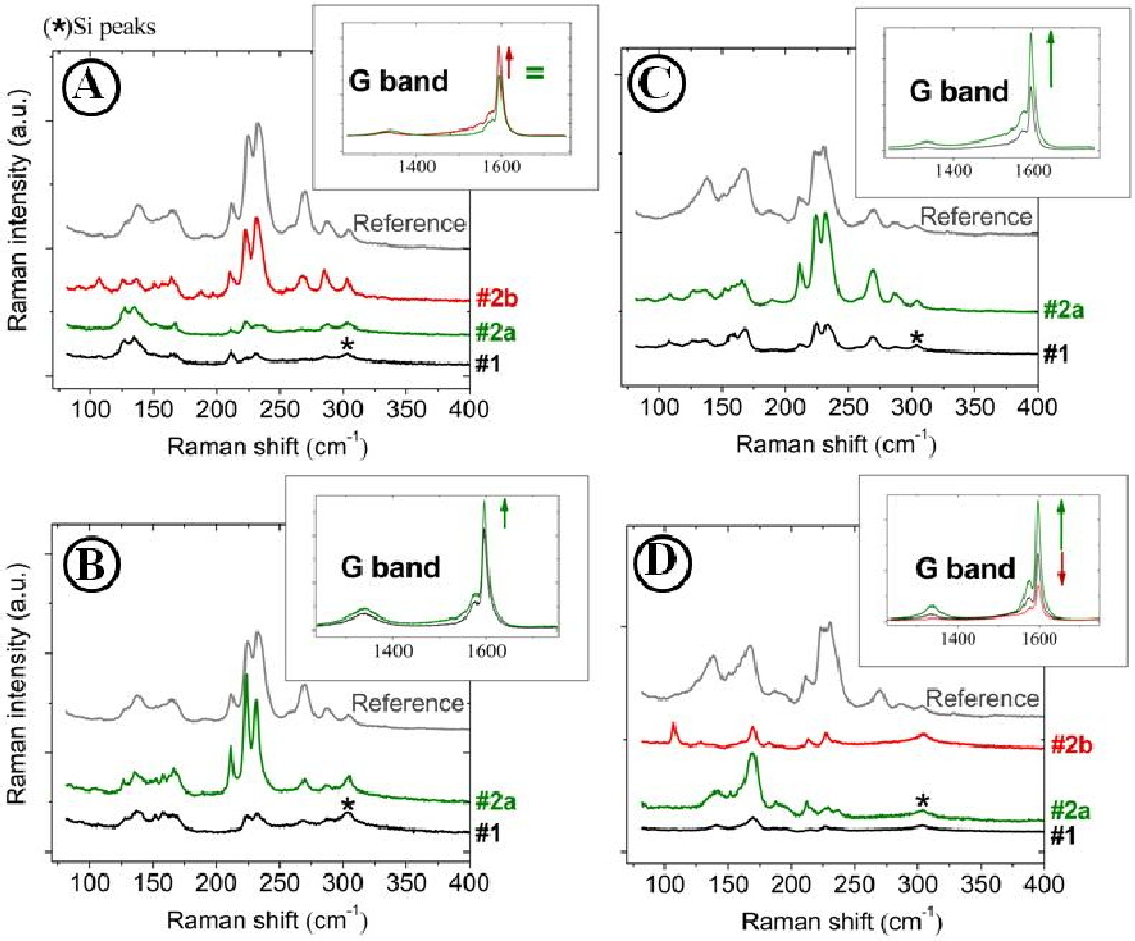

Figure 3-24. Raman spectra obtained for two-steps experiments. The conditions of each experiment are summarized in Figure 3-23. Spectrum #1 corresponds to the first growth. Spectra #2a and #2b correspond to the second growth without and after an oxidizing step, respectively. The gray curve labelled as "Reference" corresponds to a synthesis directly performed in the experimental conditions of #2. The investigated system is Ni-ethanol. All spectra were recorded post-growth at room temperature at 532 nm.

Experiments A and B were devoted to understand the absence of small diameter SWCNTs in the low temperature-high pressure domain. Figure 3-24a shows the results of experiment A. After a first growth at 4800 Pa of ethanol, the Raman spectrum #1 shows very

few small-diameter SWCNTs as expected in this domain. If the ethanol pressure is then reduced to 59 Pa so that the conditions lie in the optimum domain for small diameter tubes, the Raman spectrum #2a shows (unsurprisingly) no change. However, if the synthesis is reproduced after an oxidation step, the Raman spectrum #2b now displays an RBM profile dominated by small-diameter tubes and quite similar to that of the reference synthesis. This experiment supports that the growth of small-diameter SWCNTs is blocked in the low T-high P domain by the encapsulation of the smallest particles by carbon material. Kinetic studies described in §3.7 also support that catalyst deactivation is induced by carbon in this range of growth conditions. HRTEM pictures of samples grown in this range of conditions actually display many catalyst particles covered by defective layers of crumpled carbon (Figure 3-25).

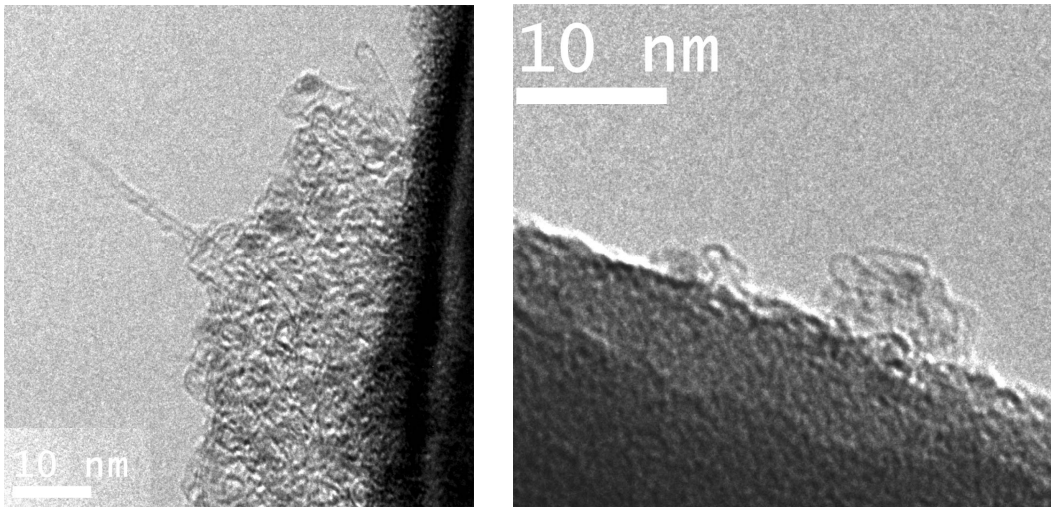

Figure 3-25. HRTEM pictures of Ni catalyst particles after CCVD with EtOH at low temperature (575°C).

Experiment B also starts in the low T-high P domain but corresponds to an increase of temperature from 550°C to 625°C between the first and the second synthesis. As shown in Figure 3-24b, this increase of temperature induces the growth of small diameter tubes and results in an RBM profile (spectrum #2a) quite similar to the reference synthesis. Two interpretations can be made. If associated with the results of experiment A, these results support that the carbon material poisoning the smallest particles in the low T-high P domain have been removed or rearranged by annealing. Such an interpretation is in tune with the observation of Marchand *et al.* [297] by *in situ* field emission imaging that increasing the temperature by a few tens of degrees can reactivate the growth of an individual nanotube. This interpretation is also backed by simulations at low temperature and high carbon supply showing that growth deactivation is caused by the encapsulation of the particle by a defective carbon layer. Such a catalytically-grown layer is not to be confused with amorphous pyrolytic carbon which has been shown by Schünemann *et al* [296] to display high reactivity and to cause no catalyst deactivation at standard growth temperatures. Retrospectively, with the knowledge of §3.4, an alternative interpretation is that the reduction of the smallest catalyst particles was kinetically blocked during the first growth at low temperature. This interpretation gets also support from the *in situ* RBM measurements described in the following section. In addition, it would explain the discrepancy between acetylene and other precursors by the much higher reducing ability of acetylene compared to other precursors. However, it cannot account for the inactivity of the smallest particles in experiment A. Taken together, carbon encapsulation of the smallest particles remain the most convincing interpretation for experiments A and B although lower reducibility of small catalyst particles could play an additional role for their lack of activity at low temperature.

Experiments C and D addressed the absence of small-diameter tubes in the high T-low P domain. Experiment C corresponds to an increase of precursor pressure from 8 Pa to 59 Pa between the first and the second growths. One can observe in Figure 3-24c that this increase of precursor pressure induces the growth of small diameter tubes and results in an RBM profile quite similar to the reference synthesis. This result is reminiscent of those reported in §3.4.4 showing that smaller particles display a higher activation pressure. We initially thought that this effect may be related to the enhanced solubility of impurities in nanoparticles reported by many authors (see §2.2.2). Based on the results reported in §3.4.4 and in heterogeneous catalysis literature, a lower reducibility of smaller metal nanoparticles supported on SiO_2 now appears as the best explanation for the lack of growth of small-diameter SWCNTs at low precursor pressure. Reproducing experiment C on a pre-reduced catalyst would be a good way to confirm this explanation.

Experiment D also corresponds to an increase of precursor pressure from the high T-low P domain to the small-diameter island but at a much higher temperature (850°C). As shown in Figure 3-24d, the increase of precursor pressure induces the growth of new tubes but of larger diameters than expected from the reference synthesis. This result is quite different from the one obtained in experiment C at a much lower temperature (625°C). If the synthesis is performed again after an oxidation step, even less tubes are obtained and some very large-diameter tubes start appearing. These results support that the catalyst is rapidly rearranging at these high temperatures in agreement with the modifications of kinetic behaviour described in §3.7. They support that in this domain, the nanotube distribution mainly results from the kinetic competition between SWCNT growth and catalyst restructuring. The nature of this restructuring is not clear although previous studies tend to support the formation of a mixed compound with the oxide support (see TEM picture in Figure 3-52).

Figure 3-26 summarizes the results of this study. At low temperature-high precursor pressure, the results support that the absence of small-diameter tubes is primarily caused by the encapsulation of the smallest catalyst particles by defective carbon structures. In this domain, catalyst particles can be reactivated by oxidation or by thermal annealing. Lower reducibility of smaller oxide nanoparticles may also play an additional role in the lack of small-diameter SWCNTs at the lowest temperatures and for the weakest reducers. At low pressure, the lack of small diameter tubes originates from the higher threshold pressure of activation of smaller particles. As detailed in §3.4.4, this effect is accounted for by the lower reducibility of smaller oxide particles on SiO_2. At high temperature, catalyst coarsening appears as the main cause of the shift of the nanotube population toward large diameters.

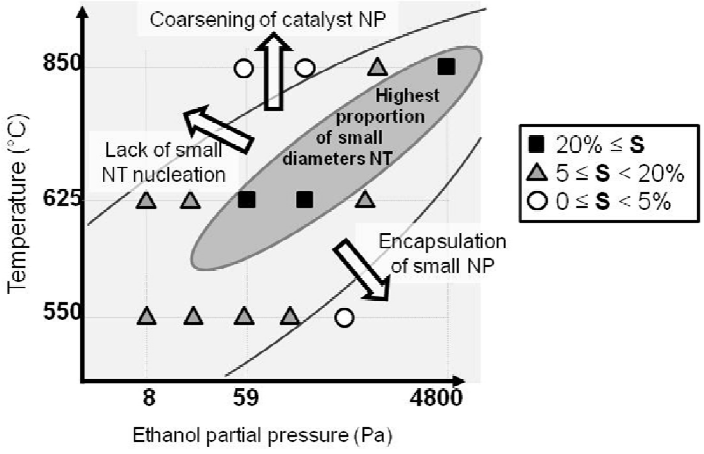

Figure 3-26. Fraction of small diameter tubes (S) as a function of temperature and ethanol partial pressure for the Ni-ethanol couple. The processes influencing the nanotube diameter distribution in each domain are presented.

3.5.3 Evolution of the diameter distribution during growth

To study the processes influencing the diameter distribution, another approach consists in monitoring the diameter distribution as a function of time. That can be achieved by two ways. First, one can perform syntheses interrupted at different times by stopping the precursor supply and rapidly cooling the sample. The results of this "freezing" approach are illustrated in Figure 3-27. One can observe that the RBM profile displays significant evolutions with synthesis time. In this example, one can notably observe that the RBM profile is initially very narrow (a single peak at 170 cm^{-1}) and that small-diameter SWCNTs appear at later times. At long synthesis times, the large-diameter side of each RBM bunch increases progressively. However, we found this low-throughput approach quite impractical for a systematic study as a function of the growth parameters.

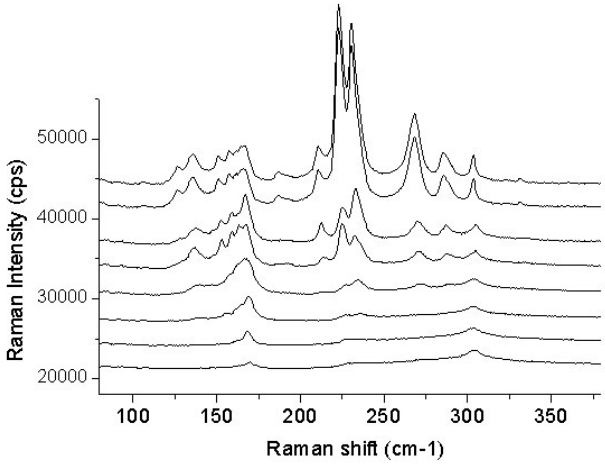

Figure 3-27. Evolution of the RBM profile as a function of the synthesis time by the freezing method. The system is Ni/SiO_2 – EtOH and the growth temperature is 575°C. Synthesis times progressively increase from bottom to top from 3 s to 320 s. The spectra are recorded at room temperature at 532 nm.

Second, the RBM profile can be monitored in real time by *in situ* Raman measurements. This high-throughput approach is in practice limited to the catalyst systems and the growth conditions generating the highest yields since RBMs are commonly an order of magnitude less intense than the G band and since their intensities decrease by an order of magnitude at typical growth temperatures. Figure 3-28 illustrates two evolutions of RBM profiles as a function of time in the case of the couple cobalt-ethanol. On the left side, one can observe a behaviour quite comparable to the one previously described. On the right side, one can observe a situation where the intensity ratio of the small-diameter to large-diameter RBMs remains quite constant over time.

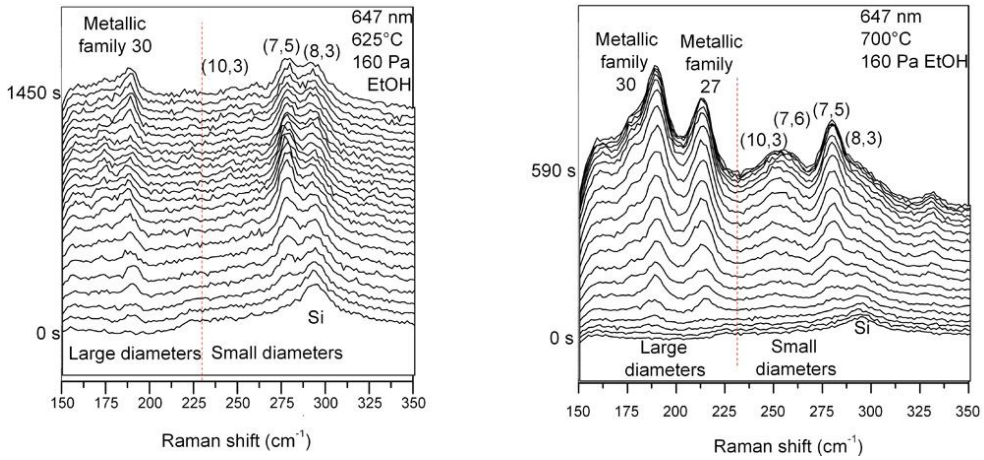

Figure 3-28. Two types of RBM evolution monitored *in situ* at λ=647 nm. The catalyst is Co/SiO_2.

Generally speaking, we observed three types of behaviours as a function of the growth conditions (Figure 3-29). Type 1 (red curve) corresponds to a decrease of the proportion of the small-diameter RBMs during the growth. Type 2 (green curve) corresponds to an increase followed by a decrease of the small-diameter fraction. Type 3 (blue curve) corresponds to no or little evolution of the diameter distribution during the growth. The distribution of these behaviours as a function of the growth conditions is shown in Figure 3-29b. Type 1 is the dominant behaviour at high temperature and high pressure while type 2 is observed at low temperature and low pressure. Type 3 can be decomposed into two subtypes: type 3A corresponding to an absence of profile evolution at high T-low P, and type 3B corresponding to an absence of profile evolution change at low T-high P. At room temperature, the highest proportions of small-diameter tubes are found along a diagonal line passing through the domains associated with types 1 and 2.

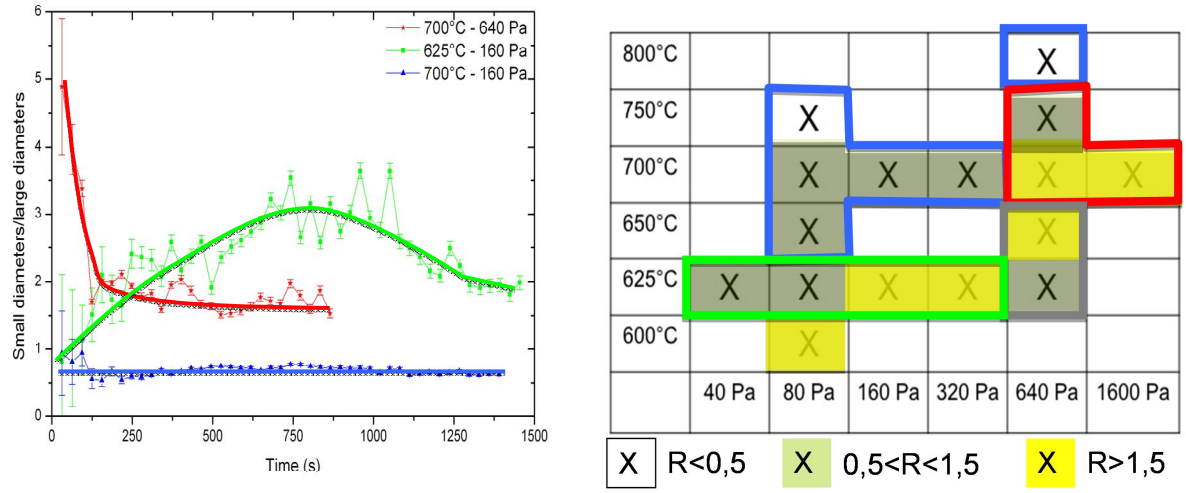

Figure 3-29. (a) Evolution of the ratio of small diameter (<1.05 nm) to large diameter (>1.05 nm) SWCNTs as a function of the synthesis time in three different growth regimes. The catalyst system is Co/SiO_2 and the carbon precursor is ethanol. (b) Summary of the observed RBM evolutions as a function of the growth conditions. The blue and grey domains correspond to an absence of evolution of the RBM profile during the growth at, respectively high T-low P and low T-high P. The red domain corresponds to an increase of the proportion of large-diameter tubes during the growth. The green domain corresponds to an increase then a decrease of the small-diameter fraction. The tested growth conditions are marked by a cross. The filling colour of the cell illustrates the value of the ratio R of small-diameter to large-diameter RBMs measured at room temperature.

Based on our previous observations of catalyst coarsening at high temperature, one can attribute the type 1 evolution at high T-high P to a regime where nanotube growth and catalyst coarsening have similar characteristic times and occur concomitantly. It follows that type 3A would correspond to a regime where nanotube growth occurs essentially after catalyst restructuring. The decrease of the small-diameter fraction observed at the end of type 2 would also be attributed to the effect of catalyst coarsening which would here impact later due to the lower temperatures.

The increase of the small diameter fraction observed at the beginning of type 2 deserves more discussion. If one keeps catalyst coarsening in mind, Ostwald ripening is a possible explanation since during an intermediate stage, it would cause a splitting of the size distribution of particles into increasingly smaller particles and increasingly larger ones until complete vanishing of the smallest particles. At the present time, the measured RBM profiles do not provide a clear evidence of such a split in the diameter distribution. Another possibility is to relate the initial increase in type 2 to the threshold activation pressure previously reported in §3.4.4 and lying in the same range of growth conditions. This threshold activation pressure

was attributed to the reduction of the catalyst particles and shown to be dependent on the particle size. One could explain the initial increase in small diameter tubes by a progressive conversion of the smallest particles from a metastable inactive state to an active one. If so, the rate of conversion would be expected to increase with increasing the precursor supply contrary to Ostwald ripening. Experimental curves actually show this behaviour: the increase of the small-diameter fraction at the beginning of type 2 is accelerated when increasing the precursor pressure. This effect also explains for the higher abundance of small-diameter SWCNTs in the type 2 domain (green part in Figure 3-29b) with increasing precursor supply, which cannot be accounted for by the Ostwald ripening hypothesis.

Finally, type 3B corresponds to the parameter domain found to be dominated in §3.5.2 by particle deactivation by an excess of carbon. If one follows the same line of reasoning as for type 2, it follows that, at higher precursor pressure, type 3B would correspond to a domain where the rate of particle encapsulation by carbon becomes faster than the rate of activation of the smallest particles. The ratio of small-diameter nanotubes at low T-high P would therefore be controlled by the kinetic competition between these two processes. Another possibility would be that small particles are more liable to carbon encapsulation than large ones but such an effect remains to be demonstrated.

3.5.4 Conclusion

Based on the evolution of the RBM profile during nanotube growth and between two consecutive growths in different regimes, the parameter dependence of the diameter distribution is explained as follows.

At low precursor pressure and low temperature, the lack of small diameter tubes originates from their higher threshold pressure of activation. In this domain, small-diameter tubes also appear later during the growth than large-diameter ones. Both features can be accounted for by a higher barrier of activation for smaller catalyst particles. This size effect was already reported in §3.4.4 and attributed to the lower reducibility of smaller catalyst particles.

At high temperature, catalyst particles display a significant restructuring at timescales shorter (or close) to those of nanotube growth. The exact nature of the coarsening process is presently unclear (alloying with the substrate, decoration by the oxide support or Ostwald/Smoluchowski ripening) and may vary with the catalyst system. Catalyst restructuring causes a shift toward larger-diameter SWCNTs. This effect can be counterbalanced by increasing the nanotube growth rate by increasing the precursor pressure.

At high precursor pressure and low temperature, the growth of small diameter tubes is impeded by an excessive precursor supply but can be reactivated by oxidation or by thermal annealing. These features together with TEM observations support that the smallest catalyst particles are encapsulated by a defective carbon material. The reason may be that the encapsulation of small particles is faster than their activation in such conditions of pressure and temperature, or that small particles are intrinsically more liable to carbon encapsulation.

3.6. Crystalline quality and carbon by-products

3.6.1 Introduction

It is frequently observed that as-grown CNTs contain defects. Controlling the defect density of CNTs is a key issue for the control of their properties. Defects severely affect the electronic and optical properties of SWCNTs and act as preferential sites of chemical functionnalization [412-414]. Contrary to the structure-properties relationship, little is known

about how defects are created during nanotube growth and how much they impact on the growth mechanism. In theory, the incorporation of a single point defect may dramatically influence the growth of a one-dimensional crystal such as a SWCNT. From Euler's rule, the integration of a single pentagonal or heptagonal ring will convert a growing tube into a cone. The integration of such a defect would theoretically lead to the termination of the tube growth. Alternatively, the curvature induced by certain defects may be compensated by others in a dynamic fashion, which would still induce elbows and chirality changes along the tube [415]. In growth simulations, defective structures, such as carbon chains and non-hexagonal rings, are commonly observed to form at the nanotube rim [361,362]. Despite that, centimetre-long CNTs are experimentally grown at several tens of microns per second [345]. This suggests the existence of remarkably efficient mechanisms to prevent the formation of defects or to anneal them.

Raman spectroscopy is commonly used to assess defects in graphene-like materials [266,267] through the measurement of the intensity ratio of the defect-induced D band to the graphenic G band [264,416]. The D band is theoretically non-active in Raman scattering but is activated in the presence of defects through a double resonance process involving the elastic scattering of electrons by defects [1,268]. When the distance between defects (L_D) is sufficiently large (more than a few nm), the I_G/I_D ratio was shown to be inversely proportional to the surface density of defects (σ) according to:

$$\frac{I_G}{I_D} = K\sigma^{-1}$$

where K is a parameter that depends on the laser energy [265]. For L_D values lower than a few nanometres, the D band broadens significantly and I_G/I_D starts to decrease with increasing defect density. This latter case corresponds to I_G/I_D values lower than unity, which were not encountered in our studies. The D band is dispersive which means that its frequency ω_D changes with the excitation laser energy, E_{laser}, with $\Delta\omega_D/\Delta E_{laser} \sim 50$ cm^{-1}/eV, a value that was shown to be almost independent of the type of sp^2 carbon material [267]. The D-band profile is also dependent on the type and structure of sp^2 carbon material. For instance, Souza Filho *et al.* [269] showed that for SWCNTs, the frequency of the D band is dependent on the nanotube diameter following the general trend $\omega_D = 1354.8\text{-}16.5/d$ for $E_{laser} = 2.41$ eV. For a SWCNT sample, this translates into a downshift of 10-30 cm^{-1} (depending on the diameter distribution) relatively to graphene and other flat sp^2 carbon materials. The linewidth of the D band significantly depends on the type and structure of sp^2 carbon material. An individual SWCNT usually displays a narrow D-band: the typical linewidth is 20 cm^{-1} [270] and can be as narrow as 7 cm^{-1} [271]. It follows that the D-band of a SWCNT sample is commonly broader than the D-band of an individual SWCNT and that the linewidth depends on the diameter distribution of the sample. Single-layer graphene with a small amount of defects also displays a quite narrow D-band with a linewidth around 20 cm^{-1} which broadens for L_D<5 nm [265]. Graphitic sp^2 carbon materials (graphite polyhedral crystal, graphite whiskers) can also display D-band linewidth around 20 cm^{-1} [272] while less ordered materials (CVD multi-walled nanotubes [273], turbostratic carbon [272], short stacked graphene patches [274], polycrystalline graphite [275] amorphous carbon [276]…) display a broad D band with linewidths ranging from 45 cm^{-1} to 100 cm^{-1}.

As detailed in §2.3.5, the D band of a SWCNT sample is generally considered as the sum of two contributions: a first one related to defects in the SWCNTs and a second one related to defective carbonaceous impurities. However, the nature of the defective by-products (pyrolitic amorphous carbon, catalytically-grown defective structures, carbon filaments, carbon shells…) is usually poorly known. Vinten *et al.* [279] and Kwok *et al.* [280] reported

that the I_G/I_D ratio increases with increasing growth temperature until an optimal temperature, then stabilizes and finally decreases at higher temperatures. In addition, Kwok *et al.* showed that the decrease of the I_G/I_D ratio observed at high temperature was amplified when increasing the growth duration, which they attributed to the co-deposition of amorphous carbon at high temperature in agreement with the *in situ* thermal analysis and TEM observations of Feng *et al.* [281]. It is clear that these studies essentially addressed the contamination of SWCNT samples by pyrolytic carbon and poorly described nanotube defects and other catalytically-produced carbon forms.

The aim of the following part is to account for the experimental features of the D band and of the G/D ratio of CCVD-grown CNT samples and for their evolutions with the growth conditions.

3.6.2 Biases in the measurement of the I_G/I_D ratio of CNT samples grown by CCVD

A first result of our *in situ* Raman measurements is that the D band of as-grown CNTs can be masked by other effects, notably the slow deposition of pyrolytic carbon during nanotube growth and the modification of the D band by air exposure.

Figure 3-30 shows two Raman spectra acquired at different times during a growth in the high temperature-high precursor pressure range. After a rapid increase, the G band unexpectedly displays a slow and continuous decrease after 100s. Importantly, this is accompanied by an increase and broadening of the D band and a decrease of all the Si peaks. The full width at half maximum (FWHM) of the D band is in this case of the order of 100-120 cm^{-1}. All these features agree with the deposition of a thick and optically absorbent layer of pyrolytic carbon as already described by several groups in similar growth conditions [277,280,417]. During our investigations, we only observed this behaviour in the high temperature-high precursor pressure corner of the parameter range, which may be explained by the use of a cold-wall reactor.

In most growth conditions, both the G and D bands increase continuously until reaching a plateau after a time ranging from several seconds to tens of minutes depending on the growth conditions (Figure 3-31a). Consequently, the I_G/I_D ratio reaches a stable value at the end of the growth. This value depends only on the growth conditions and not on the growth duration contrary to the high T-high P case displaying a continuous decrease of G/D with synthesis time (Figure 3-31b).

Hereafter, we only consider growth conditions that displayed no sign of pyrolytic carbon deposition during the *in situ* Raman monitoring of the growth (*i.e.* no increase and broadening of the D band with increasing temperature, no decrease of the G band and silicon peaks with increasing time). Under these conditions, we observed no decrease of the G/D ratio at high temperatures. The Raman spectra can therefore be considered free of pyrolytic carbon contributions and only characteristic of the carbon structures that were catalytically grown.

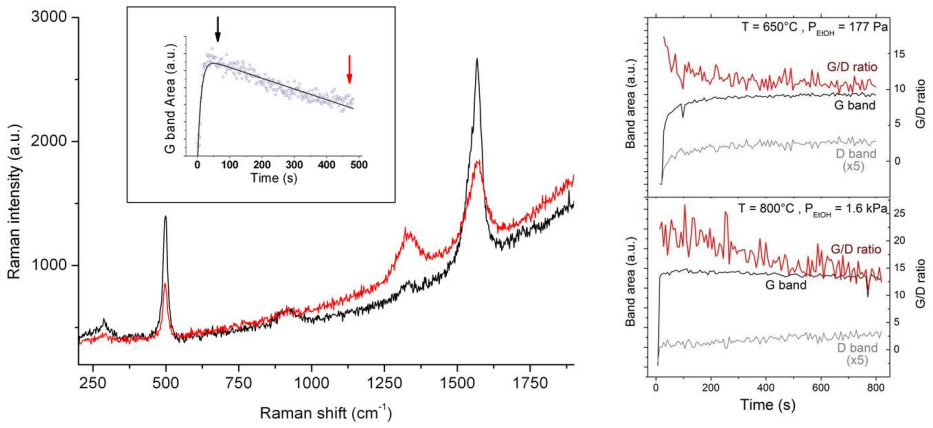

Figure 3-30. **(a) Raman spectra recorded at different synthesis times and illustrating the slow deposition of pyrolytic carbon in the high temperature-high precursor pressure range. The arrows in the inset indicate when each spectrum was acquired. Note that the increase of the D band is accompanied by a decrease of the G band and of all the Si peaks (at 300 cm^{-1}, 521 cm^{-1} and 900 cm^{-1}). The background increase at high frequency is caused by black body radiation at T=900°C. (b-c) Time evolutions of the intensities of G, D and of the G/D ratio: (b) standard behaviour, (c) high temperature/high pressure behaviour.**

While the sample remains under argon in the cell, the Raman spectrum does not display any modification. However, we observed that the intensity and the shape of the D band were significantly modified after a few hours of exposition to air (Figure 3-31). Just after opening the cell to air, no modification of the D band could be observed compared to the spectra measured under argon inside the cell. However, after several hours of air exposure, the D band could be increased by as much as a factor 8 and the I_G/I_D ratio decreased by a factor 10. The I_G/I_D ratio can be considerably (but not completely) recovered by annealing the samples under argon (Figure 3-31). This phenomenon was most apparent after several hours of air exposure and was then observed all over the sample even at the lowest laser powers. Our latest observations demonstrate that the phenomenon is strongly amplified by the laser exposure. A similar phenomenon was observed by Shim *et al.* when exposing SWCNTs to pure oxygen [418]. This phenomenon is attributed to a laser-activated reaction of molecules adsorbed on the nanotubes although additional studies are required for providing a complete explanation. For the present study, it is important to prevent this phenomenon in order to measure the intrinsic I_G/I_D ratio of as-grown SWCNTs. This is why all the post-growth Raman data presented hereafter were recorded under argon just after cooling the sample to room temperature and before opening the cell to air.

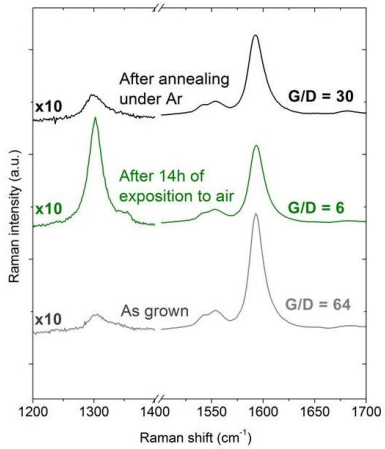

Figure 3-31. Evolution of the Raman spectra of SWCNT samples: as-grown (gray line), after 14 h of exposition to air (green line) and after annealing under Ar at 650°C (black line). The laser line is 647 nm.

3.6.3 Profile analysis of the D and G' bands

Given these precautions, the G/D ratio and the D band display the features shown in Figure 3-12 and Figure 3-13. All the studied catalyst-precursor systems display a downshift and narrowing of the D band with increasing temperature. A closer look actually reveals that the D-band displays an asymmetric profile (Figure 3-8 and Figure 3-32a). In most cases, the D band of the samples can be fitted by two Lorentzian peaks: a narrow D_L peak at $\omega_{DL} \sim 1320$ cm^{-1} and a broader D_H band at $\omega_{DH} \sim 1340$ cm^{-1} (for a laser excitation line of 2.33 eV). For a laser excitation line of 1.92 eV, ω_{DL} decreases to ~1300 cm^{-1} and ω_{DH} to ~ 1322 cm^{-1} (Figure 3-33) as expected from the dispersive relation of ω_D. Importantly, the D_L component is best resolved for samples displaying radial breathing modes characteristic of very small-diameter SWCNTs (see Figure 3-8 for instance). In most cases, the narrow D_L component is well fitted by a single Lorentzian peak. The D_H component can be correctly fitted by a broad Lorentzian component but is best fitted by two or three narrow Lorentzian components as shown later. This suggests that the broad D_H band is actually composed of two (or more) components. However, the two sub-components of D_H usually display a correlated behaviour as a function of the growth conditions so that, in many cases, the D_H peak can be treated as a single broad component.

Figure 3-32b-c shows the evolution of the position and linewidths of each of the two components as a function of the reciprocal growth temperature. The positions of D_L and D_H are essentially independent of the growth temperature. The full width at half maximum (FWHM) of D_L is about 30 cm^{-1} and displays a weak variation with increasing temperature. The FWHM of D_H is ~75 cm^{-1} at the lowest temperatures (650-675°C) and more markedly decreases with increasing temperature. D_L is the dominant feature of the D band at high temperature while D_H dominates the D band at low temperatures. The increase of the intensity ratio D_L/D_H with increasing temperature and decreasing precursor pressure is at the origin of the observed downshift and narrowing of the D-band. As shown in Figure 3-33, the same trends are observed at a different laser energy.

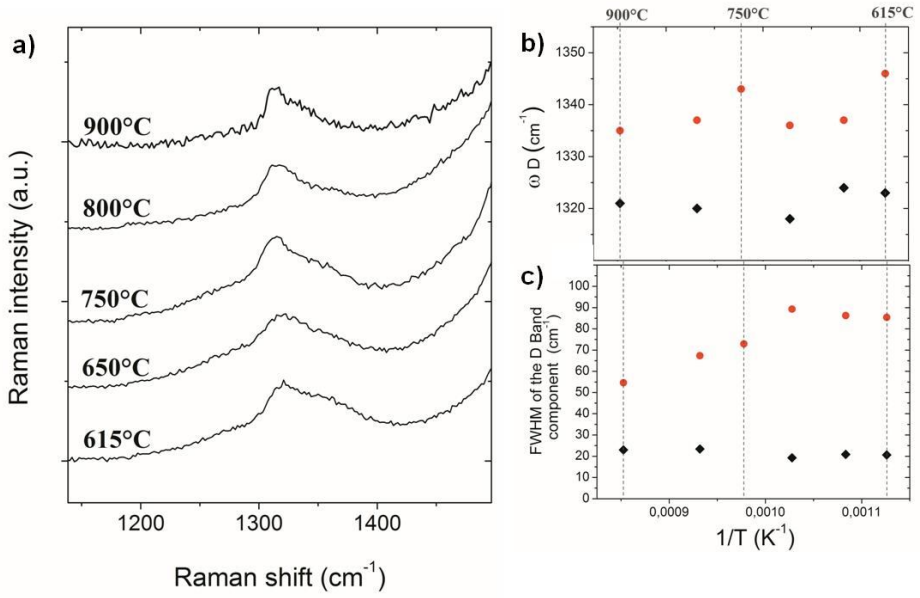

Figure 3-32. Raman measurements on cobalt-acetylene samples at E_{laser}=2.33 eV. (a) Growth temperature dependence of the Raman spectra (acquired at room temperature). Growth temperature dependence of (b) the position and (c) the FWHM of the D_L (black diamonds) and D_H (red circles) components of the D band.

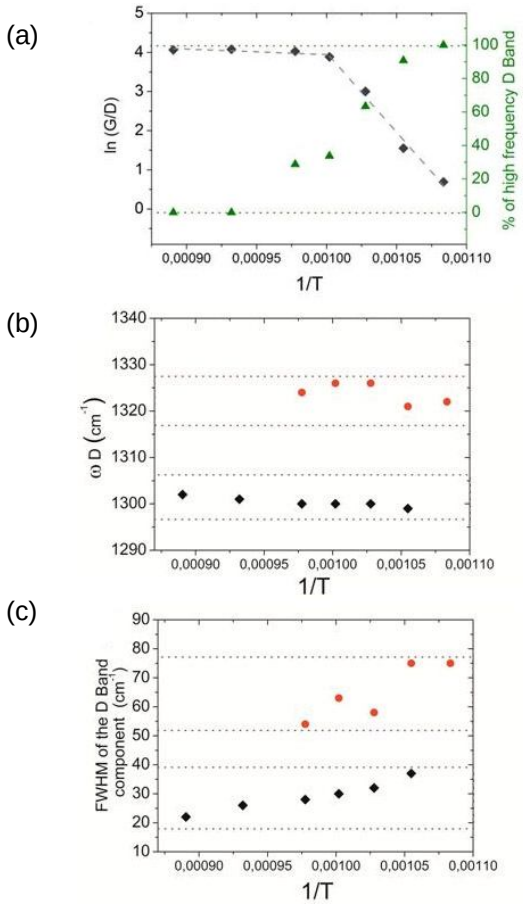

Figure 3-33. Raman features of the D band of samples grown with Co-C_2H_2 (E_{laser}=1.92 eV): (a) G/D ratio (diamonds) and proportion of the high frequency component (D_H) in the D band (triangles), (b) positions and (c) FWHM of the D_L (black diamonds) and D_H (red circles) components against inverse temperature. The dashed lines in (b) are fitted curves based on model B (see §3.6.5). The corresponding Raman spectra are shown in Figure 3-8.

Recently, we also studied the evolution of the G' band which is the two-phonon process associated to the one-phonon process causing the D band scattering. When performing this comparison, one must keep in mind that there is experimentally no exact matching between the D and G' band (for instance, $\omega_{G'} \neq 2\omega_D$) since the resonance processes are different for the two modes: the G' band involves two phonons, instead of one phonon and one defect for the D band. The D band is only activated in the presence of defects while the G' band is an intrinsic feature of graphene-type systems which is particularly sensitive to variations in the electron and phonon structures.

Figure 3-34 compares the evolution of the D and G' bands for CNT samples grown at different temperatures and with different types of carbon supply. One can observe that the G' band displays an asymmetric shape. We found that three or four Lorentzian peaks (depending on the precursor-catalyst-system) were required to correctly fit its profile. For a given system, the position of these Lorentzian features remains quite constant whatever the growth conditions of the samples but that their relative intensities vary significantly. In addition, the evolution of the G' profile is correlated with that of the D band: similarly to the high-frequency components of the D-band, the high-frequency components of the G' band decrease in intensity with increasing synthesis temperature.

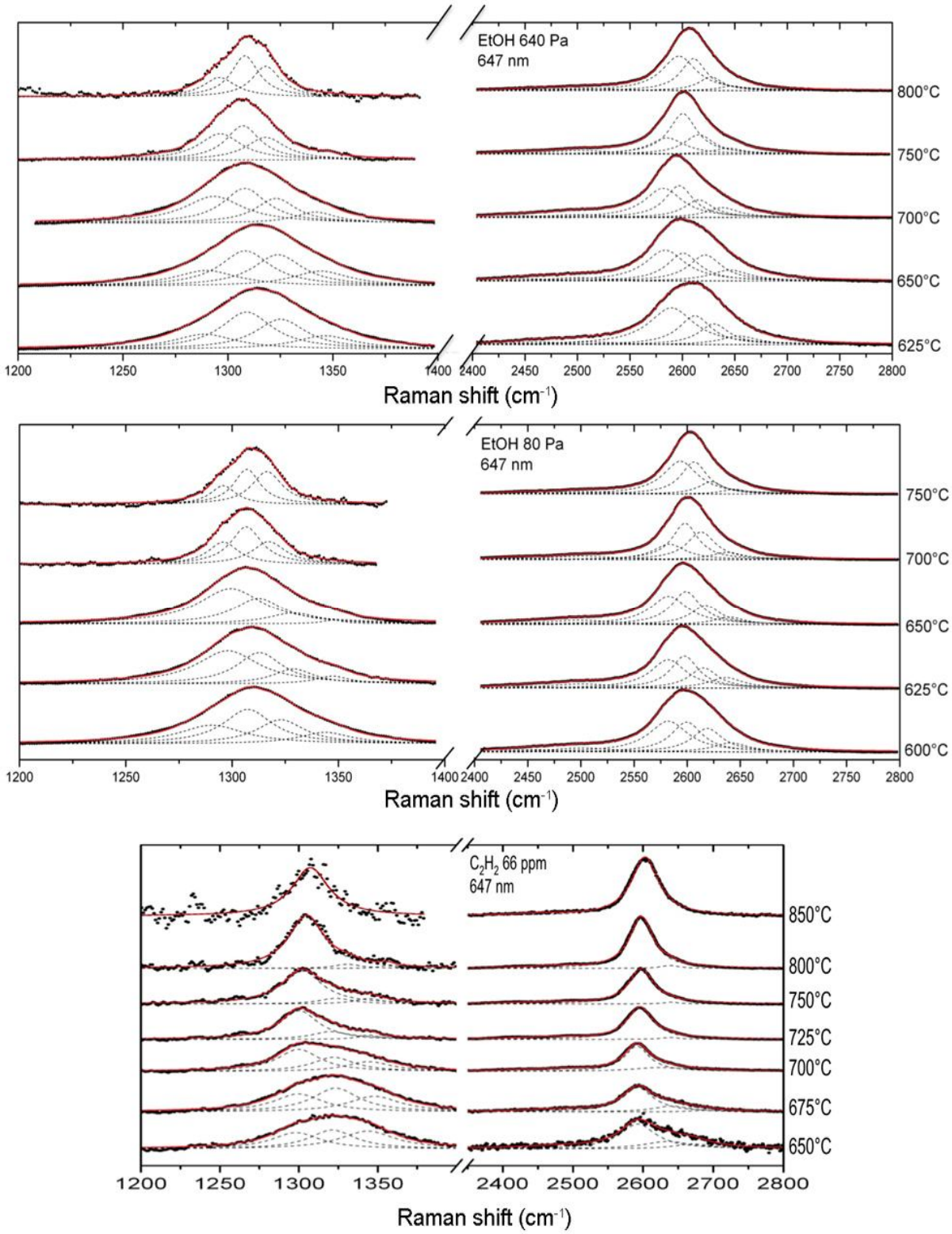

Figure 3-34. Compared evolution of the D and G' bands with increasing growth temperature for three conditions: (a) Co/EtOH 640 Pa, (b) Co/EtOH 80 Pa, (c) Co/C_2H_2. The laser excitation line is 647 nm.

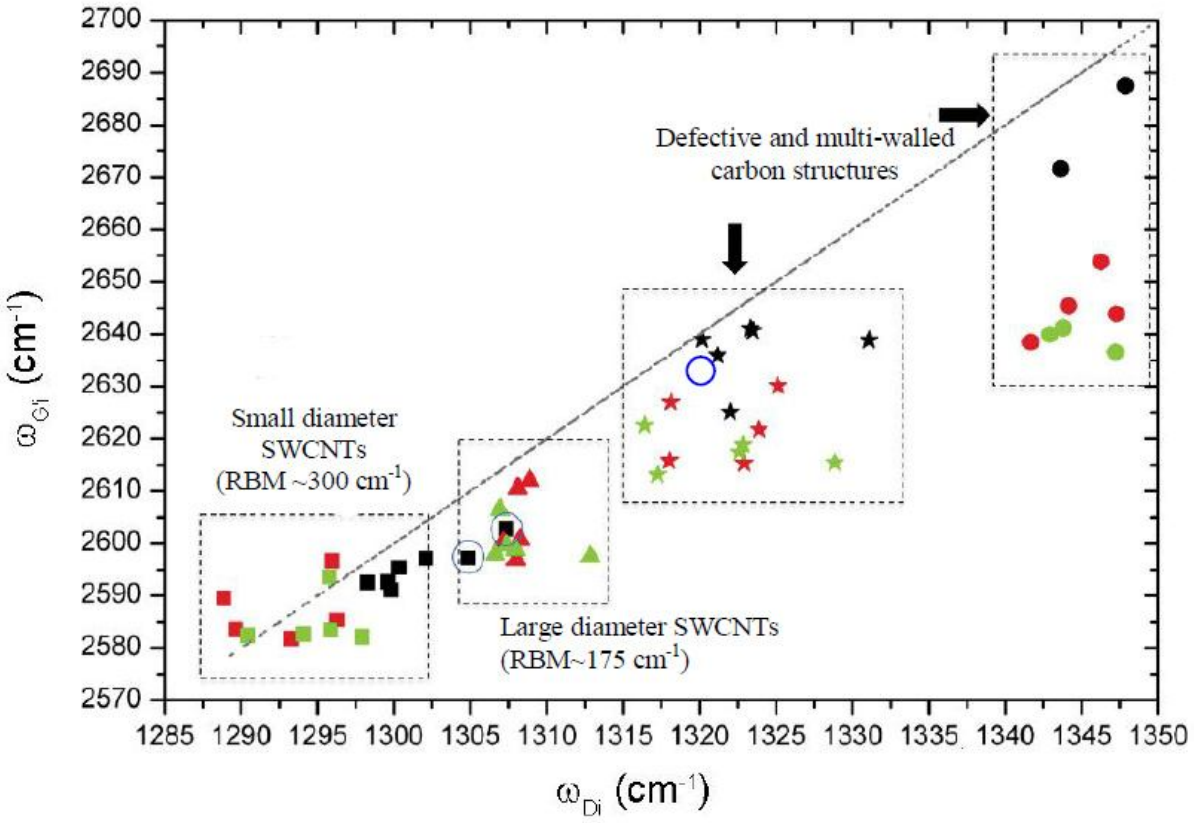

Figure 3-35. Position frequency of G'$_i$ components as a function of the associated Di component (i = 1, 2, 3) for samples grown with C_2H_2 or EtOH with Co/SiO_2. The dash line illustrates the relation expected if $\omega_{G'}=2\omega_D$. The laser energy is 1.92 eV. The open blue circle indicates the reference case of graphene.

If the D and G' bands are both fitted by the same number of components, a good match is observed between the frequency of the G'$_i$ component and the double frequency of the D_i component with the same i value (Figure 3-35). The G'$_i$ component is not exactly the double of the D_i frequency but usually lower by several cm^{-1}. This is in close agreement with the ω_D-$\omega_{G'}/2$ difference of 4-5 cm^{-1} commonly reported in the literature and accounted for by the two different scattering mechanisms possible for the D band process (defect first and phonon second, or phonon first and defect second) while for the G' band, only one mechanism is possible [266]. This frequency match further supports that the G'$_i$ and D_i peaks are associated. A significant difference between the D and G' bands is that the high-frequency components are much more intense in the former than in the latter.

The dependence of the D and G' bands on the laser energy was also investigated (Figure 3-36). An overall upshift of the D and G' bands with increasing laser energies is observed as expected from the dispersive nature of these modes. At all laser energies, the D band requires at least three Lorentzian peaks for a good fit. Fitting the G' band also requires three Lorentzian peaks at all laser energies except at 2.54 eV where the low frequency peak appears to be made of two Lorentzian peaks. Contrary to the G' band, the low-frequency component of the D band is not sufficiently resolved to evidence a similar double feature.

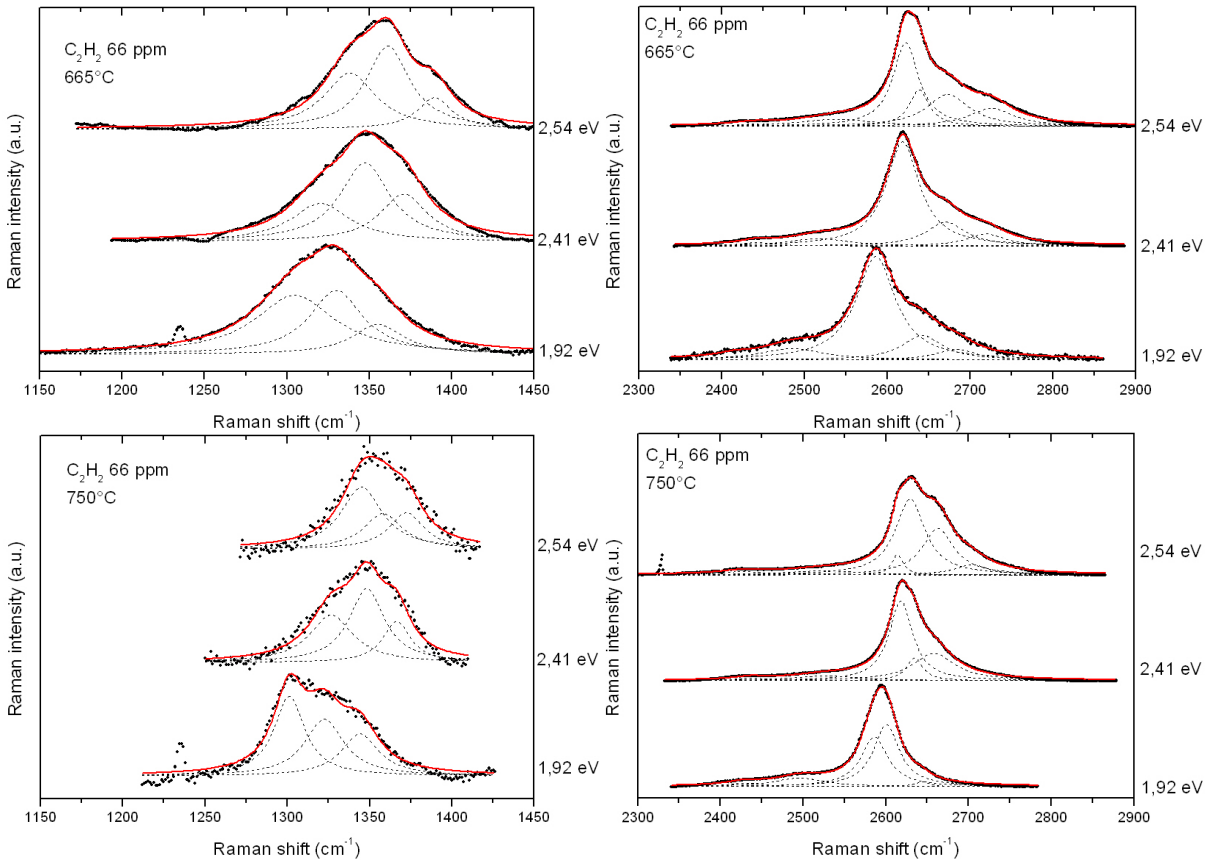

Figure 3-36. Evolution of the D and G' bands as a function of the laser energy for two samples grown at 665°C (upper panels) and 750°C (bottom panels).

3.6.4 Attribution of the components of the D and G' bands

The D-band of a SWCNT and of other graphene-related materials is frequently reported to be intrinsically a two-peak structure. Cançado et al.[419] showed that the D-band of disordered turbostratic graphite is made of two Lorentzian peaks distant of a few wave numbers which is explained by the different resonant scattering processes possible for the D band. Calculations by Maultsch et al. predicted that the D mode of a SWCNT is intrinsically a two-peak structure [420]. However, this intrinsic feature of SWCNTs is not expected to be appreciably modified by the conditions of growth and post-treatment as observed in our experiments. Hereafter, different hypotheses are considered for the attribution of the components of the D and G' bands observed in our CNT samples.

- *Different types of defects:*

Chemical addends versus core defects

It is known that the D-band of CNT samples is particularly sensitive to the chemical functionnalization of CNT walls which induces the symmetry breaking required for the activation of the D band. For instance, Figure 3-37 displays some results of Romanos *et al.* on pristine and acid-treated SWCNT samples [421]. Figure 3-37a-c shows that acid-treated CNTs have a high density of oxygen-containing functionalities that can be characterized by Temperature Programmed Desorption monitored my Mass Spectrometry (TPD-MS). Most of these functions desorb between 100 and 900°C. Figure 3-37d shows that the Raman D/G ratio is directly proportional to the density of functional groups as assessed by TPD-MS. These functional groups can be desorbed by thermal treatment under Ar at 500°C (Figure 3-37e).

This is accompanied by a decrease of the D/G ratio, by the appearance of a narrow low-frequency component in the D band and of an intense low-frequency component in the G' band.

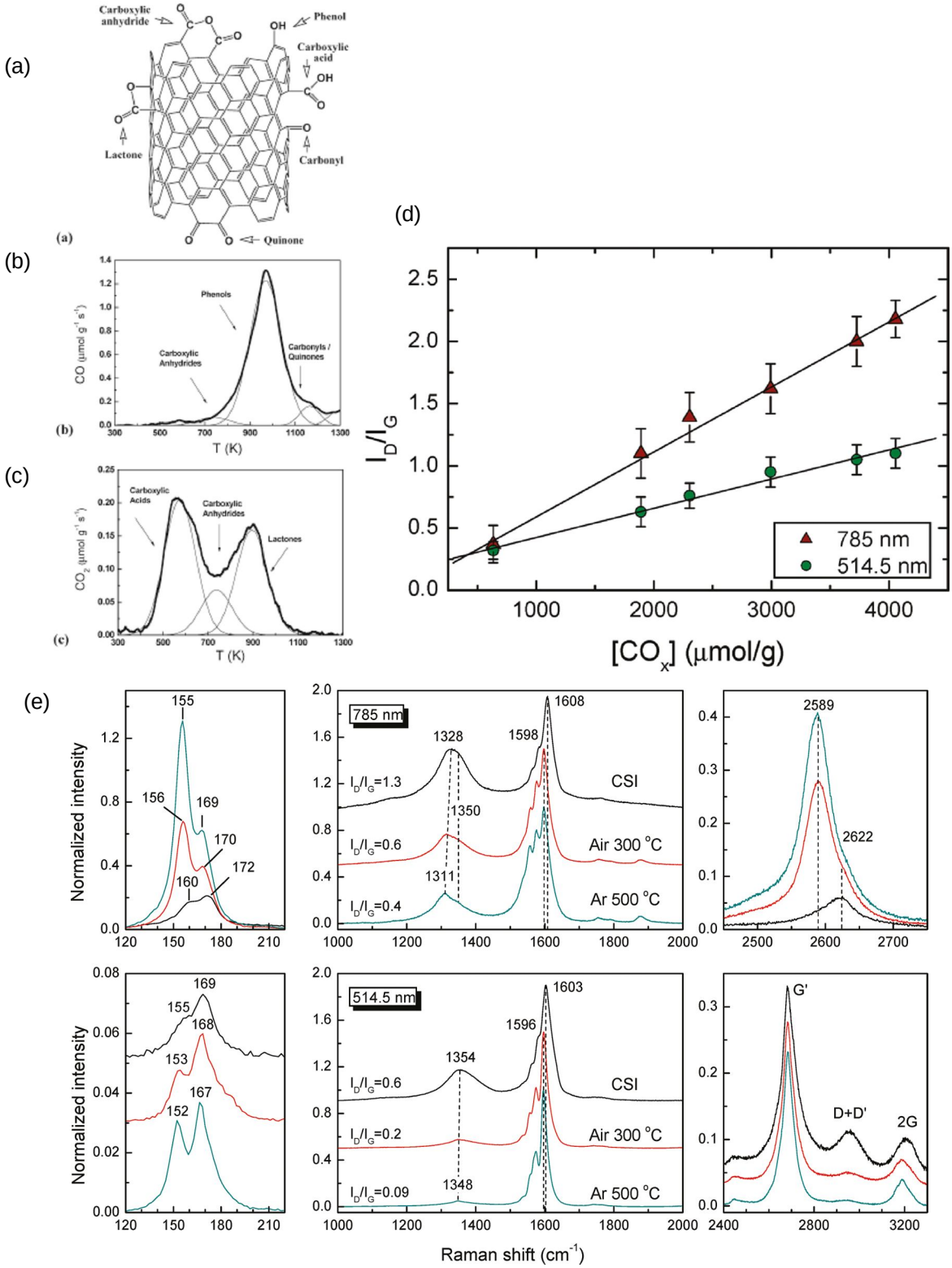

Figure 3-37. (a) Schematic representation of oxygen-containing functional groups on CNTs; Deconvolution of TPD-MS spectra for CNT sample treated with 0.30 M of HNO_3 at 473 K: (b) CO spectrum, (c) CO_2 spectrum. (e) Raman spectra of the pristine and thermally treated CNT sample in air (300°C) and Ar (500°C) in the low, intermediate, and high frequency spectral regions at 785 nm (upper panels) and 514.5 nm (lower panels). From [421].

These features are very close to the ones observed for our CCVD-grown samples. It may therefore be proposed that the high-frequency components correspond to functional groups at the surface of CNTs. Such groups would be caused by the reaction with oxygen-containing contaminants such as O_2 and H_2O. Increasing synthesis temperature would cause desorption of these groups, which would account for the decrease of D_H with temperature. At the opposite, the D_L component would correspond to intrinsic CNT defects.

To test this hypothesis, we submitted CNT samples displaying both low- and high frequency D components to a thermal annealing under argon up to 950°C (Figure 3-38). Contrary to Romanos *et al.*, we did not observe the appearance of a low-frequency component in the G' or D bands after thermal treatment. We only observed a slight upshift of the D band and G' bands which can be accounted for by the effect of the nanotube diameter distribution (see after). This result shows that the D_H component is stable at high temperature and cannot be attributed to functional groups at the surface of CNTs.

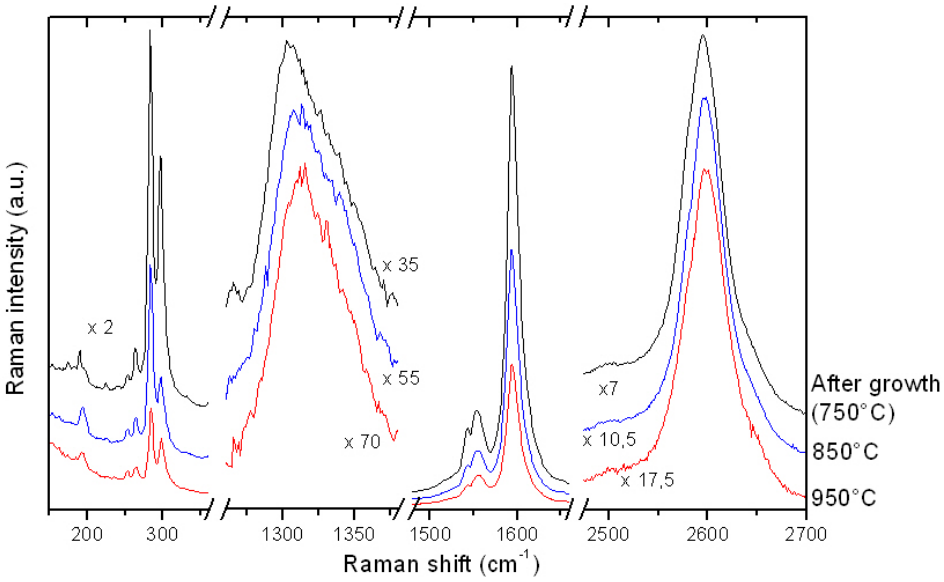

Figure 3-38. Raman spectra of a CNT sample as-grown and after thermal annealing under argon at 850°C and 950°C.

Charged versus uncharged defects

Maciel *et al.* [399] reported that charged defects caused by substitutional dopants (such as nitrogen or boron) leads locally to an electron and phonon renormalization manifesting by a secondary G'_D component beside the main G'_P peak of pristine CNTs. As shown on Figure 3-39a, n-doped SWCNTs display a G' component at lower frequency while p-doped SWCNTs display a higher-frequency G' component. Both the pristine and doped components display a dispersive behaviour with the laser energy. The high frequency component is dominant at high laser energy while the low frequency component dominates at low laser energy (Figure 3-39b). Unfortunately, Maciel *et al.* did not report on the influence of the doping on the D band. Since the D band scattering corresponds to the one-phonon process related to of the G' scattering, one may expect the D band to be also influenced by an electron and phonon renormalization caused by doping defects.

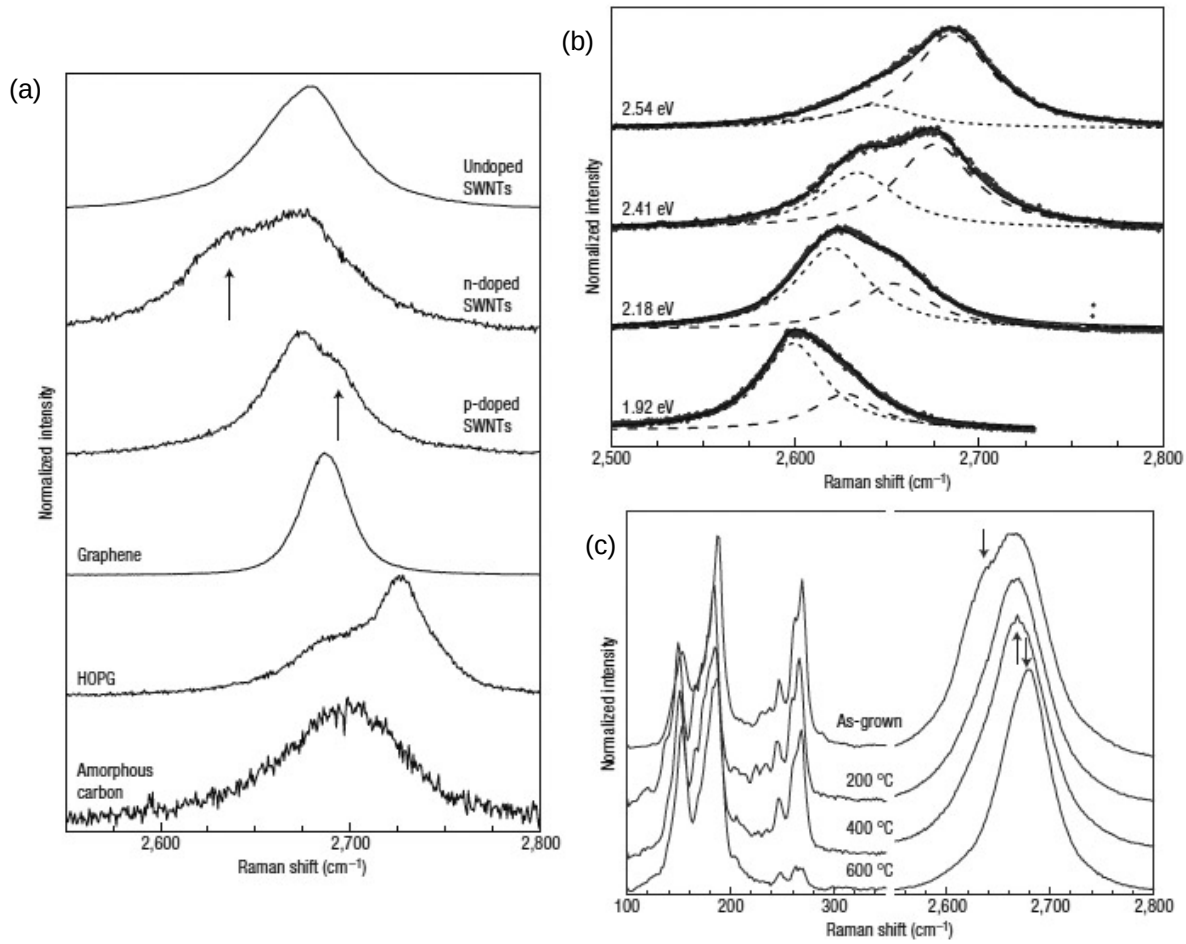

Figure 3-39. (a) The G' Raman band in different sp^2 carbon materials measured at room temperature with E_{laser} =2.41 eV (514 nm). The arrows point to defect-induced peaks in the G' for doped SWCNTs. The p/n doping comes from substitutional boron/nitrogen atoms. (b) Dependence of the G' band on E_{laser} for the n-doped SWCNT sample. (c) The effect of heat treatment under argon on the RBM and G' band spectra of pristine (unintentionally doped) CVD-grown SWCNTs (with E_{laser} =2.41 eV). From [399].

Once again, these features are quite close to those observed for our samples. Following the interpretation of Maciel., one may propose that the two main components of the D band of our samples correspond to uncharged and charged defects. For the G' band, the two main components would correspond to undoped and locally doped portions of CNTs.

To test this hypothesis, we first calculated the position of the G'_P peak of undoped CNTs as expected from the empiric law reported by Maciel *et al.*: $\omega_{G'P}$ (cm^{-1}) = 97 E_{laser} (eV) -35.4/d_t (nm) + 2474. The position primarily depends on the laser energy and on the diameter distribution of the sample. For the CNT samples shown in Figure 3-8 and displaying a narrow distribution of RBMs around 300 cm^{-1} (d~0.8 nm) at E_{laser}=1.92 eV, the G'_P peak would be expected at around 2616 cm^{-1}. However, the validity of this law must be tempered by the fact that Maciel *et al.* also reported a G'_P at 2610 cm^{-1} at E_{laser}= 1.96 eV for a single (9,1) tube (d~0.8 nm), which is 10 cm^{-1} lower than expected from the empirical law. Associated with the reported oscillatory dispersion of 5-10 cm^{-1} for $\omega_{G'}$ due to resonance effects in SWCNT bundles [422], it appears reasonable to expect the G'_P peak to be between 2600 and 2616 cm^{-1} for 0.8 nm tubes at E_{laser}=1.92 eV. An n-type doping would give rise to a G'_D component 20 to 40 cm^{-1} lower (depending on the type of dopants [423] and a p-type doping to a G'_D component about 20 cm^{-1} higher. In the charged defect interpretation of Maciel *et al.*, the G'_1 component of our samples could therefore be attributed to the G'_P peak of pristine SWCNTs of small diameters while the higher G'_i components could be attributed to two G'_D bands

associated with p-type dopants. However, there is no G' component that can be reasonably attributed to n-type doping based on Maciel's data.

Maciel *et al.* also observed that pristine CCVD samples can display a low-frequency shoulder in the G' band that they attributed to unintentional n-doping (Figure 3-39c). They observed that this component disappeared when the sample was submitted to argon annealing at 400-600°C. This is reminiscent of the effect observed by Romanos *et al.* for weakly grafted chemical addends (Figure 3-37). For our CCVD samples, we also observed a slight upshift of the D band and G' bands when submitting them to Ar annealing at up to 950°C as already described (Figure 3-38). However, in our case as in the case of Maciel *et al.*, the argon annealing led to a modification of the RBM profile characterized by a disappearance of the highest-frequency RBMs. As a consequence, the evolution of the D and G' profiles can be accounted for by the effect of the diameter distribution alone without invoking doping effects. In addition, there is no obvious source of doping in our growth conditions contrary to Maciel *et al.* who intentionally used precursors containing N, Si or P.

For these reasons, doping effects may be a secondary source of variations for the D and G' band but cannot explain the main features of the D and G' bands of our CNT samples.

- *Different types of carbon nanostructures*

Small-diameter SWCNTs versus large diameter SWCNTs

Souza Filho *et al.* [269] reported that for individual SWCNTs, the frequencies of the D and G' bands are dependent on the nanotube diameter according to the relations: $\omega_D = 1354.8-16.5/d$ and $\omega_{G'} = 2708.1-35.4/d$ for $E_{laser} = 2.41$ eV. These laws were established using tubes of intermediate diameter (d~1.3-2.2 nm) but have some obvious flaws for large diameter and small diameter tubes. For instance, the D-band position of graphene at 2.41 eV is 1345 cm^{-1} [265] and not 1354.8 cm^{-1}. For a (9,1) tube of ~0.8 nm, Maciel *et al.* [399] reported a G' frequency much lower than expected from the Souza Filho's law. However, in the absence of other laws, those laws already give an approximated value of the expected positions of D and G' as a function of SWCNT diameters. Compared to graphene, one can notably expect a downshift of 0-30 cm^{-1} for a SWCNT sample (depending on the diameter distribution).

If one looks to the D_i and G'_i positions observed in our samples (Figure 3-35), only the components with frequencies lower than those of graphene could be attributed to SWCNTs and to the diameter effect. For instance, the (D_1, G'_1) components could be attributed to SWCNTs of very small diameter (d~0.7-0.8 nm) while the (D_2, G'_2) components could be attributed to SWCNTs of intermediate diameters (d~1.4-1.8 nm) (see Figure 3-35). This interpretation correlates remarkably well with the RBM profiles of the samples grown with ethanol and acetylene. Samples grown with ethanol display both small-diameter semiconducting tubes and intermediate-diameter metallic tubes in their RBM profile and display both the (D_1,G'_1) and (D_2, G'_2) components. At the opposite, the samples grown with acetylene display only small-diameter semiconducting tubes in their RBM profile and only the (D_1,G'_1) components. This interpretation would also account for the separation of the (D_1,G'_1) and (D_2, G'_2) components due to the separation of the metallic and semiconducting branches in the Kataura plot. It would also explain why the lowest-frequency part of G' displays two components at 2.54 eV since the RBM display two sets of well separated small diameter tubes. This would also explain why the frequencies of (D_1,G'_1) and (D_2, G'_2) do not strictly follow the dispersive behaviour expected for the D and G' bands (~50 cm^{-1}/eV and ~100 cm^{-1}/eV respectively) but fluctuate around the expected value as already reported by Souza Filho et al. [422] for SWCNT bundles.

From this analysis, the D_i and G'_i components lying below the frequencies of the D and G' peaks of graphene (e.g. (D_1,G'_1) and (D_2, G'_2)) are attributed to SWCNTs. The downshift in frequency compared to graphene is attributed to the diameter dependence of ω_D and $\omega_{G'}$ in the case of SWCNTs.

SWCNTs versus other carbon structures

(D_i, G'_i) components with frequencies higher than graphene cannot be attributed to SWCNTs. If one looks at the D-band frequencies of different sp^2 materials, it is apparent that only graphitic materials experimentally have G' bands higher in frequency than graphene (Table 3-1). As demonstrated by studies of multi-layer graphene, stacking causes a modification of the electronic structure of graphene which causes the G' band of graphitic materials to become a multi-peak structure whose average frequency is upshifted compared to the G' peak of a single layer of graphene. For defective graphitic materials, these features are averaged and the G' band appears as a single broad band.

It follows that the (D_i, G'_i) components with frequencies higher than graphene could be attributed to graphitic materials present in the samples. To test this hypothesis, we observed CNT samples displaying particularly intense high-frequency (D_i, G'_i) components by HRTEM. The studied samples were typically those grown at low temperatures with the Co/C_2H_2 couple (see Raman spectra of low temperatures in Figure 3-8). As shown in Figure 3-40a, we found that these samples mostly consisted of large diameter multi-walled carbon structures. Such a transition from MWCNT at low temperature to SWCNT/DWCNT at high temperature is commonly reported in the nanotube literature [424]. However, such multi-walled structures are not observed for all samples displaying intense high-frequency (D_i, G'_i). In the case of the samples grown at low temperatures with the Ni-EtOH system, crumpled highly-disordered single-walled carbon structures were the dominant by-products observed by HRTEM (Figure 3-40b). Contrary to SWCNTs, large MWCNTs and defective carbon forms do not display Raman enhancement by electronic resonance. This explains why the Raman spectra of these samples remain largely dominated by the SWCNT features (*i.e.* intense RBMs, G^+ at 1590 cm^{-1}, well-resolved and intense G^- shoulders). Both types of structures are expected to display quite similar Raman features: a broad G band at ~1580 cm^{-1} (which is probably hidden in the G band of SWCNTs) and broad and intense D and G' bands at frequencies higher than those for SWCNTs.

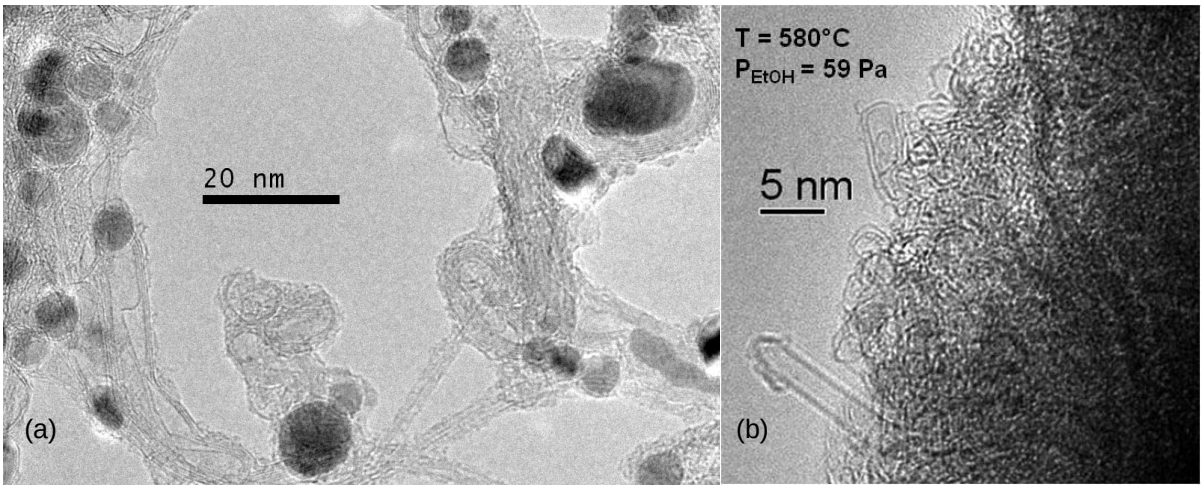

Figure 3-40. HRTEM pictures of typical carbonaceous impurities in CNT samples grown at low temperature with (a) the Co/C_2H_2 system and (b) the Ni/EtOH system (thesis M. Picher).

	780 nm (1.59 eV)	647 nm (1.92 eV)	633 nm (1.96 eV)	532 nm (2.33 eV)	514 nm (2.41 eV)	488 nm (2.54 eV)	458 nm (2.71 eV)
Graphene [265]	1304	1321	1323	1341	1345	1352	1360
Carbon black [425]	1313	1330	1332	1351	1363	1370	1378
Glassy carbon [274]	1304	1321	1323	1342	1346	1353	1361
Microcrystalline graphite [275]	1308	1324	1326	1345	1349	1355	1364
Graphite crystal edges (D_1/D_2) [272]	1310/1335	1327/1352	1324/1346	1343/1365	1352/1369	1359/1376	1367/1384
Graphite whisker [272]	1315	1331	1333	1352	1356	1362	1371
Graphite cones (D_1/D_2) [272]	1314/1324	1330/1340	1332/1342	1351/1361	1355/1365	1361/1371	1370/1380
Graphite polyhedral crystal [272]	1311	1328	1330	1348	1352	1359	1367
Natural carbon cones [272]	1322	1339	1341	1359	1363	1370	1378
MWCNT[273] (ω_{min}-ω_{max})	1305-1309	1322-1326	1324-1328	1342-1346	1346-1350	1353-1357	1361-1365
Individual SWCNTs (1.5 nm<d<2.5 nm) [269]	1300-1311	1316-1327	1318-1329	1337-1348	1341-1352	1347-1358	1356-1367
Individual SWCNTs (1.5 nm<d<2 nm) [270]	1304-1309	1321-1326	1323-1328	1341-1346	1345-1350	1352-1357	1360-1365
Individual SWCNTs (1.25 nm<d<2 nm) [269]	1293-1301	1309-1317	1311-1319	1330-1338	1334-1342	1340-1348	1349-1357
Individual SWCNTs (1.25 nm<d<1.5 nm) [269]	1299-1305	1315-1321	1317-1323	1336-1342	1340-1346	1346-1352	1355-1361
Individual SWCNTs (1 nm<d<1.5 nm) [270]	1300-1314	1317-1331	1319-1333	1337-1351	1341-1355	1348-1362	1356-1370
Individual SWCNTs (0.8 nm<d<1 nm) [270]	1283-1294	1300-1311	1302-1313	1320-1331	1324-1335	1331-1342	1339-1350

Table 3-1. Experimental values of ω_D (cm^{-1}) for different sp^2 carbon materials Data in black: experimental values. Data in grey: calculated values applying a correction factor of 50 cm^{-1}/eV (except for glassy carbon where the empirical relation $\omega_D=1223+51*E_{exc}$ from reference [274] was used).

From this analysis, the (D_i, G'_i) components with frequencies higher than graphene (e.g. (D_3,G'_3) and (D_4, G'_4) in Figure 3-35) are attributed to disordered non-SWCNTs carbon structures that vary with the type of catalyst: large-diameter multi-walled (*e.g.* in the case of Co/SiO_2) or crumpled single-walled (*e.g.* in the case of Ni/SiO_2).

Following this assignment, the relative contributions of each carbon species to the D and G' bands can now be evaluated. Their evolution as a function of the growth temperature is illustrated in Figure 3-41 for the cobalt-acetylene system. At low temperature, the D band is dominated by the contribution of disordered by-products (~70%) while at high temperature, the D band is essentially made of the SWCNT contribution. The G' band is dominated by the SWCNT contribution at all temperatures but the latter decreases down to 60% with decreasing temperature.

It would also be interesting to evaluate the contribution of each species to the G band. However, resolving them by fitting the G band is made difficult by the close frequencies of the contributions of each species and by the different SWCNT components in the G band (*i.e.* D', G^+, G^-). Alternatively, estimated values could be extrapolated from the G'_i/G' values (Figure 3-41b) but this would require the knowledge of the G_i/G'_i conversion factor for each species. This is further complicated by the fact that the conversion factor may also vary with the structural features of each species (*e.g.* number of walls, doping, diameter) and therefore with their growth temperature. At that stage, a quantitative assessment is therefore difficult but a qualitative analysis can be given as detailed in §3.7.3.

Qualitatively, however, it may be concluded that, at the lowest growth temperatures, the G band may contains a significant contribution of non-SWCNT species while, at high growth temperatures, it is essentially made of the SWCNT contribution.

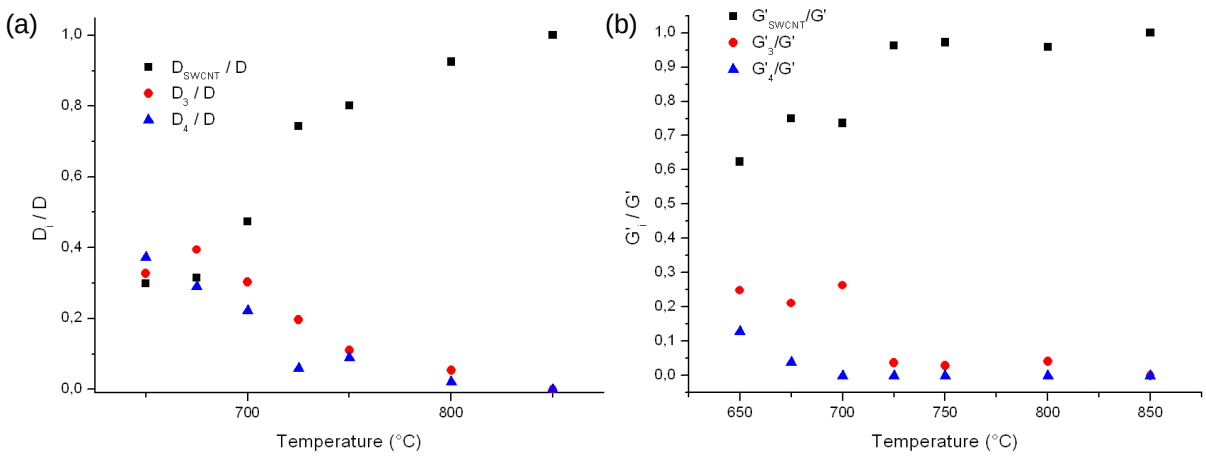

Figure 3-41. Area fraction of each D_i (a) and G'_i (b) component as a function of the growth temperature for the cobalt-acetylene system.

3.6.5 Modeling the experimental dependence of the I_G/I_D ratio

The I_G/I_D ratio is commonly used to assess the defect density of CNT samples. Its evolution with the growth temperature and the precursor pressure was shown in Figure 3-12 and Figure 3-13 for different catalyst-precursor systems. In first approximation, the defect density decreases with increasing temperature and decreasing precursor supply. This is a common observation in non-catalytic thin film deposition (e.g. MBE, PVD, CVD) that the defect density of the layer decreases with increasing growth temperature and decreasing

precursor supply [426 ,427]. This phenomenon is commonly attributed to the kinetic competition between the gaseous precursor supply and the diffusion / rearrangement of the surface intermediates.

In our growth experiments, the general decrease of crystalline quality with increasing precursor supply could also be explained by this competition. In simulations of nanotube growth for instance, an excessive supply of carbon atoms is frequently observed to freeze growing carbon structures in an intermediate defective state [361,362]. In other words, carbon atoms are supplied too fast to allow surface carbon atoms to diffuse / rearrange and form well-ordered structures. Such a model would be characterized by an Arrhenius law whose activation energy reflects the activation barriers for the diffusion of carbon species or their integration into the nanotube.

However, this simple model cannot account for the temperature dependence of I_G/I_D in our experiments since I_G/I_D systematically displays two different Arrhenius regimes as a function of temperature. In addition, this transition is accompanied by a decrease of the characteristic activation energy with increasing temperature. In the literature, such features are referred to under the term of *convex Arrhenius plots* [428] and put additional constraints on the possible microscopic models [428]. Hereafter are proposed and discussed different microscopic models susceptible to account for the experimental dependence of I_G/I_D. Three models are considered and illustrated in Figure 3-42. The details of the calculations are given in Annex 1.

In these models, the molecules of gaseous carbon precursor (P) decompose at the surface of the catalyst particle to form reactive surface carbon species (C). Surface mobility allows the latter to link to the nanotube rim by creating intermediate carbon structures. Model A (Figure 3-42a) hypothesizes that hexagonal carbon rings at the nanotube rim (H_R) can be formed either directly from surface carbon or through annealing of imperfect rim structures (D_R). Addition of further carbon atoms leads to the incorporation of these rim hexagons and defects in the nanotube core (H and D, respectively). Model B (Figure 3-42b) generalizes this concept by considering two possible intermediate states in rapid equilibrium: I_{LT} is the dominant intermediate state at low temperature and I_{HT} at high temperatures. The notion of intermediate state is here quite general. For example, the intermediate states may differ by the chemical or physical state of the catalyst (solid/liquid, metal/carbide…) or of the carbon structures at the nanotube rim (*e.g.* pentagons or heptagons, sp / sp^2 / sp^3 hybridization, hydrogen or oxygen content). By addition of carbon atoms, both intermediate states can give rise to either an ordered sp^2 patch or to a defective structure in the nanotube core but with differing rates. Model C (Figure 3-42c) considers only one intermediate state but two mechanisms of defect formation. As in model B, the intermediate state can be converted in either a sp^2 hexagonal ring or a defect in the nanotube core. In addition, model C considers another mechanism of creation of defects that is activated at high temperature. The nature of the two mechanisms of formation of defects is left open by the mathematical model. As an example, the low-temperature mechanism may correspond to the formation of defects containing only carbon atoms while the high-activation-energy path may correspond to the formation of defects by reaction with foreign species such as water or oxygen.

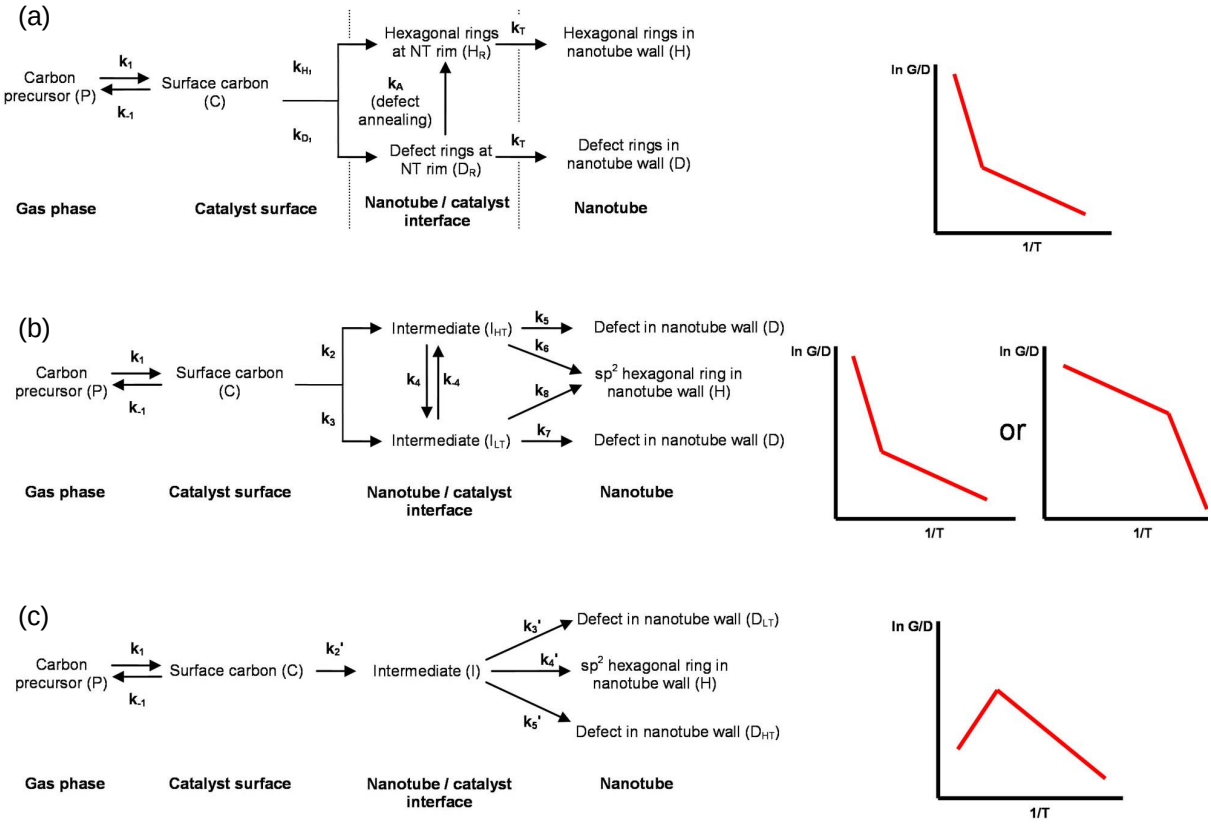

Figure 3-42. Models of defect density of CCVD-grown CNT samples: (a) thermally-activated annealing of defects, (b) thermally-activated transition of intermediate state, (c) thermally-activated mechanism of creation of defects. The right-hand insets illustrate the type of Arrhenius plots yielded by each model.

In the following, E_x, n_x and k^0_x are respectively the activation energy, reaction order for carbon and pre-exponential factor associated to the kinetic constant k_x of step x. All models assume that the local precursor pressure remains constant at the timescale of nanotube growth and that the gaseous carbon precursors are in rapid quasi-equilibrium with the surface carbon feedstock. This leads to a surface concentration of carbon which is constant with time but depends on the precursor pressure P and decomposition temperature T.

$$C = (K_1 P/P_0)^{1/n_1} \text{ with } K_1 = k_1/k_{-1} = \exp(-\Delta_r G_1/kT).$$

For each model, the expression of the H/D ratio in the steady state regime is extracted and assimilated to the inverse defect density σ^{-1} in the relation $\frac{I_G}{I_D} = K\sigma^{-1}$ [266] to obtain the experimental dependence of I_G/I_D.

- *Model A: thermally-activated annealing of defects*

At low temperature, the annealing of defects is negligible at the timescale of nanotube growth (*i.e.* $E_A > E_T$ and $k_A << k_T$) and the model yields:

$$\ln\left(\frac{I_G}{I_D}\right) = A''_{LT} - \frac{E''_{LT}}{kT} + n''_{LT} \ln\frac{P}{P_0}$$

$$\text{with } A''_{LT} = \ln\left(K\frac{k^0_H}{k^0_D}\right),\ E''_{LT} = E_H - E_D + n''_{LT}\Delta_r G_1 \text{ and } n''_{LT} = \frac{n_H - n_D}{n_1}.$$

It is apparent that I_G/I_D displays an Arrhenius law with regard to temperature and a power law dependence on the precursor pressure.

At the opposite, in the high temperature case where $k_A >> k_T$ and $k_H >> k_D$, model A yields:

$$\ln\left(\frac{I_G}{I_D}\right) = A''_{HT} - \frac{E''_{HT}}{kT} + n''_{HT} \ln\frac{P}{P_0}$$

$$\text{with } A''_{HT} = \ln\left(K\frac{k_A^0 k_H^0}{k_T^0 k_D^0}\right),\ E''_{HT} = E_A + E_H - E_T - E_D + n''_{HT}\,\Delta_r G_1 \text{ and } n''_{HT} = \frac{n_H - n_D}{n_1}.$$

It is apparent that I_G/I_D also displays an Arrhenius law with regard to temperature and a power law with regard to precursor pressure. However, in the high temperature case, the apparent activation energy is higher by the value E_A-E_T.

Since E_A-E_T is always positive, the apparent activation energy in the high temperature case is always higher than the apparent activation energy at low temperature. In other words, this model intrinsically yields a concave Arrhenius plot and cannot account for the experimental observations.

- *Model B: Thermally-activated transition of intermediate states*

In the high temperature case where the high-temperature intermediate is dominant (i.e. $K_4(T) = \frac{I_{LT}}{I_{HT}} \sim 0$), the defect density is ruled by the competition between steps 5 and 6 and the model yields:

$$\ln\left(\frac{I_G}{I_D}\right) = A_{HT} - \frac{E_{HT}}{kT} + n_{HT} \ln\frac{P}{P_0}$$

$$\text{with } A_{HT} = \ln\left(K\frac{k_6^0}{k_5^0}\right),\ E_{HT} = E_6 - E_5 + n_{HT}\Delta_r G_1 \text{ and } n_{HT} = \frac{n_6 - n_5}{n_1}.$$

At the opposite, in the low temperature case where K_4 tends toward very large values, the defect density is controlled by the competition between steps 7 and 8 and the model yields:

$$\ln\left(\frac{I_G}{I_D}\right) = A_{LT} - \frac{E_{LT}}{kT} + n_{LT} \ln\frac{P}{P_0}$$

$$\text{with } A_{LT} = \ln\left(K\frac{k_8^0}{k_7^0}\right),\ E_{LT} = E_8 - E_7 + n_{LT}\Delta_r G_1 \text{ and } n_{LT} = \frac{n_8 - n_7}{n_1}.$$

Since the model imposes no conditions on the sign of $(E_6$-$E_5)$-$(E_8$-$E_7)$, it can yield either a concave or a convex Arrhenius plot. A convex Arrhenius plot can notably be obtained if the high-temperature intermediate state lowers the barrier for hexagon formation (E_6) or increases the barrier for defect formation (E_5).

- *Model C: Thermally-activated formation of defects*

From this relation, it is seen that, in the case $k_3'C^{n_3'} >> k_5'C^{n_5'}$, the defect density will be governed by the competition between steps 4' and 3', while, in the case $k_3'C^{n_3'} << k_5'C^{n_5'}$, the defect density will be controlled by the competition between steps 4' and 5'.

In the high temperature case where $k_3'C^{n_3'} << k_5'C^{n_5'}$, the defect density will be controlled by the competition between steps 4' and 5' and the model yields:

$$\ln\left(\frac{I_G}{I_D}\right) = A'_{HT} - \frac{E'_{HT}}{kT} + n'_{HT} \ln\frac{P}{P_0}$$

$$\text{with } A'_{HT} = \ln\left(K\frac{k_4^{0\,\prime}}{k_5^{0\,\prime}}\right),\ E'_{HT} = E_4' - E_5' + n'_{HT}\,\Delta_r G_1 \text{ and } n'_{HT} = \frac{n_4' - n_5'}{n_1}.$$

In the low temperature case where $k_3'C^{n_3'} >> k_5'C^{n_5'}$, the defect density will be governed by the competition between steps 4' and 3' and the model leads to:

$$\ln\left(\frac{I_G}{I_D}\right) = A'_{LT} - \frac{E'_{LT}}{kT} + n'_{LT} \ln\frac{P}{P_0} \qquad (k')$$

$$\text{with } A'_{LT} = \ln\left(K\frac{k_4^{0\,\prime}}{k_3^{0\,\prime}}\right),\ E'_{LT} = E_4' - E_3' + n'_{LT}\,\Delta_r G_1 \text{ and } n'_{LT} = \frac{n_4' - n_3'}{n_1}.$$

Since the model is based on $E_3' < E_5'$, it follows that $E'_{HT} < E'_{LT}$ and that model C corresponds to a convex Arrhenius. But, since $\triangle_g G_1$ is negative (*i.e.* the precursor decomposition is thermodynamically favoured) and the model imposes that $E_5' > E_4' > E_3'$, it follows that the apparent activation energy at high temperature will be negative. In other words, this model intrinsically leads to a decrease of I_G/I_D in the high temperature regime which disagrees with the slow increase experimentally observed.

It follows from this analysis that only model B can qualitatively account for the experimental dependence of I_G/I_D. The model was used to fit the experimental dependences of I_G/I_D as a function of the temperature (all systems) and precursor pressure (ethanol-nickel). As illustrated in Figure 3-12, Figure 3-13 and Figure 3-33, an excellent agreement is found with the experimental data. The obtained parameter values are summarized below in Table 3-2 and Table 3-3. The threshold temperature T_D varies from 600-680°c for the Ni/SiO_2 catalyst to 700°C for Co/SiO_2. The activation energy is in the range of 0.1-0.7 eV in the high temperature regime and of 1.1-3.5 eV in the low temperature regime.

Couple	E_{HT} (eV)	E_{LT} (eV)	n_{HT}	n_{LT}	A_{HT}	A_{LT}	Threshold temperature T_D (°C)
Ni – ethanol	0.32 (+/- 0.06)	1.3 (+/- 0.1)	-0.32 (+/- 0.02)	-0.54 (+/- 0.03)	5.0 (+/- 0.7)	16 (+/- 1)	680

Table 3-2. Fit parameters of the temperature and precursor pressure dependences of I_G/I_D for the nickel-ethanol couple.

Couples	E_{HT} (eV)	E_{LT} (eV)	Threshold temperature T_D (°C)
Ni – methane	0.7 +/- 0.1	1.5 +/- 0.4	625
Ni - ethanol	0.32 +/- 0.06	1.3 +/- 0.1	
Ni – ethylene	0.3 +/- 0.1	1.4 +/- 0.1	625
Ni – acetylene	0.4 +/- 0.1	2.3 +/- 0.1	600
Co – ethanol	0.4 +/- 0.1	1.1 +/- 0.1	700
Co – acetylene	0.1 +/- 0.1	3.5 +/- 0.1	700

Table 3-3. Apparent activation energies at high growth temperatures (E_{HT}) and low growth temperatures (E_{LT}) for the different precursor-catalyst couples.

3.6.6 Conclusion

Carbonaceous impurities are common by-products of SWCNT growth by CCVD. During our investigations, we evidenced three types of carbonaceous impurities.

The first type is pyrolytic carbon issued from the self-decomposition of the carbon precursor molecules in the gas phase. The formation of pyrolytic carbon is highest at high temperature and high precursor pressure. During *in situ* Raman measurements, it manifests by a slow decrease of the signals of SWCNT and of the oxide support (due to the high optical absorption of pyrolytic carbon) and by an increase and broadening of the D band (due to its high defectiveness). In post-growth Raman spectra, it is characterized by a very broad D band (FWHM of ~120 cm^{-1}).

The second type is made of defective multi-walled filaments and shells that grow from large catalyst particles. During our investigations, they constituted the main carbonaceous impurities of the samples grown with the Co/SiO_2 catalyst. Their formation is favoured at low temperatures and high precursor pressure. In post-growth Raman spectra, they manifest by a broad multi-peak structure on the high-frequency side of the D and G' bands.

The third type is constituted by short crumpled single-layer carbon structures that grow from small catalyst particles. During our investigations, they constituted the main carbonaceous impurities of the samples grown with the Ni/SiO_2 catalyst. Their formation is favoured at low temperatures and high precursor pressure. In post-growth Raman spectra, they manifest by a broad band on the high-frequency side of the D and G' bands.

From the results of §3.4.2, the difference of carbonaceous impurities between the Ni and Co catalyst clearly originate from their different coarsening during the calcination pre-treatment: calcination of Co/SiO_2 led to the formation of large oxide particles (up to 10 nm) while the surface roughness of Ni/SiO_2 was slightly modified.

The D and G' bands displays systematic and correlated behaviours as a function of the growth conditions. The observation that the D and G' bands downshift and narrow with increasing temperature and increasing precursor pressure is qualitatively explained by the contamination of the samples by multi-walled and/or short crumpled single-walled carbon structures characterized by high-frequency D and G' features. In favourable cases, these high-frequency contributions can be deconvoluted from the low-frequency contributions of SWCNTs. Since the D band of a SWCNT downshifts with decreasing diameter, the contributions of each RBM bunch to the D and G' bands can be resolved if RBMs are

sufficiently separated. This approach may potentially be used for an experimental determination of the dependence of the (D,G') frequencies on the nanotube diameter.

The convex shape of the I_G/I_D Arrhenius plot cannot be explained by a thermally-activated process of defect annealing or defect formation. However, it can be accounted for by a change of the intermediate state controlling the integration of carbon atoms in the nanotube core. The nature of this change (*e.g.* a change of physical or chemical state of the catalyst particles) is now investigated by surface characterization techniques. From the model, the measured activation energy can be understood as the difference of energy barriers between the integration into a well-ordered sp^2 lattice and the formation of a lattice defect. In the high-temperature state and for SWCNTs, this energy barrier is measured to be of the order of 0.1-0.7 eV. In the low-temperature state, the activation barrier is much higher (~1-3.5 eV) which causes a decrease of crystalline quality of the carbon structures with decreasing temperature.

In addition to this dramatic loss of crystalline quality, we previously noted that growth temperatures below the transition temperature T_D are also marked by an exponential decrease of the SWCNT yield as characterized by the G-band intensity. The next part is devoted to determining how the SWCNT yield is influenced by the kinetics of growth and deactivation.

3.7. Kinetics of SWCNT growth and deactivation

3.7.1 Introduction

The growth kinetics of CNT forests has been investigated by several groups using both *ex situ* and *in situ* approaches. Experimentally, the growth kinetics of CNTs is characterized by a self-exhausting process expressed by the differential equation $d^2L/dt^2 = -1/\tau \cdot dL/dt$ or, after integration, $L(t) = \upsilon\tau\,(1-\exp(-t/\tau))$, where L(t) represents the nanotube length at time t, υ the initial growth rate and τ the characteristic time of deactivation (*i.e.* the lifetime) [312-314]. This kinetic behaviour is illustrated in Figure 3-44a. On a conceptual point of view, this relation can be obtained when two consecutive steps of a reaction are coupled by a secondary process. The dependence of υ reflects the variations of the rate-determining step of the reaction while the lifetime informs about the secondary deactivating process. In certain cases, an induction period [367] or an initial stage of exponential increase [311] is also observed. Geohegan *et al.* studied the growth kinetics of vertically aligned CNTs by *in situ* reflectivity measurements. They found that, at low temperature, the initial growth rate increases with increasing temperature then rapidly decreases above an optimal temperature [424]. However, the evolution of the lifetime was poorly characterized.

To account for this behaviour, Puretzky *et al.* [313] proposed a model for the growth of a CNT sitting on a metal particle. They proposed that the rate determining step of nanotube growth is the supply of carbon atoms to the surface (noted F and which includes both the gas phase diffusion and the precursor decomposition) and that the deactivating process is the formation of a carbonaceous layer which progressively decreases the surface of the catalyst particle. A main aspect of this model is that growth and deactivation are both driven by the carbon supply of the catalyst surface, which mathematically means that, in the steady state, υ and τ are coupled by F as apparent in the following relations.

$$\upsilon \approx \frac{F}{z} \quad , \quad \tau \approx \frac{\alpha S n}{F}\,\frac{k_g}{k_d}$$

where k_g is the kinetic constant of the nanotube growth, k_d the kinetic constant of formation of the encapsulating layer, z is the number of walls of the nanotube, α the number of walls of the

deactivating layer, S the surface area of the particle and n the surface density of a monolayer of carbon. This model yields that the initial growth rate exponentially increases and the lifetime exponentially decreases with increasing temperature. The terminal length $L(\infty)=\upsilon\tau$ would also exponentially increase with temperature with an apparent activation energy equal to E_g-E_d but should display very little dependence on the precursor supply. Obviously, this model could only account for the low temperature regime of CNT growth. In addition, the proposed model gives no explanation for the transition from MWCNTs to SWCNTs observed by the authors with increasing temperature [424].

The Puretzky model describes the elongation rate of one nanotube as a function of the growth conditions. When studying the growth of an ensemble of CNTs, one has to keep in mind that the nanotube yield also depends on the number of active catalyst particles which can significantly change with the growth conditions and potentially with time. As shown in §3.4, the reduction of the catalyst particles by the carbon precursor is the main activation requirement in our experimental conditions. The redox properties of metal nanoparticles are significantly dependent on their size and interaction with the oxide support [429]. As apparent on Figure 3-43, the reduction rate of oxide nanoparticles frequently displays a sigmoid shape at low temperature and low reducer pressure.

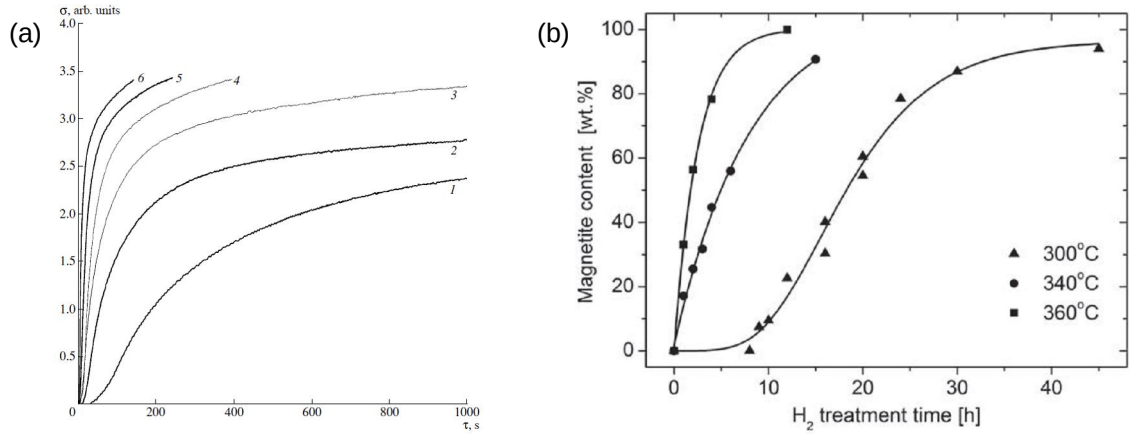

Figure 3-43. Kinetics of reduction of CoO particles supported on SiO_2 at various hydrogen partial pressures: (1) 0.6, (2) 2.5, (3) 5, (4) 18, (5) 30, and (6) 100% H_2 monitored my magnetization . From [429]. (b) Conversion of nanoparticles into magnetite as a function of the treatment time at different temperatures. From [430].

The Avrami equation is commonly used to fit such kinetics of solid-state phase transformation [430]:

$$f = 1 - \exp(-\beta^n)$$

with $\beta = k_0 t \exp(-E_a / kT)$ for isothermal conversion and n a phenomenological parameter characterizing the number of growth dimensions and the growth mode. If coupled with the model of CNT growth of Puretzky, an induction phase becomes apparent at the first stage of nanotube growth (Figure 3-44b). If one considers two populations of catalyst nanoparticles characterized by slightly different activation energies, the kinetic curve of nanotube growth will appear as the superposition of two sigmoids (Figure 3-44c). The Avrami equation can also be used to model the deactivation of catalyst particles caused by a phase transformation. In such a case, the nanotube growth kinetics will display a more abrupt termination than expected from the Puretzky model alone (Figure 3-44d). Other cases may also be envisaged such as the deactivation of two populations of particles with different activation energies, the decrease of one particle population and increase of another (*e.g.* Ostwald ripening), a fast activation followed by a slow deactivation, etc.

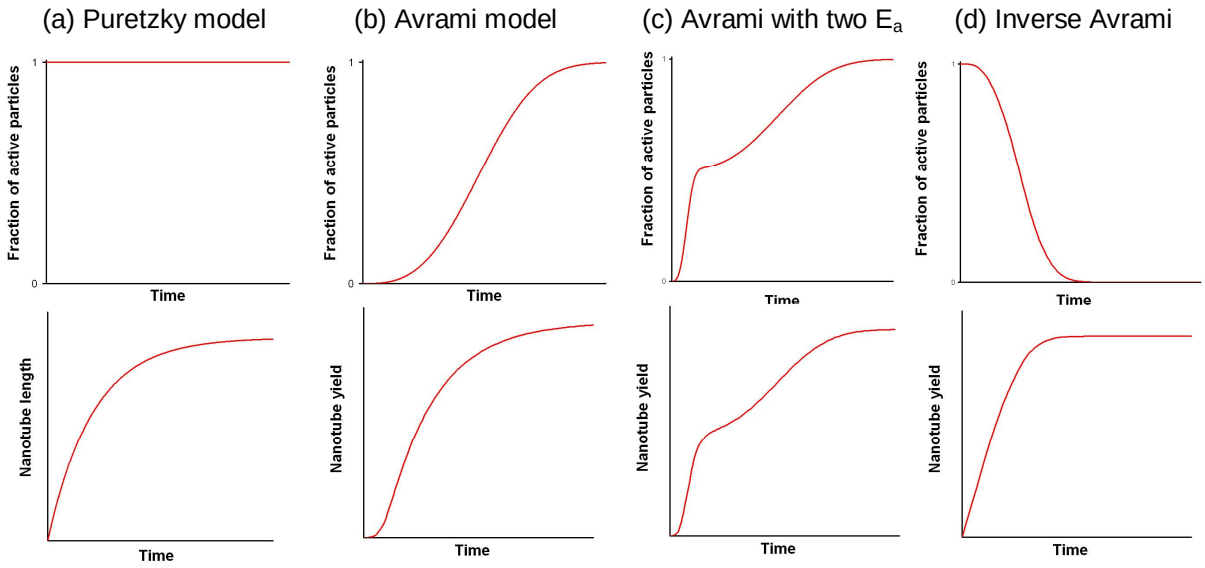

Figure 3-44. Illustration of different kinetic models of nanoparticle activation/deactivation associated with nanotube growth.

3.7.2 Methods

In situ Raman measurements were performed at a laser wavelength of 532 nm and laser power of 12 mW (spot size of ~ 1µm), which prevented from substrate heating by the laser beam. As shown in Figure 3-45a, the G band of SWCNTs appears in the Raman spectra between 1560 and 1580 cm^{-1}. The peak position is down-shifted when increasing the synthesis temperature due to the softening of the C-C bonds. In the extreme limits of the parameter range, growth kinetics could not be recorded or exploited because of a too weak signal or a too short growth (shorter than a few seconds).

From SEM observations (§3.3.1), the nanotube thickness of the samples is of the order of 10-50 nm As a consequence, it can be considered that (1) the measured Raman intensity is directly proportional to the amount of SWCNTs and (2) that the feedstock diffusion resistance is negligible.

Kinetic curves were obtained by integrating the surface area of the G band as a function of time. Typical kinetic curves are shown in Figure 3-45b. One can observe a progressive decrease of the nanotube growth rate until complete termination of the growth. We found that the vast majority of kinetic curves were well fitted by the relation $G(t) = \upsilon\tau(1-\exp(-t/\tau))$ of the Puretzky's model I.

In a few cases, an induction phase was apparent in the recorded kinetics. The origin of this induction phase is discussed hereafter. To allow comparisons with the other growth conditions and to keep a fitting model with a reasonably small number of parameters, the kinetic curves were fitted in such cases by the adapted relation $G(t) = \upsilon\tau(1-\exp(-(t-\delta)/\tau))$ where δ correspond to the time shift caused by the induction phase.

For quantitative comparison of different sets of data, the intensity of each spectrum was normalized to that of the reference peak of the silicon support at 521 cm^{-1}. In addition, to account for the temperature variation of the Raman intensity, each spectrum was normalized to the corresponding room temperature intensity. The temperature calibration curve was obtained by measuring in the same conditions (λ=532 nm) the G-band intensity of Hipco SWCNTs under argon at different temperatures from 900°C to 23°C (see Figure 3-4b).

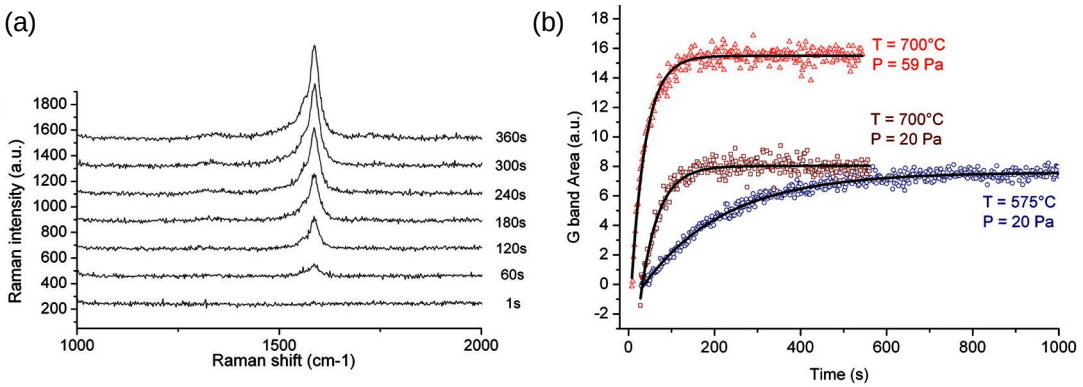

Figure 3-45. (a) Raman spectra recorded at different times during an *in situ* CCVD experiment (acquisition time: 1s, temperature: 575°C, ethanol partial pressure: 20 Pa). (b) Temporal evolution of the G band area for different growth conditions. The data are fitted by G(t) = υτ(1-exp(-t/τ)) (solid lines).

3.7.3 Features and attribution of the G band

From the results of section 3.6, it is clear than SWCNT samples can contain other carbonaceous by-products whose structure and abundance depend on the type of catalyst and on the growth conditions. This is most notable in the case of samples grown at low temperature which display particularly abundant carbonaceous by-products (short crumpled carbon structures in the case of Ni/SiO_2 and large diameter MWCNT structures for Co/SiO_2). An important question is how much do these carbonaceous by-products contribute to the G-band of each sample? For the D and G' bands, we showed that the relative contributions of each species could be resolved thanks to the diameter and stacking dependence of these modes. However, the G band is much less dependent on the diameter and stacking. CCVD-grown MWCNT commonly display a broad and featureless G-band at ~1580 cm^{-1} (Figure 3-46a). However, this G-band stands just in between the G^+ and G^- contributions of SWCNTs. In addition, for very defective samples, the contribution of the D' band which appears as a shoulder at around 1620 cm^{-1} is no more negligible. Defective graphene displays a narrow featureless G peak at 1580 cm^{-1}. With increasing defect density, the G and D′ bands widen and start to overlap. If a single lorentzian is used to fit the G and D′ bands, this results in an apparently upshifted and broad G band at ~1600 cm^{-1}. In both cases, it is apparent that for such defective materials, the D band intensity is generally of the order or even higher than that of the G band. Contrary to SWCNTs, the Raman scattering of these materials is not enhanced by the resonance effect.

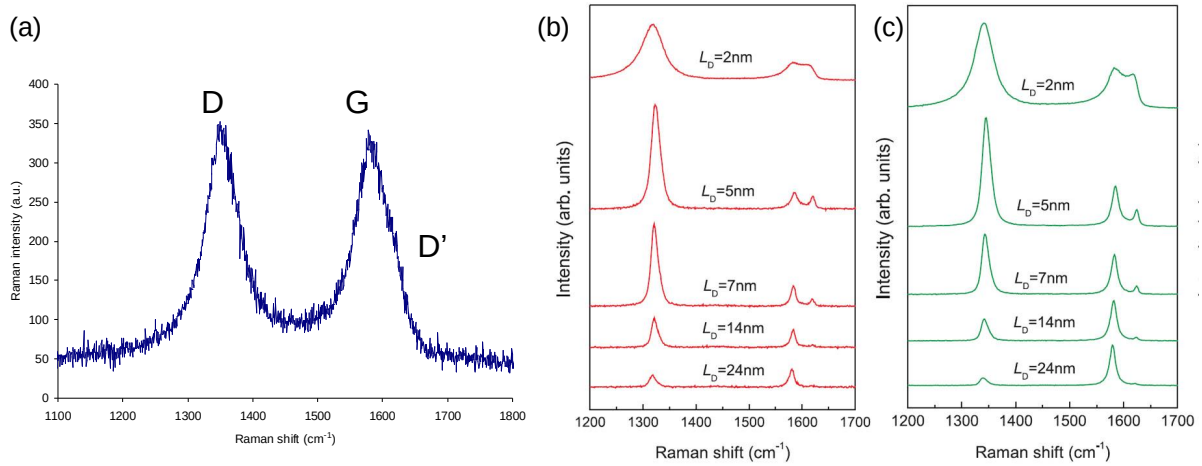

Figure 3-46. Reference Raman spectra of CCVD-grown MWCNTs at 514 nm (a) [431] and of ion-bombarded graphene at 633 nm (b) and 514 nm (c) for decreasing distance L_D between defects [432].

As a consequence, the G band frequency of SWCNT samples is little affected by the contributions of carbonaceous by-products. All our samples display a G^+ band at *circa* the same position of 1590-1595 cm^{-1} and G^- shoulders at 1540-1570 cm^{-1}, which are both typical features of SWCNTs. A better criterion is probably constituted by the fwhm of the main G^+ mode. In the case of a HipCo SWCNT sample taken as reference, this fwhm was measured to be of the order of 16 cm^{-1}. A comparable fwhm was measured for all samples grown with Ni-EtOH and Ni-CH_4 (fwhm~17 cm^{-1}) and to a lower extent with Ni-C_2H_4 (fwhm ~ 21 cm^{-1}). This value remains constant whatever the growth temperature of the sample. For these samples, the G band can be considered as essentially made of SWCNT contributions.

For Co-EtOH, the three samples grown at the lowest temperatures display a broad G band (fwhm from 75 to 25 cm^{-1}) which could be related to the high intensity of the D' band, although other contributions cannot be ruled out. Other Co-EtOH samples have G band fwhm of the order of 21-22 cm^{-1}. For Ni-C_2H_2, the two samples grown at the lowest temperatures display broad G bands with fwhm of 50-25 cm^{-1} which is much broader than the Ni-EtOH samples displaying a comparable G/D ratio. Other Ni-C_2H_2 samples have G-band fwhm of the order of 21-22 cm^{-1}. Since these large fwhm values signal a significant contribution of carbonaceous by-products to the G band, these five samples (blue circles in Figure 3-48d-e) are to be excluded from our discussion on the kinetics of SWCNT growth.

3.7.4 Results and discussion

- *Precursor pressure dependence*

The evolution of the initial growth rate ν and of the lifetime τ as a function of the precursor partial pressure is shown in Figure 3-47 for the system nickel-EtOH at 575°C and 800°C. The evolution of the product $\nu\tau$ which corresponds to the terminal yield (or terminal intensity of G) in the Puretzky model is also shown together with a reminder of the Raman data acquired post-growth. Two different regimes are observed. (i) At low partial pressures, ν increases and τ decreases proportionally to the partial pressure. (ii) Above a threshold partial pressure, ν and τ become independent of the partial pressure. This behaviour is observed at both high (800°C) and low (575°C) temperatures with the only difference that the threshold occurs at a lower partial pressure at lower temperature. A similar evolution of the initial growth rate with the precursor partial pressure was reported by Einarsson *et al.*[314].

Such features are in qualitative agreement with the Puretzky model since ν and τ are expected to display opposite evolutions with the precursor supply which is included in the term F. However, ν and τ do not display opposite values of reaction orders as expected from the model: ν and τ respectively have reaction orders of 0.6 and -0.9 at 575°C, and of 1.4 and -1.1 at 800°C. As a consequence, the product $\nu\tau$ (*i.e.* the nanotube yield) displays a significant dependence on the precursor pressure. This is contrary to Puretzky's model which stipulates that the yield should be largely independent of the precursor supply. The only domain where $\nu\tau$ could be considered as relatively constant is in the intermediate pressure range at 800°C. For higher and lower pressures, $\nu\tau$ decreases. At 575°C, $\nu\tau$ displays a power law dependence with P with a slope of -0.39.

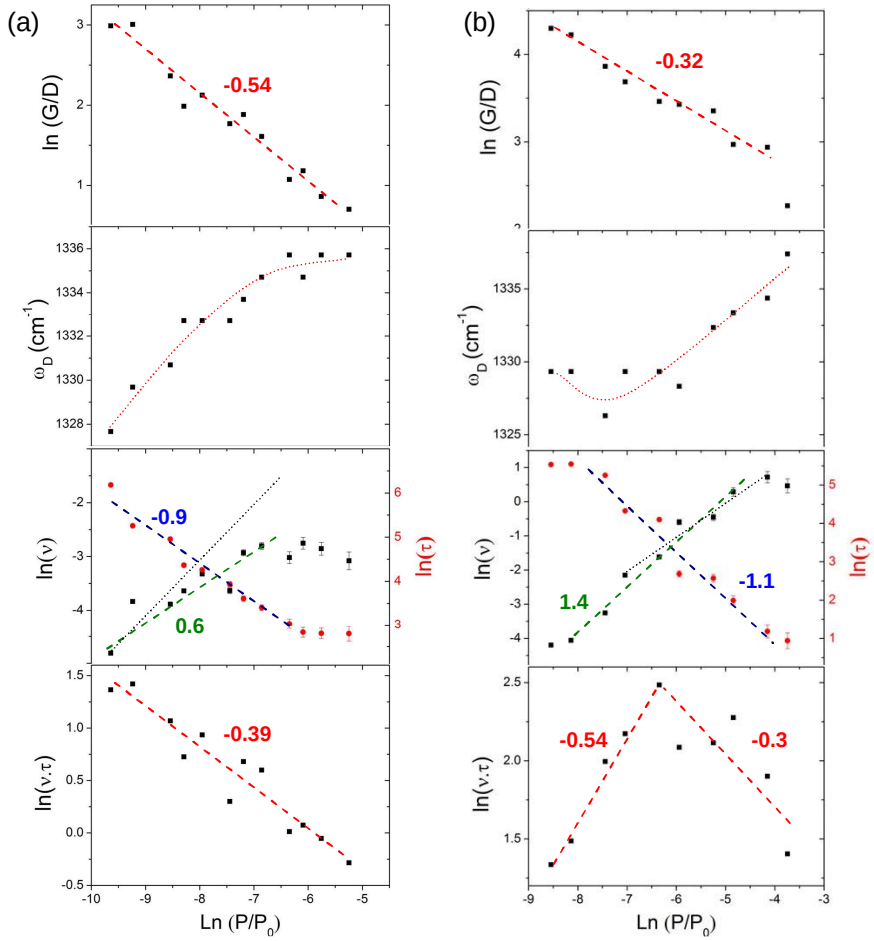

Figure 3-47. Kinetic data from *in situ* Raman measurements and structural data from post-growth Raman measurements as a function of ln (P/P_0) for Ni-EtOH at 575°C (a) and 800°C (b): G-band intensity, G/D ratio, D-band position, initial growth rate ν, lifetime τ and their product ν τ. The excitation wavelength is 532 nm. The dotted line in the ν plot illustrates the hypothetical case of a reaction order equal to 1.

How to explain this discrepancy with the model of Puretzky? The major difference between our experimental situation and the situation modelled by Puretzky is that our measurements are sensitive to the total amount of SWCNTs and not to their length. In other words, our measurements are additionally affected by the surface density of active particles under the laser spot. If one looks to the evolution of RBMs with the precursor pressure (Figure 3-9), it is apparent that the drop in yield is well correlated with a drop in the formation of small-diameter SWCNTs. In §3.5, the lack of small-diameter SWCNTs at too high precursor pressure was attributed to the encapsulation of the smallest particles by disordered carbon structures. If this process would cause the fraction of active particles to display an apparent reaction order of 0.3-0.4 with regard to ethanol, this would account for the discrepancy between the experimental data and the Puretzky's model. If one applies this correction, it leads to a reaction order for the initial growth rate close to 1 which is the expected value for the unimolecular reaction of ethanol decomposition (see dotted lines in the ν plots of Figure 3-47).

How to explain the apparent stagnation of ν and τ above a threshold pressure? If we keep on the same line of reasoning, it means that the decrease in the number of active particles stops to be partially compensated by the increase of precursor flux at the catalyst surface. This is expected to happen when the catalyst surface becomes saturated. In other words, the threshold pressure would correspond to a transition in the carbon supply from a low-pressure regime limited by the gas-phase diffusion of precursor molecules at low pressure

to a high-pressure regime limited by the surface availability and the kinetics of surface processes (dissociative adsorption, desorption). This transition between a diffusion regime and a surface regime is commonly observed in thin film growth and heterogeneous catalysis. When increasing the temperature, the transition occurs at higher pressure when the temperature is increased since surface processes are thermally activated contrary to gas-phase diffusion. This agrees well with our experimental observation of a higher threshold pressure at higher temperature. This transition should also be apparent in the temperature dependence of ν. However, this regime transition should not lead to an apparent stagnation of ν but actually to a decrease of ν since the number of active particles would keep decreasing with increasing pressure. However, the present data for ν at high pressure are insufficient to confirm this prediction.

This kinetic study additionally explains why there is an optimal pressure whose value increases with increasing temperature (§3.3.3). This optimal pressure corresponds to the activation of the highest number of particles (*i.e.* of small ones as attested by the RBM profiles) at a given temperature. From §3.5.4, the density of active particles decreases at high pressure because of the encapsulation of the smallest particles by carbon species. At lower pressure, small particles are either not reduced (intermediate temperature case) or disappear too rapidly by coarsening. With increasing temperature, the encapsulation rate decreases which allows the use of higher precursor pressures. However, the increase of coarsening rate with temperature prevents the use of low precursor pressures. This combined effects results in an overall shift of the optimal pressure range with increasing temperature.

- *Temperature dependence*

Figure 3-48 shows the evolution of the initial growth rate ν and of the lifetime τ against the inverse growth temperature for five different systems: Ni-EtOH, Ni-C_2H_4, Ni-CH_4 and Co-EtOH. The evolution of the product $\nu\tau$ is also shown together with a reminder of the Raman data acquired post-growth. One can observe that the change of behaviours previously observed for G/Si at the two transition temperatures T_L and T_H are also correlated with evolution changes for ν and τ. These evolutions are discussed for each temperature domain.

Kinetics of SWCNT growth below T_L

From the pressure dependence study at 575°C, this temperature regime is characterized by a strong deactivation of the catalyst particles caused by an excessive carbon supply. This conclusion is corroborated by HRTEM observations and by the strong signatures of defective carbon structures in the Raman spectra (low G/D) at these temperatures. Such a deactivation mechanism comes into the frame of the Puretzky's model. At the lowest temperatures, the growth kinetics is characterized by an exponential increase of ν and an exponential decrease of τ with increasing temperature. Such features are expected from the Puretzky's model since ν are respectively proportional and inversely proportional to the carbon supply *F*. If the carbon supply is controlled by the dissociative adsorption of the precursor (*i.e.* surface regime), *F* is expected to increase with increasing temperature.

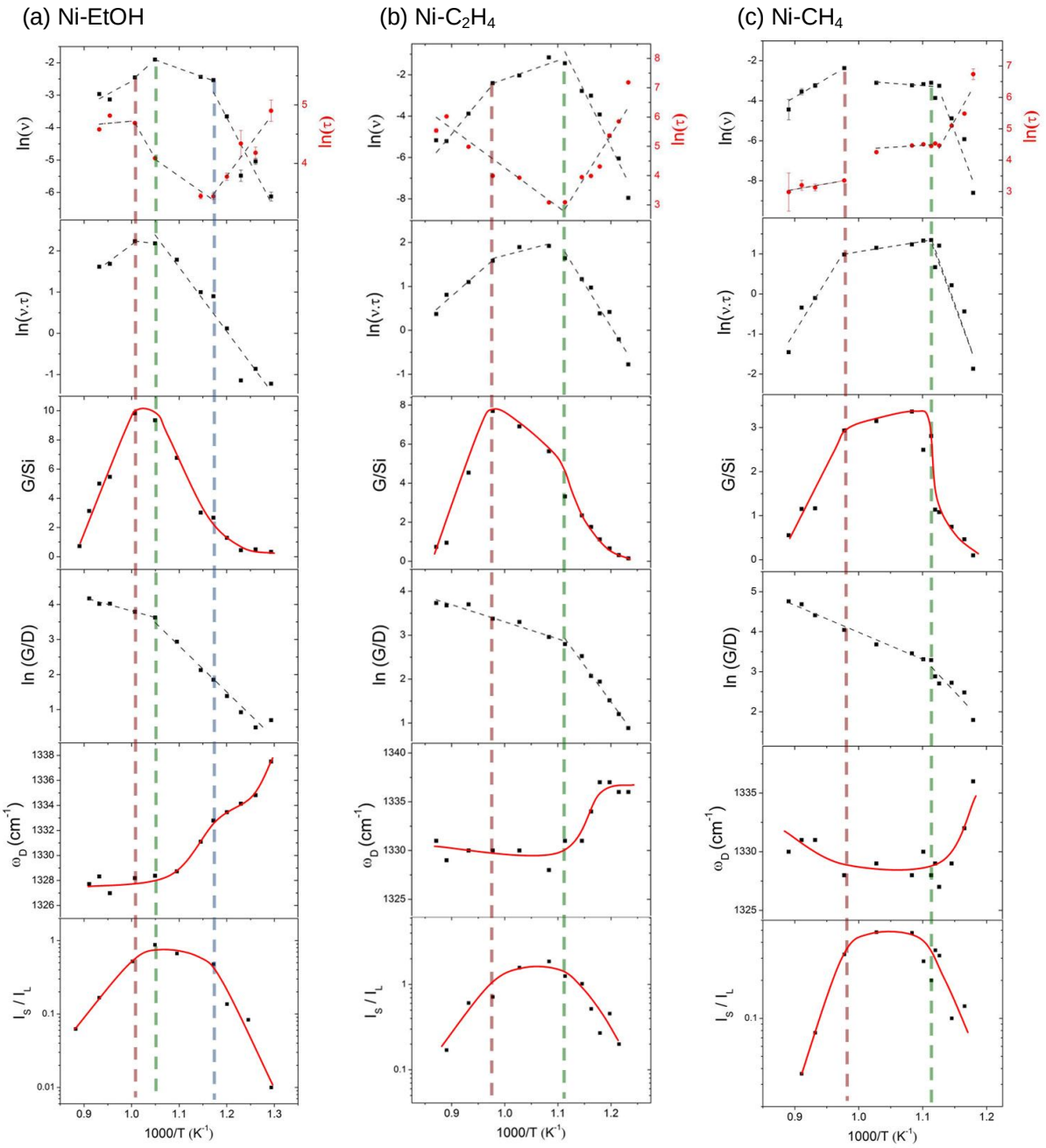

Figure 3-48. Kinetic data from *in situ* Raman measurements and structural data from post-growth Raman measurements as a function of the inverse growth temperature for five different systems: initial growth rate ν, lifetime τ, G-band intensity, G/D ratio, D-band position, ratio of small- (ω>250 cm^{-1}) over large-diameter (ω<250 cm^{-1}) RBMs. The excitation wavelength is 532 nm.

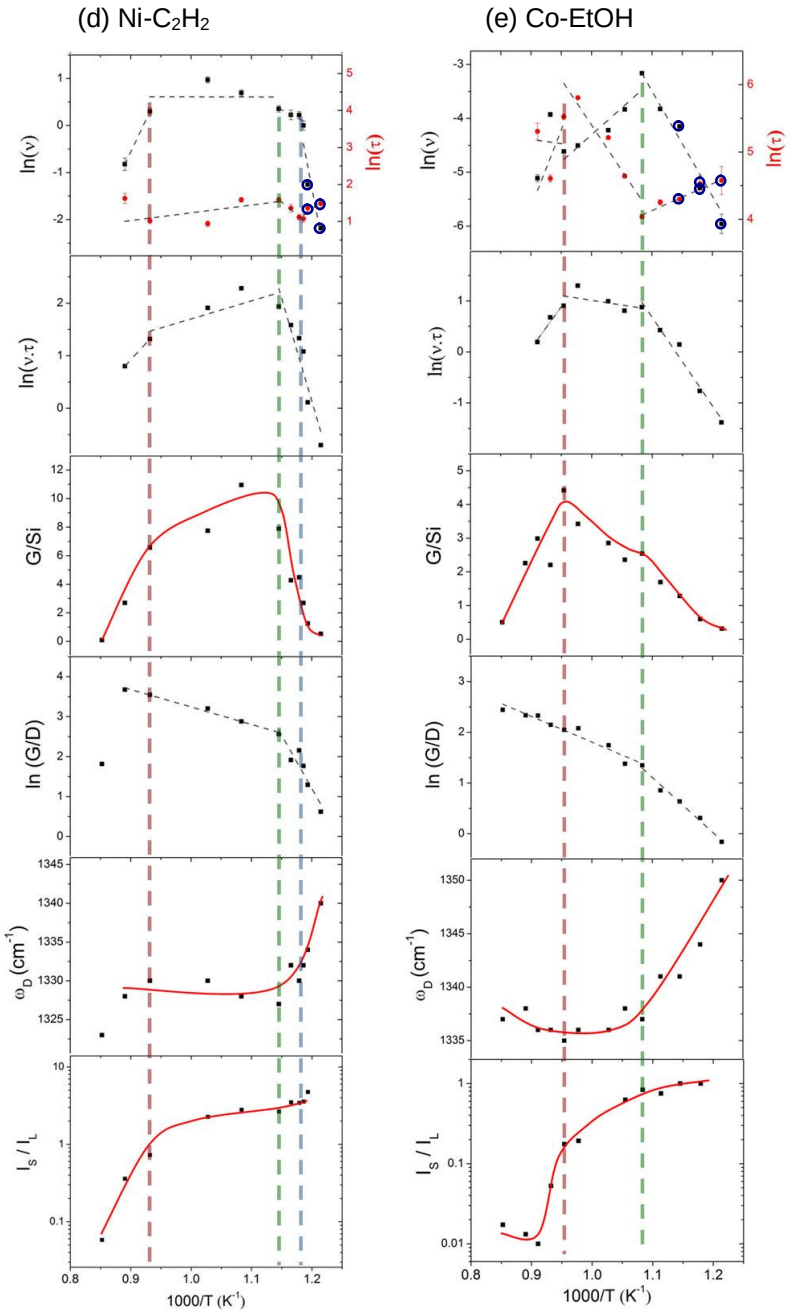

Figure 3.48 (continued). Kinetic data from *in situ* Raman measurements and structural data from post-growth Raman measurements as a function of the inverse growth temperature for Ni-C_2H_2 and Co-EtOH: initial growth rate ν, lifetime τ, G-band intensity, G/D ratio, D-band position, ratio of small- (ω>250 cm^{-1}) over large-diameter (ω<250 cm^{-1}) RBMs. The excitation wavelength is 532 nm, except for the post-growth data of Co-EtOH for which λ=514 nm. The open blue circles correspond to G bands too broad to be assigned to SWCNTs only (see 3.7.3).

Following this line of reasoning, the activation energy of ν should be attributed to the activation energy for the dissociative adsorption of the carbon precursor. The measured activation energies of ν are 2.4 eV for Ni-EtOH, 4.5 eV for C_2H_4-Ni, 5 eV for CH_4-Ni, 1.7eV for Co-EtOH and 6 eV for C_2H_2-Ni (see Table in Annex 2). These values are generally higher than those theoretically expected for each system [82,433,434]. In the frame of the Puretzky's model, the activation energy of τ corresponds to a composite of activation energies of three steps making it difficult to discuss. The measured values are -0.9 eV for Ni-EtOH, -2.5 eV for C_2H_4-Ni, -2.1 eV for CH_4-Ni, -1 eV for C_2H_2-Ni and -0.34 eV for Co-EtOH. Interestingly, the activation energy of F vanishes if one considers the product ντ whose activation energy should be the difference of activation energies between the integration of carbon in the nanotube and in the deactivating layer. The measured values for ντ are 1.3 eV for Ni-EtOH, 1.7 eV for C_2H_4-Ni, 3.7 eV for CH_4-Ni, 3.4 eV for C_2H_2-Ni and 1.7 eV for Co-EtOH. These values should be intrinsic to the carbon-metal interaction and should therefore not be significantly dependent on the precursor type or pressure. At first sight, this is not the case. If some points at the lowest temperatures are omitted, the agreement improves noticeably with activation energies of 2.8 eV for CH_4-Ni, 1.7 eV for C_2H_2-Ni, 1.5 eV for C_2H_4-Ni, 1.3 eV for Ni-EtOH, and 1.4 eV for Co-EtOH. The Puretzky's model therefore gives a good qualitative agreement with the measured and a correct quantitative agreement if some of the lowest temperature points are omitted. The major disagreement is the too high activation energies of ν.

In line with the discrepancies with the Puretzky's model observed for the pressure dependence, it is proposed that the present discrepancies also originate from an evolution of the fraction of active particles. The low-temperature regime is actually marked by a lack of small-diameter SWCNTs (low I_S/I_L) for most systems. This lack is not apparent for Ni-C_2H_2 and Co-EtOH but, at these temperatures, these systems produce copious amounts of carbonaceous impurities (see 3.6 and 3.7.3) making difficult the determination of the SWCNT behaviour. This hypothesis is additionally supported by the fact that low temperature growths frequently display an induction phase. This induction phase is not possible with the Puretzky's model but is theoretically obtained if a progressive increase of the number of active particles is considered (see Avrami model in Figure 3-44b). The CH_4-Ni system is characteristic of this low temperature behaviour (Figure 3-49). It is apparent on Figure 3-49b that this induction phase is associated with the reduction of the metal oxide particles by the carbon precursor. This effect could explain the low ν values measured at the lowest temperatures.

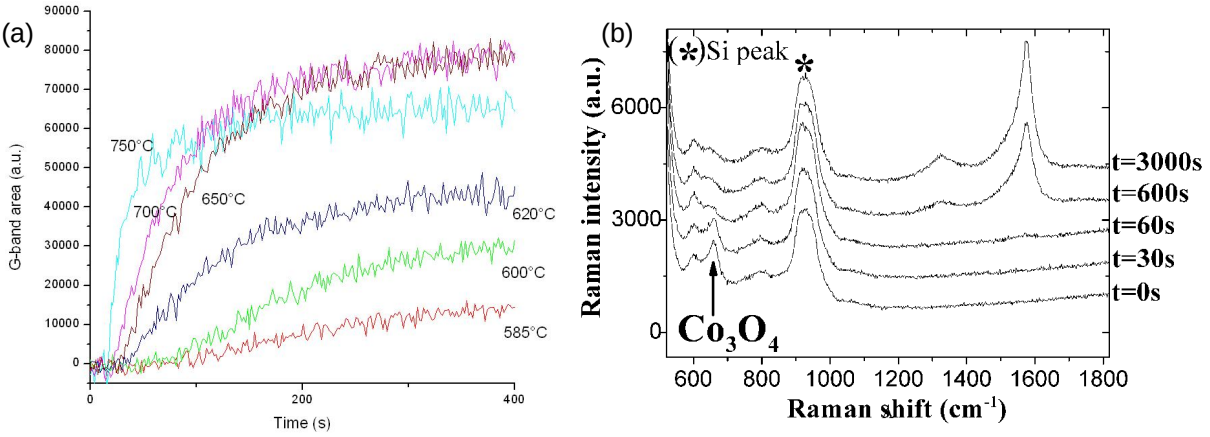

Figure 3-49. (a) Growth kinetics of SWCNTs for the Ni-CH_4 system at different temperatures. The atmosphere is pure methane. (b) Raman spectra for the couple Co-CH_4 showing that the induction phase is associated with the reduction of the metal oxide particles by methane.

In the particular case of the Ni-EtOH system, a change of evolution of ν and τ is additionally observed at 580°C (see blue dashed line in Figure 3-48a): ν stops increasing and stagnates while τ stops decreasing and starts increasing. This change has no consequence on the evolutions of G/Si or G/D with temperature. Similarly to the change of evolution in the precursor pressure dependence, this change can be interpreted as a change in the kinetics of carbon supply from surface–controlled (below 580°C) to diffusion-controlled (above 580°C). In the Puretzky's model, that would correspond to a constant value of F in the diffusion-controlled regime. This does not modify the previous interpretation of the regime below T_L but adds to the complexity of the possible phenomena in this temperature domain.

Kinetics of SWCNT growth above T_H

At the highest temperatures, the SWCNT growth displays a strong decrease of the yield. Growth kinetics shows that this drop is primarily caused by a decrease of ν and, to a lower extent, by a decrease or inflexion of τ (Figure 3-48). The G/D evolution is not modified which rules out the hypothesis of deposition of disordered carbon species (*e.g.* pyrolytic carbon). By contrast, the regime is systematically marked by a strong decrease of the fraction of small-diameter SWCNTs in the RBM profile. Many kinetic curves display a more abrupt termination (which makes them more difficult to fit with the Puretzky's model). Such a profile modification is theoretically expected if the growth is concomitant with a decrease of the number of active particles (see for instance the inverse Avrami model in Figure 3-44d). A few kinetic curves display a re-increase of the growth rate after a long time. This effect is theoretically expected if a population of particles is converted into another or if a fraction of particles has slower kinetics of activation (see Figure 3-44c). In any case, both phenomena are signatures of a significant restructuring of the catalyst particles during SWCNT growth in this high-temperature range.

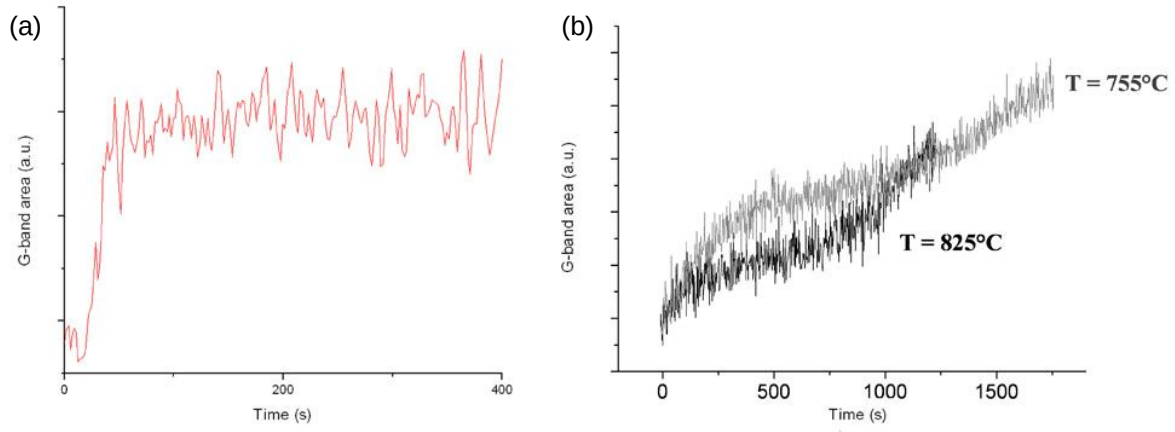

Figure 3-50. (a) G-band kinetics for the CH_4-Ni system at 800°C. (b) G-band kinetics for the EtOH-Co system at 755 and 825°C.

To confirm this hypothesis, we submitted a Ni catalyst to different pre-treatments in this high-temperature range (Figure 3-51) before performing a standard growth (T = 675°C, P_{EtOH} = 59 Pa). If the standard pre-treatment (ramp under O_2 followed by 5 min under Ar) is performed at 860°C instead of 700°C, the profile and overall intensity of the Raman spectra of the grown samples remain unchanged. However, if a small amount of EtOH (10 Pa) is added during the Ar pre-treatment at 860°C, the yield of the subsequent growth is dramatically reduced. This is accompanied by the disappearance of the smallest-diameter SWCNTs in the

RBM profile. These results confirm that the catalyst undergoes a significant restructuring at high temperature in presence of reducing species such as ethanol.

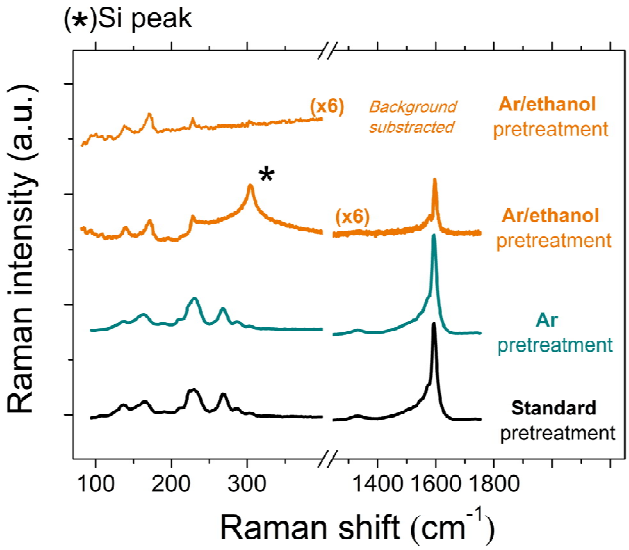

Figure 3-51. Evolution of the Raman spectra of samples grown at 700°Cwith Ni-EtOH as a function of the pre-treatment conditions. From bottom to top: standard pre-treatment at 700°C under O_2 followed by 5 min under Ar), pre-treatment at 860°C under O_2 followed by 5 min under Ar, (without and with subtracted silicon background).

To assess the nature of the catalyst restructuring, we used a transfer technique based on SiO_2 etching to directly transfer the grown materials to TEM grids. However, our TEM investigations did not reveal a more important fraction of large catalyst particles in the high-temperature samples compared to the low-temperature ones. Since the sample preparation technique did not preserve the interface with the SiO_2 support, this may be the sign that the catalyst restructuring corresponds to a reaction with the SiO_2 support (*e.g.* silicate or silicide formation). In a preliminary study, we actually performed growths directly on TEM grids made of a thin SiO_x layer. As shown in the TEM picture in Figure 3-52, Ni nanoparticles displayed a strong interfacial reactivity with the SiO_x support when exposed to ethanol at high temperature. This suggests that the same phenomenon may be at play for the Ni and Co particles supported on plain SiO_2/Si used for our growth kinetic studies. The use of sample preparation techniques preserving the interface with the SiO_2 support should allow addressing this question.

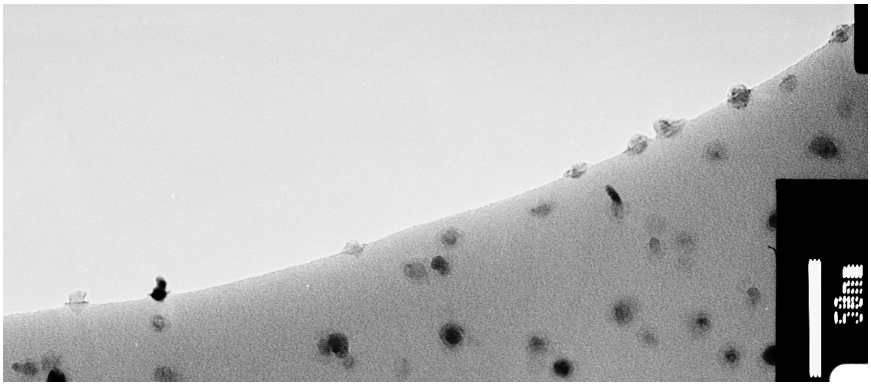

Figure 3-52. TEM picture of Ni nanoparticles on a SiO_x TEM grid after a high-temperature treatment under ethanol. The SiO_x films were annealed under O_2 at 1200°C for 100 min before particle deposition and ethanol exposure.

Kinetics of SWCNT growth between T_L and T_H

This temperature regime is characterized by little variation of the RBM profile and of the D band position (Figure 3-48). Compared to the low-temperature regime, the G/D ratio now increases slowly with increasing temperature. Such features support that most catalyst particles are now active and that the influence of carbonaceous by-products (*e.g.* MWCNT, carbon tar) is negligible. These conditions *a priori* appear as the closest to the Puretzky's model. This is confirmed by the excellent fit of the kinetic curves in this domain by the relation $G(t)=\upsilon\tau\ (1-\exp(-t/\tau))$ without the need of an induction time (see Figure 3-45). In this domain of temperature, ν stagnates or slightly decreases while τ increases or stagnates with increasing temperature. Such features are qualitatively in correct agreement with Puretzky's model with a carbon supply controlled by gas-phase diffusion. If one follows this line of reasoning, the activation energy in this domain should be equal to the difference of activation energies between the integration of carbon in the nanotube and in the encapsulating layer. The measured values are actually close to zero: -0.23 eV for CH_4-Ni, -0.3 eV for C_2H_2-Ni, -0.3 eV for C_2H_4-Ni, ~0 eV for Ni-EtOH, and 0.2 eV for Co-EtOH. Given the similarity of the two materials and of their formation process, this difference is not expected to be very large but it should be positive for the yield to increase with temperature as experimentally required. This discrepancy principally originates from the too low values of ν. There are therefore also some disagreements with the Puretzky's model in this case. They may originate from a slight decrease of the number of active particles which is the dominant process at higher temperatures (above T_H). For several systems, the number of small-diameter SWCNTs is actually observed to slightly decrease at the end of this regime.

3.7.5 Conclusion

The kinetics of SWCNT growth displays different regimes as a function of the temperature and precursor pressure. In most cases, the Puretzky's model based on a progressive deactivation of the catalyst particle by by-products of the precursor decomposition qualitatively reproduces the experimental kinetic curves. The temperature and pressure dependence of the two model parameters ν and τ are also in qualitative agreement with the Puretzky's model. The best agreement is found at intermediate growth temperatures and precursor pressures. There are however different quantitative discrepancies when moving away from this domain. They can be accounted for by changes in the density of active particles which are not included in the Puretzky's model but severely affect the growth rates experimentally measured.

At low temperature and high pressure, the activation energy and the reaction order of ν are, respectively, higher and lower than expected from the model. Theoretically, this can be accounted for by an inactivation of a certain population of catalyst particles caused an excessive precursor supply. From the RBM profiles, this population appears constituted by the smallest catalyst particles. From the drop of the G/D ratio, the excessive precursor supply causes an abundant growth of disordered carbon materials which are the likely cause of the deactivation in this domain.

In addition, for the weakest reducers at the lowest temperatures, the kinetics displays an induction phase which is correlated with the reduction of the catalyst. This behaviour is nicely accounted for by the slow reduction of the catalyst particles at the lower temperature limit of the growth domain.

At high temperature and low precursor supply, the activation energy and reaction order of ν are both lower than expected from the Puretzky's model. In addition, kinetic curves frequently display shapes (abrupt termination, re-growth) in disagreement with the single

exponential form of the Puretzky's model. Theoretically, those can be accounted for by a thermally-activated decrease of the density of active particles or by a conversion of one population of particles into another. Additional experiments and observations additionally support a significant restructuring of the catalyst particles at these high temperatures. From the RBM profiles, small catalyst particles appear as the most affected by the restructuring.

4. General conclusion

The described studies evidenced several processes influencing the catalytic growth of SWCNTs.

- **Size-dependent activation of the catalyst particles by the carbon precursor.** Reduction of the catalyst particles is a prerequisite for SWCNT growth from TM nanoparticles. Standard carbon precursors were shown to efficiently reduce nickel and cobalt oxides provided a sufficient temperature and partial pressure. For oxidized catalyst, this effect fixes the limit of carbon material deposition at low temperature and low partial pressure. In addition, smaller SiO_2-supported catalyst particles display a lower reducibility. This effect manifests by a higher precursor pressure of activation for small catalyst particles. This causes a drop of the SWCNT yield and a lack (or slower appearance) of small-diameter SWCNTs at low precursor pressure due to the inactivation (or slower activation) of the smallest catalyst particles.

- **Thermally-activated restructuring of the catalyst particles at high temperature.** The evolution of diameter and the growth kinetics of SWCNTs show that significant catalyst restructuring occurs at high temperature at timescales shorter (or close) to those of nanotube growth. At high temperature, the yield and diameter distribution of SWCNTs is primarily controlled by the kinetic competition between nanotube growth and catalyst restructuring. Catalyst restructuring causes a decrease of the yield and a shift of the diameter distribution toward larger diameters.

- **Size-dependent deactivation of the catalyst particles by the carbon precursor.** Growth kinetics are qualitatively well accounted for by a self-deactivation model where growth termination is caused by by-products of the precursor decomposition. However, qualitative and quantitative discrepancies with this model appear when moving away from the central parameter range. These discrepancies can be explained by variations of the density of active particles caused by carbon encapsulation and by the aforementioned processes of activation and restructuring. Diameter evolution studies notably suggest that small particles are more liable to this process of carbon encapsulation. This process causes the SWCNT yield and the fraction of small-diameter SWCNTs to decrease at high precursor pressure and low temperature.

- **Thermally-induced change of dominant catalytic intermediate**

  The temperature dependence of I_G/I_D demonstrates a large difference of activation barriers for the formation of a well-ordered sp^2 lattice between the defective structures formed at low temperature (~1-3.5 eV) and the well-crystalline SWCNTs formed at high temperature (0.1-0.7 eV). This shift cannot be explained by a thermally-activated process of defect annealing or defect formation but can be accounted for by a change of the catalytic intermediate controlling the integration of carbon atoms. Its origin may be a change of physical or chemical state of all the particles or of the dominant type of active particles (*e.g.* large particles at low temperature, small ones at high temperature).

This work also allowed us to assess the pros and cons of the application of Raman spectroscopy to the study of the growth of carbon nanostructures.

- **A high-throughput approach**

  The rapidity of Raman measurements coupled with a CCVD cell with negligible thermal inertia allows large systematic investigations of the influence of the growth

parameters. Current microscopy techniques (e.g. ETEM) do not allow this high-throughput approach.

- **Rich in structural information**

Raman spectroscopy provides structural information about SWCNTs (diameter, M/SC character, defect density) but also on other involved species such as carbonaceous by-products and oxide particles. However, the conversion of spectral data in structural information usually requires an *a priori* knowledge of the spectral features of each species.

- **Highly sensitive to resonant species**

Due to the resonance effect, Raman scattering is dominated by the signal of SWCNTs in resonance with the laser energy. On the plus side, this brings an intense Raman signal allowing a good temporal resolution during in situ measurements. It also allows one to monitor specifically the behaviour of a population of SWCNTs without interference from the contributions of other materials. On the minus side, non resonant species such as defective carbonaceous materials can be easily overlooked and underestimated even when they are the dominant species. This means that high-throughput Raman studies have to be coupled with other non-resonant characterization techniques such as TEM and XPS.

- **A protected environment**

Growing SWCNTs in an optical cell allows a direct and rapid characterization without the biases caused by air exposure and sample aging.

The same high-throughput approach could be applied to study the formation or modifications of other types of nanostructures. Most important limitations are the intrinsic Raman intensity of the materials and the process temperature. Resonant species and low temperature will be clearly preferred.

References

1. Reich, S., C. Thomsen, and J. Maultzsch, *Carbon Nanotubes: Basic Concepts and Physical Properties.* 1st Edition ed. 2004, Berlin: Wiley-VCH.
2. Journet, C., M. Picher, and V. Jourdain, *Carbon nanotube synthesis: from large-scale production to atom-by-atom growth.* Nanotechnology, 2012. **23**(142001).
3. Irle, S., et al., *Milestones in molecular dynamics simulations of single-walled carbon nanotube formation: A brief critical review.* Nano Research, 2009. **2**(10): p. 755-767.
4. Moisala, A., A.G. Nasibulin, and E.I. Kauppinen, *The role of metal nanoparticles in the catalytic production of single-walled carbon nanotubes—a review.* Journal of Physics: Condensed Matter, 2003. **15**: p. S3011-S3035.
5. Dupuis, A.C., *The catalyst in the CCVD of carbon nanotubes--a review.* Progress in Materials Science, 2005. **50**(8): p. 929-961.
6. Harutyunyan, A.R., *The Catalyst for Growing Single-Walled Carbon Nanotubes by Catalytic Chemical Vapor Deposition Method.* Journal of Nanoscience and Nanotechnology, 2009. **9**(4): p. 2480-2495.
7. Baird, T., J.R. Fryer, and B. Grant, *Structure of Fibrous Carbon.* Nature (London), 1971. **233**(5318): p. 329-330.
8. Koyama, T., M. Endo, and Y. Onuma, *Carbon fibers obtained by thermal decomposition of vaporized hydrocarbon.* Jpn. J. Appl. Phys, 1972. **11**(4): p. 445-449.
9. Baker, R.T.K., et al., *Nucleation and growth of carbon deposits from the nickel catalyzed decomposition of acetylene.* Journal of Catalysis, 1972. **26**: p. 51-62.
10. Baker, R.T.K., et al., *Formation of filamentous carbon from iron, cobalt and chromium catalyzed decomposition of acetylene.* Journal of Catalysis, 1973. **30**: p. 86-95.
11. Oberlin, A., M. Endo, and T. Koyama, *Filamentous growth of carbon through benzene decomposition.* Journal of Crystal Growth, 1976. **32**: p. 335-349.
12. Harris, P.J.F., *Carbon nanotube science: synthesis, properties and applications.* 2009: New York.
13. Nessim, G.D., *Properties, synthesis, and growth mechanisms of carbon nanotubes with special focus on thermal chemical vapor deposition.* Nanoscale, 2010. **2**(8): p. 1306-1323.
14. Tessonnier, J.P. and D.S. Su, *Recent Progress on the Growth Mechanism of Carbon Nanotubes: A Review.* Chemsuschem, 2011. **4**(7): p. 824-847.
15. Hong, G., et al., *Controlling the growth of single-walled carbon nanotubes on surfaces using metal and non-metal catalysts.* Carbon, 2012. **50**(6): p. 2067-2082.
16. Kong, J., A.M. Cassel, and H. Dai, *Chemical vapor deposition of methane for single-walled carbon nanotubes.* Chemical Physics Letters, 1998. **292**: p. 567-574.
17. Mayne, M., et al., *Pyrolytic production of aligned carbon nanotubes from homogeneously dispersed benzene-based aerosols.* Chemical Physics Letters, 2001. **338**(2-3): p. 101-107.

18. Maruyama, S., et al., *Low-temperature synthesis of high-purity single-walled carbon nanotubes from alcohol.* Chemical Physics Letters, 2002. **360**(3-4): p. 229-234.

19. Tian, Y., et al., *In Situ TA-MS Study of the Six-Membered-Ring-Based Growth of Carbon Nanotubes with Benzene Precursor.* Journal of the American Chemical Society, 2003. **126**(4): p. 1180-1183.

20. Rodríguez-Manzo, J.A., et al., *In situ nucleation of carbon nanotubes by the injection of carbon atoms into metal particles.* Nature Nanotechnology, 2007. **2**(5): p. 307-311.

21. Tsui, F. and P. Ryan, *Self-Organization of Carbide Superlattice and Nucleation of Carbon Nanotubes.* Journal of Nanoscience and Nanotechnology, 2003. **3**(6): p. 529-534.

22. Thurakitseree, T., et al., *Diameter-Controlled and Nitrogen-Doped Vertically Aligned Single-Walled Carbon Nanotubes.* Carbon, 2012. **50**(7): p. 2635-2640.

23. Maciel, I.O., et al., *Synthesis, Electronic Structure, and Raman Scattering of Phosphorus-Doped Single-Wall Carbon Nanotubes.* Nano Letters, 2009. **9**(6): p. 2267-2272.

24. Lyu, S.C., et al., *Synthesis of boron-doped double-walled carbon nanotubes by the catalytic decomposition of tetrahydrofuran and triisopropyl borate.* Carbon, 2011. **49**(5): p. 1532-1541.

25. Shatynski, S.R., *The thermochemistry of transition metal carbides.* Oxidation of Metals, 1979. **13**(2): p. 105-118.

26. Haynes, W.M., *CRC Handbook of Chemistry and Physics.* Vol. 92. 2011-2012: CRC press Boca Raton, FL.

27. Couttenye, R.A., M.H. De Vila, and S.L. Suib, *Decomposition of methane with an autocatalytically reduced nickel catalyst.* Journal of Catalysis, 2005. **233**(2): p. 317-326.

28. Lee, J. and S. Oyama, *Oxidative coupling of methane to higher hydrocarbons.* Catalysis Reviews Science and Engineering, 1988. **30**(2): p. 249-280.

29. Lunsford, J.H., *The catalytic oxidative coupling of methane.* Angewandte Chemie International Edition in English, 1995. **34**(9): p. 970-980.

30. Skukla, B., et al., *Interdependency of Gas Phase Intermediates and Chemical Vapor Deposition Growth of Single Wall Carbon Nanotubes.* Chemistry of Materials, 2010. **22**(22): p. 6035–6043.

31. Plata, D.L., et al., *Early evaluation of potential environmental impacts of carbon nanotube synthesis by chemical vapor deposition.* Environmental science & technology, 2009. **43**(21): p. 8367-8373.

32. Zhang, Y., et al., *Ethanol-Promoted High-Yield Growth of Few-Walled Carbon Nanotubes.* The Journal of Physical Chemistry C, 2010. **114**(14): p. 6389-6395.

33. Galvita, V., et al., *Synthesis gas production by steam reforming of ethanol.* Applied Catalysis A: General, 2001. **220**(1-2): p. 123-127.

34. Geurts, F. and A. Sacco Jr, *The relative rates of the boudouard reaction and hydrogenation of CO over Fe and Co foils.* Carbon, 1992. **30**(3): p. 415-418.

35. Tope, B., *Selective activation of lower alkanes: Selective oxychlorination of methane and oxidative dehydrogenation of ethane*. 2006.

36. Esconjauregui, S., C.M. Whelan, and K. Maex, *The reasons why metals catalyze the nucleation and growth of carbon nanotubes and other carbon nanomorphologies.* Carbon, 2009. **47**(3): p. 659-669.

37. Yamada, M., M. Kawana, and M. Miyake, *Synthesis and diameter control of multi-walled carbon nanotubes over gold nanoparticle catalysts.* Applied Catalysis A: General, 2006. **302**(2): p. 201-207.

38. Deck, C.P. and K. Vecchio, *Prediction of carbon nanotube growth success by the analysis of carbon-catalyst binary phase diagrams.* Carbon, 2006. **44**(2): p. 267-275.

39. Takagi, D., et al., *Single-walled carbon nanotube growth from highly activated metal nanoparticles.* Nano Letters, 2006. **6**(12): p. 2642-2645.

40. Qian, Y., et al., *Surface growth of single-walled carbon nanotubes from ruthenium nanoparticles.* Applied Surface Science, 2010. **256**(12): p. 4038-4041.

41. Zhou, W.H.Z., et al., *Copper catalyzing growth of single-walled carbon nanotubes on substrates.* Nano Letters, 2006. **6**(12): p. 2987-2990.

42. Bhaviripudi, S., et al., *CVD synthesis of single-walled carbon nanotubes from gold nanoparticle catalysts.* Journal of the American Chemical Society, 2007. **129**(6): p. 1516-1517.

43. Liu, B., et al., *Manganese-catalyzed surface growth of single-walled carbon nanotubes with high efficiency.* The Journal of Physical Chemistry C, 2008. **112**(49): p. 19231-19235.

44. Li, Y., et al., *How Catalysts Affect the Growth of Single Walled Carbon Nanotubes on Substrates.* Advanced Materials, 2010. **22**(13): p. 1508-1515.

45. Yuan, D., et al., *Horizontally Aligned Single-Walled Carbon Nanotube on Quartz from a Large Variety of Metal Catalysts.* Nano Letters, 2008. **8**(8): p. 2576-2579.

46. Takagi, D., Y. Kobayashi, and Y. Homma, *Carbon nanotube growth from diamond.* Journal of the American Chemical Society, 2009. **131**(20): p. 6922-6923.

47. Takagi, D., et al., *Carbon nanotube growth from semiconductor nanoparticles.* Nano Letters, 2007. **7**(8): p. 2272-2275.

48. Swierczewska, M., I. Rusakova, and B. Sitharaman, *Gadolinium and europium catalyzed growth of single-walled carbon nanotubes.* Carbon, 2009. **47**(13): p. 3139-3142.

49. Qi, H., C. Qian, and J. Liu, *Synthesis of uniform double-walled carbon nanotubes using iron disilicide as catalyst.* Nano Letters, 2007. **7**(8): p. 2417-2421.

50. Bachmatiuk, A., et al., *Investigating the graphitization mechanism of SiO2 nanoparticles in chemical vapor deposition.* ACS Nano, 2009. **3**(12): p. 4098-4104.

51. Liu, B., et al., *Metal-catalyst-free growth of single-walled carbon nanotubes.* Journal of the American Chemical Society, 2009. **131**(6): p. 2082-2083.

52. Huang, S., et al., *Metal-catalyst-free growth of single-walled carbon nanotubes on substrates.* Journal of the American Chemical Society, 2009. **131**(6): p. 2094-2095.

53. Gao, F., L. Zhang, and S. Huang, *Zinc oxide catalyzed growth of single-walled carbon nanotubes.* Applied Surface Science, 2010. **256**(8): p. 2323-2326.

54. Chiang, W.H. and R.M. Sankaran, *Linking catalyst composition to chirality distributions of as-grown single-walled carbon nanotubes by tuning NixFe1- x nanoparticles.* Nature Materials, 2009. **8**(11): p. 882-886.

55. Li, Y., et al., *Preparation of monodispersed Fe-Mo nanoparticles as the catalyst for CVD synthesis of carbon nanotubes.* Chemistry of Materials, 2001. **13**(3): p. 1008-1014.

56. Alvarez, W., et al., *Synergism of Co and Mo in the catalytic production of single-wall carbon nanotubes by decomposition of CO.* Carbon, 2001. **39**(4): p. 547-558.

57. Flahaut, E., et al., *Synthesis of single-walled carbon nanotubes using binary (Fe, Co, Ni) alloy nanoparticles prepared in situ by the reduction of oxide solid solutions.* Chemical Physics Letters, 1999. **300**(1-2): p. 236-242.

58. Shibuta, Y. and S. Maruyama, *A molecular dynamics study of the effect of a substrate on catalytic metal clusters in nucleation process of single-walled carbon nanotubes.* Chemical Physics Letters, 2007. **437**(4-6): p. 218-223.

59. Hoch, M., *Phase stability of carbon in FCC and BCC metals.* Calphad, 1988. **12**(1): p. 83-88.

60. Yazyev, O.V. and A. Pasquarello, *Effect of Metal Elements in Catalytic Growth of Carbon Nanotubes.* Physical Review Letters, 2008. **100**: p. 156102.

61. Yang, R., et al., *Solubility and diffusivity of carbon in metals.* Journal of Catalysis, 1990. **122**(1): p. 206-210.

62. Samsonov, G., *On the problem of the classification of carbides.* Powder Metallurgy and Metal Ceramics, 1965. **4**(1): p. 75-81.

63. Sinfelt, J.H., *Heterogeneous Catalysis: Some Recent Developments.* Science (Washington, D. C., 1883-), 1977. **195**(4279): p. 641-646.

64. Yasuda, H. and H. Mori, *Phase diagrams in nanometer-sized alloy systems.* Journal of Crystal Growth, 2002. **237-239, Part 1**(0): p. 234-238.

65. Andrievski, R., *Size-dependent effects in properties of nanostructured Materials.* Rev. Adv. Mater. Sci, 2009. **21**: p. 107-133.

66. Lee, J.G. and H. Mori, *Direct Evidence for Reversible Diffusional Phase Change in Nanometer-Sized Alloy Particles.* Physical Review Letters, 2004. **93**(23): p. 235501.

67. Straumal, B.B., et al., *Increase of Co solubility with decreasing grain size in ZnO.* Acta Materialia, 2008. **56**(20): p. 6246-6256.

68. Lee, J.G., H. Mori, and H. Yasuda, *Alloy phase formation in nanometer-sized particles in the In-Sn system.* Physical Review B, 2002. **65**(13): p. 132106.

69. Sutter, E.A. and P.W. Sutter, *Giant carbon solubility in Au nanoparticles.* Journal of Materials Science, 2011. **46**: p. 7090–7097.

70. Petropoulos, J., et al., *A simple thermodynamic model for the doping and alloying of nanoparticles.* Nanotechnology, 2011. **22**: p. 245704.

71. L'vov, P., V. Svetukhin, and A. Obukhov, *Thermodynamics of phase equilibrium of binary alloys containing nanprecipitates.* Physics of the Solid State, 2011. **53**(2): p. 421-427.

72. Oksengendler, B., et al., *Effect of abnormal high solubility of impurity in nanocrystalls and its metrological aspects.* Journal of Physics: Conference Series, 2011. **291**: p. 012010.

73. Ouyang, G., et al., *Solid solubility limit in alloying nanoparticles.* Nanotechnology, 2006. **17**: p. 4257.

74. Koshkin, V. and V. Slezov, *Doping nanoparticles.* Technical Physics Letters, 2004. **30**(5): p. 367-369.

75. Diarra, M., et al., *Carbon Solubility in Nickel Nanoparticles : a Grand Canonical Monte Carlo Study.* Physica Status Solidi A: Applied Research, 2012.

76. Barrer, R.M., *Diffusion in and through Solids.* 1951: University Press Cambridge.

77. Smithells, C.J., *Smithells metals reference book.* Seventh edition ed, ed. E.A. Brandes and G. Brook. 1992, Oxford: Butterworth-Heinemann.

78. Le Claire, A.D., in *Landolt-Börnstein - Numerical Data and Functional Relationships in Science and Technology*, H. Mehrer, Editor. 1992, Springer-Verlag: Berlin. p. 471.

79. Krishtal, M., *Thermodynamics of Carbon Diffusion in Iron.* Amerind Publishing Co. Pvt. Ltd., Protective Coatings on Metals., 1984. **6**: p. 96-106.

80. Gegner, J. *Concentration-and temperature-dependent diffusion coefficient of carbon in FCC iron mathematically derived from literature data. .* in *4th Int Conf Mathematical Modeling and Computer Simulation of Materials Technologies* 2006. Ariel, College of Judea and Samaria.

81. Wells, C., W. Batz, and R.F. Mehl, Trans. AIME, 1950. **188**: p. 553-560.

82. Xu, J. and M. Saeys, *First Principles Study of the Stability and the Formation Kinetics of Subsurface and Bulk Carbon on a Ni Catalyst.* The Journal of Physical Chemistry C, 2008. **112**(26): p. 9679-9685.

83. Mittemeijer, E.J., *Fundamentals of Materials Science.* 2010, Heidelberg: Springer Verlag.

84. Andrievsky, R. and K. Gurov, *Self-diffusion in interstitial phases.* Fiz. Met. Metalloved., 1968. **26**(5): p. 818-822.

85. Hillert, M., L. Höglund, and J. Ågren, *Diffusion in interstitial compounds with thermal and stoichiometric defects.* Journal of Applied Physics, 2005. **98**: p. 053511.

86. Ozturk, B., V. Fearing, and J. Ruth, *The Diffusion Coefficient of Carbon in Cementite, Fe sub 3 C, at 450 deg C.* Solid State Ionics, 1984. **12**(1): p. 145-151.

87. Schneider, A. and G. Inden, *Carbon diffusion in cementite (Fe3C) and Hägg carbide (Fe5C2).* Calphad, 2007. **31**(1): p. 141-147.

88. van Loo, F.J.J. and G. Bastin, *On the diffusion of carbon in titanium carbide.* Metallurgical and Materials Transactions A, 1989. **20**(3): p. 403-411.

89. DePoorter, G.L. and T. Wallace, *Diffusion in binary carbides.* Adv. High Temp. Chem, 1970. **4**: p. 107.

90. Shovensin, A., G. Shcherbedinskii, and A. Minkevich, *Some characteristics of the diffusion of carbon in molybdenum carbide.* Powder Metallurgy and Metal Ceramics, 1966. **5**(11): p. 880-884.

91. Borisova, A. and O. Evtushenko, *Diffusional processes in the welding of some refractory carbides to metals.* Powder Metallurgy and Metal Ceramics, 1979. **18**(7): p. 481-487.

92. Sharma, R., et al., *Evaluation of the Role of Au in Improving Catalytic Activity of Ni Nanoparticles for the Formation of One-Dimensional Carbon Nanostructures.* Nano Letters, 2011. **11**(6): p. 2464-2671.

93. Lander, J., H. Kern, and A. Beach, *Solubility and Diffusion Coefficient of Carbon in Nickel: Reaction Rates of Nickel Carbon Alloys with Barium Oxide.* Journal of Applied Physics, 1952. **23**(12): p. 1305-1309.

94. Massaro, T.A. and E.E. Petersen, *Bulk Diffusion of Carbon 14 through Polycrystalline Nickel Foil between 350 and 700° C.* Journal of Applied Physics, 1971. **42**(13): p. 5534-5539.

95. Cermak, J., F. Rollert, and H. Mehrer, *Diffusion of carbon-14 in fcc cobalt.* Zeitschrift fuer Metallkunde, 1990. **81**(2): p. 81-83.

96. Powers, R. and M.V. Doyle, *The diffusion of carbon and oxygen in vanadium.* Acta Metallurgica, 1958. **6**(10): p. 643-646.

97. Son, P., et al., *Diffusion of carbon in vanadium.* J. Japan Inst. Metals, 1969. **33**(1): p. 1-3.

98. Yokoyama, H., H. Numakura, and M. Koiwa, *The solubility and diffusion of carbon in palladium.* Acta Materialia, 1998. **46**(8): p. 2823-2830.

99. Ling, C. and D.S. Sholl, *First-principles evaluation of carbon diffusion in Pd and Pd-based alloys.* Physical Review B, 2009. **80**(21): p. 214202.

100. Fromm, E. and E. Gebhardt, *Gase und Kohlenstoff in Metallen.* 1976, Berlin: Springer Verlag.

101. Agarwala, R. and A. Paul, *Diffusion of carbon in zirconium and some of its alloys.* Journal of Nuclear Materials, 1975. **58**(1): p. 25-30.

102. Smoluchowski, R., *Diffusion Rate of Carbon in Iron-Cobalt Alloys.* Physical Review, 1942. **62**(11-12): p. 539.

103. Hofmann, S., et al., *Surface Diffusion: The Low Activation Energy Path for Nanotube Growth.* Physical Review Letters, 2005. **95**(3): p. 36101.

104. Mojica, J.F. and L.L. Levenson, *Bulk-to-surface precipitation and surface diffusion of carbon on polycrystalline nickel.* Surface Science, 1976. **59**(2): p. 447-460.

105. Portavoce, A., et al., *Nanometric size effect on Ge diffusion in polycrystalline Si.* Journal of Applied Physics, 2008. **104**(10): p. 104910-104918.

106. Cinquini, F., F. Delbecq, and P. Sautet, *A DFT comparative study of carbon adsorption and diffusion on the surface and subsurface of Ni and Ni3Pd alloy.* Phys. Chem. Chem. Phys., 2009. **11**(48): p. 11546-11556.

107. Gracia, L., et al., *Migration of the subsurface C impurity in Pd (111).* Physical Review B, 2005. **71**(3): p. 033407.

108. Kalibaeva, G., et al., *Ab initio simulation of carbon clustering on an Ni (111) surface: A model of the poisoning of nickel-based catalysts.* The Journal of Physical Chemistry B, 2006. **110**(8): p. 3638-3646.

109. Ramirez-Caballero, G.E., J.C. Burgos, and P.B. Balbuena, *Growth of Carbon Structures on Stepped (211) Co Surfaces.* The Journal of Physical Chemistry C, 2009. **113**(35): p. 15658-15666.

110. Klinke II, D.J., S. Wilke, and L.J. Broadbelt, *A theoretical study of carbon chemisorption on Ni (111) and Co (0001) surfaces.* Journal of Catalysis, 1998. **178**(2): p. 540-554.

111. Klink, C., et al., *Interaction of C with Ni (100): Atom-resolved studies of the ''clock''reconstruction.* Physical Review Letters, 1993. **71**(26): p. 4350-4353.

112. Stolbov, S., et al., *Origin of the C-induced p4g reconstruction of Ni (001).* Physical Review B, 2005. **72**(15): p. 155423.

113. Hong, S., *Surface energy anisotropy of iron surfaces by carbon adsorption.* Current Applied Physics, 2003. **3**(5): p. 457-460.

114. Begtrup, G.E., et al., *Facets of nanotube synthesis: High-resolution transmission electron microscopy study and density functional theory calculations.* Physical Review B: Condensed Matter, 2009. **79**(20): p. 205409.

115. Riikonen, S., A. Krasheninnikov, and R. Nieminen, *Submonolayers of carbon on α-Fe facets: An ab initio study.* Physical Review B, 2010. **82**(12): p. 125459.

116. Fujii, J., et al., *C–Fe chains due to segregated carbon impurities on Fe (100).* Surface Science, 2006. **600**(18): p. 3884-3887.

117. Panaccione, G., et al., *Local and long-range order of carbon impurities on Fe (100): Analysis of self-organization at a nanometer scale.* Physical Review B, 2006. **73**(3): p. 035431.

118. Siegel, D.J. and J. Hamilton, *First-principles study of the solubility, diffusion, and clustering of C in Ni.* Physical Review B, 2003. **68**(9): p. 094105.

119. Medlin, J.W. and M.D. Allendorf, *Theoretical study of the adsorption of acetylene on the (111) surfaces of Pd, Pt, Ni, and Rh.* The Journal of Physical Chemistry B, 2003. **107**(1): p. 217-223.

120. Moors, M., et al., *Early stages in the nucleation process of carbon nanotubes.* ACS Nano, 2009. **3**(3): p. 511-516.

121. Reich, S., L. Li, and J. Robertson, *Epitaxial growth of carbon caps on Ni for chiral selectivity.* Physica Status Solidi B: Basic Research, 2006. **243**(13): p. 3494-3499.

122. Ding, F., et al., *The Importance of Strong Carbon-Metal Adhesion for Catalytic Nucleation of Single-Walled Carbon Nanotubes.* Nano Letters, 2008. **8**(2): p. 463-468.

123. Larsson, P., et al., *Calculating carbon nanotube–catalyst adhesion strengths.* Physical Review B, 2007. **75**(11): p. 115419.

124. Lacovig, P., et al., *Growth of dome-shaped carbon nanoislands on Ir (111): the intermediate between carbidic clusters and quasi-free-standing graphene.* Physical Review Letters, 2009. **103**(16): p. 166101.

125. Somorjai, G.A., *Introduction to surface chemistry and catalysis.* 1994, New York: Wiley. p. 347.

126. Nørskov, J., *Covalent effects in the effective-medium theory of chemical binding: Hydrogen heats of solution in the 3d metals.* Physical Review B, 1982. **26**(6): p. 2875.

127. Sinfelt, J., *Catalytic hydrogenolysis on metals.* Catalysis Letters, 1991. **9**(3): p. 159-171.

128. Teschner, D., et al., *The roles of subsurface carbon and hydrogen in palladium-catalyzed alkyne hydrogenation.* Science (Washington, D. C., 1883-), 2008. **320**(5872): p. 86-89.

129. Bertolini, J., J. Billy, and J. Massardier. *Adsorption of CO on the Face of Monocrystalline Nickel(III): the Influence of Surface Carbides.* in *IVth Colloquium on Solid Surface Physics and Chemistry, Gas/Solid and Liquid/Solid Interfaces.* 1978. Antibes-Juan les Pins.

130. Bridge, M.E., K.A. Prior, and R.M. Lambert, *The effects of surface carbide formation on the adsorption-desorption kinetics of CO on smooth and stepped cobalt surfaces.* Surface Science, 1980. **97**(1): p. L325-L329.

131. Didziulis, S.V., et al., *Coordination Chemistry of Transition Metal Carbide Surfaces: Detailed Spectroscopic and Theoretical Investigations of CO Adsorption on TiC and VC (100) Surfaces.* The Journal of Physical Chemistry B, 2001. **105**(22): p. 5196-5209.

132. Oyama, S., *Preparation and catalytic properties of transition metal carbides and nitrides.* Catalysis Today, 1992. **15**(2): p. 179-200.

133. Kharlamov, A. and N. Kirillova, *Catalytic properties of powdered refractory compounds of transition elements. Carbides and nitrides—A review.* Powder Metallurgy and Metal Ceramics, 1983. **22**(2): p. 123-134.

134. Yoshihara, N., H. Ago, and M. Tsuji, *Growth Mechanism of Carbon Nanotubes over Gold-Supported Catalysts.* Japanese Journal of Applied Physics-Part 1 Regular Papers and Short Notes, 2008. **47**(4): p. 1944-1948.

135. Solomon, E.I., P.M. Jones, and J.A. May, *Electronic structures of active sites on metal oxide surfaces: definition of the copper-zinc oxide methanol synthesis catalyst by photoelectron spectroscopy.* Chemical Reviews, 1993. **93**(8): p. 2623-2644.

136. Meier, D.C. and D.W. Goodman, *The Influence of Metal Cluster Size on Adsorption Energies: CO Adsorbed on Au Clusters Supported on TiO2.* Journal of the American Chemical Society, 2004. **126**(6): p. 1892-1899.

137. Skurnik, S. and M. Steinberg, *Heat of Adsorption of Carbon Monoxide on Coprecipitated Nickel Oxide-Silica Catalyst.* Industrial & Engineering Chemistry Fundamentals, 1967. **6**(3): p. 459-460.

138. Bolis, V., et al., *Surface acidity of metal oxides. Combined microcalorimetric and IR-spectroscopic studies of variously dehydrated systems.* Thermochimica Acta, 1998. **312**(1-2): p. 63-77.

139. Magrez, A., et al., *Striking Influence of the Catalyst Support and Its Acid–Base Properties: New Insight into the Growth Mechanism of Carbon Nanotubes.* ACS Nano, 2011. **5**(5): p. 3428-3437.

140. Haruta, M., et al., *Gold catalysts prepared by coprecipitation for low-temperature oxidation of hydrogen and of carbon monoxide.* Journal of Catalysis, 1989. **115**(2): p. 301-309.

141. Tsunoyama, H., H. Sakurai, and T. Tsukuda, *Size effect on the catalysis of gold clusters dispersed in water for aerobic oxidation of alcohol.* Chemical Physics Letters, 2006. **429**(4-6): p. 528-532.

142. Henry, C.R., *Surface studies of supported model catalysts.* Surface Science Reports, 1998. **31**(7-8): p. 231-325.

143. Somorjai, G.A., *Introduction to surface chemistry and catalysis.* 1994: New York: Wiley.

144. Novotny, V., et al., *Corrosion of thin film cobalt based magnetic recording media.* IEEE Transactions on Magnetics, 1987. **23**(5): p. 3645-3647.

145. Flis-Kabulska, I., *Oxide growth on evaporated thin film and bulk iron exposed to humid air and HCl or HNO3 vapours.* Journal of Electroanalytical Chemistry, 2001. **508**(1-2): p. 89-96.

146. Nessim, G.D., et al., *Tuning of Vertically-Aligned Carbon Nanotube Diameter and Areal Density through Catalyst Pre-Treatment.* Nano Letters, 2008. **8**(11): p. 3587-3593.

147. Cantoro, M., et al., *Catalytic chemical vapor deposition of single-wall carbon nanotubes at low temperatures.* Nano Letters, 2006. **6**(6): p. 1107-1112.

148. Picher, M., E. Anglaret, and V. Jourdain, *High temperature activation and deactivation of single-walled carbon nanotube growth investigated by in situ Raman measurements.* Diamond and Related Materials, 2010. **19**(5-6): p. 581-585.

149. Lu, J.Q., *Nanocatalysts with Tunable Properties Derived from Polystyrene-b-poly (vinyl pyridine) Block Copolymer Templates for Achieving Controllable Carbon Nanotube Synthesis.* The Journal of Physical Chemistry C, 2008. **112**(28): p. 10344-10351.

150. Stempo, M.J., *The Ellingham Diagram: How to Use it in Heat-Treat-Process Atmosphere Troubleshooting.* Industrial Heating, 2011. **April** p. 55-60.

151. Fu, Q. and T. Wagner, *Interaction of nanostructured metal overlayers with oxide surfaces.* Surface Science Reports, 2007. **62**(11): p. 431-498.

152. Yoon, B., et al., *Charging Effects on Bonding and Catalyzed Oxidation of CO on Au8 Clusters on MgO.* Science (Washington, D. C., 1883-), 2005. **307**(5708): p. 403-407.

153. Bauer, E., *Phänomenologische Theorie der Kristallabscheidung an Oberflächen. II.* Zeitschrift für Kristallographie, 1958. **110**(1-6): p. 395-431.

154. Fu, Q. and T. Wagner, *Thermal stability of Cr clusters on SrTiO3 (1 0 0).* Surface Science, 2002. **505**: p. 39-48.

155. Diebold, U., J.M. Pan, and T.E. Madey, *Ultrathin metal film growth on TiO2 (110): an overview.* Surface Science, 1995. **331**: p. 845-854.

156. Hu, M., S. Noda, and H. Komiyama, *A new insight into the growth mode of metals on TiO2 (110).* Surface Science, 2002. **513**(3): p. 530-538.

157. Lee, W.H., et al., *The Equilibrium Shape and Surface-Energy Anisotropy of Clean Platinum.* Journal of Catalysis, 1990. **126**(2): p. 658-670.

158. Harris, P., *Growth and structure of supported metal catalyst particles.* International Materials Reviews, 1995. **40**(3): p. 97-115.

159. Thiel, P.A., et al., *Coarsening of Two-Dimensional Nanoclusters on Metal Surfaces.* The Journal of Physical Chemistry C, 2009. **113**(13): p. 5047-5067.

160. Layson, A.R., J.W. Evans, and P.A. Thiel, *Additive-enhanced coarsening and smoothening of metal films: Complex mass-flow dynamics underlying nanostructure evolution.* Physical Review B, 2002. **65**(19): p. 193409.

161. Kuo, H.K., P. Ganesan, and R.J. De Angelis, *The sintering of a silica-supported nickel catalyst.* Journal of Catalysis, 1980. **64**(2): p. 303-319.

162. Kim, K.-T. and S.-K. Ihm, *Sintering behavior of nickel particles supported on alumina model catalyst in hydrogen atmosphere.* Journal of Catalysis, 1985. **96**(1): p. 12-22.

163. Beck, D.D. and C.J. Carr, *A study of thermal aging of PtAl2O3 using temperature-programmed desorption spectroscopy.* Journal of Catalysis, 1988. **110**(2): p. 285-297.

164. Sasaki, T., et al. *Raman Study of Low-Temperature Formation of Nickel Silicide Layers.* in *14th IEEE International Conference on Advanced Thermal Processing of Semiconductors* 2006. IEEE.

165. Teo, K., et al., *Characterization of plasma-enhanced chemical vapor deposition carbon nanotubes by Auger electron spectroscopy.* Journal of Vacuum Science & Technology B, 2002. **20**: p. 116-121.

166. Malik, I.J., et al. *Cobalt Silicide Formation Characteristics in a Single Wafer Rapid Thermal Furnace (SRTF) System.* in *RTP Conference*. 2006. IEEE.

167. Simmons, J.M., et al., *Critical Oxide Thickness for Efficient Single-walled Carbon Nanotube Growth on Silicon Using Thin SiO2 Diffusion Barriers.* Small, 2006. **2**: p. 902-909.

168. De los Arcos, T., et al., *Influence of iron–silicon interaction on the growth of carbon nanotubes produced by chemical vapor deposition.* Applied Physics Letters, 2002. **80**: p. 2383-2385.

169. Meschel, S. and O. Kleppa, *Standard enthalpies of formation of some 3d transition metal silicides by high temperature direct synthesis calorimetry.* Journal of Alloys and Compounds, 1998. **267**(1-2): p. 128-135.

170. Lamber, R., N. Jaeger, and G. Schulz-Ekloff, *On the metal-support interaction in the Ni-SiO2 system.* Surface Science, 1990. **227**(3): p. 268-272.

171. Penner, S., et al., *Platinum nanocrystals supported by silica, alumina and ceria: metal–support interaction due to high-temperature reduction in hydrogen.* Surface Science, 2003. **532**: p. 276-280.

172. Wang, D., et al., *Silicide formation on a Pt/SiO2 model catalyst studied by TEM, EELS, and EDXS.* Journal of Catalysis, 2003. **219**(2): p. 434-441.

173. Pretorius, R., J.M. Harris, and M.A. Nicolet, *Reaction of thin metal films with SiO2 substrates.* Solid-State Electronics, 1978. **21**(4): p. 667-675.

174. Zhao, X.-A., E. Kolawa, and M.-A. Nicolet, *Reaction of thin metal films with crystalline and amorphous Al2O3.* Journal of Vacuum Science & Technology A: Vacuum, Surfaces, and Films, 1986. **4**(6): p. 3139-3141.

175. Mattevi, C., et al., *In-situ X-ray Photoelectron Spectroscopy Study of Catalyst-Support Interactions and Growth of Carbon Nanotube Forests.* The Journal of Physical Chemistry C, 2008. **112**(32): p. 12207-12213.

176. Li, N., et al., *Role of Surface Cobalt Silicate in Single-Walled Carbon Nanotube Synthesis from Silica-Supported Cobalt Catalysts.* ACS Nano, 2010. **4**(3): p. 1759-1767.

177. Lucas, S., et al., *Surface phenomena involved in the formation of Co nanoparticles on amorphous carbon and SiO 2 deposited by magnetron sputtering.* Applied Physics A, Materials Science & Processing, 2010. **99**(1): p. 125-138.

178. Oshima, H., et al., *Analysis of Fe Catalyst during Carbon Nanotube Synthesis by Mo ssbauer Spectroscopy.* The Journal of Physical Chemistry C, 2009. **113**(43): p. 18523-18526.

179. Murakami, T., et al., *Effective catalyst on SiO2 in ethanol CVD for growth of single-walled carbon nanotubes.* Diamond and Related Materials, 2008. **17**(7-10): p. 1467-1470.

180. Yu, Z., et al., *Effect of catalyst preparation on the carbon nanotube growth rate.* Catalysis Today, 2005. **100**(3-4): p. 261-267.

181. Malesevic, A., et al., *Study of the catalyst evolution during annealing preceding the growth of carbon nanotubes by microwave plasma-enhanced chemical vapour deposition.* Nanotechnology, 2007. **18**: p. 455602.

182. Rog, G., et al., *Calcium zirconate: preparation, solid oxide properties and application to the galvanic cells.* Electrochimica Acta, 2002. **47**(28): p. 4523-4529.

183. Huber, G.W., et al. *Hydrothermal stability of CO/SiO2 Fischer-Tropsch synthesis catalysts.* in *Proceedings of the 9th International Symposium on Catalyst Deactivation.* 2001. Elsevier.

184. Zhong, Q. and F. Ohuchi, *Surface science studies on the Ni/Al2O3 interface.* Journal of Vacuum Science & Technology A: Vacuum, Surfaces, and Films, 1990. **8**(3): p. 2107-2112.

185. Kogelbauer, A., J.C. Weber, and J.G. Goodwin, *The formation of cobalt silicates on Co/SiO2 under hydrothermal conditions.* Catalysis Letters, 1995. **34**(3): p. 259-267.

186. Cheung, C.L., et al., *Diameter-controlled synthesis of carbon nanotubes.* Journal of Physical Chemistry B, 2002. **106**: p. 2429-2433.

187. Schäffel, F., et al., *Tailoring the diameter, density and number of walls of carbon nanotubes through predefined catalyst particles.* Physica Status Solidi A: Applied Research, 2008. **205**(6): p. 1382-1385.

188. Chen, Y. and J. Zhang, *Diameter controlled growth of single-walled carbon nanotubes from SiO2 nanoparticles.* Carbon, 2011. **49**(10): p. 3316–3324.

189. Nasibulin, A.G., et al., *Correlation between catalyst particle and single-walled carbon nanotube diameters.* Carbon, 2005. **43**(11): p. 2251-2257.

190. Hiraoka, T., et al., *Control on the diameter of single-walled carbon nanotubes by changing the pressure in floating catalyst CVD.* Carbon, 2006. **44**: p. 1853-1859.

191. Zhang, Y., et al., *Imaging as-grown single-walled carbon nanotubes originated from isolated catalytic nanoparticles.* Applied Physics A, Materials Science & Processing, 2002. **74**(3): p. 325-328.

192. Fiawoo, M.F.C., et al., *Evidence of Correlation between Catalyst Particles and the Single-Wall Carbon Nanotube Diameter: A First Step towards Chirality Control.* Physical Review Letters, 2012. **108**(19): p. 195503.

193. Helveg, S., et al., *Atomic-scale imaging of carbon nanofibre growth.* Nature (London), 2004. **427**: p. 426-429.

194. Hofmann, S., et al., *In-situ observations of catalyst dynamics during surface-bound carbon nanotube nucleation.* Nano Letters, 2007. **7**: p. 602-608.

195. Lin, M., et al., *Dynamical Observation of Bamboo-like Carbon Nanotube Growth.* Nano Letters, 2007. **7**(8): p. 2234-2238.

196. Yoshida, H., et al., *Atomic-scale in-situ observation of carbon nanotube growth from solid state iron carbide nanoparticles.* Nano Letters, 2008. **8**(7): p. 2082-2086.

197. Yoshida, H., et al., *Atomic-scale analysis on the role of molybdenum in iron-catalyzed carbon nanotube growth.* Nano Letters, 2009. **9**(11): p. 3810-3815.

198. Gamalski, A., et al., *Diffusion-gradient-induced length instabilities in the catalytic growth of carbon nanotubes.* Applied Physics Letters, 2009. **95**(23): p. 233109-233111.

199. Yoshida, H., et al., *Environmental transmission electron microscopy observations of the growth of carbon nanotubes under nanotube–nanotube and nanotube–substrate interactions.* Applied Surface Science, 2008. **254**(23): p. 7586-7590.

200. Zhu, W., A. Börjesson, and K. Bolton, *DFT and tight binding Monte Carlo calculations related to single-walled carbon nanotube nucleation and growth.* Carbon, 2010. **48**(2): p. 470-478.

201. Noda, S., et al., *Combinatorial method to prepare metal nanoparticles that catalyze the growth of single-walled carbon nanotubes.* Applied Physics Letters, 2005. **86**: p. 173106.

202. Zhao, B., et al., *Exploring advantages of diverse carbon nanotube forests with tailored structures synthesized by supergrowth from engineered catalysts.* ACS Nano, 2008. **3**(1): p. 108-114.

203. Pisana, S., et al., *The role of precursor gases on the surface restructuring of catalyst films during carbon nanotube growth.* Physica E, 2007. **37**(1): p. 1-5.

204. Jin-Ju, K., et al., *Size engineering of metal nanoparticles to diameter-specified growth of single-walled carbon nanotubes with horizontal alignment on quartz.* Nanotechnology, 2012. **23**(10): p. 105607.

205. Song, W., et al., *Synthesis of Bandgap-Controlled Semiconducting Single-Walled Carbon Nanotubes.* ACS Nano, 2010. **4**(2): p. 1012-1018.

206. Jeong, G.H., et al., *Size control of catalytic nanoparticles by thermal treatment and its application to diameter control of single-walled carbon nanotubes.* Applied Physics Letters, 2007. **90**: p. 043108.

207. Kim, S.Y., et al., *Heat-driven size manipulation of Fe catalytic nanoparticles for precise control of single-walled carbon nanotube diameter.* Journal of Physics D: Applied Physics, 2012. **45**(25): p. 255302.

208. Wang, W.L., et al., *Low temperature growth of single-walled carbon nanotubes: Small diameters with narrow distribution.* Chemical Physics Letters, 2006. **419**(1-3): p. 81-85.

209. Li, N., et al., *Diameter tuning of single-walled carbon nanotubes with reaction temperature using a Co monometallic catalyst.* The Journal of Physical Chemistry C, 2009. **113**(23): p. 10070-10078.

210. Tanioku, K., T. Maruyama, and S. Naritsuka, *Low temperature growth of carbon nanotubes on Si substrates in high vacuum.* Diamond and Related Materials, 2008. **17**(4-5): p. 589-593.

211. Ishigami, N., et al., *Crystal plane dependent growth of aligned single-walled carbon nanotubes on sapphire.* Journal of the American Chemical Society, 2008. **130**(30): p. 9918-9924.

212. Zoican Loebick, C., et al., *Selective synthesis of subnanometer diameter semiconducting single-walled carbon nanotubes.* Journal of the American Chemical Society, 2010. **132**(32): p. 11125–11131.

213. He, M., et al., *Low temperature growth of SWNTs on a nickel catalyst by thermal chemical vapor deposition.* Nano Research, 2011. **4**(4): p. 334-342.

214. Yao, Y., et al., *Temperature-mediated growth of single-walled carbon-nanotube intramolecular junctions.* Nature Materials, 2007. **6**(4): p. 293-296.

215. Mahjouri-Samani, M., et al., *Diameter modulation by fast temperature control in laser-assisted chemical vapor deposition of single-walled carbon nanotubes.* Nanotechnology, 2010. **21**: p. 395601.

216. Yao, Y., et al., *Tuning the Diameter of Single-Walled Carbon Nanotubes by Temperature-Mediated Chemical Vapor Deposition.* The Journal of Physical Chemistry C, 2009. **113**(30): p. 13051-13059.

217. Lu, C. and J. Liu, *Controlling the diameter of carbon nanotubes in chemical vapor deposition method by carbon feeding.* Journal of physical chemistry. B, Condensed matter, materials, surfaces, interfaces, & biophysical chemistry, 2006. **110**(41): p. 20254-20257.

218. Geohegan, D.B., et al., *Flux-Dependent Growth Kinetics and Diameter Selectivity in Single-Wall Carbon Nanotube Arrays.* ACS Nano, 2011. **5**(10): p. 8311–8321.

219. Saito, T., et al., *Selective diameter control of single-walled carbon nanotubes in the gas-phase synthesis.* Journal of Nanoscience and Nanotechnology, 2008. **8**(11): p. 6153-6157.

220. Wang, B., et al., *Pressure-Induced Single-Walled Carbon Nanotube (n,m) Selectivity on Co-Mo Catalysts.* The Journal of Physical Chemistry C, 2007. **111**: p. 14612-14616.

221. Picher, M., et al., *Self-Deactivation of Single-Walled Carbon Nanotube Growth Studied by in Situ Raman Measurements.* Nano Letters, 2009. **9**(2): p. 542-547.

222. Tibbetts, G.G., *Why are carbon filaments tubular?* Journal of Crystal Growth, 1984. **66**: p. 632-638.

223. Chiodarelli, N., et al., *Correlation between number of walls and diameter in multiwall carbon nanotubes grown by chemical vapor deposition.* Carbon, 2012. **50**(5): p. 1748-1752.

224. Chiang, W.H. and R.M. Sankaran, *In-flight dimensional tuning of metal nanoparticles by microplasma synthesis for selective production of diameter-controlled carbon nanotubes.* The Journal of Physical Chemistry C, 2008. **112**(46): p. 17920-17925.

225. Yamada, T., et al., *Size-selective growth of double-walled carbon nanotube forests from engineered iron catalysts.* Nature Nanotechnology, 2006. **1**(2): p. 131-136.

226. Sharma, R., et al., *Dynamic observations of the effect of pressure and temperature conditions on the selective synthesis of carbon nanotubes.* Nanotechnology, 2007. **18**(12): p. 125602.

227. Zhang, H., et al., *Influence of ethylene and hydrogen flow rates on the wall number, crystallinity, and length of millimeter-long carbon nanotube array.* The Journal of Physical Chemistry C, 2008. **112**(33): p. 12706-12709.

228. Jourdain, V., et al., *Controlling the morphology of multiwall carbon nanotubes by sequential catalytic growth induced by phosphorus.* Advanced Materials (Weinheim, Federal Republic of Germany), 2004. **16**(5): p. 447-453.

229. Mudimela, P., et al., *Incremental Variation in the Number of Carbon Nanotube Walls with Growth Temperature.* The Journal of Physical Chemistry C, 2009. **113**(6): p. 2212-2218.

230. Wei, J., et al., *The effect of sulfur on the number of layers in a carbon nanotube.* Carbon, 2007. **45**(11): p. 2152-2158.

231. Ci, L., et al., *Double wall carbon nanotubes promoted by sulfur in a floating iron catalyst CVD system.* Chemical Physics Letters, 2002. **359**(1–2): p. 63-67.

232. Ci, L., et al., *Double Wall Carbon Nanotubes with an Inner Diameter of 0.4 nm.* Chemical Vapor Deposition, 2003. **9**(3): p. 119-121.

233. Pan, Y., et al., *Inner-diameter enlargement of multi-walled carbon nanotubes by adding HBO3 in catalyst.* Materials Letters, 2011. **65**(23–24): p. 3362-3364.

234. Jorio, A., et al., *Carbon nanotube population analysis from Raman and photoluminescence intensities.* Applied Physics Letters, 2006. **88**: p. 023109.

235. Tsyboulski, D.A., et al., *Structure-dependent fluorescence efficiencies of individual single-walled carbon nanotubes.* Nano Letters, 2007. **7**(10): p. 3080-3085.

236. Miyauchi, Y., et al., *Fluorescence spectroscopy of single-walled carbon nanotubes synthesized from alcohol.* Chemical Physics Letters, 2004. **387**(1): p. 198-203.

237. Oyama, Y., et al., *Photoluminescence intensity of single-wall carbon nanotubes.* Carbon, 2006. **44**: p. 873-879.

238. Wang, H., et al., *Selective synthesis of (9, 8) single walled carbon nanotubes on cobalt incorporated TUD-1 catalysts.* Journal of the American Chemical Society, 2010. **132**(47): p. 16747–16749.

239. Hirahara, K., et al., *Chirality correlation in double-wall carbon nanotubes as studied by electron diffraction.* Physical Review B, 2006. **73**(19): p. 195420.

240. Paillet, M., et al., *Selective growth of large chiral angle single-walled carbon nanotubes.* Diamond and Related Materials, 2006. **15**: p. 1019-1022.

241. Arenal, R., et al., *Direct evidence of atomic structure conservation along individual ultralong carbon nanotubes.* Journal of Physical Chemistry C, 2012. **116**(26): p. 14103–14107.

242. Ciuparu, D., et al., *Uniform-diameter single-walled carbon nanotubes catalytically grown in cobalt-incorporated MCM-41.* The Journal of Physical Chemistry B, 2004. **108**(2): p. 503-507.

243. Bachilo, S.M., et al., *Narrow (n, m)-distribution of single-walled carbon nanotubes grown using a solid supported catalyst.* Journal of the American Chemical Society, 2003. **125**(37): p. 11186-11187.

244. Wang, B., et al., *(n, m) Selectivity of single-walled carbon nanotubes by different carbon precursors on Co-Mo catalysts.* Journal of the American Chemical Society, 2007. **129**(29): p. 9014-9019.

245. Li, X., et al., *Selective Synthesis Combined with Chemical Separation of Single-Walled Carbon Nanotubes for Chirality Selection.* Journal of the American Chemical Society, 2007. **129**(51): p. 15770-15771.

246. He, M., et al., *Predominant (6, 5) Single-Walled Carbon Nanotube Growth on a Copper-Promoted Iron Catalyst.* Journal of the American Chemical Society, 2010. **132**(40): p. 13994–13996.

247. Kajiwara, K., et al., *Chirality-selective synthesis of carbon nanotubes by catalytic-chemical vapor deposition using quasicrystal alloys as catalysts.* Zeitschrift für Kristallographie, 2009. **224**(1-2): p. 5-8.

248. Lolli, G., et al., *Tailoring (n,m) Structure of Single-Walled Carbon Nanotubes by Modifying Reaction Conditions and the Nature of the Support of CoMo Catalysts.* Journal of Physical Chemistry B, 2006. **110**: p. 2108-2115.

249. Ghorannevis, Z., et al., *Narrow-chirality distributed single-walled carbon nanotube growth from nonmagnetic catalyst.* Journal of the American Chemical Society, 2010. **132**(28): p. 9570-9572.

250. Koziol, K., M. Shaffer, and A. Windle, *Three-Dimensional Internal Order in Multiwalled Carbon Nanotubes Grown by Chemical Vapor Deposition.* Advanced Materials, 2005. **17**(6): p. 760-763.

251. Pattinson, S.W., et al., *Nitrogen-Induced Catalyst Restructuring for Epitaxial Growth of Multiwall Carbon Nanotubes.* ACS Nano, 2012. **6**(9): p. 7723–7730.

252. Li, Y., et al., *On the origin of preferential growth of semiconducting single-walled carbon nanotubes.* The Journal of Physical Chemistry B, 2005. **109**(15): p. 6968-6971.

253. Mizutani, T., et al., *A study of preferential growth of carbon nanotubes with semiconducting behavior grown by plasma-enhanced chemical vapor deposition.* Journal of Applied Physics, 2009. **106**: p. 073705.

254. Qu, L., F. Du, and L. Dai, *Preferential syntheses of semiconducting vertically aligned single-walled carbon nanotubes for direct use in FETs.* Nano Letters, 2008. **8**(9): p. 2682-2687.

255. Hong, G., et al., *Direct growth of semiconducting single-walled carbon nanotube array.* Journal of the American Chemical Society, 2009. **131**(41): p. 14642-14643.

256. Yu, B., et al., *Selective removal of metallic single-walled carbon nanotubes by combined in situ and post-synthesis oxidation.* Carbon, 2010. **48**(10): p. 2941-2947.

257. Parker, J., et al., *Increasing the Semiconducting Fraction in Ensembles of Single-Walled Carbon Nanotubes.* Carbon, 2012. **50**(14): p. 5093–5098.

258. Wang, Y., et al., *Direct Enrichment of Metallic Single-Walled Carbon Nanotubes Induced by the Different Molecular Composition of Monohydroxy Alcohol Homologues.* Small, 2007. **3**(9): p. 1486-1490.

259. Ding, L., et al., *Selective growth of well-aligned semiconducting single-walled carbon nanotubes.* Nano Letters, 2009. **9**(2): p. 800-805.

260. Che, Y., et al., *Selective Synthesis and Device Applications of Semiconducting Single-Walled Carbon Nanotubes Using Isopropanol as Feedstock.* ACS Nano, 2012. **6**(8): p. 7454–7462.

261. Harutyunyan, A.R., et al., *Preferential growth of single-walled carbon nanotubes with metallic conductivity.* Science (Washington, D. C., 1883-), 2009. **326**(5949): p. 116-120.

262. Chiang, W.H., et al., *Nanoengineering Ni x Fe1− x Catalysts for Gas-Phase, Selective Synthesis of Semiconducting Single-Walled Carbon Nanotubes.* ACS Nano, 2009. **3**(12): p. 4023-4032.

263. Qian, Y., et al., *Preferential Growth of Semiconducting Single-Walled Carbon Nanotubes on Substrate by Europium Oxide.* Nanoscale research letters, 2010. **5**(10): p. 1578-1584.

264. Tuinstra, F. and J. Koenig, *Raman spectrum of graphite.* The Journal of Chemical Physics, 1970. **53**: p. 1126-1130.

265. Lucchese, M., et al., *Quantifying ion-induced defects and Raman relaxation length in graphene.* Carbon, 2010. **48**(5): p. 1592-1597.

266. Dresselhaus, M., et al., *Defect characterization in graphene and carbon nanotubes using Raman spectroscopy.* Philosophical Transactions of the Royal Society a-Mathematical Physical and Engineering Sciences 2010. **368**(1932): p. 5355-5377.

267. Pimenta, M., et al., *Studying disorder in graphite-based systems by Raman spectroscopy.* Phys. Chem. Chem. Phys., 2007. **9**(11): p. 1276-1290.

268. Dresselhaus, M.S., et al., *Raman spectroscopy of carbon nanotubes.* Physics Reports, 2005. **409**(2): p. 47-99.

269. Souza Filho, A., et al., *Competing spring constant versus double resonance effects on the properties of dispersive modes in isolated single-wall carbon nanotubes.* Physical Review B, 2003. **67**(3): p. 035427.

270. Gao, B., et al., *Systematic Comparison of the Raman Spectra of Metallic and Semiconducting SWNTs.* The Journal of Physical Chemistry C, 2008. **112**(22): p. 8319-8323.

271. Jorio, A., et al., *Linewidth of the Raman features of individual single-wall carbon nanotubes.* Physical Review B, 2002. **66**(11): p. 115411.

272. Tan, P.H., S. Dimovski, and Y. Gogotsi, *Raman scattering of non–planar graphite: arched edges, polyhedral crystals, whiskers and cones.* Philosophical Transactions of the Royal Society a-Mathematical Physical and Engineering Sciences, 2004. **362**(1824): p. 2289.

273. Xu, Z., et al., *Structural changes in multi-walled carbon nanotubes caused by [gamma]-ray irradiation.* Carbon, 2011. **49**(1): p. 350-351.

274. Matthews, M., et al., *Origin of dispersive effects of the Raman D band in carbon materials.* Physical Review B, 1999. **59**(10): p. 6585-6588.

275. Pócsik, I., et al., *Origin of the D peak in the Raman spectrum of microcrystalline graphite.* Journal of Non-Crystalline Solids, 1998. **227**: p. 1083-1086.

276. Ferrari, A.C. and J. Robertson, *Raman spectroscopy of amorphous, nanostructured, diamond–like carbon, and nanodiamond.* Philosophical Transactions of the Royal Society a-Mathematical Physical and Engineering Sciences, 2004. **362**(1824): p. 2477-2512.

277. Yasuda, S., et al., *Existence and kinetics of graphitic carbonaceous impurities in carbon nanotube forests to assess the absolute purity.* Nano Letters, 2009. **9**(2): p. 769-773.

278. Picher, M., et al., *Influence of the growth conditions on the defect density of single-walled carbon nanotubes.* Carbon, 2012. **50**(7): p. 2407–2416.

279. Vinten, P., J. Lefebvre, and P. Finnie, *Kinetic critical temperature and optimized chemical vapor deposition growth of carbon nanotubes.* Chemical Physics Letters, 2009. **469**(4-6): p. 293-297.

280. Kwok, C., et al., *Temperature and time dependence study of single-walled carbon nanotube growth by catalytic chemical vapor deposition.* Carbon, 2010. **48**(4): p. 1279-1288.

281. Feng, X., et al., *Thermal analysis study of the growth kinetics of carbon nanotubes and epitaxial graphene layers on them.* The Journal of Physical Chemistry C, 2009. **113**(22): p. 9623-9631.

282. Jacobson, P., et al., *Disorder and Defect Healing in Graphene on Ni (111).* Journal of Physical Chemistry Letters, 2012. **3**: p. 136-139.

283. Noda, S., et al., *A Simple Combinatorial Method Aiding Research on Single-Walled Carbon Nanotube Growth on Substrates.* Japanese Journal of Applied Physics, 2010. **49**(2).

284. Gao, F., et al., *Quality of horizontally aligned single-walled carbon nanotubes: Is methane as carbon source better than ethanol?* Applied Surface Science, 2010. **256**(11): p. 3357-3360.

285. Karoui, S., et al., *Nickel-Assisted Healing of Defective Graphene.* ACS Nano, 2010. **4**(10): p. 6114–6120.

286. Paillet, M., et al., *Versatile synthesis of individual single-walled carbon nanotubes from nickel nanoparticles for the study of their physical properties.* J. Phys. Chem. B, 2004. **108**(44): p. 17112-17118.

287. Paillet, M., et al., *Growth and physical properties of individual single-walled carbon nanotubes.* Diamond and Related Materials, 2005. **14**(9): p. 1426-1431.

288. Ishida, M., et al., *Diameter-controlled carbon nanotubes grown from lithographically defined nanoparticles.* Japanese Journal of Applied Physics, 2004. **43**: p. 1356.

289. Li, Y., et al., *Growth of Single-Walled Carbon Nanotubes from Discrete Catalytic Nanoparticles of Various Sizes.* Journal of Physical Chemistry B, 2001. **105**(46): p. 11424-11431.

290. Lin, M., et al., *Direct observation of single-walled carbon nanotube growth at the atomistic scale.* Nano Letters, 2006. **6**(3): p. 449-452.

291. Rümmeli, M., et al., *Catalyst volume to surface area constraints for nucleating carbon nanotubes.* Journal of Physical Chemistry B, 2007. **111**(28): p. 8234-8241.

292. Ding, F., et al., *Graphitic encapsulation of catalyst particles in carbon nanotube production.* Journal of Physical Chemistry B, 2006. **110**(15): p. 7666-7670.

293. Davis, S.M., et al., *Radiotracer and thermal desorption studies of dehydrogenation and atmospheric hydrogenation of organic fragments obtained from [14C]ethylene chemisorbed over Pt(111) surfaces.* Journal of Catalysis, 1985. **92**(2): p. 240-246.

294. Somorjai, G. and F. Zaera, *Heterogeneous catalysis on the molecular scale.* Journal of Physical Chemistry, 1982. **86**(16): p. 3070-3078.

295. Wu, G., B. Bartlett, and W.T. Tysoe, *The effect of hydrogen on the carbonaceous layer formed on molybdenum model catalysts during high temperature propylene metathesis.* Journal of Catalysis, 1998. **173**(1): p. 172-176.

296. Schünemann, C., et al., *Catalyst Poisoning by Amorphous Carbon During Carbon Nanotube Growth; Fact or Fiction?* ACS Nano, 2011. **5**(11): p. 8928–8934.

297. Marchand, M., et al., *Growing a Carbon Nanotube Atom by Atom:"And Yet It Does Turn".* Nano Letters, 2009. **9**(8): p. 2961-2966.

298. Hata, K., et al., *Water-Assisted Highly Efficient Synthesis of Impurity-Free Single-Walled Carbon Nanotubes.* Science (Washington, D. C., 1883-), 2004. **306**: p. 1362-1364.

299. Futaba, D.N., et al., *84% Catalyst Activity of Water-Assisted Growth of Single Walled Carbon Nanotube Forest Characterization by a Statistical and Macroscopic Approach.* Journal of Physical Chemistry B, 2006. **110**: p. 8035-8038.

300. Futaba, D.N., et al., *General rules governing the highly efficient growth of carbon nanotubes.* Advanced Materials, 2009. **21**(47): p. 4811-4815.

301. Zhou, W., et al., *Synthesis of High Density, Large-Diameter and Aligned Single-Walled Carbon Nanotubes by Multiple-Cycle Growth Methods.* ACS Nano, 2011. **5**(5): p. 3849–3857.

302. Wu, B., et al., *Ultrahigh density modulation of aligned single-walled carbon nanotube arrays.* Nano Research, 2011: p. 1-7.

303. Hasegawa, K. and S. Noda, *Millimeter-tall single-walled carbon nanotubes rapidly grown with and without water.* ACS Nano, 2011. **5**(2): p. 975–984.

304. Zhu, L., D.W. Hess, and C.P. Wong, *Monitoring carbon nanotube growth by formation of nanotube stacks and investigation of the diffusion-controlled kinetics.* The Journal of Physical Chemistry B, 2006. **110**(11): p. 5445-5449.

305. Noda, S., et al., *Millimeter-thick single-walled carbon nanotube forests: Hidden role of catalyst support.* Japanese Journal of Applied Physics, 2007. **46**(17): p. L399–L401.

306. Amama, P.B., et al., *Influence of alumina type on the evolution and activity of alumina-supported Fe catalysts in single-walled carbon nanotube carpet growth.* ACS Nano, 2010. **4**(2): p. 895-904.

307. Burt, D.P., et al., *Effects of metal underlayer grain size on carbon nanotube growth.* The Journal of Physical Chemistry C, 2009. **113**(34): p. 15133-15139.

308. Esconjauregui, S., et al., *Growth of high-density vertically aligned arrays of carbon nanotubes by plasma-assisted catalyst pretreatment.* Applied Physics Letters, 2009. **95**: p. 173115.

309. Amama, P.B., et al., *Role of Water in Super Growth of Single-Walled Carbon Nanotube Carpets.* Nano Letters, 2008. **9**(1): p. 44-49.

310. Hasegawa, K. and S. Noda, *Moderating carbon supply and suppressing Ostwald ripening of catalyst particles to produce 4.5-mm-tall single-walled carbon nanotube forests.* Carbon, 2011. **49**(13): p. 4497-4504.

311. Finnie, P., A. Li-Pook-Than, and J. Lefebvre, *The dynamics of the nucleation, growth and termination of single-walled carbon nanotubes from in situ Raman spectroscopy during chemical vapor deposition.* Nano Research, 2009. **2**: p. 783-792.

312. Futaba, D.N., et al., *Kinetics of Water-Assisted Single-Walled Carbon Nanotube Synthesis Revealed by a Time-Evolution Analysis.* Physical Review Letters, 2005. **95**: p. 056104.

313. Puretzky, A.A., et al., *In situ measurements and modeling of carbon nanotube array growth kinetics during chemical vapor deposition.* Applied Physics A, Materials Science & Processing, 2005. **81**(2): p. 223-240.

314. Einarsson, E., et al., *Growth dynamics of vertically aligned single-walled carbon nanotubes from in situ measurements.* Carbon, 2008. **46**: p. 923-930.

315. Wirth, C.T., et al., *Diffusion-and reaction-limited growth of carbon nanotube forests.* ACS Nano, 2009. **3**(11): p. 3560-3566.

316. Baker, R.T.K., et al., *The formation of filamentous carbon from decomposition of acetylene over vanadium and molybdenum.* Carbon, 1983. **21**(5): p. 463-468.

317. Baker, R.T.K., J.J. Chludzinski Jr, and C.R.F. Lund, *Further studies of the formation of filamentous carbon from the interaction of supported iron particles with acetylene.* Carbon, 1987. **25**(2): p. 295-303.

318. Zaikovskii, V.I., V.V. Chesnokov, and R.A. Buyanov, *The Relationship between the State of Active Species in a Ni/Al2O3Catalyst and the Mechanism of Growth of Filamentous Carbon.* Kinetics and Catalysis, 2001. **42**(6): p. 813-820.

319. Cooper, B.J. and D.L. Trimm, *Carbon deposition from propylene on polycrystalline and single crystal iron.* Journal of Catalysis, 1980. **62**(1): p. 35-43.

320. Bartsch, K., et al., *On the diffusion-controlled growth of multiwalled carbon nanotubes.* Journal of Applied Physics, 2005. **97**: p. 114301.

321. In, J.B., et al., *Growth Kinetics of Vertically Aligned Carbon Nanotube Arrays in Clean Oxygen-free Conditions.* ACS Nano, 2011. **5**(12): p. 9602-9610.

322. Bronikowski, M.J., *Longer nanotubes at lower temperatures: the influence of effective activation energies on carbon nanotube growth by thermal chemical vapor deposition.* The Journal of Physical Chemistry C, 2007. **111**(48): p. 17705-17712.

323. Ducati, C., et al., *Temperature selective growth of carbon nanotubes by chemical vapor deposition.* Journal of Applied Physics, 2002. **92**: p. 3299.

324. Meshot, E.R., et al., *Engineering vertically aligned carbon nanotube growth by decoupled thermal treatment of precursor and catalyst.* ACS Nano, 2009. **3**(9): p. 2477-2486.

325. Ni, L., et al., *Kinetic study of carbon nanotube synthesis over Mo/Co/MgO catalysts.* Carbon, 2006. **44**(11): p. 2265-2272.

326. Cervantes-Sodi, F., et al., *Viscous State Effect on the Activity of Fe Nanocatalysts.* ACS Nano, 2010. **4**(11): p. 6950–6956.

327. Ma, H., L. Pan, and Y. Nakayama, *Modelling the growth of carbon nanotubes produced by chemical vapor deposition.* Carbon, 2011. **49**(3): p. 854-861.

328. Huang, Z.P., et al., *Effect of nickel, iron and cobalt on growth of aligned carbon nanotubes.* Applied Physics A, Materials Science & Processing, 2002. **74**: p. 387-391.

329. Lee, D.H., S.O. Kim, and W.J. Lee, *Growth Kinetics of Wall-Number Controlled Carbon Nanotube Arrays.* The Journal of Physical Chemistry C, 2010. **114**(8): p. 3454-3458.

330. Hasegawa, K. and S. Noda, *Real-time monitoring of millimeter-tall vertically aligned single-walled carbon nanotube growth on combinatorial catalyst library.* Japanese Journal of Applied Physics, 2010. **49**(8): p. 5104.

331. Patole, S.P., et al., *Kinetics of catalyst size dependent carbon nanotube growth by growth interruption studies.* Applied Physics Letters, 2010. **96**(9): p. 094101.

332. Borgström, M.T., et al., *Synergetic nanowire growth.* Nature Nanotechnology, 2007. **2**(9): p. 541-544.

333. Jeong, G.H., et al., *Effect of catalyst pattern geometry on the growth of vertically aligned carbon nanotube arrays.* Carbon, 2009. **47**(3): p. 696-704.

334. Chiang, W.H. and R.M. Sankaran, *Relating carbon nanotube growth parameters to the size and composition of nanocatalysts.* Diamond and Related Materials, 2009. **18**(5-8): p. 946-952.

335. Page, A.J., et al., *Comparison of single-walled carbon nanotube growth from Fe and Ni nanoparticles using quantum chemical molecular dynamics methods.* Carbon, 2010. **48**(11): p. 3014-3026.

336. Liu, B., et al., *Growth velocity and direct length-sorted growth of short single-walled carbon nanotubes by a metal-catalyst-free chemical vapor deposition process.* ACS Nano, 2009. **3**(11): p. 3421-3430.

337. Liu, H., et al., *Investigation of catalytic properties of Al2O3 particles in the growth of single-walled carbon nanotubes.* Journal of Nanoscience and Nanotechnology, 2010. **10**(6): p. 4068-4073.

338. Motta, M.S., et al., *The Role of Sulphur in the Synthesis of Carbon Nanotubes by Chemical Vapour Deposition at High Temperatures.* Journal of Nanoscience and Nanotechnology, 2008. **8**(5): p. 2442-2449.

339. Zhu, L., D.W. Hess, and C.-P. Wong, *Monitoring Carbon Nanotube Growth by Formation of Nanotube Stacks and Investigation of the Diffusion-Controlled Kinetics.* The Journal of Physical Chemistry B, 2006. **110**(11): p. 5445-5449.

340. Xiang, R., et al., *Growth Deceleration of Vertically Aligned Carbon Nanotube Arrays: Catalyst Deactivation or Feedstock Diffusion Controlled?* J. Phys. Chem. C, 2008. **112**(13): p. 4892-4896.

341. Zheng, L.X., et al., *Ultralong single-wall carbon nanotubes.* Nature Materials, 2004. **3**: p. 673-676.

342. Jin, Z., et al., *Ultralow Feeding Gas Flow Guiding Growth of Large-Scale Horizontally Aligned Single-Walled Carbon Nanotube Arrays.* Nano Letters, 2007. **7**(7): p. 2073-2079.

343. Wen, Q., et al., *Growing 20 cm Long DWNTs/TWNTs at a Rapid Growth Rate of 80–90 μm/s.* Chemistry of Materials, 2010. **22**(4): p. 1294-1296.

344. Huang, L., et al., *Cobalt Ultrathin Film Catalyzed Ethanol Chemical Vapor Deposition of Single-Walled Carbon Nanotubes.* The Journal of Physical Chemistry B, 2006. **110**(23): p. 11103-11109.

345. Wang, X., et al., *Fabrication of Ultralong and Electrically Uniform Single-Walled Carbon Nanotubes on Clean Substrates.* Nano Letters, 2009. **9**(9): p. 3137-3141.

346. Diarra, M., et al., *Importance of carbon solubility and wetting properties of nickel nanoparticles for single wall nanotube growth.* Submitted, 2012.

347. Baker, R.T.K. and P.S. Harris, in *Chemistry and Physics of Carbon, volume 14*, P.L.W. Jr. and P.A. Thrower, Editors. 1978, Marcel Dekker: New York. p. 83.

348. Wagner, R.S. and W.C. Ellis, *Vapor-Liquid-Solid Mechanism of Single Crystal Growth.* Applied Physics Letters, 1964. **4**(5): p. 89-90.

349. Kukovitsky, E.F., S.G. L'vov, and N.A. Sainov, *VLS-growth of carbon nanotubes from the vapor.* Chemical Physics Letters, 2000. **317**: p. 65-70.

350. Page, A.J., et al., *SWNT Nucleation from Carbon-Coated SiO2 Nanoparticles via a Vapor−Solid−Solid Mechanism.* Journal of the American Chemical Society, 2010. **133**(3): p. 621-628.

351. Wirth, C.T., S. Hofmann, and J. Robertson, *State of the catalyst during carbon nanotube growth.* Diamond and Related Materials, 2009. **18**(5–8): p. 940-945.

352. Hofmann, S., et al., *State of Transition Metal Catalysts During Carbon Nanotube Growth.* The Journal of Physical Chemistry C, 2009. **113**(5): p. 1648-1656.

353. Emmenegger, C., et al., *Synthesis of carbon nanotubes over Fe catalyst on aluminium and suggested growth mechanism.* Carbon, 2003. **41**(3): p. 539-547.

354. Sharma, R., et al., *Site-Specific Fabrication of Fe Particles for Carbon Nanotube Growth.* Nano Letters, 2009. **9**(2): p. 689-694.

355. He, Z., et al., *Iron Catalysts for the Growth of Carbon Nanofibers: Fe, Fe3C or Both?* Chemistry of Materials, 2011. **23**(24): p. 5379-5387.

356. Wang, Q., et al., *The mechanism of single-walled carbon nanotube growth and chirality selection induced by carbon atom and dimer addition.* ACS Nano, 2010. **4**(2): p. 939-946.

357. Lee, G.D., et al., *Catalytic decomposition of acetylene on Fe (001): A first-principles study.* Physical Review B, 2002. **66**(8): p. 081403.

358. Vasenkov, A., D. Sengupta, and M. Frenklach, *Multiscale Modeling Catalytic Decomposition of Hydrocarbons during Carbon Nanotube Growth.* The Journal of Physical Chemistry B, 2009. **113**(7): p. 1877-1882.

359. Maruyama, S. and Y. Miyauchi. *ACCVD Growth, Raman and Photoluminescence Spectroscopy of Isotopically Modified Single-Walled Carbon Nanotubes.* in *AIP Conference Proceedings.* 2005.

360. Vesselli, E., et al., *Ethanol Decomposition: C-C Cleavage Selectivity on Rh (111).* ChemPhysChem, 2004. **5**(8): p. 1133-1140.

361. Page, A.J., et al., *Mechanisms of Single-Walled Carbon Nanotube Nucleation, Growth, and Healing Determined Using QM/MD Methods.* Accounts of Chemical Research, 2010. **43**: p. 1375-1385.

362. Amara, H., C. Bichara, and F. Ducastelle, *Understanding the Nucleation Mechanisms of Carbon Nanotubes in Catalytic Chemical Vapor Deposition.* Physical Review Letters, 2008. **100**: p. 056105.

363. Neyts, E.C., et al., *Catalyzed Growth of Carbon Nanotube with Definable Chirality by Hybrid Molecular Dynamics-Force Biased Monte Carlo Simulations.* ACS Nano, 2010. **4**(11): p. 6665-6672.

364. Wesep, R.G.V., et al., *Stable carbon nanoarches in the initial stages of epitaxial growth of graphene on Cu(111).* The Journal of Chemical Physics, 2011. **134**(17): p. 171105.

365. Loginova, E., et al., *Evidence for graphene growth by C cluster attachment.* New Journal of Physics, 2008. **10**: p. 093026.

366. Feng, H., J. Ma, and Z. Hu, *Six-membered-ring-based radical mechanism for catalytic growth of carbon nanotubes with benzene precursor.* The Journal of Physical Chemistry C, 2009. **113**(37): p. 16495-16502.

367. Eres, G., et al., *Model for self-assembly of carbon nanotubes from acetylene based on real-time studies of vertically aligned growth kinetics.* The Journal of Physical Chemistry C, 2009. **113**(35): p. 15484-15491.

368. Plata, D.L., et al., *Multiple alkynes react with ethylene to enhance carbon nanotube synthesis, suggesting a polymerization-like formation mechanism.* ACS Nano, 2010. **4**(12): p. 7185–7192.

369. Dai, H., et al., *Single-wall nanotubes produced by metal-catalyzed disproportionation of carbon monoxide.* Chemical Physics Letters, 1996. **260**: p. 471-475.

370. Kuznetsov, V.L., et al., *Thermodynamic analysis of nucleation of carbon deposits on metal particles and its implications for the growth of carbon nanotubes.* Physical Review B, 2001. **64**(23): p. 235401.

371. Dijon, J., et al., *How to switch from a tip to base growth mechanism in carbon nanotube growth by catalytic chemical vapour deposition.* Carbon, 2010. **48**(13): p. 3953-3963.

372. Kanzow, H., C. Lenski, and A. Ding, *Single-wall carbon nanotube diameter distributions calculated from experimental parameters.* Physical Review B: Condensed Matter, 2001. **63**: p. 125402.

373. Schebarchov, D., et al., *Interplay of Wetting and Elasticity in the Nucleation of Carbon Nanotubes.* Physical Review Letters, 2011. **107**(18): p. 185503.

374. Zhao, J., A. Martinez-Limia, and P.B. Balbuena, *Understanding catalysed growth of single-wall carbon nanotubes.* Nanotechnology, 2005. **16**(7): p. S575-S581.

375. Page, A.J., S. Irle, and K. Morokuma, *Polyyne Chain Growth and Ring Collapse Drives Ni-Catalyzed SWNT Growth: A QM/MD Investigation.* Journal of Physical Chemistry C, 2010. **114**(18): p. 8206-8211.

376. Neyts, E.C., A.C.T. van Duin, and A. Bogaerts, *Changing Chirality during Single-Walled Carbon Nanotube Growth: A Reactive Molecular Dynamics/Monte Carlo Study.* Journal of the American Chemical Society, 2011. **133**(43): p. 17225-17231.

377. Ribas, M., et al., *Nanotube nucleation versus carbon-catalyst adhesion–Probed by molecular dynamics simulations.* The Journal of Chemical Physics, 2009. **131**: p. 224501.

378. Pigos, E., et al., *Carbon Nanotube Nucleation Driven by Catalyst Morphology Dynamics.* ACS Nano, 2011. **5**(12): p. 10096-10101.

379. Brinkmann, G., et al., *A census of nanotube caps.* Chemical Physics Letters, 1999. **315**(5): p. 335-347.

380. Reich, S., L. Li, and J. Robertson, *Structure and formation energy of carbon nanotube caps.* Physical Review B: Condensed Matter, 2005. **72**: p. 165423.

381. Reich, S., L. Li, and J. Robertson, *Control the chirality of carbon nanotubes by epitaxial growth.* Chemical Physics Letters, 2006. **421**: p. 469–472.

382. Liu, Y., A. Dobrinsky, and B.I. Yakobson, *Graphene Edge from Armchair to Zigzag: The Origins of Nanotube Chirality?* Physical Review Letters, 2010. **105**(23): p. 235502.

383. Koziol, K.K.K., C. Ducati, and A.H. Windle, *Carbon Nanotubes with Catalyst Controlled Chiral Angle.* Chemistry of Materials, 2010. **22**(17): p. 4904-4911.

384. Luo, Z., et al., *Growth Mechanism of Hexagonal Shape Graphene Flakes with Zigzag Edges.* ACS Nano, 2011. **5**(11): p. 9154–9160.

385. Booth, T.J., et al., *Discrete Dynamics of Nanoparticle Channelling in Suspended Graphene.* Nano Letters, 2011. **11**(7): p. 2689–2692.

386. Zhang, Y., et al., *Anisotropic Hydrogen Etching of Chemical Vapor Deposited Graphene.* ACS Nano, 2012. **6**(1): p. 126–132.

387. Shu, H., et al., *Edges Structural Stability and Kinetics of Graphene Chemical Vapor Deposition (CVD) Growth.* ACS Nano, 2012. **6**(4): p. 3243–3250.

388. Rao, R., et al., *In situ evidence for chirality-dependent growth rates of individual carbon nanotubes.* Nature Materials, 2012. **11**(3): p. 213-216.

389. Zhao, J. and P.B. Balbuena, *Structural and reactivity properties of finite length cap-ended single-wall carbon nanotubes.* Journal of Physical Chemistry A, 2006. **110**(8): p. 2771-2775.

390. Wang, Q., et al., *Charge Transfer between Metal Clusters and Growing Carbon Structures in Chirality-Controlled Single-Walled Carbon Nanotube Growth.* The Journal of Physical Chemistry Letters, 2011. **2**: p. 1009-1014.

391. Gomez-Gualdron, D.A. and P.B. Balbuena, *Effect of metal cluster-cap interactions on the catalyzed growth of single-wall carbon nanotubes.* The Journal of Physical Chemistry C, 2008. **113**(2): p. 698-709.

392. Ding, F., A.R. Harutyunyan, and B.I. Yakobson, *Dislocation theory of chirality-controlled nanotube growth.* Proceedings of the National Academy of Sciences, 2009. **106**(8): p. 2506.

393. Dumlich, H. and S. Reich, *Chirality-dependent growth rate of carbon nanotubes: A theoretical study.* Physical Review B, 2010. **82**(8): p. 085421.

394. Chandra, B., et al., *Molecular-Scale Quantum Dots from Carbon Nanotube Heterojunctions.* Nano Letters, 2009. **9**(4): p. 1544-1548.

395. Kim, J., et al., *Dynamics of Local Chirality during SWCNT Growth: Armchair versus Zigzag Nanotubes.* Journal of the American Chemical Society, 2012. **134**(22): p. 9311-9319.

396. Börjesson, A. and K. Bolton, *First Principles Studies of the Effect of Ostwald Ripening on Carbon Nanotube Chirality Distributions.* ACS Nano, 2011. **5**(2): p. 771-779.

397. Chiashi, S., et al., *Cold wall CVD generation of single-walled carbon nanotubes and in situ Raman scattering measurements of the growth stage.* Chemical Physics Letters, 2004. **386**: p. 89-94.

398. Saito, R., et al., *Raman spectroscopy of graphene and carbon nanotubes.* Advances in Physics, 2011. **60**(3): p. 413-550.

399. Maciel, I.O., et al., *Electron and phonon renormalization near charged defects in carbon nanotubes.* Nature Materials, 2008. **7**(11): p. 878-883.

400. Graupner, R., *Raman spectroscopy of covalently functionalized single-wall carbon nanotubes.* Journal of Raman Spectroscopy, 2007. **38**(6): p. 673-683.

401. Zhou, Z.P., et al., *Temperature dependence of the Raman spectra of individual carbon nanotubes.* Journal of Physical Chemistry B, 2006. **110**(3): p. 1206-1209.

402. Thomsen, C. and S. Reich, *Raman scattering in carbon nanotubes.* Light Scattering in Solids Ix, 2007. **108**: p. 115-235.

403. Castner, D.G., P.R. Watson, and I.Y. Chan, *X-ray absorption spectroscopy, x-ray photoelectron spectroscopy, and analytical electron microscopy studies of cobalt catalysts. 1. Characterization of calcined catalysts.* The Journal of Physical Chemistry, 1989. **93**(8): p. 3188-3194.

404. Chernavskii, P., G. Pankina, and V. Lunin, *The influence of preparation conditions on the size of Co particles in cobalt-deposited catalysts of the fischer-tropsch synthesis.* Russian Journal of Physical Chemistry A, Focus on Chemistry, 2006. **80**(4): p. 546-550.

405. Khodakov, A.Y., et al., *Reducibility of Cobalt Species in Silica-Supported Fischer–Tropsch Catalysts.* Journal of Catalysis, 1997. **168**(1): p. 16-25.

406. Girardon, J.-S., et al., *Effect of cobalt precursor and pretreatment conditions on the structure and catalytic performance of cobalt silica-supported Fischer–Tropsch catalysts.* Journal of Catalysis, 2005. **230**(2): p. 339-352.

407. Bulavchenko, O., et al., *In situ XRD study of nanocrystalline cobalt oxide reduction.* Kinetics and Catalysis, 2009. **50**(2): p. 192-198.

408. Khodakov, A.Y., R. Bechara, and A. Griboval-Constant, *Structure and catalytic performance of cobalt Fischer Tropsch catalysts supported by periodic mesoporous silicas.* Studies in Surface Science and Catalysis, 2002. **142**: p. 133.

409. Khodakov, A.Y., R. Bechara, and A. Griboval-Constant, *Fischer–Tropsch synthesis over silica supported cobalt catalysts: mesoporous structure versus cobalt surface density.* Applied Catalysis A: General, 2003. **254**(2): p. 273-288.

410. Prieto, G., et al., *Cobalt particle size effects in Fischer–Tropsch synthesis: structural and< i> in situ</i> spectroscopic characterisation on reverse micelle-synthesised Co/ITQ-2 model catalysts.* Journal of Catalysis, 2009. **266**(1): p. 129-144.

411. Kang, J.S., et al., *Nano-Sized Cobalt Based Fischer-Tropsch Catalysts for Gas-to-Liquid Process Applications.* Journal of Nanoscience and Nanotechnology. **10**(5): p. 3700-3704.

412. Suzuki, S. and Y. Kobayashi, *Conductivity decrease in carbon nanotubes caused by low-acceleration-voltage electron irradiation.* Japanese journal of applied physics, 2005. **44**: p. L1498-L1501.

413. Zhou, Z., et al., *Control of electron transport related defects in in situ fabricated single wall carbon nanotube devices.* Applied physics letters, 2006. **89**(13): p. 133124-133124-3.

414. Lee, S., et al., *Paired gap states in a semiconducting carbon nanotube: Deep and shallow levels.* Physical review letters, 2005. **95**(16): p. 166402.

415. Dunlap, B.I., *Relating carbon tubules.* Physical Review B, 1994. **49**(8): p. 5643.

416. Tuinstra, F. and J. Koenig, *Characterization of graphite fiber surfaces with Raman spectroscopy.* Journal of Composite Materials, 1970. **4**(4): p. 492-499.

417. Azam, M.A., et al., *Thermal Degradation of Single-Walled Carbon Nanotubes during Alcohol Catalytic Chemical Vapor Deposition Process.* Japanese Journal of Applied Physics, 2010.

418. Shim, M., et al., *Spectral diversity in Raman G-band modes of metallic carbon nanotubes within a single chirality.* The Journal of Physical Chemistry C, 2008. **112**(33): p. 13017-13023.

419. Pimenta, M., et al., *Studying disorder in graphite-based systems by Raman spectroscopy.* Physical Chemistry Chemical Physics, 2007. **9**(11): p. 1276-1290.

420. Maultzsch, J., S. Reich, and C. Thomsen, *Chirality-selective Raman scattering of the D mode in carbon nanotubes.* Physical Review B, 2001. **64**(12).

421. Romanos, G.E., et al., *Controlling and Quantifying Oxygen Functionalities on Hydrothermally and Thermally Treated Single-Wall Carbon Nanotubes.* The Journal of Physical Chemistry C, 2011. **115**(17): p. 8534-8546.

422. Souza Filho, A.G., et al., *Effect of quantized electronic states on the dispersive Raman features in individual single-wall carbon nanotubes.* Physical Review B, 2001. **65**(3): p. 035404.

423. Campos-Delgado, J., et al., *Chemical Vapor Deposition Synthesis of N-, P-, and Si-Doped Single-Walled Carbon Nanotubes.* ACS Nano, 2010. **4**(3): p. 1696-1702.

424. Geohegan, D.B., et al., *In situ growth rate measurements and length control during chemical vapor deposition of vertically aligned multiwall carbon nanotubes.* Applied Physics Letters, 2003. **83**: p. 1851.

425. Mernagh, T.P., R.P. Cooney, and R.A. Johnson, *Raman spectra of Graphon carbon black.* Carbon, 1984. **22**(1): p. 39-42.

426. Saito, Y., et al., *Growth temperature dependence of indium nitride crystalline quality grown by RF-MBE.* Physica Status Solidi B-Basic Research, 2002. **234**(3): p. 796-800.

427. Golecki, I., F. Reidinger, and J. Marti, *Single-Crystalline, Epitaxial Cubic Sic Films Grown on (100) Si at 750-Degrees-C by Chemical Vapor-Deposition.* Applied Physics Letters, 1992. **60**(14): p. 1703-1705.

428. Truhlar, D.G. and A. Kohen, *Convex Arrhenius plots and their interpretation.* Proceedings of the National Academy of Sciences of the United States of America, 2001. **98**(3): p. 848-851.

429. Chernavskii, P., *Size effects in the oxidation and reduction of cobalt nanoparticles.* RUSSIAN JOURNAL OF PHYSICAL CHEMISTRY C/C OF ZHURNAL FIZICHESKOI KHIMII, 2004. **78**(8): p. 1240-1245.

430. Chappuis, T., et al., *Influence of the Hydrogen Reduction Time and Temperature on the Morphology Evolution and Hematite/Magnetite Conversion of Spindle-Type Hematite Nanoparticles.* CHIMIA International Journal for Chemistry, 2011. **65**(12): p. 979-981.

431. Jourdain, V., et al., *Sequential catalytic growth of carbon nanotubes.* Chemical Physics Letters, 2002. **364**: p. 27-33.

432. Cançado, L.G., et al., *Quantifying defects in graphene via Raman spectroscopy at different excitation energies.* Nano letters, 2011. **11**(8): p. 3190-3196.

433. Choudhary, T. and D. Goodman, *Methane activation on Ni and Ru model catalysts.* Journal of Molecular Catalysis A: Chemical, 2000. **163**(1): p. 9-18.

434. Li, J., A. Kazakov, and F.L. Dryer, *Experimental and numerical studies of ethanol decomposition reactions.* J. Phys. Chem. A, 2004. **108**(38): p. 7671-7680.

Annexes

Annex 1. Models of defect density of CCVD-grown CNT samples

- Model A: Thermally-activated annealing of defects

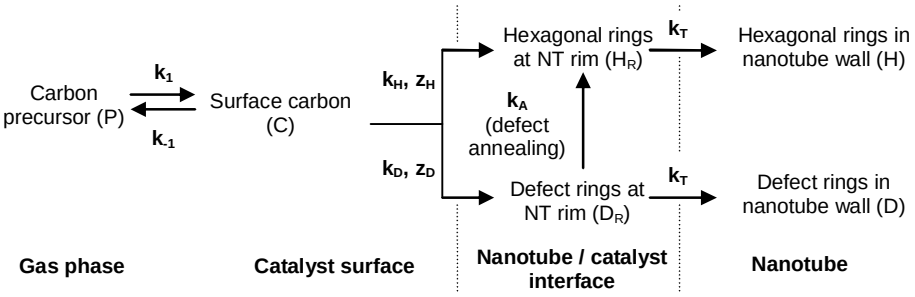

The time dependences of the species concentrations are given by the equations:

$$\dot{P} = k_{-1}C^{n_1} - k_1\frac{P}{P_0} \qquad (a)$$

$$\dot{C} = n_1 k_1 \frac{P}{P_0} - n_1 k_{-1} C^{n_1} - n_H k_H C^{n_H} - n_D k_D C^{n_D} \qquad (b)$$

$$\dot{H}_R = k_H C^{n_H} + k_A D_R - k_T H_R \qquad (c)$$

$$\dot{D}_R = k_D C^{n_D} - k_A D_R - k_T D_R \qquad (d)$$

$$\dot{H} = k_T H_R \qquad (e)$$

$$\dot{D} = k_T D_R \qquad (f)$$

where P is the partial pressure of gaseous carbon precursor; C is the concentration of surface carbon feedstock on the catalyst particle, H_R and D_R are respectively the concentration of hexagonal rings and defects at the nanotube rim, H and D are the concentrations of, respectively, hexagonal rings and defective rings integrated into the nanotube; $k_x = k_x^0 \exp(-E_x/kT)$ are kinetic constants of the elementary steps with k_x^0 and E_x the corresponding pre-exponential factors and activation energies, respectively. n_x is the reaction order of surface carbon feedstock for the corresponding elementary step. $k_x = k_x^0 \exp(-E_x/kT)$ are kinetic constants of the elementary steps with k_x^0 and E_x the corresponding pre-exponential factors and activation energies. Assuming that the gaseous carbon precursor is in rapid quasi-equilibrium with the surface carbon feedstock (*i.e.* k_1, $k_{-1} >> k_2$, k_3) yields:

$C = (K_1 P/P_0)^{1/n_1}$ with $K_1 = k_1/k_{-1} = \exp(-\Delta_r G_1/kT)$.

In these conditions, the solutions of the system are:

$$H = A\left[1 + k_T t - \exp(-k_T t)\right] + B\left[\exp(-k_T t) - 1\right] + B\frac{k_T}{k_A + k_T}\left[1 - \exp(-(k_A + k_T)t)\right] \quad (5)$$

$$D = k_T B\left[t + \frac{\exp(-(k_A + k_T)t) - 1}{k_A + k_T}\right] \quad (6)$$

with:

$$A = \frac{k_A}{k_T} B + \frac{k_H C^{n_H}}{k_T}$$

$$B = \frac{k_D C^{n_D}}{k_A + k_T}$$

In the steady-state regime, the ratio *H/D* tends toward:

$$\lim_{t\to\infty}\left(\frac{H}{D}\right) = \frac{k_A}{k_T} + \frac{k_H C^{n_H}}{k_D C^{n_D}} \frac{k_A + k_T}{k_T}$$

With regard to the parameter dependence of the ratio I_G/I_D, replacing σ^{-1} by the expression of $\lim_{t\to\infty}\left(\frac{H}{D}\right)$ in the relation $\frac{I_G}{I_D} = K\sigma^{-1}$ yields:

$$\frac{I_G}{I_D} = K\left(\frac{k_A}{k_T} + \frac{k_H C^{n_H}}{k_D C^{n_D}} \frac{k_A + k_T}{k_T}\right) \qquad \text{or, equivalently:}$$

$$\ln\left(\frac{I_G}{I_D}\right) = \ln K + \ln\left(\frac{k_A}{k_T} + \frac{k_H C^{n_H}}{k_D C^{n_D}} \frac{k_A + k_T}{k_T}\right)$$

If the annealing of defects is only activated at high temperature (*i.e.* $E_A > E_T$), then $k_A << k_T$ at low temperature and one gets:

$$\ln\left(\frac{I_G}{I_D}\right) = \ln K + \ln\left(\frac{k_H C^{n_H}}{k_D C^{n_D}}\right) = \ln K + \ln\left[\frac{k_H^0}{k_D^0}\right] - \frac{E_H - E_D}{kT} + \left(n_H - n_D\right)\ln C$$

Injecting $C = (K_1 P/P_0)^{1/n_1}$ with $K_1 = k_1/k_{-1} = \exp(-\Delta_r G_1 / kT)$, one gets:

$$\ln\left(\frac{I_G}{I_D}\right) = A''_{LT} - \frac{E''_{LT}}{kT} + n''_{LT} \ln\frac{P}{P_0}$$

with $A''_{LT} = \ln\left(K\frac{k_H^0}{k_D^0}\right)$, $E''_{LT} = E_H - E_D + n''_{LT}\,\Delta_r G_1$ and $n''_{LT} = \frac{n_H - n_D}{n_1}$.

In this case, I_G/I_D displays an Arrhenius law with regard to temperature and a power law dependence on the precursor pressure. At the opposite, in the high temperature case where $k_A >> k_T$ and $k_H >> k_D$, one gets:

$$\ln\left(\frac{I_G}{I_D}\right) = A''_{HT} - \frac{E''_{HT}}{kT} + n''_{HT} \ln\frac{P}{P_0}$$

with $A''_{HT} = \ln\left(K\frac{k_A^0 k_H^0}{k_T^0 k_D^0}\right)$, $E''_{HT} = E_A + E_H - E_T - E_D + n''_{HT}\,\Delta_r G_1$ and $n''_{HT} = \frac{n_H - n_D}{n_1}$.

It is apparent that I_G/I_D also displays an Arrhenius law with regard to temperature and a power law with regard to precursor pressure. However, in the high temperature case, the apparent activation energy is higher by the value E_A-E_T.

Since $E_A > E_T$, E_A-E_T is always positive which means that the apparent activation energy for the high temperature case is always higher than the apparent activation energy. Therefore, this model intrinsically yields a concave Arrhenius plot.

- Model B: Thermally-activated transition of intermediate states

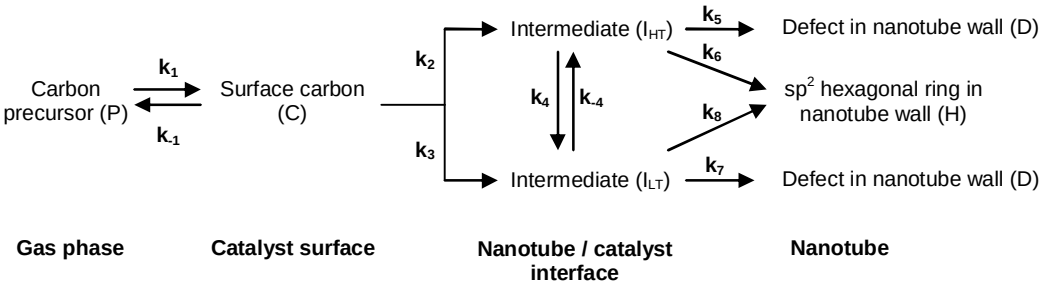

The time dependences of the species concentrations are given by the equations:

$$\dot{P} = k_{-1} C^{n_1} - k_1 \frac{P}{P_0} \qquad (a)$$

$$\dot{C} = n_1 k_1 \frac{P}{P_0} - n_1 k_{-1} C^{n_1} - n_2 k_2 C^{n_2} - n_3 k_3 C^{n_3} \qquad (b)$$

$$\dot{I}_{HT} = k_2 C^{n_2} + k_{-4} I_{LT} - k_4 I_{HT} - k_5 I_{HT} C^{n_5} - k_6 I_{HT} C^{n_6} \qquad (c)$$

$$\dot{I}_{LT} = k_3 C^{n_3} + k_4 I_{HT} - k_{-4} I_{LT} - k_7 I_{LT} C^{n_7} - k_8 I_{LT} C^{n_8} \qquad (d)$$

$$\dot{H} = k_6 I_{HT} C^{n_6} + k_8 I_{LT} C^{n_8} \qquad (e)$$

$$\dot{D} = k_5 I_{HT} C^{n_5} + k_7 I_{LT} C^{n_7} \qquad (f)$$

where P is the partial pressure of gaseous carbon precursor; C is the concentration of surface carbon feedstock on the catalyst particle; I_{LT} and I_{HT} are the concentrations of the intermediate states dominant at low and high temperatures, respectively; H and D are the concentrations of, respectively, hexagonal rings and defective rings integrated into the nanotube; $k_x = k_x^0 \exp(-E_x/kT)$ are kinetic constants of the elementary steps with k_x^0 and E_x the corresponding pre-exponential factors and activation energies, respectively. n_x is the reaction order of surface carbon feedstock for the corresponding elementary step.

In the steady-state regime, the concentrations of the reaction intermediates C, I_{LT}, I_{HT} reaching constant values, the ratio H/D finally tends toward:

$$\lim_{t\to\infty}\left(\frac{H}{D}\right) = \frac{k_6 C^{n_6} + k_8 C^{n_8} K_4}{k_5 C^{n_5} + k_7 C^{n_7} K_4}$$

with $K_4(T) = \frac{I_{LT}}{I_{HT}}$. From this relation, it is obvious that if K_4 tends toward zero, the defect density will be governed by the competition between steps 5 and 6, while, if K_4 tends toward very large values, the defect density will be controlled by the competition between steps 7 and 8. With regard to the parameter dependence of the ratio I_G/I_D, replacing σ^{-1} by the expression of $\lim_{t\to\infty}\left(\frac{H}{D}\right)$ in the relation $\frac{I_G}{I_D} = K\sigma^{-1}$ yields:

$$\frac{I_G}{I_D} = K\left(\frac{k_6 C^{n_6} + k_8 C^{n_8} K_4}{k_5 C^{n_5} + k_7 C^{n_7} K_4}\right)$$ or, equivalently:

$$\ln\left(\frac{I_G}{I_D}\right) = \ln K + \ln\left(\frac{k_6 C^{n_6} + k_8 C^{n_8} K_4}{k_5 C^{n_5} + k_7 C^{n_7} K_4}\right)$$

In the high temperature case where K_4 tends toward zero, the relation becomes:

$$\ln\left(\frac{I_G}{I_D}\right) = \ln K + \ln\left(\frac{k_6 C^{n_6}}{k_5 C^{n_5}}\right) = \ln K + \ln\left[\frac{k_6^0}{k_5^0}\right] - \frac{E_6 - E_5}{kT} + \left(n_6 - n_5\right)\ln C$$

Assuming that the gaseous carbon precursor is in rapid quasi-equilibrium with the surface carbon feedstock (*i.e.* k_1, k_{-1} >> k_2, k_3) yields $C = (K_1 P/P_0)^{1/n_1}$ in the steady state with $K_1 = k_1/k_{-1} = \exp(-\Delta_r G_1 / kT)$, the relation then becomes:

$$\ln\left(\frac{I_G}{I_D}\right) = A_{HT} - \frac{E_{HT}}{kT} + n_{HT} \ln\frac{P}{P_0}$$

with $A_{HT} = \ln\left(K\frac{k_6^0}{k_5^0}\right)$, $E_{HT} = E_6 - E_5 + n_{HT}\Delta_r G_1$ and $n_{HT} = \frac{n_6 - n_5}{n_1}$.

In the low temperature case where K_4 tends toward very large values, a similar reasoning leads to: $\ln\left(\frac{I_G}{I_D}\right) = A_{LT} - \frac{E_{LT}}{kT} + n_{LT} \ln\frac{P}{P_0}$

with $A_{LT} = \ln\left(K\frac{k_8^0}{k_7^0}\right)$, $E_{LT} = E_8 - E_7 + n_{LT}\Delta_r G_1$ and $n_{LT} = \frac{n_8 - n_7}{n_1}$.

Since there is no condition on the sign of $(E_6\text{-}E_5)\text{-}(E_8\text{-}E_7)$, this model can yield either a concave or a convex Arrhenius plot.

- Model C: Thermally-activated creation of defects

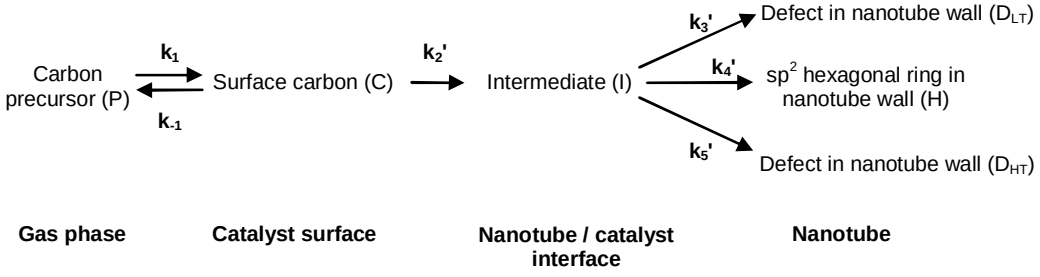

The time dependences of the species concentrations are given by the equations:

$$\dot{P} = k_{-1} C^{n_1} - k_1 \frac{P}{P_0} \qquad (a)$$

$$\dot{C} = n_1 k_1 \frac{P}{P_0} - n_1 k_{-1} C^{n_1} - n_2' k_2' C^{n_2'} \qquad (b)$$

$$\dot{I} = k_2' C^{n_2'} - k_3' C^{n_3'} I - k_4' C^{n_4'} I - k_5' C^{n_5'} I \qquad (c)$$

$$\dot{H} = k_4' C^{n_4'} I \qquad (d)$$

$$\dot{D} = \dot{D}_{LT} + \dot{D}_{HT} = k_3' C^{n_3'} I + k_5' C^{n_5'} I \qquad (e)$$

where P is the partial pressure of gaseous carbon precursor; C is the concentration of surface carbon feedstock on the catalyst particle; I is the concentration of the intermediate state at the nanotube rim; H is the concentration of hexagonal rings integrated into the nanotube; D_{LT} and D_{HT} are the concentrations of defects integrated into the nanotube by the low- and high-activation-energy mechanisms, respectively. $k_x' = k_x^0' \exp(-E_x'/kT)$ are kinetic constants of the elementary steps with k_x^0' and E_x' the corresponding pre-exponential factors and activation energies, respectively. n_x' is the reaction order of surface carbon feedstock for the corresponding elementary step.

In the steady-state regime, the concentrations of the reaction intermediates C and I reaching constant values, the ratio H/D finally tends toward:

$$\lim_{t\to\infty}\left(\frac{H}{D}\right) = \frac{k_4' C^{n_4'}}{k_3' C^{n_3'} + k_5' C^{n_5'}}$$

From this relation, it is seen that, in the case $k_3' C^{n_3'} >> k_5' C^{n_5'}$, the defect density will be governed by the competition between steps 4' and 3', while, in the case $k_3' C^{n_3'} << k_5' C^{n_5'}$, the defect density will be controlled by the competition between steps 4' and 5'. With regard to the parameter dependence of the ratio I_G/I_D, replacing σ^{-1} by the expression of $\lim_{t\to\infty}\left(\frac{H}{D}\right)$ in relation (1) yields:

$$\frac{I_G}{I_D} = K\left(\frac{k_4' C^{n_4'}}{k_3' C^{n_3'} + k_5' C^{n_5'}}\right) \qquad \text{or, equivalently:}$$

$$\ln\left(\frac{I_G}{I_D}\right) = \ln K + \ln\left(\frac{k_4' C^{n_4'}}{k_3' C^{n_3'} + k_5' C^{n_5'}}\right)$$

In the high temperature case where $k_3' C^{n_3'} << k_5' C^{n_5'}$, the relation becomes:

$$\ln\left(\frac{I_G}{I_D}\right) = \ln K + \ln\left(\frac{k_4' C^{n_4'}}{k_5' C^{n_5'}}\right) = \ln K + \ln\left[\frac{k_4^0'}{k_5^0'}\right] - \frac{E_4' - E_5'}{kT} + (n_4' - n_5')\ln C$$

Assuming that the gaseous carbon precursor is in rapid quasi-equilibrium with the surface carbon feedstock (*i.e.* k_1, k_{-1} >> k_2') yields $C = (K_1 P/P_0)^{1/n_1}$ in the steady state with $K_1 = k_1/k_{-1} = \exp(-\Delta_r G_1/kT)$, one gets:

$$\ln\left(\frac{I_G}{I_D}\right) = A'_{HT} - \frac{E'_{HT}}{kT} + n'_{HT} \ln\frac{P}{P_0}$$

with $A'_{HT} = \ln\left(K\frac{k_4^{0\prime}}{k_5^{0\prime}}\right)$, $E'_{HT} = E_4' - E_5' + n'_{HT}\,\Delta_r G_1$ and $n'_{HT} = \frac{n_4' - n_5'}{n_1}$.

In the low temperature case where $k_3' C^{n_3'} >> k_5' C^{n_5'}$, a similar reasoning leads to:

$$\ln\left(\frac{I_G}{I_D}\right) = A'_{LT} - \frac{E'_{LT}}{kT} + n'_{LT}\ln\frac{P}{P_0} \qquad (k')$$

with $A'_{LT} = \ln\left(K\frac{k_4^{0\prime}}{k_3^{0\prime}}\right)$, $E'_{LT} = E_4' - E_3' + n'_{LT}\,\Delta_r G_1$ and $n'_{LT} = \frac{n_4' - n_3'}{n_1}$.

Since $\triangle_g G_1$ is negative (*i.e.* the precursor decomposition is thermodynamically favoured) and the model imposes that $E_5' > E_4' > E_3'$, it follows that the apparent activation energy at high temperature will be negative. In other words, this model intrinsically leads to a decrease of I_G/I_D in the high temperature regime which disagrees with our experimental observations.

Annex 2. Activation energies for ν, τ, $\nu\tau$ and G/D

		E_a (eV)		
		$T < T_L$	$T_L < T < T_H$	$T > T_H$
EtOH – Ni T_K = 580°C T_L = 680°C T_H = 720°C	ν	**2.4** ± 0.6 below T_K **0.44** ± 0.06 above T_K	**-1.1** ± ?	**-0.7** ± 0.4
	τ	**-0.9** ± 0.2 below T_K **0.5** ± 0.1 above T_K	**1.2** ± ?	**-0.1** ± 0.2
	$\nu\tau$	**1.3** ± 0.2	**-0.1** ± ?	**-0.7** ±0.2
	G/D	**1.14** ± 0.09	**0.32** ± 0.03	
CH_4 – Ni T_L = 625°C T_H = 750°C	ν	**5** ± 1	**0.2** ± 0.3	**-1.6** ± 0.1
	τ	**-2.1** ± 0.3	**-0.2** ± 0.1	**-0.3** ± 0.1
	$\nu\tau$	**3.7** ± 0.6	**-0.23** ± 0.02	**-2.2** ± 0.4
	G/D	**1.47** ± 0.3	**0.58** ± 0.02	
C_2H_2 – Ni T_K = 570°C T_L = 600°C T_H = 800°C	ν	**6** ± 3 below T_K **0.6** ± 0.2 above T_K	**0.0** ± 0.3	**-2.3** ± ?
	τ	**-1.0** ± 0.7 below T_K **1.1** ± 0.1 above T_K	**-0.2** ± 0.2	
	$\nu\tau$	**3.4** ± 0.6	**-0.3** ± 0.2	**-1.1** ± ?
	G/D	**2.3** ± 0.4	**0.37** ± 0.02	
C_2H_4 – Ni T_L = 625°C T_H = 750°C	ν	**4.5** ± 0.5	**-0.8** ± 0.3	**-2.7** ± 0.3
	τ	**-2.5** ± 0.3	**1.1** ± 0.2	
	$\nu\tau$	**1.7** ± 0.2	**-0.3** ± 0.2	**-0.87** ± 0.09
	G/D	**1.4** ± 0.1	**0.**3 ± 0.3	
EtOH – Co T_L = 650°C T_H = 775°C	ν	**1.7** ± 0.2	**-0.**9 ± 0.2	**0** ± 2
	τ	**-0.34** ± 0.06	**1.2** ± 0.3	**-2** ± 2
	$\nu\tau$	**1.**5 ± 0.2	**0.2** ± 0.2	**-1.4** ± 0.4
	G/D	**0.93** ± 0.06	**0.44** ± 0.03	